Multidimensional Interpretation of Near Surface Electromagnetic Data Measured in Volvi Basin, Northern Greece

INAUGURAL-DISSERTATION

ZUR

ERLANGUNG DES DOKTORGRADES

DER MATHEMATISCH-NATURWISSENSCHAFTLICHEN FAKULTÄT
DER UNIVERSITÄT ZU KÖLN

vorgelegt von
Widodo
aus Java (Indonesien)

Institut für Geophysik und Meteorologie
Universität zu Köln

Köln 2012

Berichterstatter:	Prof. Dr. B. Tezkan
	Prof. Dr. A. Junge

Tag der mündlichen Prüfung: 20.06.2012

Contents

List of Figures

List of Tables

Abstract

The Volvi basin is an alluvial valley located 45 km northeast of the city of Thessaloniki in Northern Greece. It is a neotectonic graben (6 km wide) structure with increasing seismic activity where the large 1978 Thessaloniki earthquake occurred. The seismic response at the site is strongly influenced by local geological conditions. Therefore, the European test site "EURO-SEISTEST" for studying site effects of seismically active areas is installed in the Volvi-Mygdonian Basin.

The ambient noise measurements from the east area of EURO-SEISTEST give strong implication for a complex 3-D tectonic setting. Hence, near surface Electromagnetic (EM) measurements are carried out to understand the location of the local active fault and the top of the basement structure of the research area. The Radiomagnetotelluric (RMT) and Transientelectromagnetic (TEM) measurements are carried out along eight profiles, which include 443 RMT and 107 TEM soundings.

The correlation between the borehole data and the interpreted TEM and RMT model generally shows six layers. The layers are identified as sedimentary and metamorphic rocks which in detail are: silty sand (10 - 30 Ωm), silty clay (10 - 30 Ωm), silty clay marly (30 – 50 Ωm), sandy clay (50 - 80 Ωm) and marly silty sand (> 80 Ωm) and basement (gneiss and schist) (> 80 Ωm) with varying thicknesses.

To analyze the structure of the research area, interpretation of multidimensional models (1-D, 2-D, 3-D) is carried out. The 1-D model and the 2-D model derived from RMT data show a clear indication of the fault structure distribution in the research area. From the analysis, there can be found that the fault structure is associated with marly silty sand with a resistivity of more than 80 Ωm.

The correlation of the RMT 2-D model with the geological map provides a good fitting to the surface structure. Due to the high resistivity of the top layer, the skin depths of the RMT soundings are approximately 35 m. The TEM data gives a detailed description about the deeper structure down to the depth of 200 m. Joint and sequential inversions of RMT and TEM data can provide clear information from the surface to the deep structure. Single and joint inversions of RMT and TEM give a consistent result in which both identify the fault structure.

Three dimensional modeling of RMT data is implemented to provide a representative model of all conductivity structures in the research area. The overall number of cells in the 3-D model is 2,317,000 cells ($nx = 220$ cells, $ny = 220$ cells and $nz = 45$ cells) modeling the research area with size of 2.4 km × 2.4 km. 3-D models provide a detailed description of the normal fault structure at depths of about 5 to

25 m and thicknesses of 20 m. According to the analyses, a normal fault is located next to the EURO-SEISTEST site, with a strike direction of N 70° E.

Zusammenfassung

Das Volvi-Becken befindet sich in einem alluvialen Tal, das 45 km nordöstlich von Thessaloniki im Norden Griechenlands liegt. Es ist eine neotektonische Grabenstruktur (von 6 km Breite) mit zunehmender seismischer Aktivität, in der 1978 das relativ starke Thessaloniki-Erdbeben stattgefunden hat. Die seismische Response vor Ort ist stark beeinflußt von den lokalen geologischen Gegebenheiten. Deshalb wurde der europäische Teststandort "EURO-SEISTEST" im Volvi-Mygdonischen Becken eingerichtet, um ortsabhängige Effekte von seismisch aktiven Gebieten zu untersuchen.

Die Messungen des Hintergrundrauschens aus dem Bereich östlich des EURO - SEISTEST - Gebietes weisen deutlich auf eine eine komplexe, 3-dimensionale, tektonische Struktur hin. Daher werden zur Erkundung der Schichtung oberhalb des Grundgebirges und der Lage der lokalen, aktiven Verwerfung oberflächennahe Elektromagnetik Messungen (EM) durchgeführt. Radiomagnetotellurik (RMT) und Transientelektromagnetik (TEM)-Messungen werden entlang von 8 Profilen durchgeführt, welche 443 RMT- und 107 TEM-Sondierungen beinhalten.

Die Korrelation zwischen den Bohrlochdaten und den interpretierten TEM- und RMT-Modellen zeigt im Allgemeinen einen 6-Schicht-Fall. Die Schichten werden identifiziert als sedimentäre und metamorphe Gesteine, im Einzelnen: schluffiger Sand ($10 - 30\ \Omega$m), schluffiger Lehm ($10 - 30\ \Omega$m), schluffiger lehmiger Mergel ($30 - 50\ \Omega$m), sandiger Lehm ($50 - 80\ \Omega$m) und mergeliger schluffiger Sand ($> 80\ \Omega$m) und Grundgestein (Gneis und Schiefer) ($> 80\ \Omega$m) mit unterschiedlichen Schichtdicken.

Für die Analyse der Struktur des Untersuchungsgebietes wird die Interpretation von mehrdimensionalen Modellen (1-D, 2-D, 3-D) durchgeführt. Die 1-D- und 2-D-Modelle, die aus den RMT-Daten stammen, zeigen deutliche Auswirkungen des Verlaufs der Verwerfungen im Untersuchungsgebiet. Und aus dieser Analyse kann man erkennen, daß die Verwerfungsstruktur mit mergeliger schluffiger Sand eines spezifischen Widerstandes von mehr als $80\ \Omega$m verbunden ist.

Die Korrelation des 2-dimensionalen RMT-Modells mit der geologischen Karte liefert eine gute Anpassung an die oberflächennahe Struktur. Wegen des hohen spezifischen Widerstandes der obersten Schicht liegen die Skintiefen der RMT-Sondierungen etwa bei 35 m. Die TEM-Daten ergeben eine detaillierte Beschreibung der tieferen Struktur bis hinunter zu einer Tiefe von 200 m. Gemeinsame und sequentielle Inversion von RMT- und TEM-Daten liefern eindeutige Informationen von der oberflächennahen bis zur tiefen Struktur. Die Einzelinversionen und die gemeinsame Inversionen von RMT und TEM ergeben einen konsistenten Befund nach welchem beide die Verwerfung identifizieren.

Dreidimensionale Modellierung der RMT-Daten wird ausgeführt, um ein repräsentatives Modell für alle Leitfähigkeitsstrukturen im Messgebiet zu erhalten. Die Gesamtanzahl der Zellen des 3-D-Vorwärtsmodells ist 2.317.000 Zellen (nx = 220 Zellen, ny = 220 Zellen und nz = 45 Zellen), die das Meßgebiet mit einer Ausdehnung von 2,4 km × 2,4 km modellieren. Die 3-D-Modelle liefern eine genaue Beschreibung der Struktur der senkrechten Verwerfung in einer Tiefe von etwa 5 – 25 m bzw. mit einer Mächtigkeit von 25 m. Entsprechend der Analysen befindet sich neben dem EURO-SEISTEST-Gebiet eine senkrechte Verwerfung mit einer Streichrichtung von N 70° O.

Chapter 1

Introduction

It is well known that earthquake generally produces several damages. Moreover if it occurs near densely populated area, it is required additional efforts to provide the detailed knowledge on active faulting, shear wave velocities and its correlation with seismicity in the concerned area. Faults are not usually isolated structures mechanically, however they exist within a population of faults and they may interact with each other through their stress fields. Destructive resulting from the large earthquake amplification effect has been widely reported during recent years, such as the case of Izmit and Duzce earthquake in 1999 [*Hubert-Ferrari et al.*, 2001], Aceh, North Sumatra earthquake in Indonesia [*Ghobarah et al.*, 2006] and Pacific coast in Japan in 2011 [*Takahashi et al.*, 2012]. Prior to an earthquake hazard, it is important to evaluate the behavior of earthquake faults, the expected objective being the assessment of the future seismic hazard.

Northern Greece is an area with one of the most seismically active region in Europe. Several earthquakes occurred during 20^{th} century. The largest earthquake in recent time with magnitude of 6.5 happened in June 1978. The epicenter[1] was located between lakes of Volvi and Langada near Thessaloniki, Northern Greece [*Papazachos et al.*, 1979]. The area was characterized through a neotectonic graben (5.5 km wide) structure associated with an active fault structure, elongated in NNW-SSE direction of the mentioned lakes [*Raptakis et al.*, 2002]. Hence, the "Euroseistest Volvi-Thessaloniki" project, a strong-motion test site (Euroseistest) for Engineering Seismology was put at the location of the epicentre. The main purpose of Euroseistest was to provide high quality geophysical data due to earthquake recordings that allows studying soil-building interactions.

This presented work refers to Volvi basin located in the Mygdonian graben, ca. 45 km of northeast Thessaloniki city. Since the Volvi basin area was affected by earthquake in 1978, various types of geophysical surveys have been conducted with an intensive research. In the past, seismotectonic studies were implemented by various researchers in this area [*Papazachos et al.*, 1979, *Soufleris and Stewart*, 1981, *Mercier et al.*, 1983]. These studies aim to investigate the focal mechanism of fault structure, which was responsible for Thessaloniki earthquake in 1978. The main strike of faults in the area which produced major shock of the recent seismic se-

[1] 40.7°N , 23.3°E, depth = 16 km

quence was found along the Villages Stivos- Scholari - Evangelismos with a dip of N85°E [*Papazachos et al.*, 1979]. The earthquake sequence is a complicated pattern and having irregular direction. The complicated fault patterns are including NW-SE, NE-SW, E-W and NNE-SSW- trending faults, which are associated with active seismic [*Soufleris and Stewart*, 1981, *Pavlides et al.*, 1990, *Tranos et al.*, 2003]. Based on numerical modeling using seismic waves, geological structure in Volvi basin has been constructed with 2-D and 3-D models [*Semblat et al.*, 2005, *Manakou et al.*, 2010]. These models give information about site effects assessment which corresponds to ground motion distribution in Volvi Basin.

Several non-seismic geophysical studies have also been implemented in the Mygdonian Basin. Gravity and aeromagnetic surveys [*Thanassoulas*, 1983] aim to study the deeper structure of the area. These surveys show the existence of a tectonic horst in the basement of Langada valley. In the project, "Euroseistest Volvi-Thessaloniki", MT and gravity studies were carried out in the Volvi Basin in order to define the geological structure of the basin [*Savvaidis et al.*, 2000, *Makris et al.*, 2002]. These results proposed that the basement corresponds to gneiss and schist with rock resistivities larger than 80 Ωm. The top of the basement was located at a depth of around 200 m. *Savvaidis et al.* [2000] and *Makris et al.* [2002] analyzed that the magnetotelluric strike that can be associated with the normal fault strike has a direction of N65°E. The combination of electromagnetic methods such as Controlled Source Audio Magnetotelluric (CSAMT) and Very Low Frequency (VLF) was used to study tufa outcrops in the Mygdonian Basin [*Gurk et al.*, 2007].

Previous CSRMT (Controlled Source Radiomagnetotelluric) measurements for the investigation of the fault structure in the northwest Euroseistest was carried out by Bastani et al (2011). The CSRMT system uses two frequency bands, a CSAMT band with a frequency range from 1 kHz – 10 kHz and a RMT band (without controled source) in a frequency range from 10 - 250 kHz. *Bastani et al.* [2011] proposed that the faults in this area have direction of NE-SW to E-W. Their result provided an image of resistivity variation from surface down to a depth about 100 m. Borehole data showed the depth to the bedrock up to 132 m. Due to limitation of the Lower frequency in this method, the top of basement was not resolved towards the centre of the basin. However, detailed information of the fault structure in the northeast of their research area has not been verified so far.

The ambient noise measurements from the east area of Euroseistest experiment give strong implication for a complex 3-D tectonic setting. This corresponds to local geological structure in the study area. Geological information denotes that the study area consists of four major units [*Jongmans et al.*, 1988]: holocene deposit, fans, lower terrace deposit and the basement of Mygdonian basin composing gneiss and schist, located around 180 meter depth [*Jongmans et al.*, 1988, *Savvaidis et al.*, 2000, *Raptakis et al.*, 2002]. Based on conductivity contrast of these layers and the location of the basement, we carried out a research using shallow (0 - 200 m) EM surveys using RMT and TEM methods. In order to understand the distribution of the active fault and the top of basement structure in northeast EURO-SEISTEST, these surveys were conducted.

The RMT is a relatively new electromagnetic technique of applied geophysics and it is an extension of VLF method to higher frequencies. Müller and his group at Neuchâtel pioneered the RMT technique in its original and scalar form [*Stiefelhagen and Müller*, 1997, *Turberg et al.*, 1994]. It was applied in hydrogeological application in Switzerland. The combination of RMT (14 - 250 kHz) and CSAMT (1 - 12 kHz) measurements for groundwater exploration in an area in Sweden was implemented by *Pedersen et al.* [2005].

One of the RMT devices in environmental application was developed by *Tezkan and Saraev* [2008], *Tezkan* [1999], *Tezkan et al.* [2000], *Tezkan* [2009] and his group at the University of Cologne, Germany. This RMT was based on tensor form, but so far the data was realized as scalar. The RMT technique is one of ground based geophysical methods and is faster than the other ground based geophysical methods. In this method, a huge amount of data can be readily acquired, which corresponds to the frequencies of available radio transmitters. Now the RMT method is more effective in Europe, where transmitters in the necessary frequency range are common.

The RMT technique has been successfully applied for different purposes, mainly in environmental prospecting, such as groundwater exploration [*Pedersen et al.*, 2005, *Tezkan*, 2009] and waste disposal [*Zacher et al.*, 1996, *Tezkan et al.*, 2000]. The application of RMT method is applied for investigation of fracture zone [*Linde and Pedersen*, 2004].

TEM method has gained popularity over the past century and it is an inductive method. TEM is good for mapping the depth of and the extent of conductors, but is relatively less sensitive at distinguished conductivity contrast in low conductivity range [*Pellerin and Wannamaker*, 2005]. In the past, the TEM method was applied for groundwater exploration [*McNeill*, 1990, *Spies and Frischknecht*, 1991, *Sørensen et al.*, 2004]. Recently, the TEM technique has been successfully applied for the measurements of near surface electrical anisotropy in fault zone central North-West Victoria [*Dennis and Cull*, 2012].

The penetration depth of TEM method refers to the depth associated with the distribution of conductivities. The surface conductivity distribution is related to early transient, the deeper structure is corresponding to late time of TEM sounding. The TEM data are sensitive to vertical inhomogeneities, but less affected by lateral inhomogeneities [*Helwig*, 1994]. In order to investigate shallow penetration, a combination of TEM and RMT is recommended.

This dissertation uses a combination of RMT and TEM methods, in order to get overall description of the fault structures in the study area. The joint inversion algorithm for magnetotelluric and direct current was introduced by *Vozoff and Jupp* [1975]. The application of 1-D joint inversion an EM methods (MT and TEM) was used by *Meju* [1996]. *Harinarayana* [1999] provided a summary on the combination of electrical and electromagnetic techniques. Combining data from two different methods of RMT and TEM is beneficial because they are complementary. The RMT data give information about the top layers, whereas the deeper structures can be resolved by TEM data. Combining TEM and RMT inversion was successfully applied on geological and engineering problems in the past [*Tezkan et al.*, 1996, *Schwinn*, 1999, *Steuer*, 2002, *Farag*, 2005].

Joint inversion can increase the number of important model parameters and it can also decrease the ambiguity of the model [*Vozoff and Jupp*, 1975]. Hence, the joint inversion of RMT and TEM data will produce good resolution of model parameters in shallow and deeper parts of fault structure.

Finally, the application of near-surface electromagnetic methods, RMT and TEM, are promising methods to derive geological structure and the top of basement in the graben structure of the Volvi basin. The correlation between a priori information (boreholes data) and the conductivity models of 1-D and 2-D provides accurate interpretation of local geological structure in the study area. The representative conductivity model of structure in the research area can be performed by 3-D forward modeling of RMT data to obtain clear description of fault structure.

1.1 Scope of Presented Thesis

The objective of the presented study is to investigate local geological structure and the top of the basement of the Volvi Basin, Northern Greece. The geophysical surveys are carried out using electromagnetic methods (RMT and TEM). The investigations are limited to near surface studies with shallow depth (< 200 m). It is expected that the complex geological structure and the vertical distribution of resistivity layers can be defined by RMT and TEM methods.

DIKTI (Directorate General of Higher Education of Indonesia) scholarship financed me to pursue during my PhD studies at University of Cologne, Germany. The field campaign was supported by Marie Curie project: IGSEA – Integrated Neoseismic Geophysichal Studies to Asses the Site Effect of the EURO-SEISTEST Area in Northern Greece-PERG03-GA-2008-230915.

The entire work is presented systematically in the form of the following eight chapters. The brief descriptions of these are mentioned below:

Chapter - 2 describes the conceptual background of RMT and TEM methods.

Chapter - 3 deals with the theory of EM data inversion.

Chapter - 4 consists of geology and EM field campaign. Geological problem of unclear local active fault structure in the Volvi Basin is mentioned. For this purpose, the RMT and TEM measurements are performed at various geological units in the research area. RMT surveys are carried out along eight profiles with distances among stations of 25 m. The total length is around 12 km with total of 443 RMT soundings. The TEM data is spread along three profiles with distances among stations of 50 m. The overall 107 soundings are obtained from TEM data. The problem of geophysical measurements in the research area also describes in this chapter.

Chapter - 5 comprises results and interpretations of single inversions of RMT and TEM data. The RMT and TEM data quality are shown in this chapter. In order to calibrate the geophysical data, boreholes data as priori information have been correlated. Two schemes are used to analyze the fault structure: the importance value of model parameters and geological point of view. The clear existence of fault structure in the Volvi basin can be seen cleary in single 1-D and 2-D models of RMT data. The correlation between all 2-D conductivities of RMT models and the geological map identifies that the research area has a normal fault structure with direction of N70° E.

Chapter - 6, the joint and sequential inversion of RMT and TEM data is realized. The sequential inversion uses resistivity of first layer ρ_1, second layer ρ_2 and thickness h_1 of RMT models, as priori models for the inversion process of TEM data. These inversions are implemented with four approches: all fixed parameters (ρ_1, ρ_2 and h_1) with either fixed or free Calibration Factor (CF) and other two approches using free parameters with either free and fixed CF. The result of joint inversion was in agreement with assumption as the RMT data are resolved the surface layer at depth down to 40 m, and TEM data is small enough to resolve the surface structure ($z < 10$ m), however it can resolve the deeper structure down to 200 m of depth, depending on the resistivity structure. The joint and sequential models can both represent 1-D single inversion of RMT and TEM data. The model parameters are well resolved in joint inversion in comparison with the single RMT and TEM inversions. Joint and sequential inversions have proven to be able to replace the information on the shallow depths missing from the TEM data due to a technical problem of Nano TEM data .

Chapter - 7 discusses how 3-D forward modeling is created on RMT data. The verification 3-D model with homogenous half space and 2-D models also performed in this chapter. The 3-D forward modeling of RMT data provide a representative model of all conductivity structures in the research area.

Finally the major findings of this dissertation are summarized and concluded. Suggestions for the future work in the area are also given in **Chapter - 8**.

Chapter 2

Basic Electromagnetic Theory

This chapter presents the two electromagnetic methods, namely Radiomagnetotalluric and Transientelectromagnetic. The principle of RMT and TEM are discussed, i.e. data acquisition, processing and interpretation. In the EM methods, the subsurface electrical resistivity is essential due to the penetration depth of the EM fields.

2.1 Archie's Law

The resistivity of water bearing rocks or soil depends on the salinity of water, porosity and saturation. The electrical conductivity of the sediment is essentially influenced by porosity, permeability and the amount of water content. The relationship between the resistivity and the porosity of the matrix in a sedimentary rock is given by the empirical formula of *Archie* [1942]:

$$\rho_0 = \rho_w \times a \times S^{-n} \varphi^{-m} \tag{2.1}$$

where ρ_0 is bulk resistivity (Ωm), ρ_w = resistivity of the pore fluid (Ωm), a = proportional factor ($0.5 < a < 1$), S = saturation ($0 < S \leq 1$), n = saturation exponent ($n \approx 2$), φ = effective porosity ($0 < \varphi \leq 1$) and m = cementation exponent ($1.3 < m < 2.5$). A classification of resistivity ranges for different rock types and fluids types can be seen in Table 2.1.

The EM geophysical methods commonly provide information about the earth's conductivity distribution. The elementary laws of EM fields are governed by Maxwell's equations. The physical earth parameters determining the response are the electrical resistivity (ρ), the magnetic permeability (μ) and the electric permittivity (ϵ). The parameters commonly used for describing EM fields and there S I units are listed in Table 2.2. A detailed information of geophysical EM methods are given in *Nabighian* [1979] and *Ward and Hohmann* [1988].

Table 2.1: *Resistivity values for different materials [Palacky, 1988]*

Material	Resistivity [Ωm]
Massive sulphides	0.01 - 1
Salt water	0.1 - 1
Fresh water	3 - 100
Clays	3 - 100
Shales	3 - 50
Sandstone	50 - 1000
Igneous and Metamorphic	$10^3 - 10^5$

Table 2.2: *Physical parameters and operators used for describing EM fields*

Symbol	**Property**	**SI unit**
$\vec{E}$	electric field intensity	$\frac{\mathrm{V}}{\mathrm{m}}$
$\vec{D}$	electric flux density	$\frac{\mathrm{As}}{\mathrm{m}^2}$
$\vec{B}$	magnetic flux density	Tesla $= \frac{\mathrm{Vs}}{\mathrm{m}^2}$
$\vec{H}$	magnetic field intensity	$\frac{\mathrm{A}}{\mathrm{m}}$
$\vec{j}$	current density	$\frac{\mathrm{A}}{\mathrm{m}^2}$
q	electric charge	$\frac{\mathrm{As}}{\mathrm{m}^3}$
$\epsilon_0 = 8.854 \cdot 10^{-12}$	permittivity of free space	$\frac{\mathrm{As}}{\mathrm{Vm}}$
ϵ_r	dielectric constant	non-unit
$\epsilon = \epsilon_0 \epsilon_r$	electrical permittivity	$\frac{\mathrm{As}}{\mathrm{m}}$
$\mu_0 = 4\pi \cdot 10^{-7}$	permeability of free space	$\frac{\mathrm{Vs}}{\mathrm{Am}}$
μ_r	relative permeability	non-unit
$\mu = \mu_0 \mu_r$	magnetic permeability	$\frac{\mathrm{Vs}}{\mathrm{Am}}$
σ	electric conductivity	$\frac{\mathrm{S}}{\mathrm{m}} = \frac{\mathrm{A}}{\mathrm{Vm}}$
ρ	resistivity	$\Omega\mathrm{m} = \frac{\mathrm{Vm}}{\mathrm{A}}$
f	frequency	$\mathrm{Hz} = \frac{1}{\mathrm{s}}$
$\omega = 2\pi f$	angular frequency	$\frac{1}{\mathrm{s}}$
I	current	A
k	wavenumber	non-unit
$c_0 = \frac{1}{\sqrt{\mu_0 \varepsilon_0}} = 3 \cdot 10^8$	EM wave velocity in vacuum	$\frac{\mathrm{m}}{\mathrm{s}}$
$\nabla = (\frac{\partial}{\partial x}, \frac{\partial}{\partial y}, \frac{\partial}{\partial z})$	Del operator	non-unit
$\nabla^2 = (\frac{\partial^2}{\partial x^2}, \frac{\partial^2}{\partial y^2}, \frac{\partial^2}{\partial z^2})$	Laplace operator	non-unit

2.2 Maxwell's Equations

Maxwell equations [1] describe the principle of the properties of all EM fields and can be written as:

$$\nabla \cdot \vec{D} = q \tag{2.2}$$

$$\nabla \cdot \vec{B} = 0 \tag{2.3}$$

$$\nabla \times \vec{E} = -\frac{\partial \vec{B}}{\partial t} \tag{2.4}$$

$$\nabla \times \vec{H} = \vec{j} + \frac{\partial \vec{D}}{\partial t} \tag{2.5}$$

The interaction between matter and field is described by the material equation. The current density which flows in a material medium as the result of the electric field density according to Ohm's Law is:

$$\vec{j} = \sigma \vec{E} \tag{2.6}$$

The relation between the respective electric and magnetic fields in the material is defined by

$$\vec{D} = \varepsilon \vec{E} = \varepsilon_0 \varepsilon_r \vec{E} \tag{2.7}$$

$$\vec{B} = \mu \vec{H} = \mu_0 \mu_r \vec{H} \tag{2.8}$$

2.2.1 Telegraph and Helmholtz Equations

From Faraday's (equation 2.4) and Ampere's laws (equation 2.5) by using the vector identity:

$$\nabla \times (\nabla \times \vec{A}) = \nabla(\nabla \cdot \vec{A}) - \nabla^2 \vec{A} \tag{2.9}$$

where $\vec{A}$ is an arbitrary vector field with $\vec{A} \in \mathbb{R}^3$, we get the **Telegraph equations**:

$$\nabla^2 \vec{E} = \sigma\mu \frac{\partial \vec{E}}{\partial t} + \varepsilon\mu \frac{\partial^2 \vec{E}}{\partial t^2} \tag{2.10}$$

$$\nabla^2 \vec{H} = \sigma\mu \frac{\partial \vec{H}}{\partial t} + \varepsilon\mu \frac{\partial^2 \vec{H}}{\partial t^2} \tag{2.11}$$

with $\vec{F} \in \{\vec{E},\vec{H}\}$ we can simplify:

$$\nabla^2 \vec{F} = \sigma\mu \frac{\partial \vec{F}}{\partial t} + \varepsilon\mu \frac{\partial^2 \vec{F}}{\partial t^2} \tag{2.12}$$

[1] The equation is found by JAMES CLERK MAXWELL (1864-1879)

Without losing generality, we can assume the time variation of the fields is in a simple harmonic form **(solution of the Telegraph's Equation)**:

$$\vec{F} = \vec{F_0} e^{-i\omega t} \tag{2.13}$$

where $\vec{F_0}$ is amplitude of $\vec{F}$.
From solving equation 2.12 with equation 2.13, we have **Helmholtz's Equation**:

$$\nabla^2 \vec{F} = -k^2 \vec{F} \tag{2.14}$$

with :

$$k^2 = \varepsilon\mu\omega^2 (1 + \frac{\sigma}{\omega\varepsilon} i) \tag{2.15}$$

$$\vec{F} k^2 = \underbrace{\vec{F}\varepsilon\mu\omega^2}_{\text{displacement current}} - \underbrace{\vec{F} i\sigma\omega\mu\varepsilon}_{\text{conduction current}} \tag{2.16}$$

k is the complex wave number. The first term ($\varepsilon\mu\omega^2$) and second term ($i\sigma\omega\mu\varepsilon$) on the right hand of equation 2.16 are related to the displacement current and the conduction current respectively.

2.2.2 Quasi-static approximation

From equation 2.16, we can derive the relationship beetwen conduction current and displacement current. If the conduction current is much larger than the displacement current, we have the quasi static approximation:

$$\frac{\omega\mu\sigma}{\omega^2\mu\varepsilon} = \frac{\sigma}{\omega\varepsilon} \gg 1 \tag{2.17}$$

when the angular wave number $k \gg 1$, the Helmoholtz equation is essentialy represent a diffusion equation. For average resistivity[2] of $\approx 80\ \Omega$m with highest frequency of f =1 MHz, we get:

$$\frac{\sigma}{\omega\varepsilon} = \frac{1}{\rho\omega\varepsilon} = \frac{1}{80 \times 6.3 \cdot 10^6 \times 8.85 \cdot 10^{-12}} = 224.1 \gg 1 \tag{2.18}$$

The calculation of the quasi-static approximation in formula 2.18 shows that the displacement currents for RMT frequencies (10 kHz - 1 MHz) can be neglected in the study area. However displacement currents should be considered when the investigation area has very high resistivity [*Persson and Pedersen*, 2002].

[2]The avarege resistivity distribution in the study area

2.3 Electromagnetic Methods

EM methods are powerful tools in environmental and geological investigations. Saveral techniques of EM have been developed in many applications, such as mining, geothermal, hydrogeological investigations, etc. To determine subsurface electrical resistivity, the EM methods use the principle of electromagnetic induction. A primary EM field induces electric and magnetic fields in the subsurface. There are generally two kind of sources: natural or artificial. The EM field is diffusive when the applied frequency is low, i.e the MT approximation is valid. The classification therefore also depends on the subsurface resistivity. Active source methods can be implemented in both the frequency domain and time domain mode.

Frequency domain electromagnetic (FDEM) surveys begins with the injection of a time varying current into a transmitter coil. The time varying current generates a magnetic field which induces a current in accordance with Faraday's law. The induced currents occur throughout the subsurface. These currents usually flow through the conductor in planes perpendicular to magnetic field lines from the transmitter. A secondary magnetic field is also generated from these induced currents. The magnetic field lines of the secondary magnetic field are opposite to the induced currents. As these currents occur in the subsurface, the magnitude and distribution depend on transmitter frequency, power, geometry and the distribution of the electrical resistivity of the subsurface [*Kaufman and Keller*, 1983].

There are several FDEM methods usually applied which use a frequency dependent active source: Control Source EM (CSEM), Helicopter EM (HEM), Slingram. Other FDEM methods use plane waves as the source for EM induction in the ground, i.e., EM-waves generated by radio-transmitter or generated naturally by interaction of the solar wind with the magnethosphere or lighting. The examples for these methods are: MT [*Cagniard*, 1953, *Tikhonov*, 1950], Audiomagnetotellruic (AMT), CSAMT, Audio Frequency Magnetics (AFMAG), VLF and VLF resistivity mode (VLF-R) and RMT.

The magnitude of the secondary field is very small compared to the primary field. In this case, the measurement of the secondary magnetic field is the main problem for the controlled source EM method. To avoid this problem, time domain EM methods can be applied.

Time domain electromagnetic (TDEM or TEM) methods inject EM energy with a transmitter into the ground as transient pulses instead of continuous waves. Two types of transmitters are commonly used in TEM measurements: A loop source which forms a vertical magnetic dipole with inductive coupling to the ground and a grounded wire which forms a horizontal electric dipole with both inductive and galvanic coupling [*Scholl*, 2005]. There are two types of TEM methods based on the depth of the exploration; SHOTEM (Short Offset TEM) and LOTEM (Long-Offset TEM). In the SHOTEM, the diffusion depth is greater than the transmitter and receiver separation while in LOTEM (Long-Offset TEM), the diffusion depth is equal to or less than the receiver offset. The transmitter configuration is a grounded dipole in LOTEM [*Strack*, 1992].

The Skin Depth

The amplitude of the secondary field generated in the ground is attenuated with depth. The primary magnetic field in TEM does not exist during measurement of the secondary magnetic field and this is one major advantage of TEM surveys over FDEM surveys. The absence of a primary field during TEM measurements enables the receiver loop to be put within the transmitter.

In EM methods, the terms “depth of penetration” and “skin depth” are often assumed to be synonymous. The skin depth is defined as the depth in which the field amplitude is attenuated by 1/e or approximately 37% of its value at the surface. The skin depth is largely used as rough estimation of the investigation depth of the EM systems [*Spies*, 1989]. The skin depth in frequency domain (δ_{FD}) is given by

$$\delta_{FD} = \sqrt{\frac{2}{\omega\mu\sigma}} \approx 503\sqrt{\frac{\rho}{f}} \tag{2.19}$$

Equation 2.19 is only an exact estimation for the homogeneous half space.

The RMT and TEM methods have greater penetration depth when the conductivity of the subsurface is lower. For exploring deep structures, late recording times and low frequencies are needed, respectively. In case of TEM surveys, the time-domain diffusion depths (δ_{TD}) at any time t is defined as:

$$\delta_{TD} = \sqrt{\frac{2t}{\mu\sigma}} \tag{2.20}$$

The depth of investigation is defined as the maximum depth in which a given target can be detected in a given host. The practical depth of investigation can be several skin depths in an ideal geological environment, whereas when it is in a complex or noisy geological area and for certain EM sounding systems, the depth of investigation can be much less than one skin depth. It is an empirical quantity and is influenced by the target properties and host medium as well as factors in regard to the investigation modality such as data processing and interpretation methods, sensor sensitivity, accuracy, frequency, coil configuration and ambient noise [*Huang*, 2005].

2.3.1 Radiomagnetotelluric Method

The RMT method uses distant radio-transmitters in the frequency band (10 kHz - 1 MHz) as EM source-fields. The principle of this method is demonstrated schematically in Figure 2.1. The EM fields can be assumed as plane waves. A radiated EM wave consists of coupled alternating vertical electrical and concentric horizontal magnetic fields, perpendicular to each other. The electromagnetic waves radiated from these transmitters diffuse into the conductive earth where they induce electric current systems. The magnetic field can be measured for selected frequencies with a coil and the electric field with two grounded electrodes.

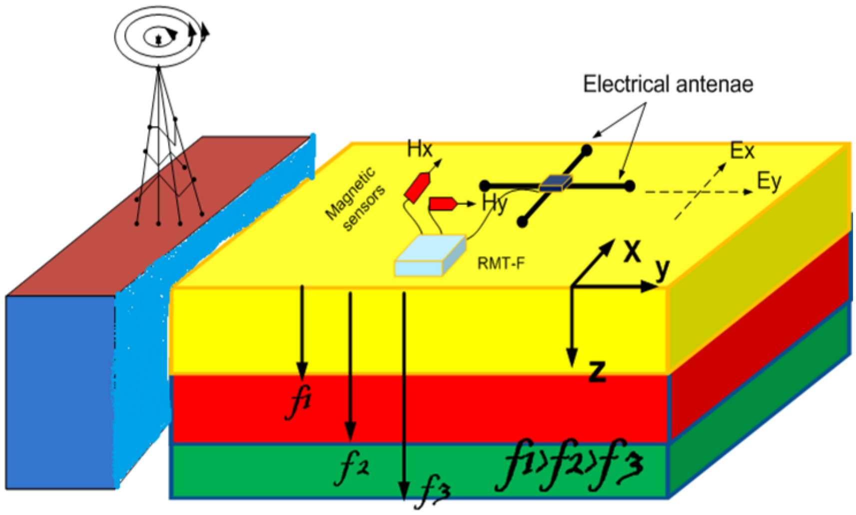

Figure 2.1: *Schematic diagram of RMT setup.*

The skin depth of electromagnetic waves can be calculated for different frequencies according to equation 2.19. Figure 2.1 indicates that the highest frequency (f_1) carries information of the shallow structure and the lowest frequency (f_3) represents the deeper structure.

The RMT device utilized here is called RMT-F (Figure 2.2). The equipment utilized uses an extended frequency range from 10 kHz up to 1 MHz. The device has 4-channel recording (H_x, H_y, E_x, E_y) and was developed by the University of Cologne, Germany in cooperation with Microcor and University of St.Petersburg [*Tezkan and Saraev*, 2008] and [*Microkor and St. Petersburg University*, 2005]. The RMT-F system consists of two capacitive grounded electric antennas to measure electric fields, two magnetic coils to observe the magnetic field.

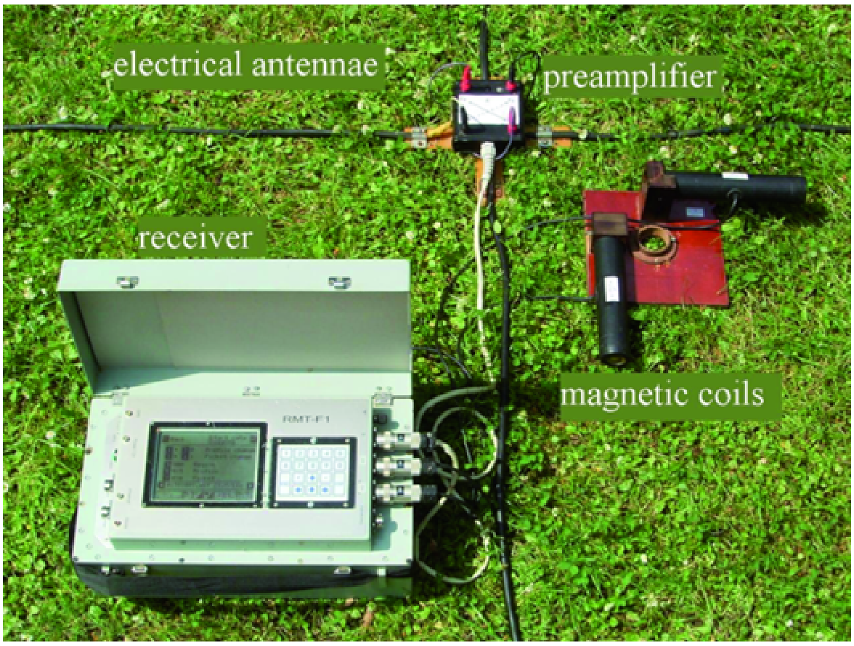

Figure 2.2: *RMT-F system from University of Cologne: Digital 4-channels receiver, electric antennae, magnetic coils and E-field preamplifier.*

A concept about definition of electrical scalar impedance was developed from layered medium usage to more complex geological environment by introducing the impedance tensor [*Sims et al.*, 1971, *Cagniard*, 1953]. They have given a linear relationship between the horizontal components of the electromagnetic field at the surface of the earth as:

$$E_x = Z_{xx}H_x + Z_{xy}H_y \tag{2.21}$$

$$E_y = Z_{yx}H_x + Z_{yy}H_y \tag{2.22}$$

The above equation (2.21 and 2.22) can be written as matrix:

$$\begin{bmatrix} E_x \\ E_y \end{bmatrix} = \underbrace{\begin{bmatrix} Z_{xx} & Z_{xy} \\ Z_{yx} & Z_{yy} \end{bmatrix}}_{\text{Z}} \begin{bmatrix} H_x \\ H_y \end{bmatrix}$$

The complex quantities $Z_{xx}, Z_{xy}, Z_{yx}, Z_{yy}$ are the components of the impedance tensor. The components of impedance tensors have a function as electrical properties, orientation of sensors and direction of primary field.

Apparent resistivities ρ_{aij} and impedance phase ϕ_{aij} [°] can be derived from complex impedance, Z, using the formula of *Cagniard* [1953]:

$$\rho_{aij} = \frac{1}{\omega\mu}|Z_{ij}|^2 \tag{2.23}$$

$$\phi_{ij} = \tan^{-1}[\frac{\Im(Z_{ij})}{\Re(Z_{ij})}] \tag{2.24}$$

where i, j $\in \{x, y\}$ and i $\neq$ j:

In a homogenous earth, the apparent resistivity equals to the time resistivity and the phase is $\frac{\pi}{4}$ (45°). But in 1-D layered earth surface, the phase decreases when EM field penetrates from higher conducting layer into lower conducting zone and reversely, it will increase when it penetrates from the lower conducting zone into the higher one.

Impedance tensor components are used as diagnostic tool to determine the dimensionality of subsurface structure seen from the intrinsic characteristics.

1. For 1-D resistivity distribution in the earth (layered model), the amplitude of impedance tensor elements are equal and the diagonal elements are zero. The impedance tensor reduces to a scalar impedance

$$Z_{xy} = -Z_{yx}, \quad Z_{xx} = Z_{yy} = 0 \tag{2.25}$$

2. If a 2-D resistivity structure represents the subsurface, of which the electric field is measured parallel or perpendicular to the strike direction, the components of impedance tensor are:

$$Z_{xy} \neq Z_{yx}, \quad Z_{xx} = Z_{yy} = 0 \tag{2.26}$$

   In the optimal 2D case, Maxwell's equations are divided into two modes of polarization: transverse electric or TE mode, in which electric field is along the strike, and transverse magnetic or TM mode, having magnetic field along the strike direction.

3. In the 3-D case, all components of the impedance tensor are non-zero. The impedance skew is used as another indicator of dimensionality of the subsurface structure. It is introduced by *Swift* [1967] and he described skew as

$$S = \frac{|Z_{xx} + Z_{yy}|}{|Z_{xy} - Z_{yx}|} \tag{2.27}$$

   In 1-D (for noise free data), and in 2-D case when the x or y is along strike, skew is zero, while in 3-D case, it is not zero [*Vozoff*, 1987]. However, due to the limited number of radio transmitters in the field, not all impedace tensor components are available and thus, the skewness could not be calculated in the present thesis.

2.3.2 Central Loop Transient Electromagnetic

The TEM method is an effective tool for investigating vertical changes in the earth. By performing groundbased measurements, it is possible to cover large areas with this method. The most used field setup is the central loop or in-loop configuration. For this setup, the receiver loop (Rx) is placed in the center of the transmitter loop (Tx) (Figure 2.3).

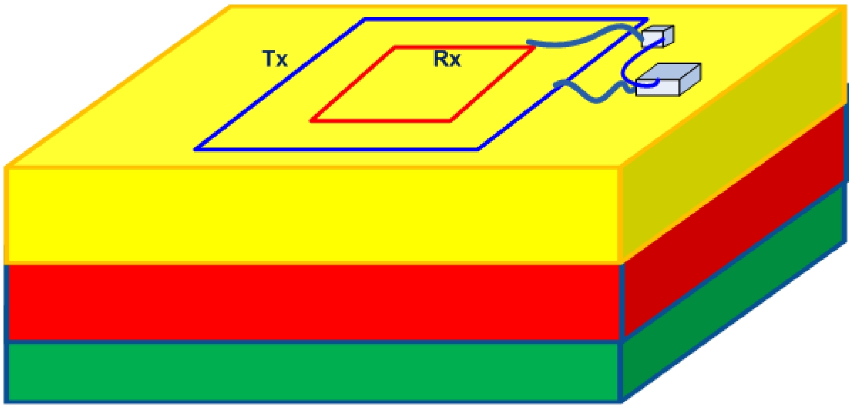

Figure 2.3: *Diagram of central loop (in loop) TEM.*

The basic principle of central loop TEM can be described with Figure 2.4 and Figure 2.5. Figure 2.4a shows the fundamental waveform used for central loop TEM. The current in the transmitter loop produces a primary magnetic field. When the current flowing in the transmitter is turned off abruptly, the primary field induces eddy currents in the conductive underground corresponding to Maxwell's equations. This eddy currents produce a secondary magnetic field of which the propagation depending on the conductivity distribution in the subsurface. After current turn-off the time derivative of the secondary magnetic field is measured in the receiver loop at distinct the time points. The decay curve is a transient (Figure 2.4b).

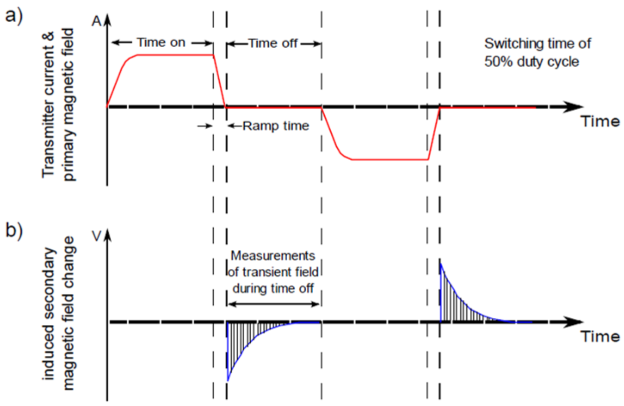

Figure 2.4: *Fundamental waveform for central loop TEM. (a) Current in the transmitter loop. (b) Secondary magnetic field measured in the receiver coil (modified after McNeill and Labson [1990]).*

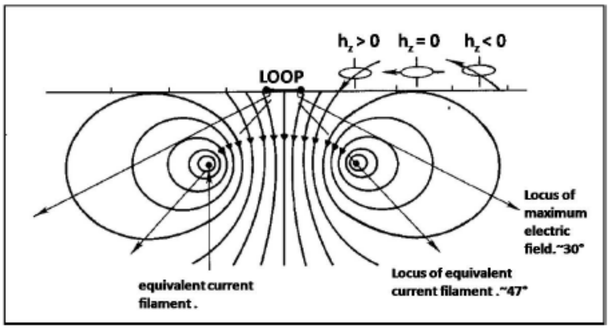

Figure 2.5: *Equivalent current filament concept in understanding the behavior of TEM fields over conducting half-space (after [Nabighian, 1979]).*

Conducting Half-Space

In a conducting half space, the smoke ring effect of induced current can be approximated with an equivalent current filament moving down at a velocity $v = \frac{2}{\pi\sigma\mu t}$ and with radius $a = \frac{4.37t}{\sigma\mu}$ [*Nabighian*, 1979].

Figure 2.5 shows that the maximum of the actual induced currents are moving down at an angle of 30°, whereas the equivalent current filament moves downward at around 47°. For central loop measurements, the analytic solution for the vertical magnetic field H_z at the surface of a homogeneous half space can be found in *Ward and Hohmann* [1988] as:

$$\frac{\partial H_z}{\partial t} = -\frac{I\rho}{\mu_0 \sigma a^3}[3\mathrm{erf}(\theta a) - \frac{2}{\sqrt{\pi}}\theta a(3 + 2\theta^2 a^2)e^{-\theta^2 a^2}] \tag{2.28}$$

where I is the transmitter current, $\theta = (\frac{\mu}{\rho^4 t})^{\frac{1}{2}}$, a is the transmitter-loop radius [m] and erf(x) is the error function given by

$$\mathrm{erf}(x) = \frac{2}{\pi}\int_0^x e^{-t^2} dt \tag{2.29}$$

There are two common transformations from induced voltage to apparent resistivity. The approximation for early and late time apparent resistivity can be derived from equation 2.28.

For early time ($t \to 0$), it gives:

$$\frac{\partial H_z^{et}}{\partial t} = -\frac{3I}{\mu_0 \sigma a^3} \tag{2.30}$$

The apparent resistivity for early time is

$$\rho_a^{et} = -\frac{\mu_0 a^3}{3I}\frac{\partial H_z}{\partial t} \tag{2.31}$$

For late time ($t \to \infty$) the relevant asympotic formula can be given as:

$$\frac{\partial H_z^{lt}}{\partial t} = -\frac{Ia^2}{20\sqrt{\pi}}(\sigma\mu_0)^{\frac{3}{2}} t^{-\frac{5}{2}} \tag{2.32}$$

The apparent resistivity for late time is

$$\rho_a^{lt} = \frac{I^{\frac{2}{3}}\mu_0 a^{\frac{4}{3}}}{20^{\frac{2}{3}}\pi^{\frac{1}{3}}t^{\frac{5}{3}}}\left(-\frac{\partial H_z}{\partial t}\right)^{-\frac{2}{3}} \tag{2.33}$$

The time behavior of the receiver coil output voltage at early time is constant, whereas at late time, it is proportional to $t^{-\frac{5}{2}}$. For the vertical magnetic field, the early time is proportional to ρ. Both, the early and late time approximation give a rough impression of the subsurface structure.

Nano TEM and Zero TEM

The investigation of shallow and deeper structures is effectively applied using Nano (Very fast turn-off) and Zero (slow-turn-off) TEM modes. The devices used are the NT-20 transmitter and GDP-32 II str (Figure 2.6)[*Zonge Engineering and Research Organisation Inc.*, 2001].

This allows to measure TEM data in two distinct modes, according to different investigation depths. The devices can be synchronized, therefore the recording is performed in appropriate time frames. More information about two combinations between Nano and Zero TEM can be found in the manual by *Zonge Engineering and Research Organisation Inc.* [2001]. NanoTEM and ZeroTEM have been successfully applied in several areas for geomorphological and hydrogeological studies [*Koch et al.*, 2003, *Mollidor*, 2008] and [*Papen*, 2011].

Figure 2.6: *NT-20 transmitter (left) and GDP32 II receiver (right).*

The injected currents in Nano and Zero TEM depend on the loop size and the location of the target. Nano TEM uses currents up to 3 A. The receiver records from 0.3 μs - 2.5 ms. In order to get information in the deeper structure, the Zero TEM mode can measure in a time window from 31 μs - 6 ms. It is using relatively high current (about 10 A) and 50 - 55 μs turn-off ramp time. Therefore, a combination between Nano and Zero TEM can give information of the subsurface structures from shallow to great depth, depending on the conductivity distribution.

Influece of Current Function

Prior to use Nano and Zero TEM modes with different ramp times, it is essential to know the behavior of the transient decay. In fact, the current function $I(t)$ during turn off is considered as a linear ramp (see Figure 2.7).

The relation of a linear current turn-off fuction $I'(t)$ with turn-off time t and induced voltage $V'(t)$ is described by *Fitterman and Anderson* [1987]. The measured voltage $V'(t)$ can be described by a convolution integral of the current-turn off function $I'(t)$ and the uninfluenced earth response $V(t)$.

$$V'(t) = \int_{-\infty}^{t} -\frac{dI'(t')}{dt'} V(t-t')\,\mathrm{d}t' \quad (2.34)$$

$$= \frac{1}{t_0}\int_{t_0}^{0} V(t-t')\,\mathrm{d}t' \quad (2.35)$$

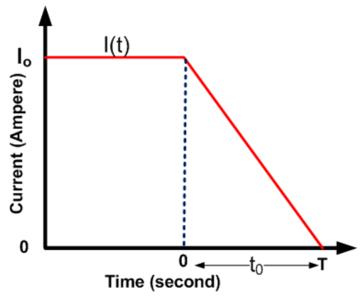

Figure 2.7: *Shutdown function with a ramptime of* t_0.

It was used that the time derivative of the current function $I'(t)$ in interval $0 < t < T$ is constant with the value of t_0^{-1} is equal to zero. In order to receive the unaffected $V(t)$, we have to deconvolute $V'(t)$ from the ramp function [*Hanstein*, 1992, *Helwig et al.*, 2003]. The deconvolution is performed with the EADEC program by *Lange* [2003].

Chapter 3

Inversion Theory

In this chapter, the inversion theory used for RMT and TEM is discussed. Inversion is the transformation of geophysical data into an earth model, whereas the process of estimating geophysical data as a result based on the calculation of an earth model is known as forward modeling.

The forward problem modeling can be described schematically:

$$\text{model parameters } \boldsymbol{m} \longrightarrow \text{forward operator } A \longrightarrow \text{model data } \boldsymbol{d'}$$

Mathematically, it can be denoted as:

$$\boldsymbol{d'} = A(\mathbf{m})$$

The inverse problem can be described as:

$$\text{measured data } \boldsymbol{d} \longrightarrow \text{inverse of the forward operator } A^{-1} \longrightarrow \text{estimated model parameters } \boldsymbol{m^p}$$

Mathematically, this can be written as:

$$\boldsymbol{m^p} = A^{-1}(\boldsymbol{d})$$

Since the forward operator A is non-linear, it is not possible to calculate its inverse A^{-1}. Moreover, the measured geophysical data can be equally represented by several equivalent models and the inversion process can therefore only provide an estimation of the model parameters. The model parameters $\boldsymbol{m}$ will be improved until the model data $\boldsymbol{d'}$ and measured data $\boldsymbol{d}$ approve within a given threshold. Therefore, the main aim of inversion is to find the best model parameters $\boldsymbol{m^p}$ from the geophysical data $\boldsymbol{d}$.

The inversion of geophysical data is possible in multiple dimensions (1-D, 2-D and 3-D). In the present thesis, the inversion of 1-D and 2-D data is used. 1-D inversions for RMT and TEM data are carried out using the EMUPLUS program . This program was developed by the Institute of Geophysics and Meteorology at the University of

Cologne, Germany [*Scholl*, 2001, *Lange*, 2003] and [*Wiebe*, 2007].

The 2-D Model of RMT data was calculated with a 2-D inversion algorithm program by *Rodi and Mackie* [2001]. Detailed information about inversion theory can be obtained in *Menke* [1984] or *Zhdanov* [2002].

3.1 1-D Inversion

One dimensional earth model shows only a variation with depth (z direction). The measured data $d_1, ..., d_N$ and model parameters $m_1, .., m_L$ can be denoted as the components of a vector:

$$\boldsymbol{d} = [d_1, d_2, d_3, ..., d_N]^T \qquad \text{measured data} \tag{3.1}$$

$$\boldsymbol{d'} = [d'_1, d'_2, d'_3, ..., d'_N]^T \qquad \text{model data} \tag{3.2}$$

$$\boldsymbol{m} = [m_1, m_2, m_3, ..., m_L] \qquad \text{model parameters} \tag{3.3}$$

Assuming that the model parameter vector $\boldsymbol{m}$ and the data vector $\boldsymbol{d}$ are related non-linearly, we can note:

$$\boldsymbol{d'} = \boldsymbol{A(m)} \tag{3.4}$$

The equation 3.5 simplifies to a matrix vector product in linear case:

$$\boldsymbol{d'} = \boldsymbol{A.m} \tag{3.5}$$

where $\boldsymbol{A}$ is a N $\times$ L matrix.

There we can minimize the misfit between measured data $\boldsymbol{d}$ and model data $\boldsymbol{d'}$. The misfit can be calculated with a least-squares approach. The notation of the misfit function ε can be written as

$$\varepsilon = (\boldsymbol{A(m)} - \boldsymbol{d})^T(\boldsymbol{A(m)} - \boldsymbol{d}) \tag{3.6}$$

In order to calculate the residual between measured data $\boldsymbol{d}$ and model data $\boldsymbol{d}'$ in equation 3.6, we can use the **weighting** factor $\boldsymbol{W} = \text{diag}(1/d_1, ., 1/d_N)$.

$$\text{The matrix } \boldsymbol{W} \text{ has a diagonal form} = \begin{pmatrix} 1/\sigma_1 & 0 & \dots & 0 \\ 0 & 1/\sigma_2 & \dots & 0 \\ \vdots & \vdots & \ddots & \vdots \\ 0 & 0 & \dots & 1/\sigma_n \end{pmatrix}$$

where $1/\sigma_1$ with data error σ.
So the equation 3.6 can be written in the form:

$$\varepsilon = (\boldsymbol{WA(m)} - \boldsymbol{Wd})^T(\boldsymbol{WA(m)} - \boldsymbol{Wd}) \tag{3.7}$$

Note that $\boldsymbol{A}(m)$ equal $\boldsymbol{A}.m$ for the linear case in equations 3.6 and 3.7.

3.1.1 The Solution of Linear Inverse Problem

The equation 3.5 describes a system of N linear equations with respect to L model parameters $m_1, m_2, m_3, ..., m_L$. If the number of model parameters is higher than the number of the measured data ($L > N$), the solution will be an *under-determined*. Whereas, the solution is *over-determined* if the number of measured data is higher than the number of model parameters ($L < N$).

In order to minimize the difference between measured data and model data, we can look for extreme values of the function $\varepsilon(\boldsymbol{m}) = 0$ in equation 3.7.

$$\frac{\partial\varepsilon(\boldsymbol{m})}{\partial\boldsymbol{m}} = 0 \tag{3.8}$$

$$\frac{\partial}{\partial\boldsymbol{m}}(\boldsymbol{WAm} - \boldsymbol{Wd})^T(\boldsymbol{WAm} - \boldsymbol{Wd}) = 0 \tag{3.9}$$

$$\frac{\partial}{\partial\boldsymbol{m}}(\boldsymbol{m}^T\boldsymbol{A}^T\boldsymbol{W}^T\boldsymbol{WAm} - \boldsymbol{m}^T\boldsymbol{A}^T\boldsymbol{W}^T\boldsymbol{Wd} - \boldsymbol{d}^T\boldsymbol{W}^T\boldsymbol{WAm} + \boldsymbol{d}^T\boldsymbol{W}^T\boldsymbol{Wd}) = 0 \tag{3.10}$$

with $\boldsymbol{W} = \boldsymbol{W}^T$:

$$(\boldsymbol{WA})^T\boldsymbol{WAm} = (\boldsymbol{WA})^T\boldsymbol{Wd}$$

$$\boldsymbol{A}^T\boldsymbol{W}^2\boldsymbol{Am} = \boldsymbol{A}^T\boldsymbol{W}^2\boldsymbol{d} \tag{3.11}$$

$$\boldsymbol{m} = (\boldsymbol{A}^T\boldsymbol{W}^2\boldsymbol{A})^{-1}\boldsymbol{A}^T\boldsymbol{W}^2\boldsymbol{d} \tag{3.12}$$

with equation 3.12, we obtained **the solution of weighted least-square inversion** and it is known as **normal equation**.

3.1.2 The Solution of Non-Linear Inverse Problem

The main model parameters for 1-D inversion consist of resistivity and layer thickness. However, the problem of resistivity-depth sounding is usually non-linear, as in frequency or time domain. The data $\boldsymbol{d}$ is related non-linearly to the model parameter $\boldsymbol{m}$. In order to solve the non-linear minimization problem of the misfit functional, we use the regularized Newton's method. Newton's method attempts to construct a sequence of model from an initial guess $\boldsymbol{m_0}$ that converges the real model $\boldsymbol{m_1}$:

$$\boldsymbol{m_1} = \boldsymbol{m_0} + \tilde{\boldsymbol{m}} \tag{3.13}$$

In order to minimize the misfit functional, we use a model update $\tilde{\boldsymbol{m}} = \boldsymbol{m_1} - \boldsymbol{m_0}$ from 3.13, which minimizes ε:

$$\frac{\partial\varepsilon(\boldsymbol{m_0} + \tilde{\boldsymbol{m}})}{\partial\tilde{\boldsymbol{m}}} = 0 = \frac{\partial}{\partial\boldsymbol{m}}(\boldsymbol{WA}(\boldsymbol{m_0} + \tilde{\boldsymbol{m}}) - \boldsymbol{Wd})^T(\boldsymbol{WA}(\boldsymbol{m_0} + \tilde{\boldsymbol{m}}) - \boldsymbol{Wd}) \tag{3.14}$$

For the *n-th* iteration, the model function $\boldsymbol{A}(\boldsymbol{m})$ is continuously differentiable and the solution of this problem can be solved by Taylor's theorem. The Taylor theorem of the starting model $\boldsymbol{m}_0$, $\boldsymbol{A}(\boldsymbol{m}) = \boldsymbol{A}(\boldsymbol{m}_0 + \tilde{\boldsymbol{m}})$, can be expressed as

$$\boldsymbol{A}(\boldsymbol{m}) = \boldsymbol{A}(\boldsymbol{m}_0) + \boldsymbol{J}|_{\boldsymbol{m}=\boldsymbol{m}_0}\tilde{\boldsymbol{m}} \tag{3.15}$$

where $\boldsymbol{J}$ is the Jacobian matrix or *sensitivity matrix* of partial derivatives.

$$\text{Jacobian matrix } (\boldsymbol{J}_{ij}) = \begin{pmatrix} \frac{\partial \boldsymbol{A_1}(\boldsymbol{m_0})}{\partial \boldsymbol{m_1}} & \cdots & \frac{\partial \boldsymbol{A_1}(\boldsymbol{m_0})}{\partial \boldsymbol{m_L}} \\ \vdots & \ddots & \vdots \\ \frac{\partial \boldsymbol{A}_N(\boldsymbol{m_0})}{\partial \boldsymbol{m_1}} & \cdots & \frac{\partial \boldsymbol{A}_N(\boldsymbol{m_0})}{\partial \boldsymbol{m_L}} \end{pmatrix}$$

where $i = 1, 2, 3, ..., N$ and $j = 1, 2, 3, ..., L$
The N x L Jacobian matrix $\boldsymbol{J}$ is a by-product of linearizing a non-linear problem.

Statistically, sensitivity values show whether the layer parameters are seen individually in the measured data or not. They qualitatively display which parameter or combination of parameters are resolved by the data. Model parameter is only well-resolved if the sensitivity is large. On the other hand, the normalized Jacobian values or relative sensitivities give an idea of each data point's sensitivity to a change of an individual parameter[*Jupp and Vozoff*, 1975, *Lines and Treitel*, 1984].

We can rewrite equation 3.14 with respect to an update of model parameters $\boldsymbol{m}_j$:

$$\frac{\partial}{\partial \tilde{\boldsymbol{m}}}(\boldsymbol{W}(\boldsymbol{A}(\boldsymbol{m}_0) + \boldsymbol{J}\tilde{\boldsymbol{m}}) - \boldsymbol{W}\boldsymbol{d})^T(\boldsymbol{W}(\boldsymbol{A}(\boldsymbol{m}_0) + \boldsymbol{J}\tilde{\boldsymbol{m}}) - \boldsymbol{W}\boldsymbol{d}) = 0 \tag{3.16}$$

The solution of the non-linear inverse problem with the update vector $\tilde{\boldsymbol{m}}$ can be derived from 3.16 by substituting $\tilde{\boldsymbol{d}} = \boldsymbol{d}$ - $\boldsymbol{A}(\boldsymbol{m}_0)$ and $\boldsymbol{W} = \boldsymbol{W}^T$:

$$\frac{\partial}{\partial \tilde{\boldsymbol{m}}}(\boldsymbol{W}(\boldsymbol{d} - \tilde{\boldsymbol{d}}) + \boldsymbol{J}\tilde{\boldsymbol{m}}) - \boldsymbol{W}\boldsymbol{d})^T(\boldsymbol{W}((\boldsymbol{d} - \tilde{\boldsymbol{d}}) + \boldsymbol{J}\tilde{\boldsymbol{m}} - \boldsymbol{W}\boldsymbol{d}) = 0 \tag{3.17}$$

$$\frac{\partial}{\partial \tilde{\boldsymbol{m}}}(\boldsymbol{W}\boldsymbol{J}\tilde{\boldsymbol{m}} - \boldsymbol{W}\tilde{\boldsymbol{d}})^T(\boldsymbol{W}\boldsymbol{J}\tilde{\boldsymbol{m}} - \boldsymbol{W}\tilde{\boldsymbol{d}}) = 0 \tag{3.18}$$

This yields the same solution as equation 3.10 to 3.12 with the model update vector $\tilde{\boldsymbol{m}}$:

$$\tilde{\boldsymbol{m}} = (\boldsymbol{J}^T\boldsymbol{W}^2\boldsymbol{J})^{-1}\boldsymbol{J}^T\boldsymbol{W}^2\tilde{\boldsymbol{d}} \tag{3.19}$$

The equation 3.19 is a general solution to minimize the function of misfit in a non-linear system known as the Gauss-Newton method. The most difficult problem of those is when the inverse matrices $(\boldsymbol{J}^T\boldsymbol{J})^{-1}$ of $(\boldsymbol{J}^T\boldsymbol{W}^2\boldsymbol{J})^{-1}$ are not available. However, even they exist, the solution still can become singular. Therefore, it is unstable. To overcome these problems, regularization strategies can be applied.

Due to the linearisation of $\boldsymbol{A}(\boldsymbol{m})$, equation 3.19 yields only the model update $\tilde{\boldsymbol{m}}$. Therefore the non-linear inversion is iterative and, for the final model $\boldsymbol{m}_n$, needs n iteration steps to minimise the misfit function ε.

3.1.3 Levenberg-Marquardt Method

The Levenberg-Marquardt algorithm is the most widely algorithm used in optimization of model data in order to prevent divergence of the solution of the normal-equation. The method is also known as *damped least squares* or *ridge regression* [*Levenberg*, 1944] and [*Marquardt*, 1963]. According to the inverse problem, they modified equation 3.19 becomes:

$$\tilde{\boldsymbol{m}} = (\boldsymbol{J}^T\boldsymbol{W}^2\boldsymbol{J} + \lambda\boldsymbol{I})^{-1}\boldsymbol{J}^T\boldsymbol{W}^2\tilde{\boldsymbol{d}} \tag{3.20}$$

where $\boldsymbol{I}$ is the identity matrix and λ is the damping factor.

The method effectively controls the unstability caused by the existance of zero or very small eigenvalue of Jacobian $\boldsymbol{J}$. Detailed analysis in terms of parameter resolution and the importance can be done using singular value decomposition (SVD) method of the Jacobian matrix $\boldsymbol{J}$.

Singular Value Decomposition (SVD)

SVD method is used to calculate inverse problems. The ill-posed inverse problem is overcome by analyzing small eigenvalue of the matrix. Every matrix can be written as a product consisting of three matrixes stated as follows:

$$\boldsymbol{J} = \boldsymbol{S}\Lambda\boldsymbol{V}^T, \tag{3.21}$$

where $\boldsymbol{S}$ is a $N \times M$ matrix containing data space eigenvector of $\boldsymbol{J}$ in its coloumns, $\boldsymbol{V}$ is a $M \times M$ matrix which contains the parameter space eigenvectors, and Λ is a $M \times M$ diagonal matrix with eigenvalues (λ_i) as its diagonal elements.

The damping factor has a behavior as threshold on each iteration. The SVD approach [*Jupp and Vozoff*, 1975] implemented in EMUPLUS code has been applied for a detailed analysis of RMT and TEM data in chapter 5 and chapter 6.

3.1.4 Occam Inversion

The smoothness constrained model or more popularly named Occam inversion was introduced by *Constable et al.* [1987]. Occam inversion has two different smoothness criteria. The first one defines "roughness" as the summed up deference between adjacent layers of a B - layer case,

$$R_1 = \sum_{i=2}^{B} (m_b - \boldsymbol{m}_{b-1})^2 \tag{3.22}$$

second roughness R_2:

$$R_2 = \sum_{i=2}^{B-1} (\boldsymbol{m}_{b+1} - 2\boldsymbol{m}_b + \boldsymbol{m}_{b-1})^2 \tag{3.23}$$

where $\boldsymbol{m}_b$ is the resistivity of the B-th layer.

The strategy of Occam inversion is to find the solution for model parameters which have the smallest roughness. The Occam inversion normally gives many layers, therefore the computation of this methods is relatively time consuming. But the advantage of Occam inversion is that it produces smooth model, therefore the user is less required to set the starting model. The Occam algorithm was also implemented in EMUPLUS code. The first and second order smoothness to generate smooth model are used in the present work.

The combination between Levenberg-Marquardt and Occam inversions is recommended. Due to the *trial and error* in the inversion process and to find the best model, the strategy is using Occam inversion in order to find reasonable starting model for Levenberg-Marquardt inversion.

3.1.5 Monte-Carlo Inversion

Usually, geophysical data are affected by an error, which is the reason why many equivalent models can fit the data identically well within the same error margin. Additionally, if parts of the model are not constrained by any data because the method might not be sensitive for them, it is possible to produce a huge number of models which all differ from each other but have the same fitting. Thus, another possibility to evaluate the quality of a final 1D-model is to generate equivalent models.

In the Monte Carlo method, Marquardt inversions are being performed with different starting models for a given number of layers n. During this process, the possibility of the model parameters to vary is being determined to a reasonable range. The information of the monte carlo inversion can be found in *Mosegaard and Tarantola* [1995] and *Sambridge and Mosegaard* [2002]. The computation of this methods is time consuming because it requires a huge amount forward calculations. Due to the existence of model equivalences in inversion, a priori information as starting model can perform the inversion of equivalance model. The calculation of Monte-Carlo inversion is also performed by the EMUPLUS program.

3.1.6 Calibration Factor

The *calibration factor* or *scaling factor* is an arbitrary factor applied to the synthetic forward curve to fit the measured transients [*Scholl*, 2005]. The residual error ε between measured data $\boldsymbol{d}$ and model data $\boldsymbol{d}'$ can be minimized with *calibration factor* CF by multiplying it to the model data $\boldsymbol{d}'$ that can be denoted as:

$$\varepsilon = (\boldsymbol{d} - CF \cdot \boldsymbol{d}') \rightsquigarrow \text{minimum} \tag{3.24}$$

The CF has been used for correction of earth model due to incorrect transmitting current receiver area or receiver effected by small conductor anomaly [*Newman et al.*, 1986]. Without the scaling factor the earth models are biased because the models cannot fit to the data. *Scholl* [2005] gives a detailed explanation about the CF in inversion process. The desirable value of the CF gives a result close to 1. In EMUPLUS program, we have an option to set CF either free or fixed.

3.1.7 Joint Inversion

In order to have a good fitting and avoid ambiguity that is inherent to the individual methods, we can use joint inversion. Joint inversion is a method for inverting two or more data sets from different geophysical methods and using the same model. Application of joint inversion was first introduced by *Vozoff and Jupp* [1975] and first applied by *Meju* [1996] for EM sounding. In near surface exploration, the combination between RMT and TEM is commonly used because they complement each other [*Tezkan et al.*, 1996, *Schwinn*, 1999].

In the joint inversion of TEM and RMT, the measured data vector $\boldsymbol{d}$ can be denoted as:

$$\boldsymbol{d}_{joint} = \begin{pmatrix} \boldsymbol{d}_{RMT} \\ \boldsymbol{d}_{TEM} \end{pmatrix} \tag{3.25}$$

with $\boldsymbol{d}_{RMT}$ and $\boldsymbol{d}_{TEM}$ are measured data of RMT and TEM respectively.
The model function $\boldsymbol{A}_{joint}$ of model parameters $\boldsymbol{m}$ and the Jacobian matrix $\boldsymbol{J}_{joint}$ for the two methods can be expressed as:

$$\boldsymbol{A}_{joint} = \begin{pmatrix} \boldsymbol{A}_{RMT} \\ \boldsymbol{A}_{TEM} \end{pmatrix}$$

$$\boldsymbol{J}_{joint} = \begin{pmatrix} \boldsymbol{J}_{RMT} \\ \boldsymbol{J}_{TEM} \end{pmatrix}$$

$$\boldsymbol{W}_{joint} = \begin{pmatrix} \boldsymbol{W}_{RMT} \\ \boldsymbol{W}_{TEM} \end{pmatrix}$$

For the joint inversion the model update vector is

$$\tilde{\boldsymbol{m}} = (\boldsymbol{J}_{joint}^T \boldsymbol{W}_{joint}^2 \boldsymbol{J}_{joint})^{-1} \boldsymbol{J}_{joint}^T \boldsymbol{W}_{joint}^2 \tilde{\boldsymbol{d}}_{joint} \tag{3.26}$$

The Jacobian matrix $\boldsymbol{J}$ determines how the model should be altered to improve the fitting:

$$\boldsymbol{J}_{ij} = \omega_i \frac{\partial \boldsymbol{A}_i}{\partial \boldsymbol{m}_j} \tag{3.27}$$

where the weight ω_i and for B -layer earth model of resistivity ρ and thickness h are given as

$$\rho_i \geq; \mathrm{i} = 1,..., \mathrm{B} + 1 \tag{3.28}$$

$$h_i >; \mathrm{h} = 1,..., \mathrm{B} \tag{3.29}$$

The elements of the matrix, the equation 3.27 can be written as

$$\boldsymbol{J}_{ij} = \omega_i \frac{\partial \boldsymbol{A}_i}{\partial \boldsymbol{m}_j} = \frac{1}{\boldsymbol{A}_i} \frac{\partial \boldsymbol{A}_i}{\partial (log\rho_j, h_j)}) = \frac{\rho_j, h_j}{\boldsymbol{A}_i} = \frac{\partial \boldsymbol{A}_i}{\partial (\rho_j, h_j)} \tag{3.30}$$

In this scheme, the Jacobian matrix is made scale free. Since the relative error will be proportional to the model, the two kinds of the data will equally influence the correction that improves the current model. Theoretically, each of them can compensate for the weaknesses of the other, and therefore the overall benefit will be a reduction of ambuguity[*Raiche et al.*, 1985].

3.1.8 Sequential Inversion

The *sequential inversion* uses one data set and applies the inversion result of another data set as a priori information in the inversion process. In the sequential inversion of TEM and RMT, I use either fixed or free model parameters (resistivity ρ, thickness h and Calibration Factor CF) for the starting models of TEM inversion. The starting models are generated from the individual RMT result of Levenberg-Marquardt inversion. In the present work, the sequential inversion is described schematically in Figure 3.1:

1. The first step is inverting the RMT data with a Levenberg-Marquardt inversion.

2. From the inversion result, we receive model parameters ρ and h which can be used as a priori information for the starting model in the inversion of TEM data.

3. The next step is using these model parameters to invert the TEM data. In the inversion process, we set the parameters either free or fixed.

4. In the last result, we have new model parameters which are derived from RMT and TEM data.

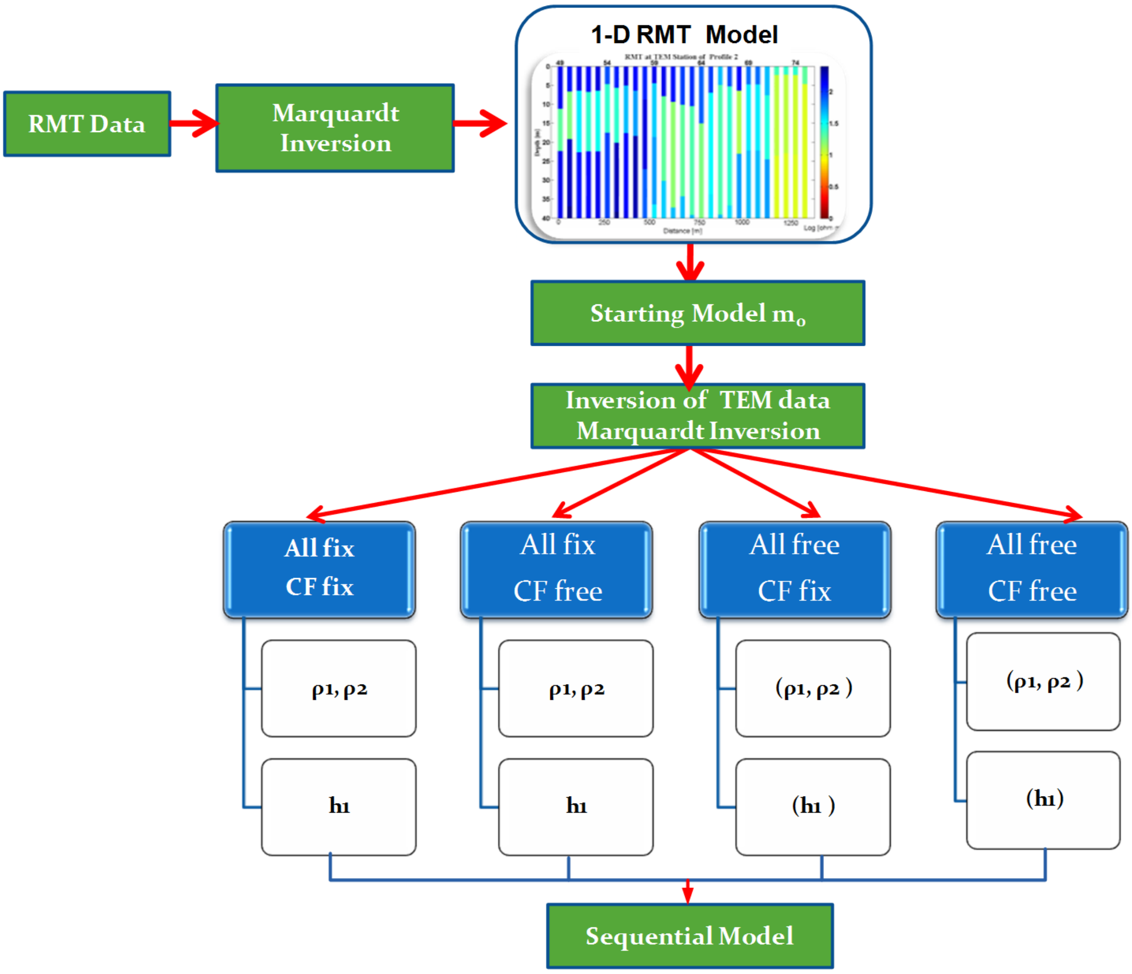

Figure 3.1: *Flowchart of sequential inversion of RMT and TEM. The setting parameters uses the CF and model parameters either free or fixed. Free model parameters of ρ_i, h_i are denoted with brackets (ρ_i, h_i) and without bracket ρ_i, h_i for fix model parameters.*

The advantage of sequential inversion is that it is able to combine two data sets from two different geophysical methods with one method as a priori information. However, the problem in sequential inversion is a huge misfit (RMS or χ) due to the fixed parameters in the starting model.

3.2 2-D Inversion

The 2-D inversion of TE and TM mode of RMT data is performed with the program *2dinv* from *Mackie et al.* [1997]. This program uses a non-linear conjugate gradient (NLCG) method. The NLGC method is based on the "steep descent" and the scheme is to minimize the objective function of $\Phi(m)$. A detail information of NLCG algorithm for 2-D inversion can be found in *Rodi and Mackie* [2001].

The cost function Φ(m) which is minimized, is denoted as

$$\Phi = \Phi_d + \tau \cdot \Phi_m \tag{3.31}$$

$$\Phi = (\boldsymbol{WA(m)} - \boldsymbol{Wd})^T(\boldsymbol{WA(m)} - \boldsymbol{Wd}) + \tau \parallel L(\boldsymbol{m}_1 - \boldsymbol{m}_0) \parallel^2 \tag{3.32}$$

where L is the second order smoothness operator or Laplace operator Δ. The regularization parameter τ weights between the data cost functional Φ_d and the model smoothness functional Φ_m.

Larger values of τ constrain the model toward smoothness with a high (Φ), whereas small values lead to overstructered models with small (Φ_d) but large (Φ_m) (Figure 3.2a).

The optimal weight between (Φ_d) and (Φ_m) can be derived from the "L-Curve" criterion [*Hansen*, 1992, *Farquharson and Oldenburg*, 2004]. They suggest to select the τ value from the L-curve, where the currature is highest.

The regularization τ of profile 5 is selected based on the L-Curve criterion with a starting model resitivity of 50 Ωm. Figure 3.2a is one example of L-Curve for profile 5 and the model norm are ploted against each other for selected regularization parameters. Figures 3.2b - e show 2-D models processed with regularization parameters of 0.5, 15, 100 and 1000, respectively.

Inverting 2-D with regularization parameter $\tau = 0.5$ results in an unclear 2-D model structure showing a distorted overstructered image (Figure 3.2b). Figure 3.2d and e show 2-D model results from regularization parameters $\tau = 100$ and 1000. They show smooth images in which the boundary of small structure among layers cannot be clearly distinguished. In order to obtain the proper image, the optimum regularization parameter τ is selected from the corner of the L-Curve. For profile 5, a regularization parameter $\tau = 15$ is selected which results in a clear image of the subsurface resistivity distribution (Figure 3.2c).

It can be concluded that the greater value of τ, the smoother the resulting image will be, and vice versa. Selecting the regularization parameter τ through the L-Curve criterion is also carried out for processing the 2-D inversion of RMT data at all other profiles (1, 2, 3, 4, 6, 7 and 8) for interpretation in chapter 5.

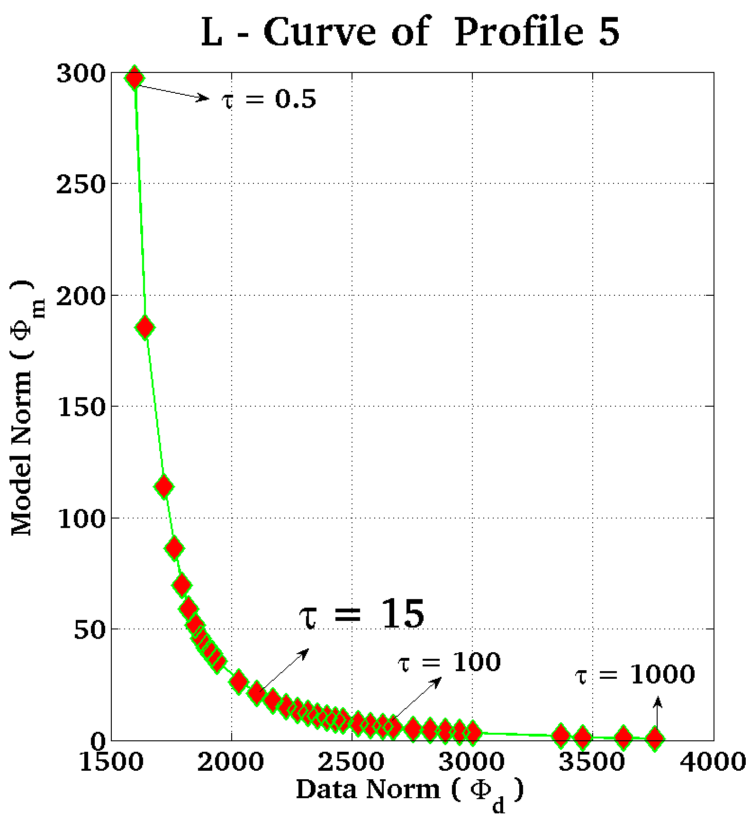

(a) The diagram of “L-Curve” between Data Norm (Φ_d) and Model Norm (Φ_m) of profile 5 shows four different τ: $\tau = 0.5$, $\tau = 15$, $\tau = 100$ and $\tau = 1000$. In this case the regularization parameter ($\tau = 15$) was chosen.

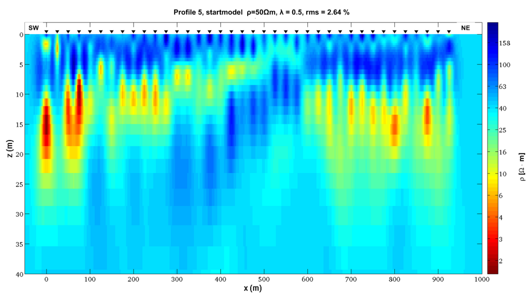

(b) 2-D conductivity model of profile 5 with $\tau = 0.5$.

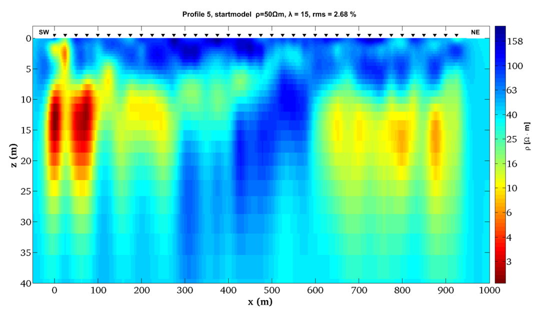

(c) 2-D conductivity model of profile 5h $\tau = 15$.

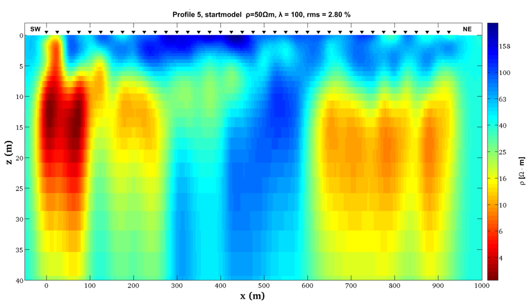

(d) 2-D conductivity model of profile 5h $\tau = 100$.

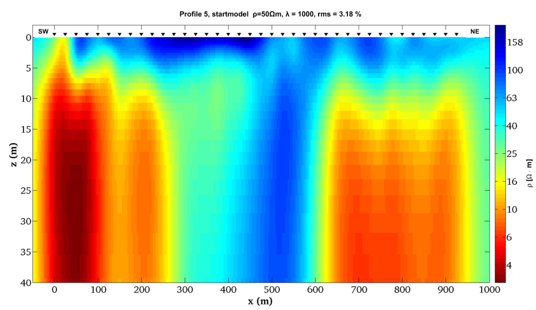

(e) 2-D conductivity model of profile 5 $\tau = 1000$

Figure 3.2: *L-Curve and 2-D conductivity model of profile 5 with different* τ*.*

3.3 Quality of Inversion Results

The quality of inversion results is depending on the misfit between measured data $\boldsymbol{d}_j$ and model data $\boldsymbol{d}'_j$. The misfit can be calculated as root mean square deviation (RMS-error) or *chi-square* χ^2.

RMS is defined as

$$\mathrm{RMS} = \sqrt{\frac{1}{N}\sum_{j=1}^{N}\frac{(\boldsymbol{d}_j - \boldsymbol{d}'_j)^2}{\boldsymbol{d}_j{}^2}} \times 100 \tag{3.33}$$

with relative error in percent (%).
In case the data errors are uncorrelated, the residual error $r = \boldsymbol{d}_j - \boldsymbol{d}'_j$ is weighted with the standard deviation σ_j of the measured data $\boldsymbol{d}_j$:

$$\chi = \sqrt{\frac{1}{N}\sum_{j=1}^{N}\frac{\left(\boldsymbol{d}_j - \boldsymbol{d}'_j\right)^2}{\sigma_j{}^2}} \tag{3.34}$$

The inversion will have an optimal fitting between measured and model data when $\chi = 1$. For $\chi < 1$, the data is overfitted. The quality of inversion results will give promising results when the resulting model can match with geological a priori information.

Chapter 4

Geology and Field Campaign

Geological problems related to the research area will be discussed in this chapter. Besides, the correlation of the application of near surface electromagnetic method will also be mentioned. Geological setting, local geology and detail description of the geophysical measurements carried out in the research area are also described in this chapter.

4.1 Motivation

The research area is located in the epicentre[1] area of 1978 earthquake, between Langada and Volvi lakes near city of Thessaloniki, Northern Greece (Figure 4.1). The biggest earthquake occured on June 20^{th} 1978 with a magnitude of Ms=6.5. At this time, arround 5000 houses were damaged and 45 people were killed [*Papazachos et al.*, 1979]. It is well known that the strong motion of such seismic activity causes irregular distribution which modifies the local geology. The objective of this work is to provide a high quality of geological data with several different geophysical methods [*Thanassoulas et al.*, 1987, *Jongmans et al.*, 1988, *Savvaidis et al.*, 2000, *Raptakis et al.*, 2002, *Bastani et al.*, 2011].

The basement of the Mygdonian Basin is composed by gneiss and schist which are located at around 200 m depth [*Raptakis et al.*, 2002]. The Mygdonian valley has a width around 4 km and the maximum thickness of the basin in Stivos village is estimated about 180 m [*Jongmans et al.*, 1988]. Therefore, we carried out near surface EM studies to understand the distribution of the active fault and the top of the basement structure of this particular area. Further information about tectonic setting and local geology of the research area will be reviewed in the next sections 4.2 and 4.3.

[1] The point on the Earth's surface where an earthquake or underground explosion originates which is determined by macroseismic information

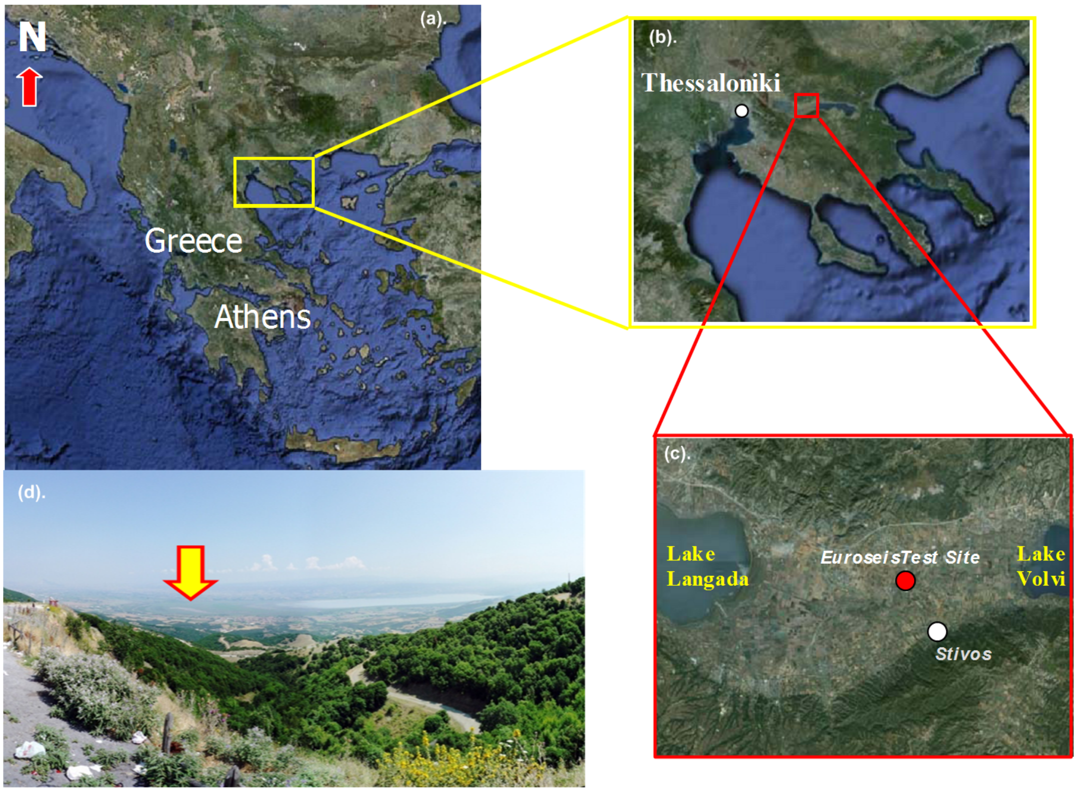

Figure 4.1: *(a-d) Research area located on the northeast of EUROSEIST TEST (red circle) between two Lakes (red square): Langada and Volvi Lake , Thessaloniki, Northern Greece. (d) Photo of the research area (yellow arrow).*

4.2 Tectonic Setting

The Hellenic subduction zone is the seismically most active region in Europe. There, the convergent plate boundary between the African lithosphere and the Aegen plate as a part of Eurasia is located at the south of Crete in the Libyan Sea (Figure 4.2a). The kinematic[2] interpretation in Figure 4.2b shows that the southern Adriatic is deposited between NW Greece which is slowly thrust and connected with coast line of the area [*Baker et al.*, 1997, *Shaw and Jackson*, 2010]. The shear zone between the Ionian Islands and the Southern Adriatic is thrust along the Kefalonia Transform Fault (KTF). The Aegen plate is influenced by the tectonic process in the Northern Greece, which is elongated E-W with tectonic depression.

A great number of large earthquakes in Northern Greece have occured in the Serbomecadonian massive. There are two main terms of active tectonics which exist along this massive: one is parallel to major river (NW-SE trend) and the second term is almost perpendicular to the first one, with complicated fault pattern variations (NW-SE,E-W,NE-SW) [*Psilovikos*, 1984].

[2]The motion of bodies (objects) and systems (groups of objects) without consideration of the forces that cause the motion

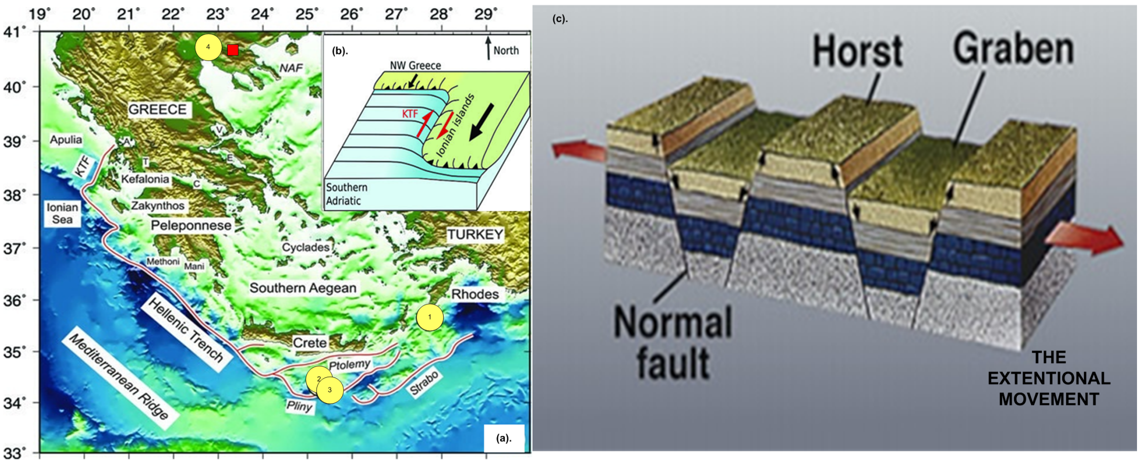

Figure 4.2: *(a) Tectonic setting of the research area (red square). The locations of the four example earthquakes are represented by yellow circles. The extensional graben of Central Greece are labelled as letters: C for Corinth; E for Evia; A for Arta; V for Volos; and T for Trichonis Lake. (b) Kinematic interpretation of Northern Greece in the Kefalonia Transform Fault. (Modified after [Shaw and Jackson, 2010]). (c) Schematic process of extension tectonic plate which produced horst and graben structures. (Modified after [Usgs.gov, 2011]).*

The extension of the Aegen region was highly distributed in the Southern part of the Serbomecadonian massive during Quartenary time. During this era, the extension was very active which is indicated by high seismicity [*Arsovski*, 1978, *Psilovikos*, 1984]. This process produced a complicated structure developed and it lifted *horst* and subsided *graben* structure. There are several minor *graben* and *horst* structures developed between Axios-Vardar Basin and Series basin. This process occured when the plate boundaries were diverging and it had an extensional motion. Geological layers were thickened and thinned throughout the process and were followed by *graben* and *horst* structure (Figure 4.2c).

There were two extensional phases in the internal Aegean area during the neotectonic age which affected the Southern part. The first occurred during the Lower-Middle Miocene when the Promygdonian basin was formed. The second phase developed during the upper Pliocene-Lower Pleistocene, when the smaller basin of Mygdonia, Zagliveri, Marathousa and Doubia were formed. During this time, a series of fluvioterresterial and lacustrine sediments were deposited in this basin. The Mygdonian basin was filled up by water forming a large lake (Mygdonia Lake). The main sedimentation of the Mygdonian basin consisted of lacustrine deposit. During the middle to late Pleistocene, the Mygdonia lake slowly subsided. The two lakes in the research area, Langada and Volvi lakes, were the residual of the initial one [*Koufosa et al.*, 2005].

Several big earthquakes have occured in the Thessaloniki area with the largest magnitudes up to M = 7.0 [*Papazachos and Papazachou*, 1997]. During this time, two destructive earthquakes happened there, the Assiros on 5 July 1902 and Stivos earthquake, 45 km northeast Thessaloniki, on 20 June 1978. Both have the same magnitude of 6.5 M. (Table 4.1).

The earthquake in 1978 occured along the villages of Gerakarou-Stivos which are known as the Thessaloniki-Gerakarou Fault Zone (TGFZ) [*Tranos et al.*, 2003]. Due to the orientation and the complex geological features, the TGFZ is divided into three main parts: Eastern, Central and Western. The eastern of the TGFZ is located to the West and South of Gerakarou and Vasilloudi villages, which belong to the Gerakorou formation section (Figure 4.3a). The Eastern part has strikes of ENE-WSW and dips to NNW. The Western part has strikes in NNE-SSW direction perpendicular to the Asvestochori-Chortiatis fault. The fault pattern of central part of the TGFZ is represented by the WNW-ESE strike faults that dip to the N with high angles. These faults are located at the westward prolongation of the Gerakarou-Stivos fault where it cuts the Chortiatis mountain(Figure 4.3b - Figure 4.3e). The western part of the TGFZ is a trough along the Asvestochori and Pefka villages with strikes of WNW-ESE (Figure 4.3f).

Table 4.1: *Historical earthquakes in Northern Greece since 500 A.D.. The epicenter area is determained by macroseismics with M is the equivalent moment magnitude [Papazachos and Papazachou, 1997]*

Year	Month	Date	Time	N°	E°	M	Reported Intensity
620				40.700	23.500	7.0	Thessaloniki (VII)
677				40.700	23.200	6.5	Thessaloniki (VII)
700				40.700	23.100	6.6	Thessaloniki (VII)
1677				40.500	23.000	6.2	Vassilika (VIII)
1759	June	22		40.600	23.800	6.5	Thessaloniki (VII)
1902	July	5	14:56:30	40.700	23.040	6.6	Assiros (IX)
1978	June	20	20:03:21	40.700	23.253	6.5	Stivos (VIII+)

An Earthquake gives a strong implication for a 3-D tectonic setting in this area. The seismic response between Langada and Volvi Lakes is strongly influenced by the local geological condition. Therefore, the EURO-SEISTEST test site is built to propose a good knowledge of the geological and physical parameters in this area (Figure 4.4).

Figure 4.3: *Active fault structure associated to the earthquake in 1978 along the Thessaloniki Gerakorou Fault Zone. (a) Eastern part of the TGFZ. Solid arrows indicate the Paraskevi fault. (b, c) Central part of the TGFZ with huge vertical fissure shown with black arrows. (d) Central part of the TGFZ in the west part of Chortiatis village (view towards SE). (e) Pilea–Panorama fault which forms a narrow rectilinear valley shown by white arrows. (f) Western part of the TGFZ. The rectilinear alignment of the Pefka–Asvestochori fault is shown by the white arrows. (After [Tranos et al., 2003]).*

Figure 4.4: *Test site of EURO-SEISTEST in Stivos, Thessaloniki. (a) Five-story building model. (b) Accelerometer sensor. (c) Bridge pier model. (d) Two boreholes for cross tomography experiments. (e) Crane.*

4.3 Geology

The geology of the research area is described in two subsections namely regional geology and local geology.

4.3.1 Regional Geology

The complex patterns of the regional geology are shown in Figure 4.5. It is indicated by irregular distribution of the geological layers along Langada and Volvi lakes. As mentioned in section 4.1 and 4.2, the irregularity pattern shows that the area has many structures around these lakes with the major fault in NE-SW and N-S directions. The regional geology of the research area between Langada and Volvi lakes corresponds to the Mygdonian basin. The Mygdonian valley is filled by sediments which are separated into two main units: the Promygdonian and the Mygdonian system [*Psilovikos*, 1984, *Koufosa et al.*, 2005].

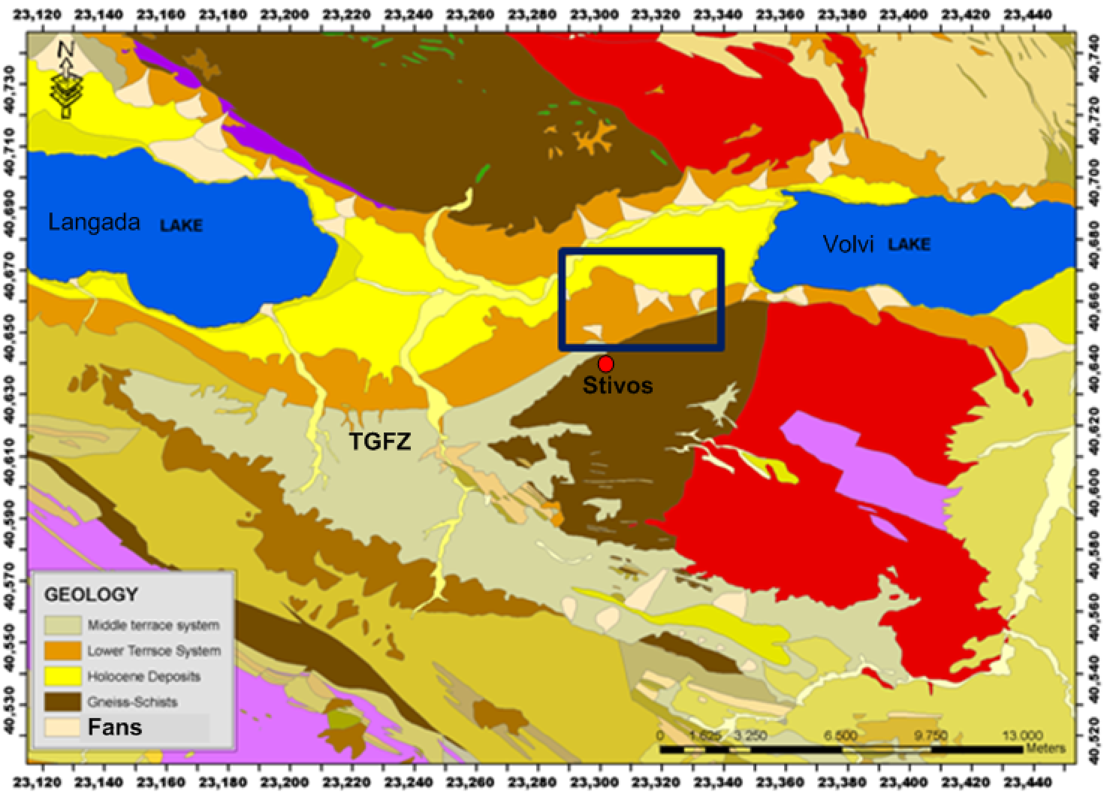

Figure 4.5: *Regional geological map. The research area (blue rengtangle) is located between Langada and Volvi lakes. The destructive earthquake of 1978 produced an active fault structure ("Thessaloniki-Gerakarou Fault Zone (TGFZ) structure") along the Gerakarou-Stivos Villages.*

1. **Promygdonian System**
   The datail description about the information of Promygdonian system is as follows *Koufosa et al.* [2005]. The **Promygdonian system** consists of three different lithologies during Neogene succession:

   (a) **Chrysavgi Formation**
   The Chrysavgi formation is the oldest formation in the Mygdonian basin and it has been formed on the top of the pre-Neogene basement. Figure 4.6a shows the lithosgraphic[3] of the Chrysavgi formation which consists of alternated lenses and lenses-shaped intercalations of grey-white, unconsolidated, coarse conglomerates (well rounded pebbles of mica-schist, gneiss, granite, quartzite, pegmatite up to 40 cm in size) and sands with silty-clayey lenses. The lower part of the formation is dominated by coarse conglomerates while a gradual decrease of the pebbles size is observed from the bottom to the top of the formation. Lenses and beds of silts, silty sands and silty clays are more commonly intercalated in the upper part of the formation. The thickness of Chrysavgi formation is around 40 - 50 m.

   (b) **Gerakarou Formation**
   The formation mainly consists of red-beds (Figure 4.6b). They are alternated lenses and lens-shaped beds of unconsolidated material from gravels, coarse sands, reddish-brown silts, clays. It was deposited in a fluvioterrestrial environment. The structure of the red-beds reveals a rhythmic deposition. Few lenses of sandstones and marls are locally intercalated in the red-beds. This formation is characterized by erosion which is forming deep and narrow valleys with stratified sides and geopyramidic shapes. This formation can be recognized by its erosion pattern and the red-brown color of the sediments. From the borehole data, the thickness of the formation is more than 100 m.

   (c) **Apollonia Formation**
   The formation is composed by fluvial, fluviolacustrine sediments (sands, sandstones, conglomerates, silty sands, silty-clays, marls, marly limestones) (Figure 4.6c). It is deposited on Gerakarou Formation. A transitional zone consisting of alternated lenses and lens-shaped beds of sandstones sandy marls and red beds can be locally observed between Gerakarou and Platanochori Formations. The occurrences of the Platanochori Formation are small and very scattered. The thickness of this formation is between 10 and 20 m. The upper part of it shows the hilly terrain as erosional remnants in the wider area of Platanochori, Riza and Apollonia villages (SE part of Mygdonia basin). The deposits of the Platanochori Formation indicate a gradual formation of small lakes before the complete filling of basin by water. It is the deposition of Mygdonian Group. Therefore, the Platanochori Formation is assosiated as a transition from the fluvioterrestrial sediments of the Gerakarou Formation into the lacustrine sediments of Mygdonian Group.

[3] The physical characteristics of a rock or stratigraphic unit

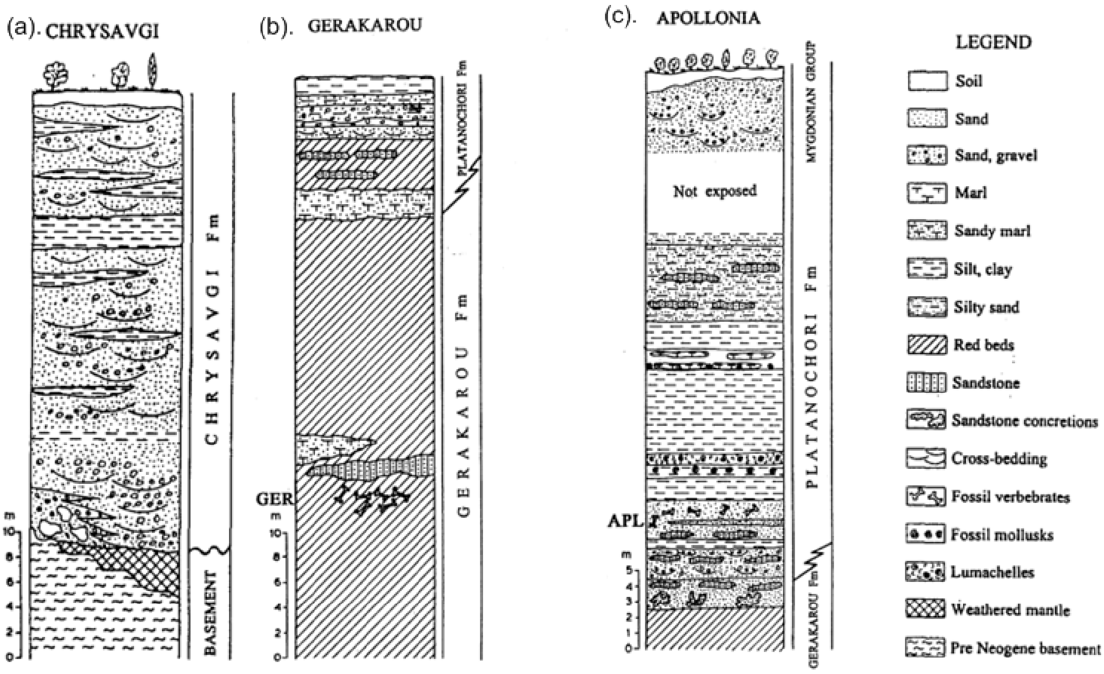

Figure 4.6: *Stratigraphic coloumn of the Premydonian system (a) Chyrsavgi Formation (b) Gerakarou Formation (c) Apollonia Formation. (Modified after [Koufosa et al., 2005]).*

2. **Mygdonian System**
The Mygdonian system corresponds to the sediments deposited unconformably during middle-late of Pleistocene. In lacustrine and deltaic sedimentations, the layers can be indicated with a wide range of colors including conglomerate, gravel, sand, silt and clay. The top of sediment was covered by travertine, but at this time, it is removed by erosion [*Jongmans et al.*, 1988]. The destruction of ground raptures in Mygdonian *graben* corresponds to the Gerakarou-Stivos fault and the detailed information of this structure will be described in the section of local geology.

4.3.2 Local Geology

The local geological map of the area is composed of four major units. The description of each layer is as follows (Figure 4.7):

- The holocene deposit[4], composed by sand, silt and clay.
- Fans[5] comprising soil and silt. This layer is called fans because the sedimentation form is like fans.
- The lower terrace deposit[6] is consisting of lacustrine and deltaic sediments including conglomerate, gravel and sand.
- The basement[7] is formed by schist and gneiss (methamorphic rock) and it is arround 200 m thickness in the research area [*Jongmans et al.*, 1988, *Raptakis et al.*, 2002].

According to law of superposition [8] in the stratigraphy concept, the stratigraphy of the local geological layers in the research area can be seen in Figure 4.7c of which the basement is consisting of schist and gneiss and the lower terrace which is deposited on the top of basement. Fans is deposited between holocene deposit and the surface layer and it is associated to holocene deposit. The conductivities of these layers are ranging from conductive to resistive values from the top to the bottom.

Based on the conductivity contrast of these layers and the location of the top of the basement, a near surface electromagnetic method will be an effective tool for the delineation of the top of the basement and the investigation of the complex geological structures.

[4]The GPS coordinates N° 40 40.183 E° 23 18.511
[5]GPS coordinates N° 40 39.732 E° 23 18.960
[6]GPS coordinates N° 40 39.407 E° 23 18.957
[7]GPS coordinates N° 40 39.052 E° 23 19.569
[8]The vertical sedimentation of rocks in which the younger rocks lie above the older rocks

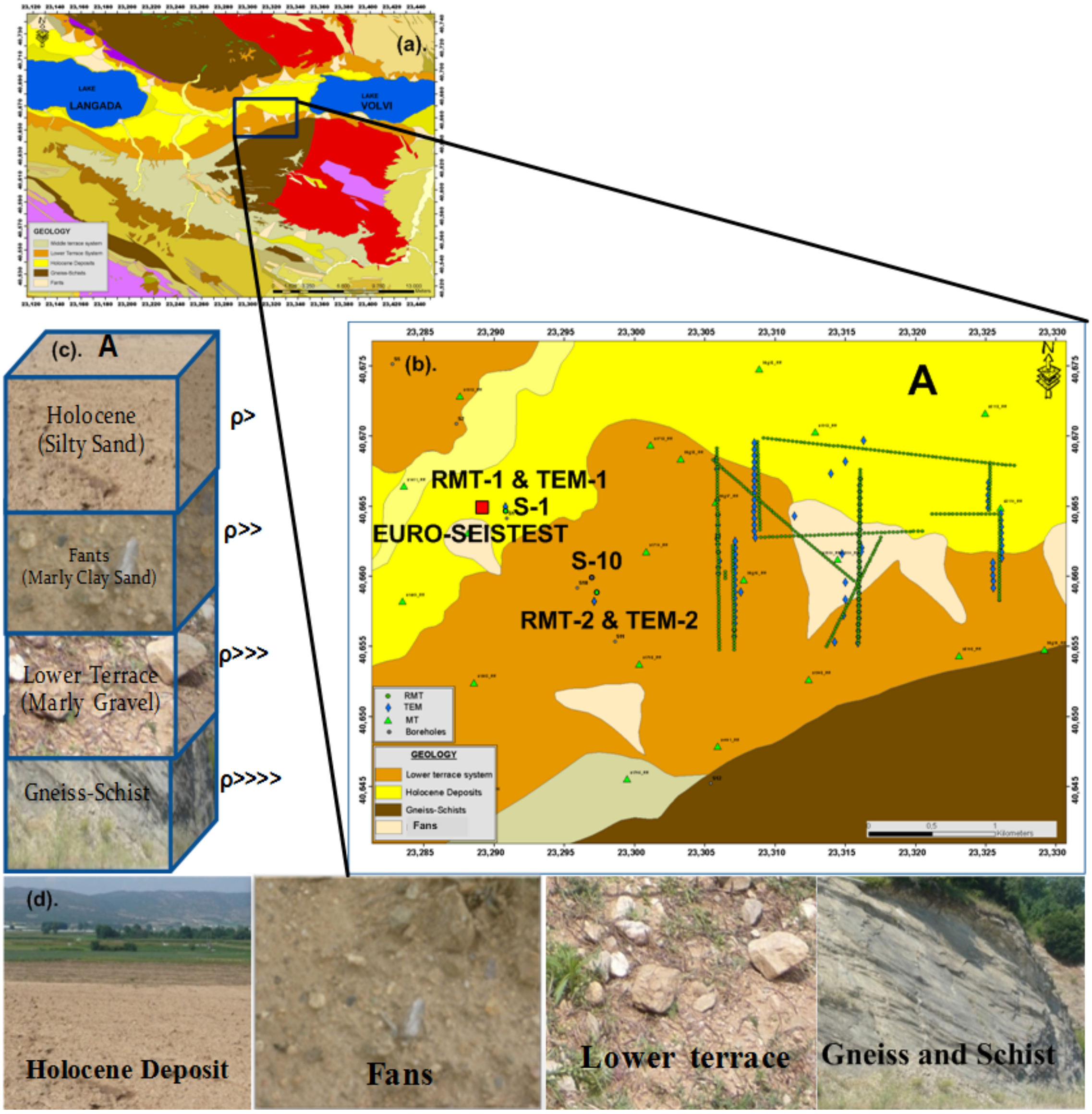

Figure 4.7: *(a) Regional geological map. (b) Local geological map consists of a unit of four layers: holocene deposit (yellow), fans (bisque1), lower terrace deposit (orange), gneiss-schist (dark-brown). The black circles are locations of bore-holes, the green dots and blue rhombs are the geophysical measurements of RMT and TEM soundings. The green triangles are the MT measurements, which are not included in the geophysical research of the present thesis. (c) Lithostratigraphy on point A is using the law of superpotition. (d) Description of each layer (holocene deposit, lower terrace deposit, fans and the basement gneiss, schist) which corresponds to the local geology of the research area.*

4.4 Geophysical Measurements

The geophysical survey was conducted on a site located between Langada and Volvi basin, which is at a distance of around 1 km east of EUROSIESTES site[9]. The study area was covered by crops (Figure 4.8a).

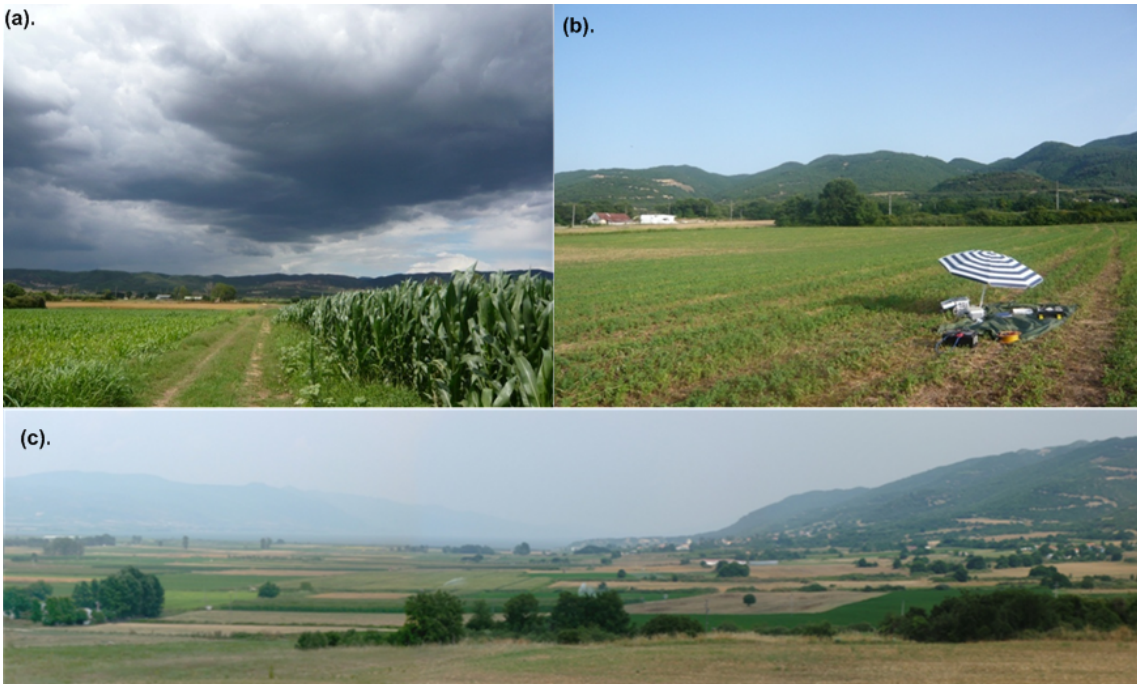

Figure 4.8: *(a) Investigation area was overgrown by agriculture. (b, c) Topography of the research area is almost flat.*

The topography of the research area is flat, however in the surrounding, the relief is dominated by hills and valleys (Figure 4.8b, c). This indicates a complex geological structure inside the Volvi basin (section 4.2). The main purpose of the geophysical investigation is to know the clear distrubution of local geological structure including the top of basement in the research area. For this purpose, two EM methods, RMT and TEM are applied.

[9]GPS coordinate of geophysical investigation with $N°$(40 39.193 - 40 40.279) and $E°$(23 17.143 - 23 19.143)

4.4.1 The First and The Second Field Campaigns of RMT and TEM

The geophysical survey was completed in two field campaigns in June 2009 and July 2010. The first campaign obtained 100 RMT soundings and 30 TEM soundings (include two soundings of RMT and TEM in borehole S-1 and S-10). On the first field campaign, the space among stations for TEM data tended to be irregular while for RMT, it was quite big gap. The reason was the limited accessibility in the research area because of the agricultural crops (Figure 4.8).

The second campaign was carried out on July 2010. A lot of RMT and TEM data were obtained. There are, respectively, 346 and 74 data for RMT and TEM with the distances of 25 m for RMT and 50 m for TEM.

During the second field campaign, a technical problem in TEM equipment occurred. The transmitter (NT-20) experienced a damage on the Nano TEM component. To solve the problem the decisition was made to use external damping factor to overcome it. This will be discussed in section 4.5.

The measurements from the first and the second field campaigns can be seen in Figure 4.9. Figure 4.10 shows the RMT and the TEM stations which are plotted on the geological map. Totally, 107 TEM and 446 RMT soundings were carried out.

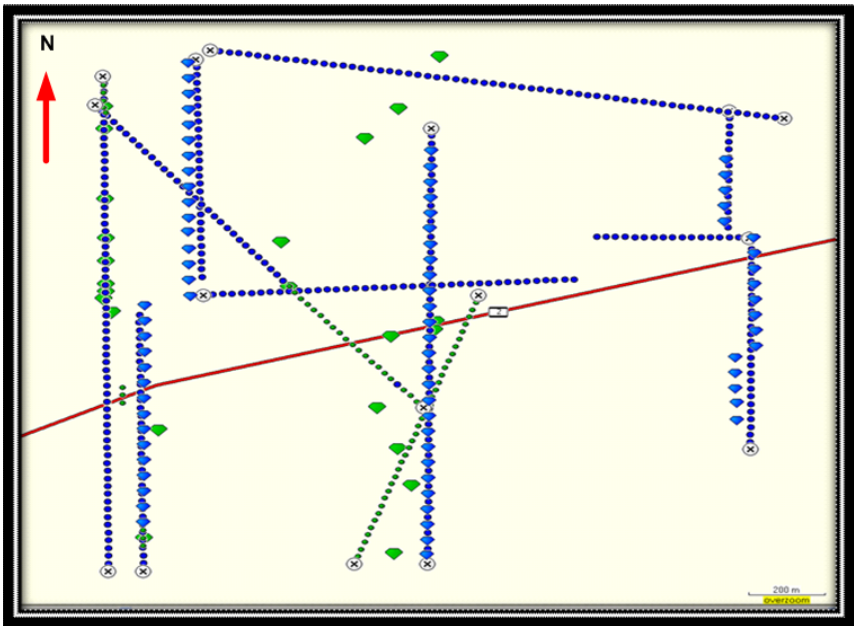

Figure 4.9: *Stations measured in the first and the second geophysical field campaign. The first measurement of RMT data is represented by green dots and the second measurement is represented by blue dots. TEM is represented by green and blue pentagons consecutively for the first and the second measurements.*

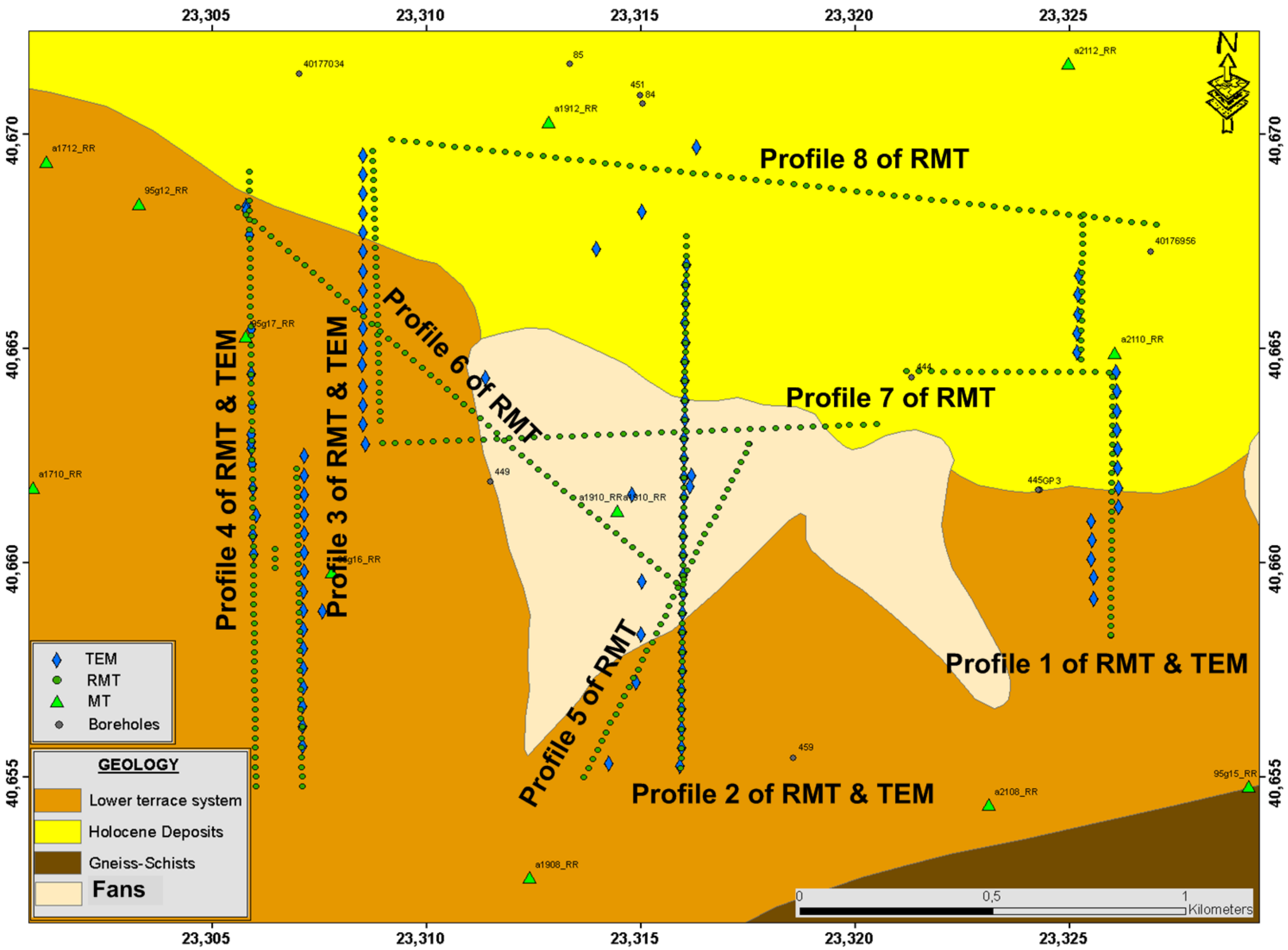

Figure 4.10: *The first and the second geophysical campaign of RMT and TEM data plotted on geological map. RMT is shown by green dots and TEM is represented by rectangular. The green triangles show MT measurement conducted by prior researcher.*

4.4.2 Field Setup of RMT Measurements

It is important to determine the radio transmitter azimuth for a radiomag- netotelluric survey correctly. For electrical antenna, the length of the dipole is 20 m. Its cable for the ungrounded lines has a substantial weight and its four components of electric and magnetic fields (Ex, Ey, Hx and Hy) are measured in the form of time series. Due to the complex geological structures and available radio transmitter, the setup of the two electric antennae of the RMT-F system is respectively parallel and perpendicular to the direction of the radio transmitters and likewise for two magnetic sensors (Figure 4.11).

The RMT measurements are carried out on eight profiles as indicated in Figure 4.12. The parameters of the survey design are listed in Table 4.2. The RMT profiles 1, 2, 3 and 4 are from 1100 m until 1700 m length with a direction of N 0° S, whereas the direction of profile 5 is located at N 21° E with 950 m length. The direction of profile 6 in this area is N 318° S with length of 1400 m, both of which are perpendicular to the radio transmitters. Profiles 7 and 8 are located N 86° S and N 98° S, respectively, which are parallel to the direction of the available radio transmitters. The advantage of RMT measurements is that they cross all geological boundaries (holocene deposit, fans and lower terrace deposit) (Figure 4.12). All coordinates of the individual RMT soundings can be seen in the Appendix J.

The measured time series consist of all the frequencies in connection with available radio transmitter station from 10 kHz to 1 MHz. In this receiver unit, gain factor, frequency range and recording length as the parameters are chosen using acquisition of SM25 software [*Microkor and St. Petersburg University*, 2005]. The software helps to display of the azimuths of all the available radio transmitters in the survey area. For example is observing available radio transmitter with various frequencies which is shown in Figure 4.13. In general, the coherence threshold chosen for related and representing the components of electric and magnetic field are 0.8. Then, from the power and cross spectra, apparent resistivity and phases can be derived.

Table 4.2: *Parameter of RMT survey design in two field campaigns*

Profile	Length [m]	Site distance [m]	Profile orientation
1	1000	25	N0°S
2	1400	25	N0°S
3	1700	25	N0°S
4	1600	25	N0°S
5	950	25	N21°S
6	1300	25	N318°S
7	1500	25	N86°S
8	1500	25	N98°S
Total soundings	443		

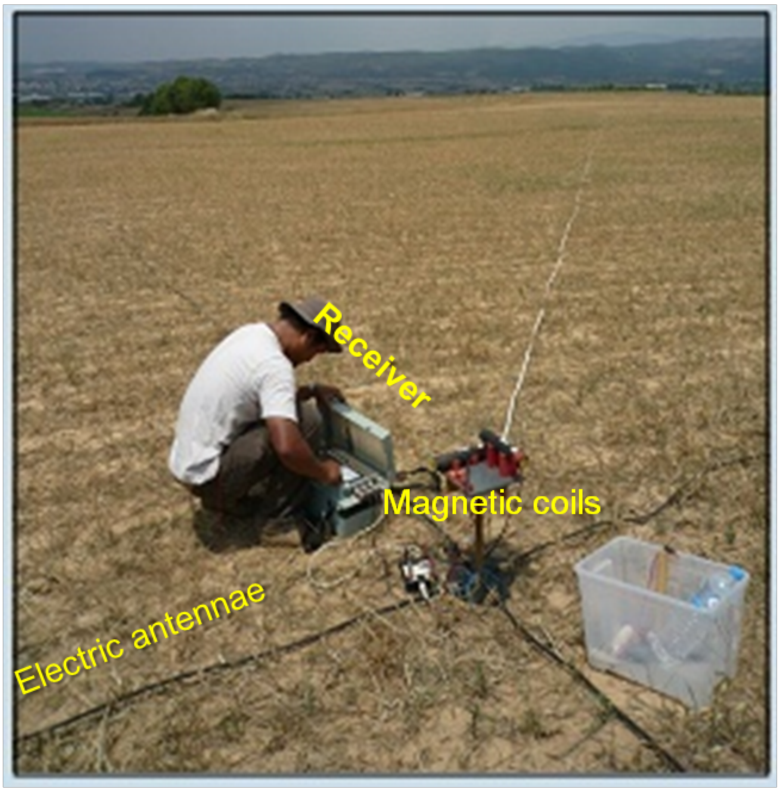

Figure 4.11: *RMT field measurement using RMT-F system in the research area.*

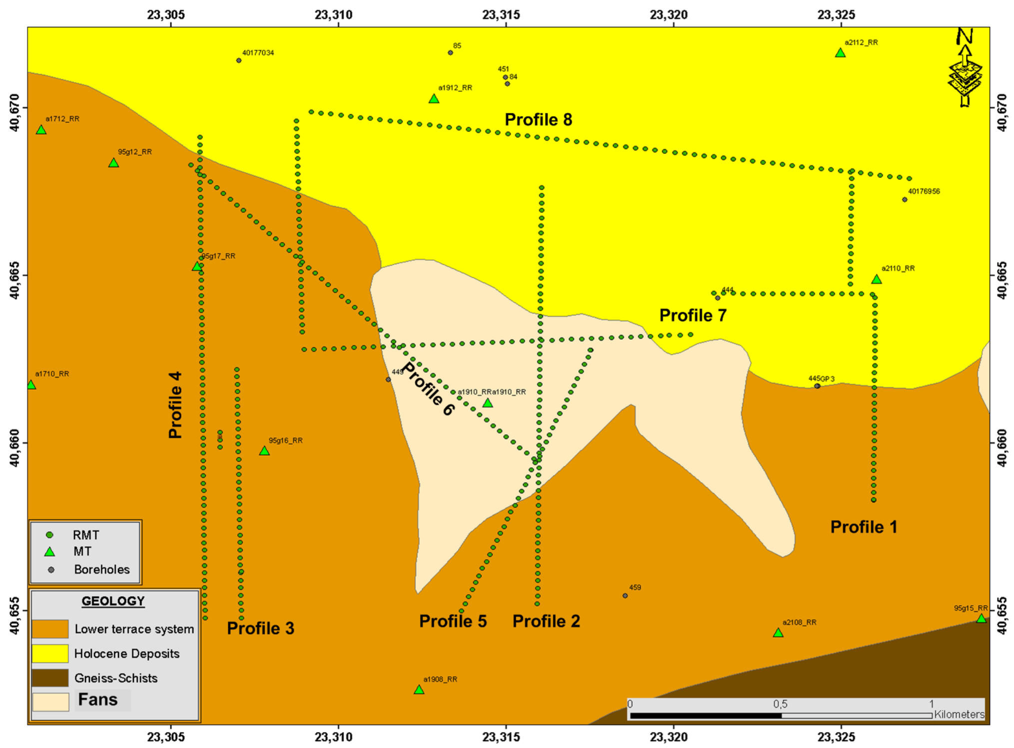

Figure 4.12: *Location of RMT measurements in the research area (green dots).*

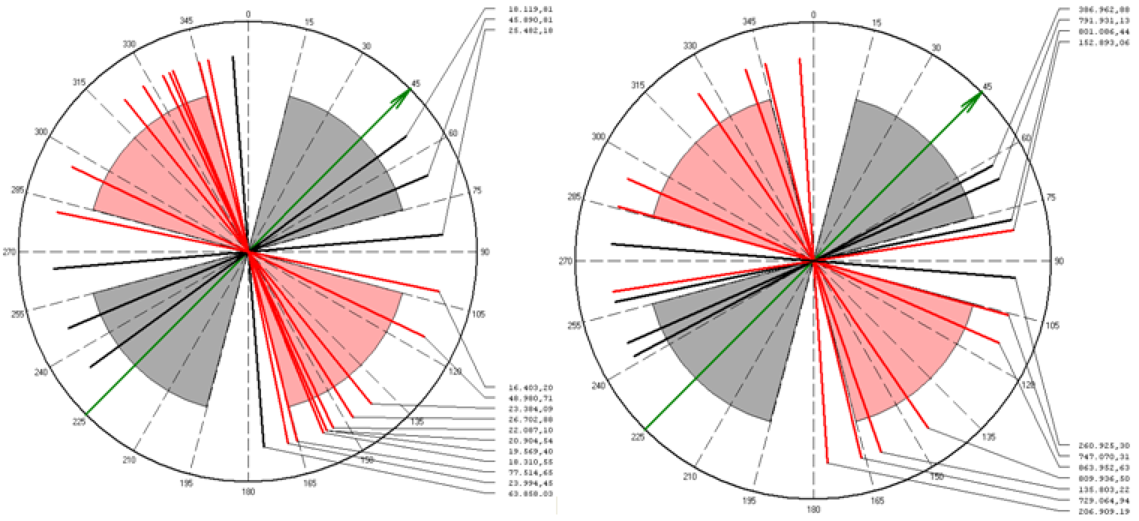

Figure 4.13: *The azimuth of existing radio transmitters in the research area. The transmitters located outside of the chosen interval are not selected.*

4.4.3 Field Setup of Transient Electromagnetic

The TEM soundings are performed using loop-loop measurements. The dimension of the transmitter Tx loop is 50 m × 50 m and receiver Rx loop is 10 m × 10 m (Figure 4.14). In general, the distances among TEM stations is 50 m and it depends on the accessibility of the area. TEM data are obtained using Zonge NT-20 transmitter and Zonge GDP32 receiver.

The TEM measurements have also crossed all geological boundaries (Figure 4.15). The detail information of the TEM setup can be described in Table 4.3. The TEM data are collected on four profiles (1, 2, 3 and 4). All of them have the same profile direction, N 0° S. Profile 1 of TEM data is crossing the lower terrace deposit and the holocene deposit. Profile 2 is crossing on three geological layers namely, the lower terrace deposit, fans and the holocene deposit. Profile 3 is on the west of profile 2 and crossing two geological boundaries of the lower terrace deposit and the holocene deposit. All coordinates of the individual RMT soundings can be seen in the Appendix K.

Table 4.3: *Parameter of TEM survey design in two field campaigns*

Profile	Lenght [m]	Site distance [m]	Orientation	Tx [m]	Rx[m]
1	850	50	N0°S	50x50	10x10
2	1350	50	N0°S	50x50	10x10
3	1500	50	N0°S	50x50	10x10
4	850	50 - 250	N0°S	50x50	10x10
Total soundings	104				

TEM and RMT data were collected on the four profiles at the same location. Each sounding of TEM data has one RMT sounding at the same location and in the middle of TEM stations (Figure 4.10). It is essential to overcome the resolution problem of TEM soundings for near surface structures. The same setup will also be used for joint inversion in chapter 6.

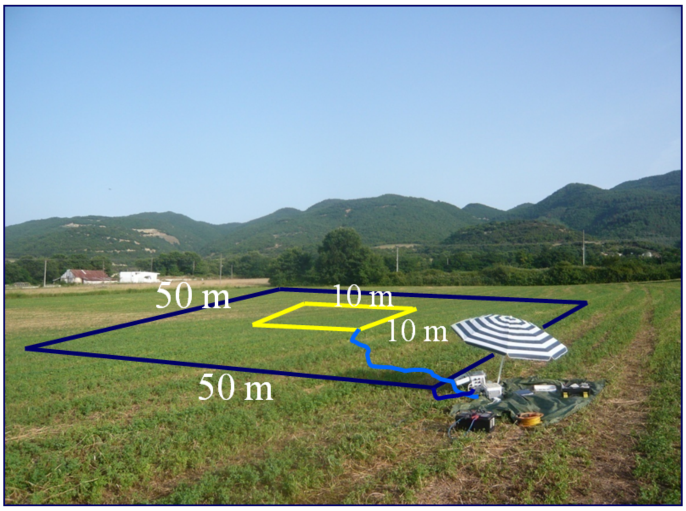

Figure 4.14: *Setup of TEM soundings performed using central loop (Tx: 50 m × 50 m and Rx:10 m × 10 m) configuration.*

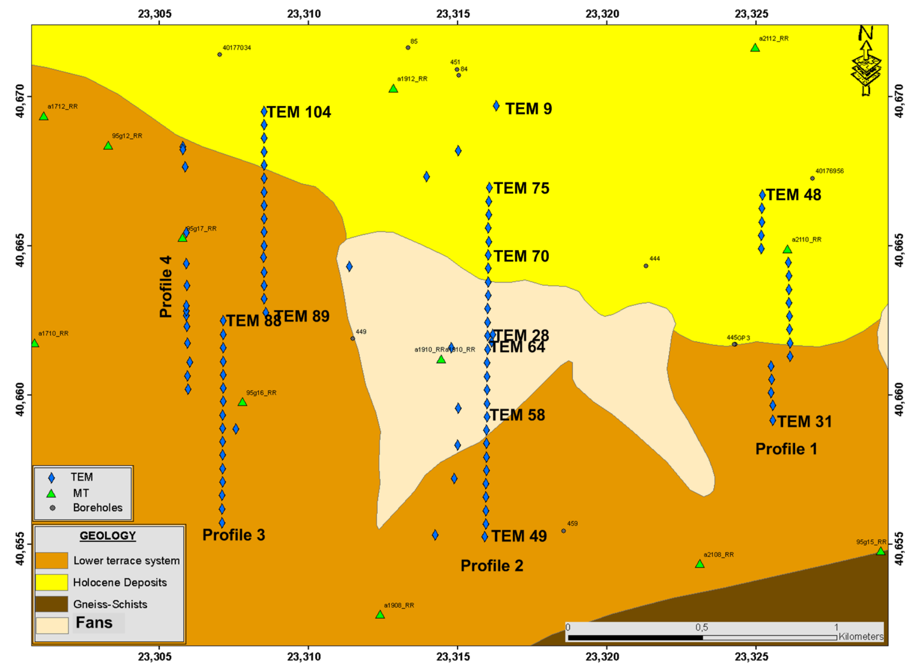

Figure 4.15: *Location of TEM measurements in the research area is represented by blue diamonds, green triangles are MT measurements and grey dots are boreholes.*

4.5 Problem

A technical problem in a component of the transmitter NT-20 equipment was found throughout the second field campaign. In Nano TEM mode at early times it caused an oscillation, which would affect the interpretation result of the surface layer.

In such condition, *Papen* [2011] provided detailed information on the effect of the component damage on the measurement result. He performed a comparison of two transients from neighboring measurement points before and after the equipment got damaged (Figure 4.16 right). The difference between the smooth unperturbed transient compared to the oscillation of the disturbed transient is clearly visible. He suggested that data affected by oscillation area can not be interpreted and has to be removed from the data.

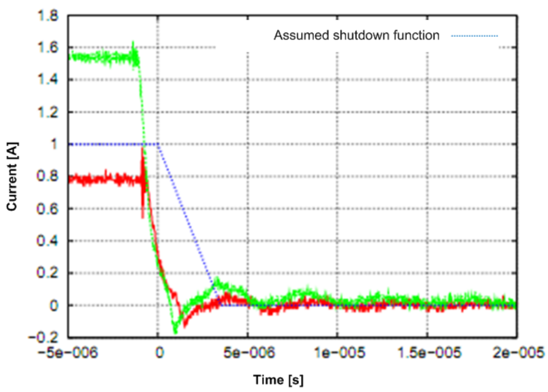

Figure 4.16: *Left: Measured current function at the end of the measurement campaign for two different currents (red, green) in NanoTEM mode. Blue line is the current function. It is assumed for deconvolution and approximately observed in an undamaged transmitter. Right: Raw data of two transients from adjacent measurement points. The time series were measured before (red) and after (green) the damage to the transmitter ([Papen, 2011]).*

To overcome the problem of the transmitter, an external damping box was used. The external damping factor 20 Ω was connected in Nano TEM mode. This aims to overcome the oscillation of the transient in Nano TEM mode. Figure 4.17 (left) shows the current function of Nano TEM data obtained by using external damping and Zero TEM data measured without external damping. Figure 4.17(left) shows the current function of Nano TEM data has a promising result (without experience oscillation). However, when looking at both transients together (Nano TEM and Zero TEM), it is obvious that the Nano TEM data is unrealible (Figure 4.17 (right)).

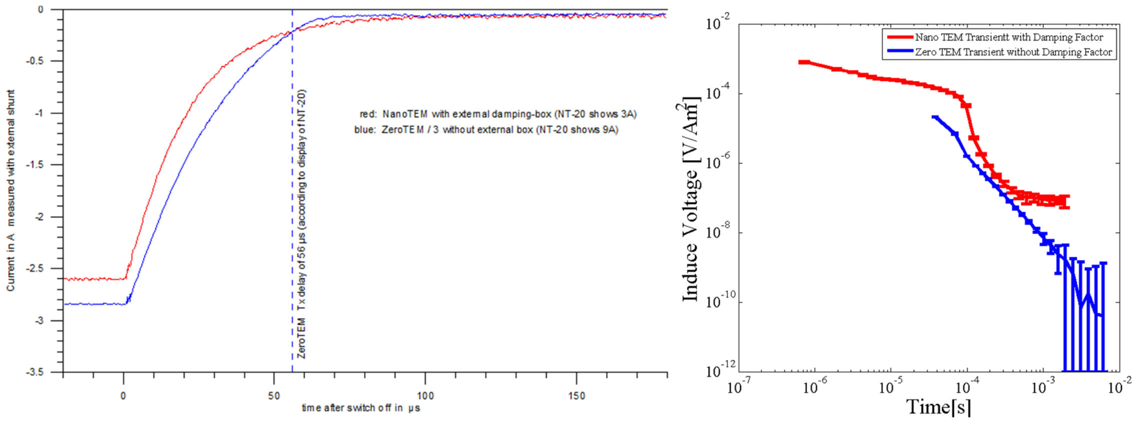

Figure 4.17: *Left: Current function between Nano TEM using external damping (red) and Zero TEM (blue) without external damping recorded at Laboratory. Right: Nano TEM Transient with external damping and Zero TEM transient without external damping recorded at TEM 64 in the field campaign.*

For further analyze, a comparison between two Nano TEM transients from the neighboring points is implemented. Nano TEM data at stations 28 and 64 are obtained from the transient before (without external damping) and after (by external damping) getting damaged, respectively (Figure 4.18). It is clearly visible that the transient recorded with external damping has an unreliable shape which could be due to the high resistence of the external damping of 20 Ω.

In this case, the external damping cannot work properly so the transient cannot be used to further process. Only the Nano TEM data is affacted by this problem, whereas the Zero TEM data has a good quality still can be used.

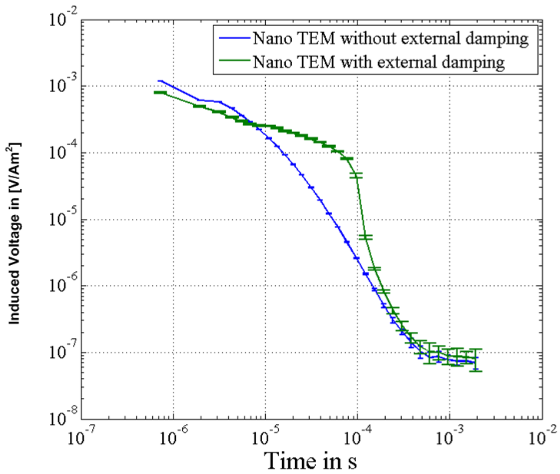

Figure 4.18: *Comparision between data using external damping (green) and without external damping (blue) of Nano TEM at station 64 and 28, respectively.*

Chapter 5

Geophysical Data Processing and Single Inversions of RMT and TEM Data

The processing of raw data and single inversions of RMT and TEM data will be explained in this chapter. In order to calibrate geophysical data, a correlation with borehole data has also been performed.

5.1 RMT and TEM Field Data

The explanation of raw data acquisition for RMT and TEM will be described in this first section (i.e. correlation between RMT raw data with geological formation and deconvolution process of TEM).

5.1.1 RMT Raw Data

As explained in the section 4.4.2, monitoring the directions of radio transmitter is very essential in RMT measurements. According to the availability of transmitters, sensor orientation and direction of profile have been specified. As an example, the raw data of profile 2 and profile 5 is explained in detail. Profile 2 has a direction from the South to the North and crosses through three geological units (lower terrace deposit, fans and holocene deposit). However, profile 5 has a direction from the Southeast to the Northwest located at lower terrace deposit and fans.

Figure 5.1 shows the raw data of profile 2 at frequencies of 20 kHz and 78 kHz. For profile 5, the raw data for frequencies of 78 kHz and 136 kHz is shown. At distance of 400 – 500 m on profile 2 for frequencies 20 kHz, the apparent resistivity is dominated by resistive structure with a resistivity more than 75 Ωm as a phase less than 45° is observed. The same distribution of apparent resistivity and phase is visible for frequency 78 kHz on profile 2. For the frequency of 78 kHz at profile 5, the apparent resistivity is relatively more conductive than that of 136 kHz at profile meter 300 on the same profile. Phases higher than 45° at profile 5 are indicating a more conductive layer at greater depth.

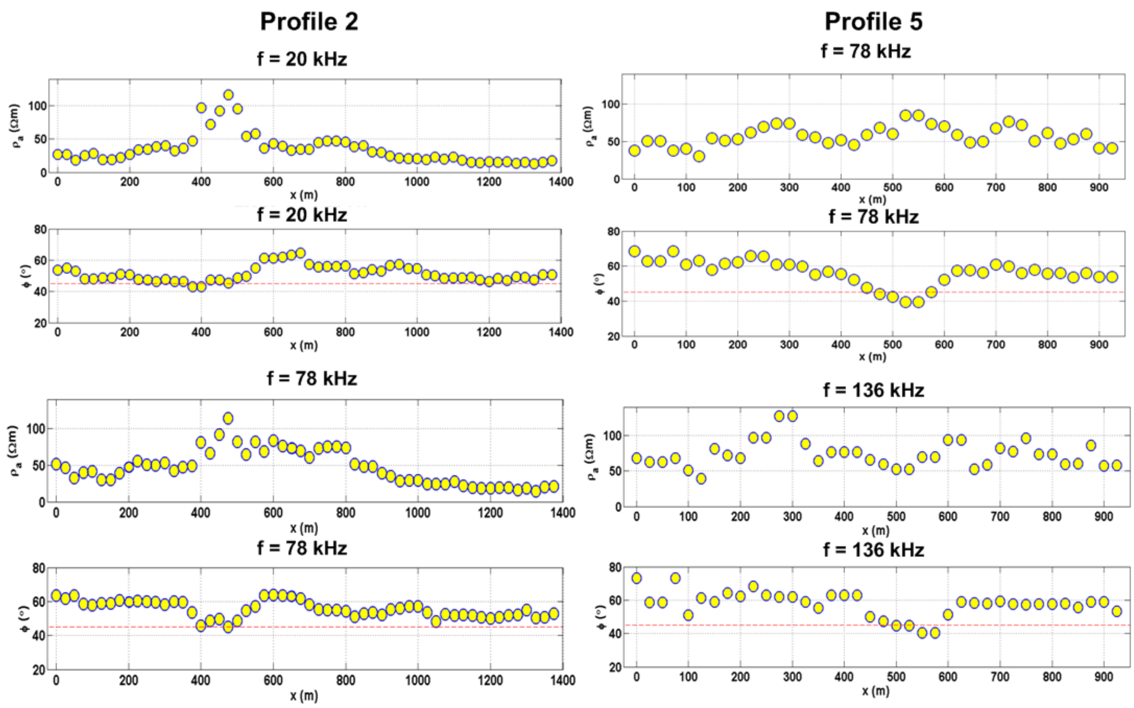

Figure 5.1: *Apparent resistivity and phase distribution for frequencies 20 kHz and 78 kHz at profile 2 (left) and frequencies 78 kHz and 136 kHz at profile 5 (right).*

Correlation between Geology and RMT Raw Data for Selected Frequencies

The correlation of RMT raw data with geological information is performed in order to check the consistency of the data. This process is done by calculating the average value of apparent resistivities at specific frequencies for stations located on each formation of the geological map (lower terrace deposit, fans and holocene deposit). There are three selected frequencies: 23 kHz, 135 kHz and 700 kHz. The average apparent resisitivity values obtained from each frequency is then averaged for all stations.

Figure 5.2 shows a histogram of the apparent resistivity distribution of each geological formation. The average values of each formation from the highest to the lowest frequency are consistent. The avarage apparent resistivity values, from the highest to the lowest, are identified by lower terrace deposit (75 Ωm), fans (60 Ωm) and holocene deposit (20 Ωm).

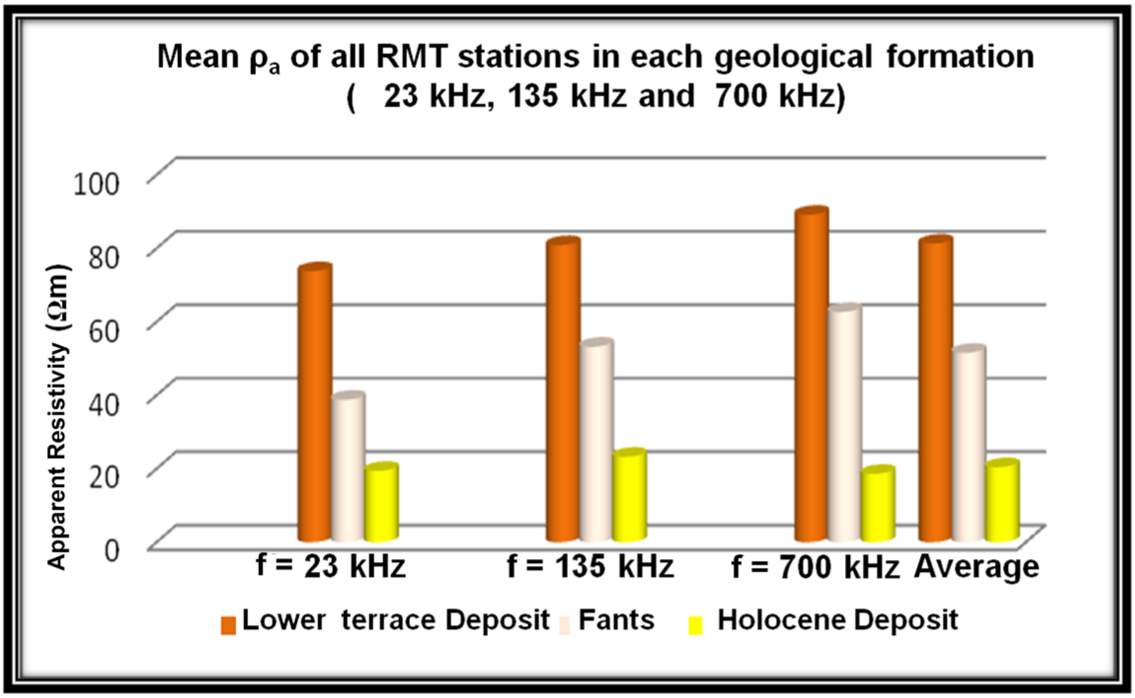

Figure 5.2: *Average apparent resistivities for different geological formations at frequencies 23 kHz, 135 kHz and 700 kHz.*

5.1.2 TEM Raw Data

TEM data is recorded in three different modes, namely Nano TEM low gain, Nano TEM high-gain and Zero TEM, for each station (see section 4.4.3). From these three measurements, a transient is formed. Nano TEM data with 10×10 m^2 receiver in 120 blocks of data was recorded (each mode has 40 data blocks). One data block consists of 1024 stacks for a single masurement with 31 data points for each transient. With this process, avarage values and standard deviations are obtained. In addition, in the data processing, the measured induced voltages are normalized by transmitter current and receiver area so that the voltage can be specified in Am^2 and we can compare the data of different modes.

Figure 5.3 shows the misfit of Nano TEM data for low and high gain as well as Zero TEM. The influence of the polarities on the transient can be estimated by comparing the two transients. *Mollidor* [2008] suggests to only use data points which show less than 20% difference for the two polarizations.

Deconvolution

Decay transient of Nano TEM and Zero TEM data is recorded sequentially by using two different currents. In such condition, the transient is recorded with a different ramp time of Nano TEM and Zero TEM and therefore, deconvolution is needed. This can be done by deconvolving the ramp time of each transient with the EADEC program [*Hanstein*, 1992, *Helwig et al.*, 2003, *Lange*, 2003]. Figure 5.4 shows the result of deconvolution of Nano TEM and Zero TEM data which is of good quality.

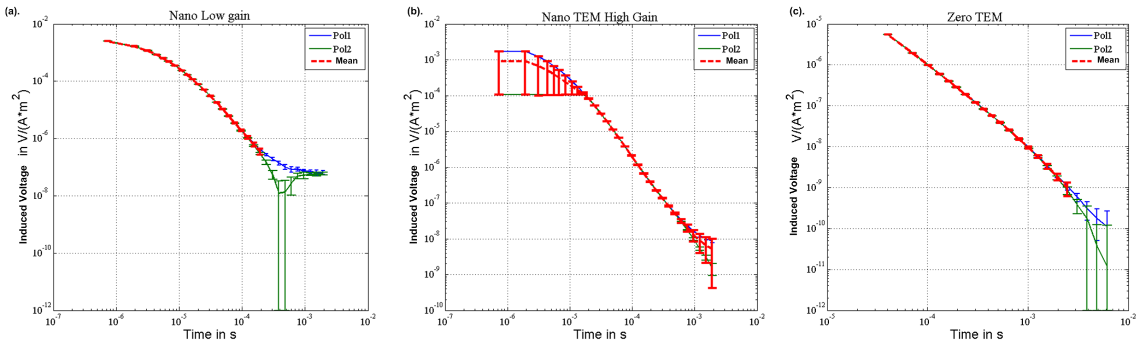

Figure 5.3: *Transients of the two polarities of each mode. (a) Nano TEM low gain (b) Nano TEM high gain (c) Zero TEM.*

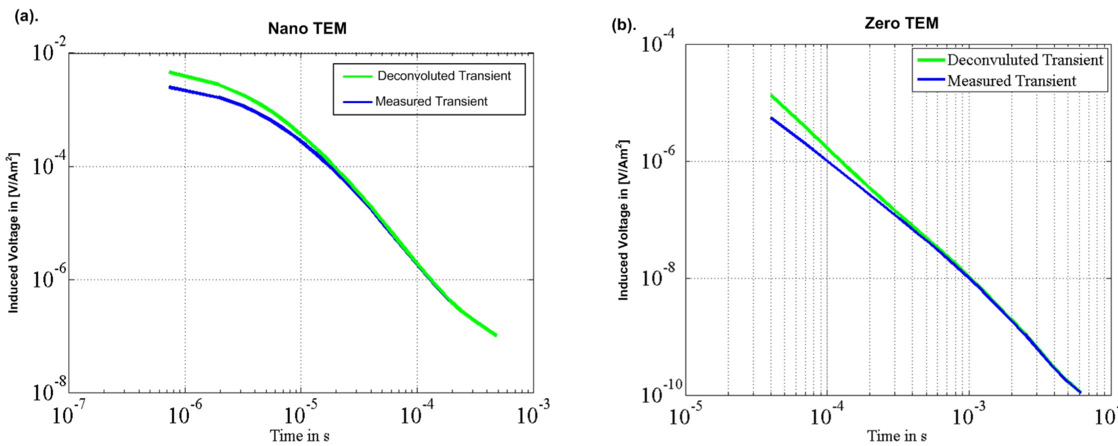

Figure 5.4: *Deconvoluted transient of (a) Nano TEM low gain and (b) Zero TEM at station 1 (TEM 1).*

Combination for All Transients

Once the deconvolution process is finished, data gained from each mode can be combined into one transient. Figure 5.5 (top) shows a combination of Nano TEM and Zero TEM data. Deconvolution of transient data is effective in early time windows [*Hanstein*, 1992]. Therefore, there are only two or three data points of Zero TEM which do not match with the late time of Nano TEM data. The first few data points of the Zero TEM transient are located underneath the two last points of the Nano TEM transient. After editing the data accordingly, all three data sets can eventually be combined into one smooth curve, the final transient (Figure 5.5 (bottom)).

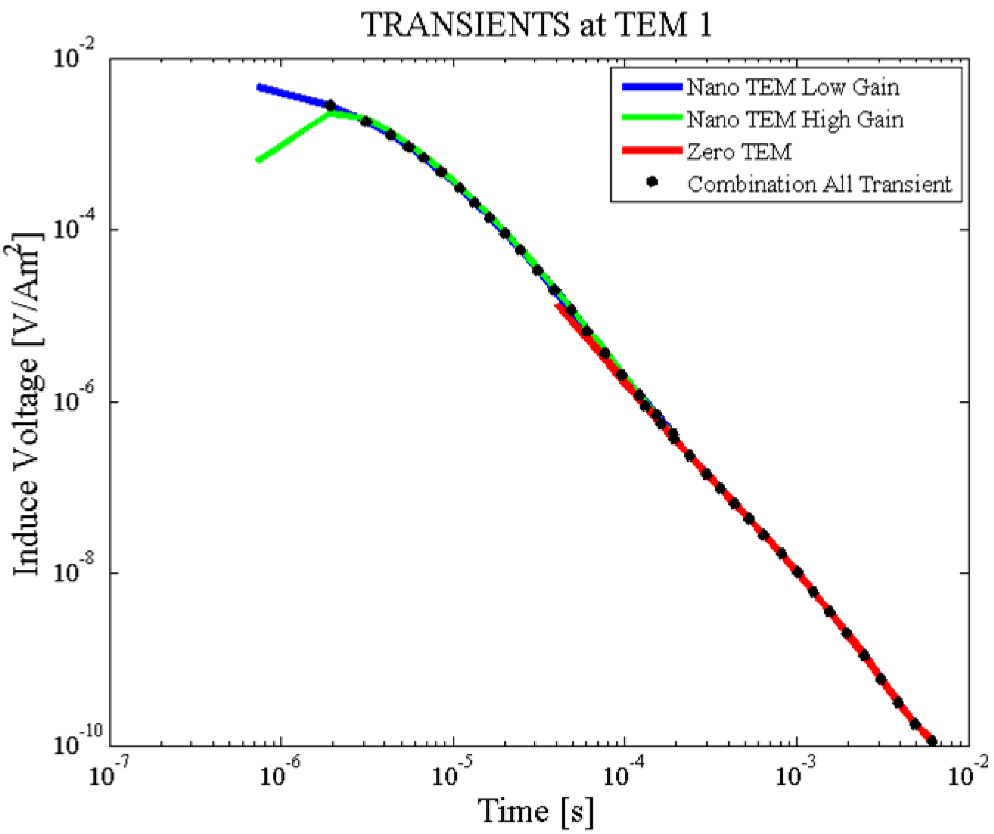

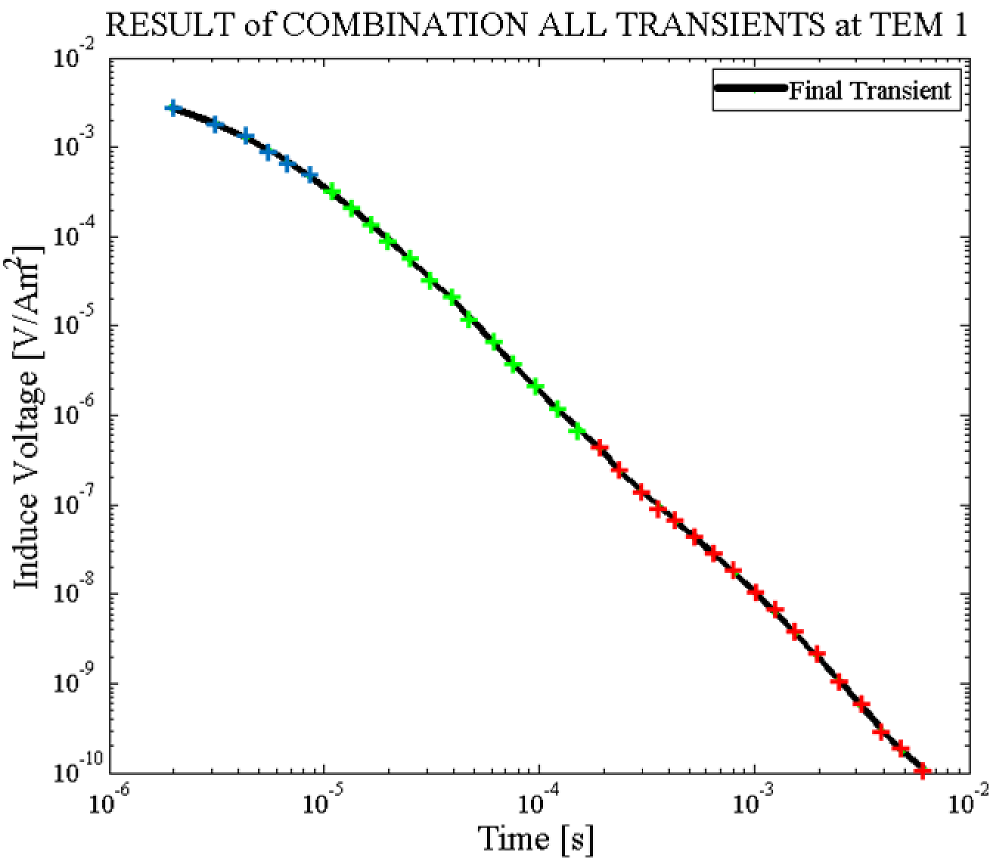

Figure 5.5: *Top: Combination of all three of deconvolution results: Nano TEM low-gain (blue), Nano TEM high-gain (yellow) and Zero TEM (red). Bottom: final result from the combination of all data.*

5.2 1-D Inversion of RMT and TEM Data

1-D inversion of RMT and TEM data is calculated using the program Emuplus. It is a scientifically proven tool for processing RMT and TEM data [*Wiebe*, 2007, *Scholl*, 2005, *Lange*, 2003]. First, the 1-D Occam inversion of data is carried out, as the Occam inversion process is less influenced by the starting model.

5.2.1 1-D Occam Inversion

As described in chapter 4, TEM and RMT measurements have been performed on three different geological units: holocene deposit, fans and lower terrace deposit. In order to obtain suitable 1-D models, RMT and TEM data inversion is carried out.

Figure 5.6 shows 1-D Occam inversion results of RMT data. RMT station 50 (RMT 50), RMT 64 and RMT 73 are located on lower terrace deposit, fans and holocene deposit, respectively. The model RMT 50 indicates a resistive layer (100 Ωm) at depth of 0 – 5 m while at the same depth, model RMT 64 has a less resistive layer (70 Ωm) and model RMT 73 is shows the most conductive layer of the three with a resistivity of 30 Ωm.

From the first and second order smoothness constraints of the Occam inversion, the resolution of each model can be specified by comparing the two derivatives. The first and the second derivative both have good fitting to a depth of 25 m for holocene deposit and 35 m for fans and lower terrace deposit (Figure 5.6).

In order to find out the RMT data sensitivity for each of the geological units, a calculation of the penetration depth is conducted. It is calculated by using equation 2.19 at frequency 18 kHz and using the resistivity values of the Occam model for the first layer (depth = 0 - 5 m). Table 5.1 shows the maximum penetration depth of RMT for holocene deposit as 20.5 m and 31.36 m for fans. Due to the lower terrace deposit being the most resistive geological unit of the three, it also offers the greatest penetration depth of 37.49 m depth.

Table 5.1: *Penetration depth of RMT measurements on holocene deposit, fans and lower terrace deposit.*

Location	f[Hz]	ρ[Ωm]	Skin Depth[m]
Holocene deposit	18000	30	20.53
Fans	18000	70	31.36
Lower terrace deposit	18000	100	37.49

Table 5.2: *Approximation of shallow penetration depth of TEM measurements on holocene deposit, fans and lower terrace deposit.*

Location	$t[\mu s]$	$\rho[\Omega m]$	Skin Depth[m]
Holocene deposit	2.5	30	10.92
Fans	2.5	70	16.69
Lower terrace deposit	2.5	100	19.95

Table 5.3: *Approximation of large penetration depth of TEM measurements on holocenen deposit, fans and lower terrace deposit.*

Location	$t[\mu s]$	$\rho[\Omega m]$	Skin depth[m]
Holocene deposit	500	30	154
Fans	500	70	236
Lower terrace deposit	500	100	282

The TEM models (TEM 2, TEM 9 and TEM 28) obtained from Occam inversion can be seen in Figure 5.6. The 1-D conductivity model is obtained from the first and the second order smoothness derivatives at three different stations. TEM 2 is located at the reference site at borehole S-10 in the lower terrace deposit. TEM 28 and TEM 9 are respectively located at fans and holocene deposit. The first and second order smoothness derivatives of TEM generally fit from 15 - 200 m depth. In order to get to know the sensitivity of TEM data in subsurface, the calculation of the penetration depth is performed using equation 2.20.

The average values for shallow and large penetration depths of TEM data in the three geological units are 15 m and 225 m, respectively, calculated for times of 2.5 μs and 500 μs (Table 5.2 and Table 5.3).

5.2.2 Monte Carlo Inversion

In the next step, RMT and TEM data are interpreted using Monte Carlo algorithm. Figure 5.7 and Figure 5.8 show the equivalent models of RMT and TEM data for the same stations previously used to demonstrate the Occam models. Deviation between the equivalent models and the best model (the lowest RMS error) is relatively low. For the first and the last layer, the equivalent models show considerable differences. However, the resistivities of the layers between these generally show similar values for each station which indicates good resolution.

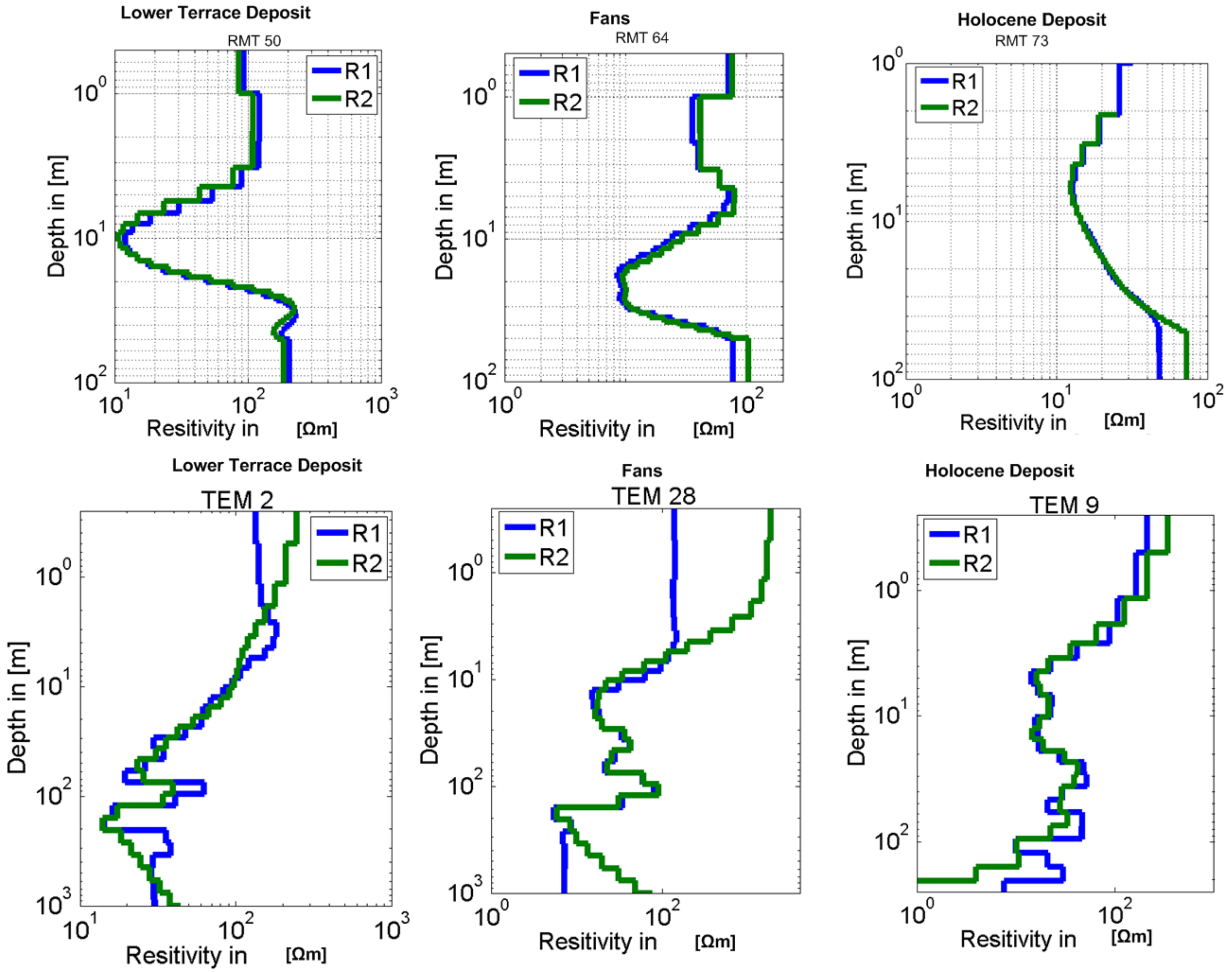

Figure 5.6: *1-D Occam inversion of RMT and TEM data results for the first (R1) and the second (R2) order of smoothness constraints at lower terrace deposit, fans and holocene deposit.*

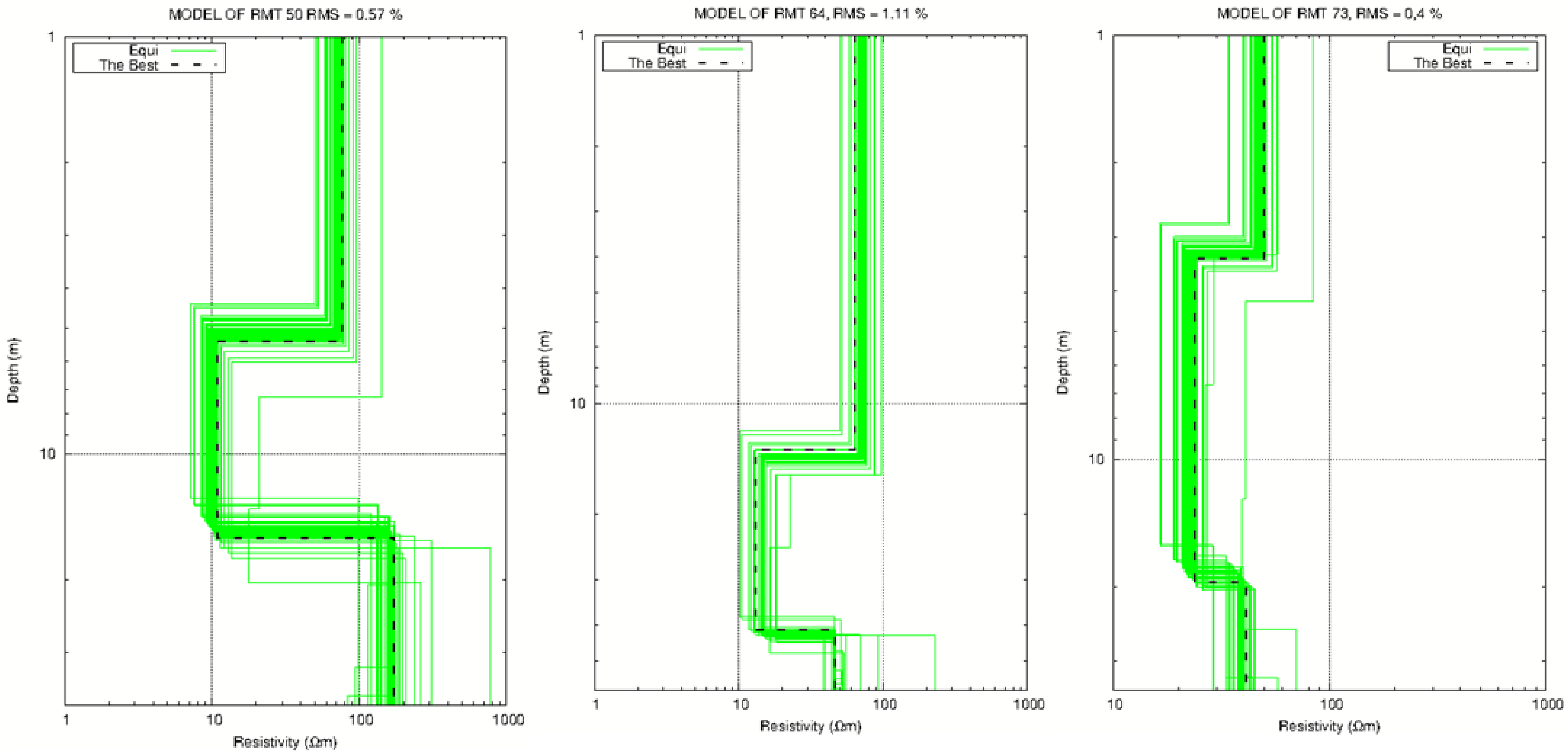

Figure 5.7: *1-D equivalence models for the RMT data at holocene deposit, fans and lower terrace deposit.*

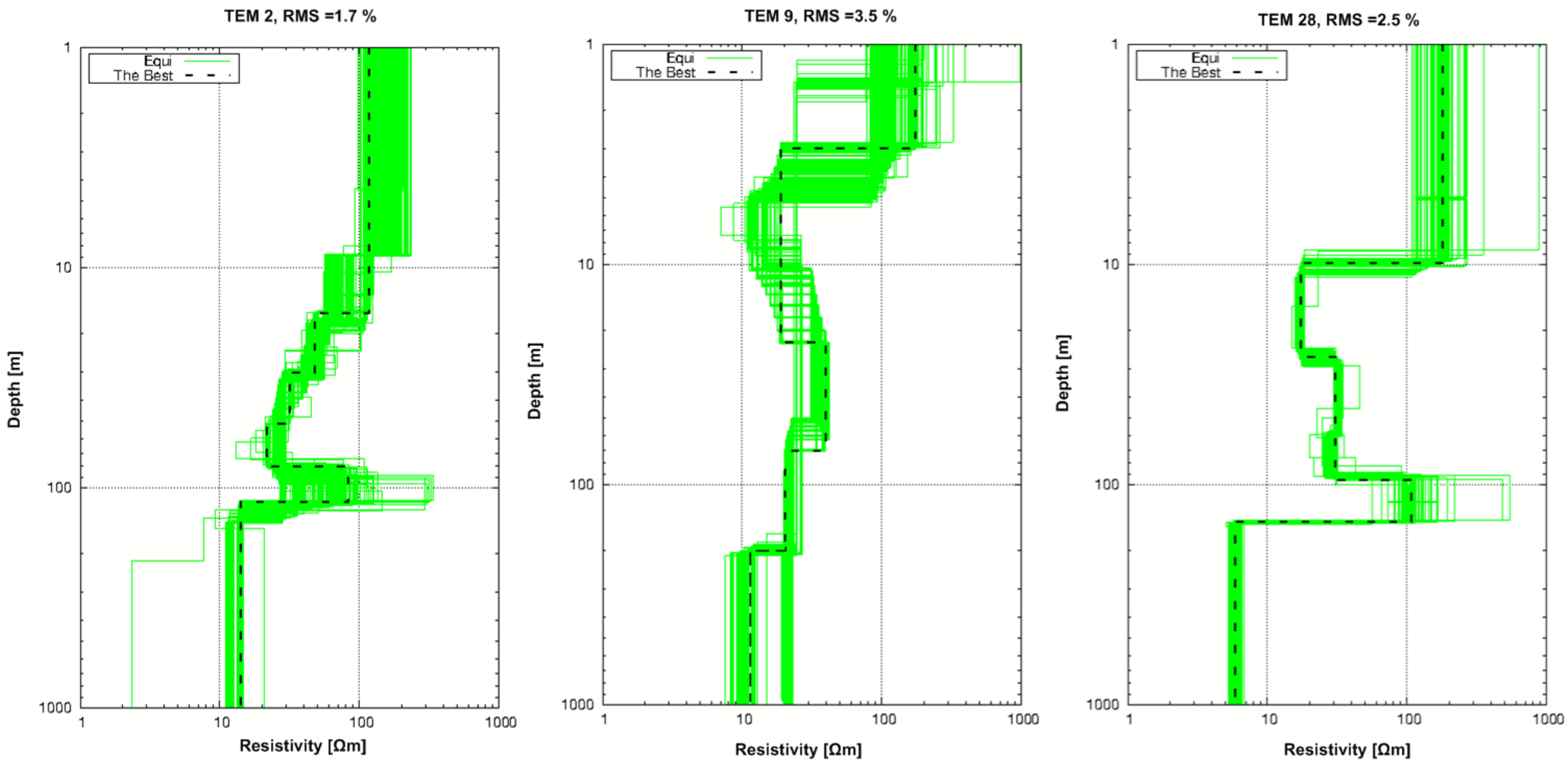

Figure 5.8: *1-D equivalence models for the TEM data at holocene deposit, fans and lower terrace deposit.*

5.2.3 Marquardt Inversion

In order to obtain the layered model using Marquardt algorithm, a proper starting model is necessary for inverting TEM and RMT data.

Starting Model in Marquardt Inversion

From the previous research [*Jongmans et al.*, 1988, *Bastani et al.*, 2011], it is known that lower terrace deposit is dominated by resistive layers with resistivity values over 80 Ωm. Fans has a lower resistivity than lower terrace deposit, while holocene deposit has the least resistivity of all three. This information has been used as a reference for the starting model.

Generally, three different starting models, for RMT and TEM data are taken for those different geological units. Moreover, we can use the result of the Occam model which is in accordance with the previous research. The first layer (h_1) of each starting model consists of 30 Ωm, 70 Ωm and 100 Ωm.

The RMT and TEM data is inverted by using six different starting models with two up to seven layers with a resisitivity ρ of 50 Ωm for the second layer and every layer underneath (Table 5.4).

Table 5.4: *Starting model for Marquardt inversion of single RMT and single TEM data*

	RMT			TEM		
	lower terrace	fans	holocene	lower terrace	fans	holocene
ρ_1	100	70	30	100	70	30
ρ_2	50	50	50	50	50	50
ρ_3	50	50	50	50	50	50
ρ_4	50	50	50	50	50	50
ρ_5	50	50	50	50	50	50
ρ_6	50	50	50	50	50	50
ρ_7	50	50	50	50	50	50
h_1	10	10	10	10	10	10
h_2	10	10	10	50	50	50
h_3	10	10	10	50	50	50
h_4	10	10	10	50	50	50
h_5	10	10	10	50	50	50
h_6	10	10	10	50	50	50

Determining the Number of Layers

In determining the number of layers, there are three interesting matters to discuss. The first is associated with the **data fitting** of measured and calculated data as seen in Figure 5.9. For the two stations, the fitting between observed and calculated data on the RMT 64 and TEM 2 is obtained by using two to seven layers of starting models (Table 5.5). Shown in the zoom view both images indicate that the more number of layers used in the starting model, the better fitting is found. This indicates that the number of layers in the starting model is essential to the data fitting.

The second matter is the distribution of the **RMS error**. Figure 5.10 shows the distribution of RMS error values for RMT (station 64, 68 and 71) and TEM (station 2, 19 and 3) obtained from Marquardt inversion by using a starting model with the number of layers ranging from 2 to 7. RMS error values are constant at a certain number of layers and are stable even though the number of layers of the inverted model continues to increase. This shows that the distribution of the RMS error is cleary influenced by the number of layers used in the starting model.

Third that must be addressed is **importance values** as the second product of Marquardt inversion. It can be known from the importance value distribution, which model parameters (resistivity and thickness) can or cannot be resolved. Importance values are classified into three groups. They are well resolved if the value is more than 0.80, shaky if the value is between 0.5 – 0.80 and unresolved for values less than 0.5.

An example for the distribution of importance value in RMT 64 is shown in Table 5.5. The importance for the resistivity will not be resolved (unimportant or irrelevant) for increasing number of layers. In the starting models using two and three layers, the resistivity is resolved well with an importance value of more than 0.9 while in the model using four to seven layers, the importance values of the resistivity will decrease or not be resolved well (unimportant, irrelevant) as the number of layers increases. But, overall, from the models with three up to seven layers, there can be seen that the resistivity of the ρ_1, ρ_2 and ρ_3 is resolved very well which is indicated by importance values higher than 0.91. As a conclusion, the appropriate number of layers for the RMT model 64 is 3 layers, with a depth penetration of about 35 m (Table 5.1).

From those reviews, it can be stated that determining the number of layers is certainly not just simply depending on the quality of the data fitting or small RMS error. Further, it needs to be analyzed the importance values of model parameters (resistivity and thickness). The advantage of using starting models with different numbers of layers is possible to specify the accurate number of layers for the final model. The disadvantage of it is taking more time. The above steps are applied in all analyses to determine the number of layers for 1-D single RMT, single TEM, joint RMT and TEM inversions using Marquardt algorithm.

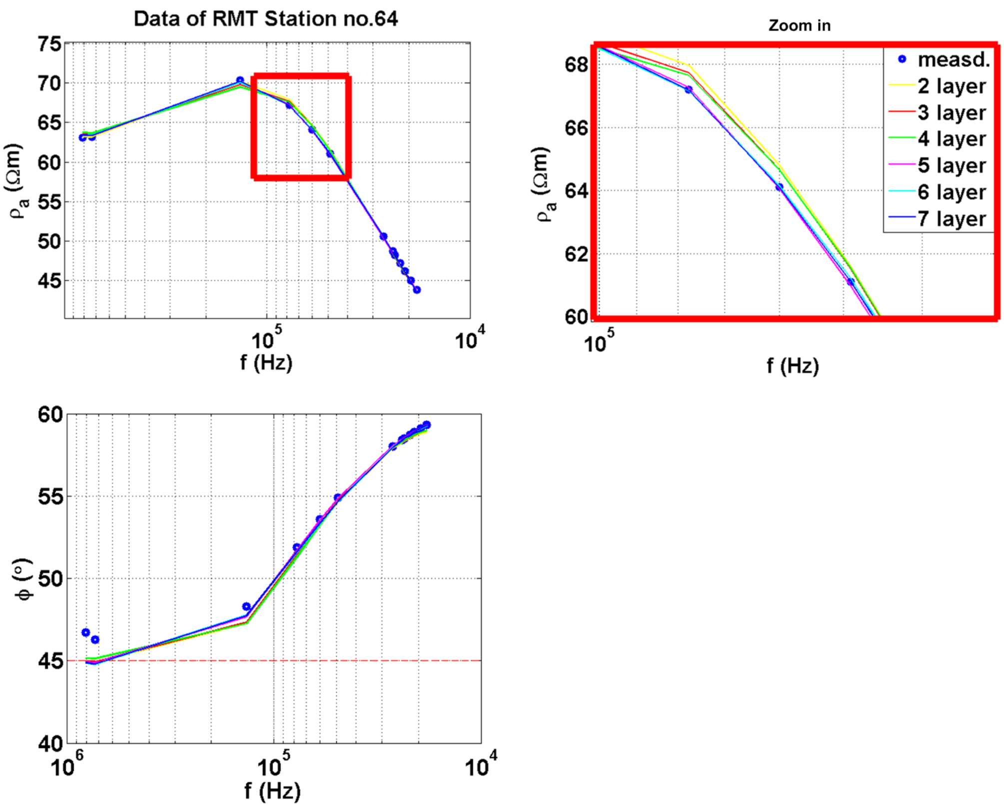

(a)

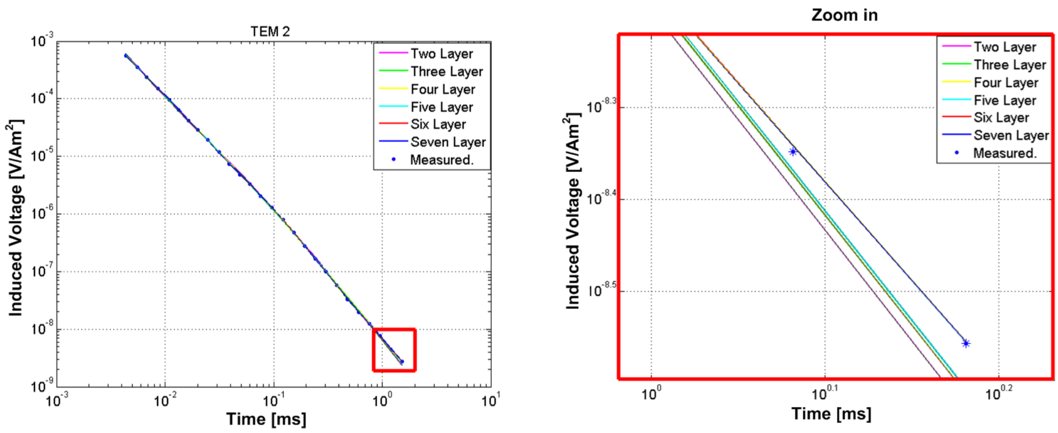

(b)

Figure 5.9: *(a) Data fitting for RMT station 64 and (b) TEM station 2 using different numbers of layers for homogenous starting model in Marquardt inversion.*

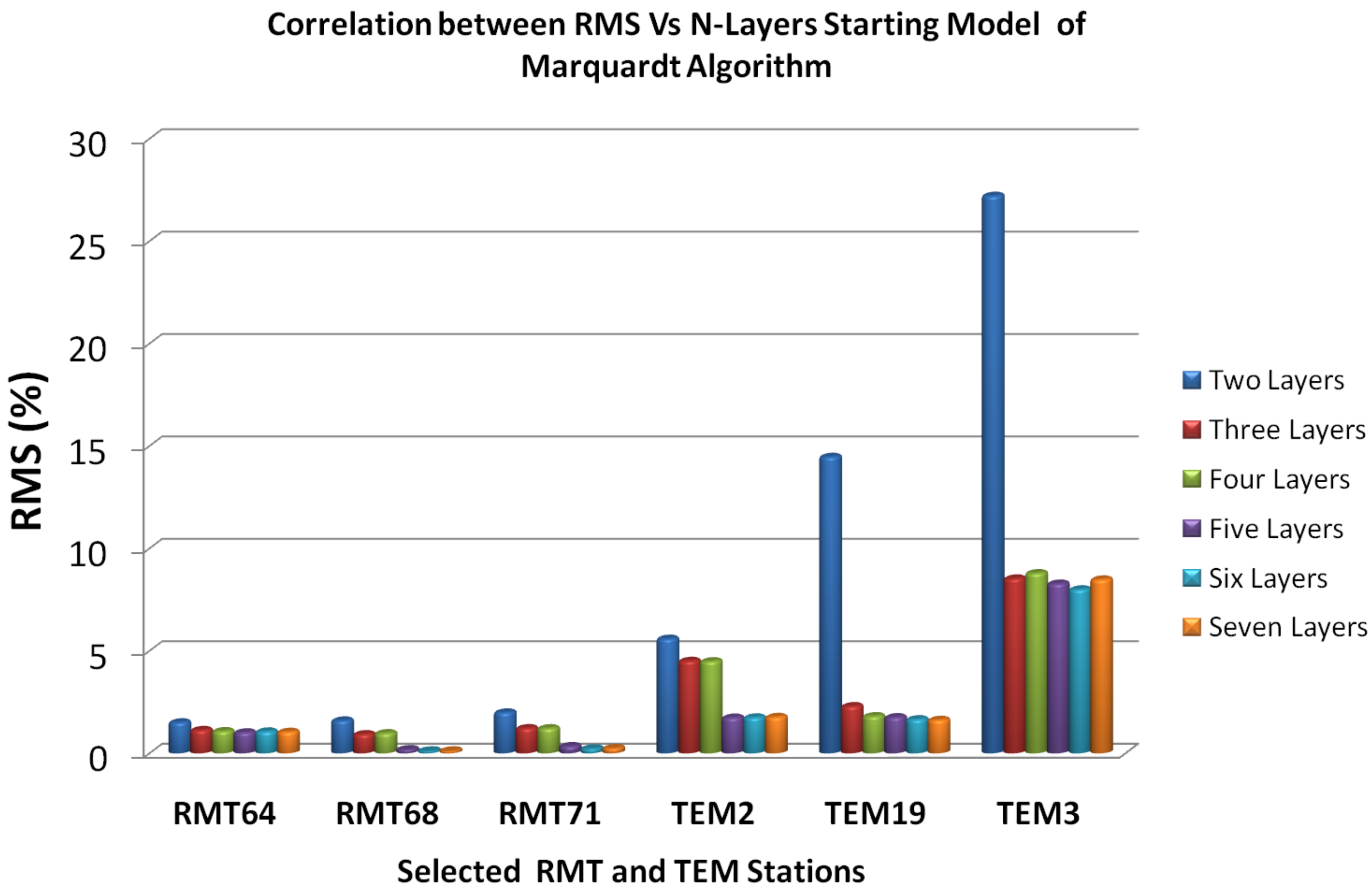

Figure 5.10: *Correlation of RMS error with homogenous starting model using different number of layers.*

Table 5.5: *Importance values for different inversion results of RMT data at station 64 with different starting models*

Start Model		Inversion results											
		2 Layers		3 Layers		4 Layers		5 Layers		6 Layers		7 Layers	
			Imp		Imp		Imp		Imp		Imp		Imp
ρ_1	70	63.4	1	63.6	1	63.8	1	63.6	1	63.63	1	63.63	1
ρ_2	50	12.9	0.99	14.05	0.96	13.44	0.98	13.42	0.98	13.43	0.99	13.43	0.98
ρ_3	50			10.34	0.96	10.04	0.92	10.23	0.92	10.2	0.92	10.19	0.92
ρ_4	50					41.97	0.08	36.74	0.09	36.7	0.08	36.68	0.08
ρ_5	50							58.18	0.03	51.85	0.02	51.82	0.02
ρ_6	50									56.05	0.02	53.77	0.01
ρ_7	50											52.03	0.0
h_1	10	13.38	1	12.89	0.99	13.04	0.99	13.05	0.99	13.05	0.99	13.05	0.99
h_2	10			7.4	0.35	10.55	0.77	10.45	0.71	10.43	0.71	10.44	0.71
h_3	10					12.43	0.44	12.27	0.44	12.24	0.44	12.26	0.44
h_4	10							9.9	0.02	9.94	0.01	9.96	0.01
h_5	10									9.97	0.00	9.99	0.00
h_6	10											10	0.00
RMS[%]			1.51		1.13		1.08		1.02		1.06		1.04

Results of Marquardt Inversion

The results of Marquardt inversion for RMT and TEM data are displayed in Figure 5.12 and Figure 5.13 for the same RMT and TEM stations. Model RMT 50 located on the lower terrace deposit has a resistive layer (more than 100 Ωm) from the surface down to 10 m. Meanwhile, the second layer in the model indicates a conductive layer of the resistivity value about 15 Ωm. The third layer is the final layer with a resistivity value equal to the first layer.

The Marquardt model of station RMT 64 data located on fans shows more conductive first layer with a resistivity value of about 80 Ωm and a thickness of about 15 m. The second and third layers are represented by the resistivity values around 18 Ωm and 50 Ωm, respectively. For RMT 73 located on holocene deposits, the first layer is represented by the lowest resistivity (50 Ωm) of three stations. From RMT 73 model, it has a good agreement with geological information. It is dominated by conductive sediment (see section 4.3.2).

For the 1-D Marquardt model from TEM data, the number of layers varies from four to six at depths down 200 m (Figure 5.13). This indicates that the deeper structure has a variying number of layers. The different distribution of the number of layers is possibly influenced by geological processes in the past associated with the 1978 earthquake [*Koufosa et al.*, 2005]. These processes allow unconformable deposition.

The correlation of measured and calculated data for RMT and TEM has good fitting and RMS values are varying from 0.5 – 2%. Figure 5.11 shows that the resulting Occam and Marquardt models are consistent with one another.

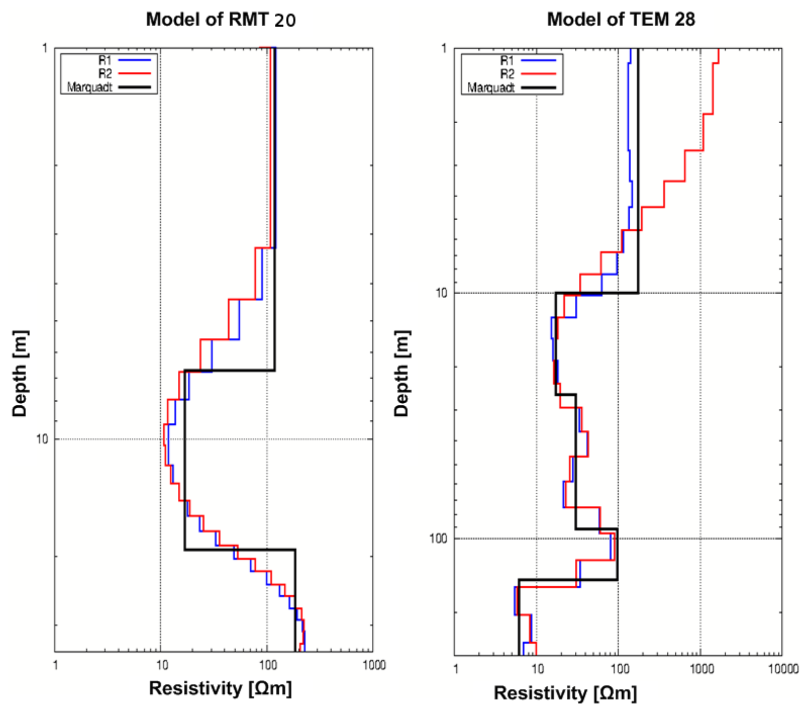

Figure 5.11: *1-D Marquardt and Occam's (first (R1) and second (R2) order of smoothness constraints) inversion models for RMT station 20 and TEM station 28.*

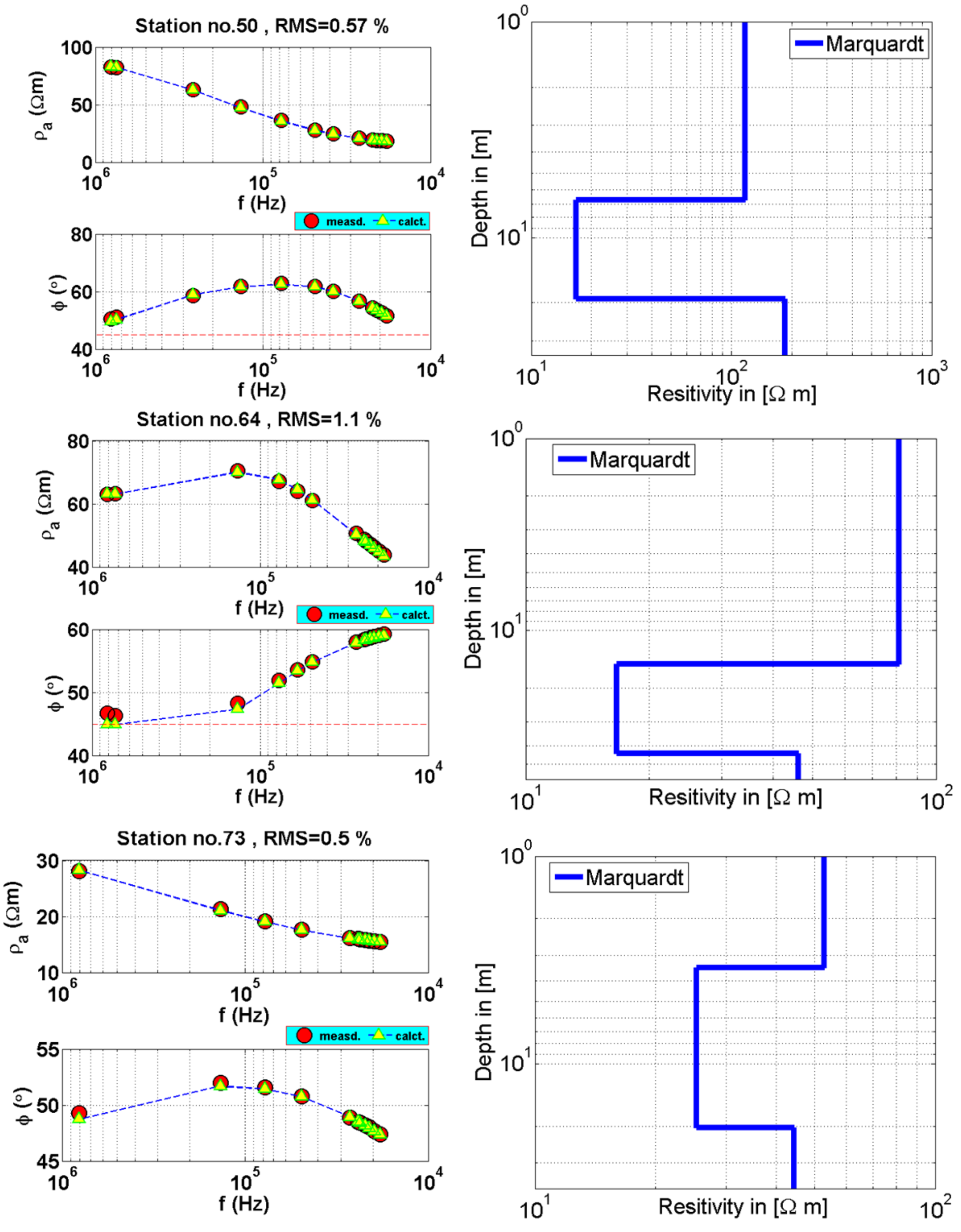

Figure 5.12: *1-D Marquardt inversion models for RMT station 50 located on lower terrace deposit, RMT station 64 on fans and RMT station 73 on holocene deposit.*

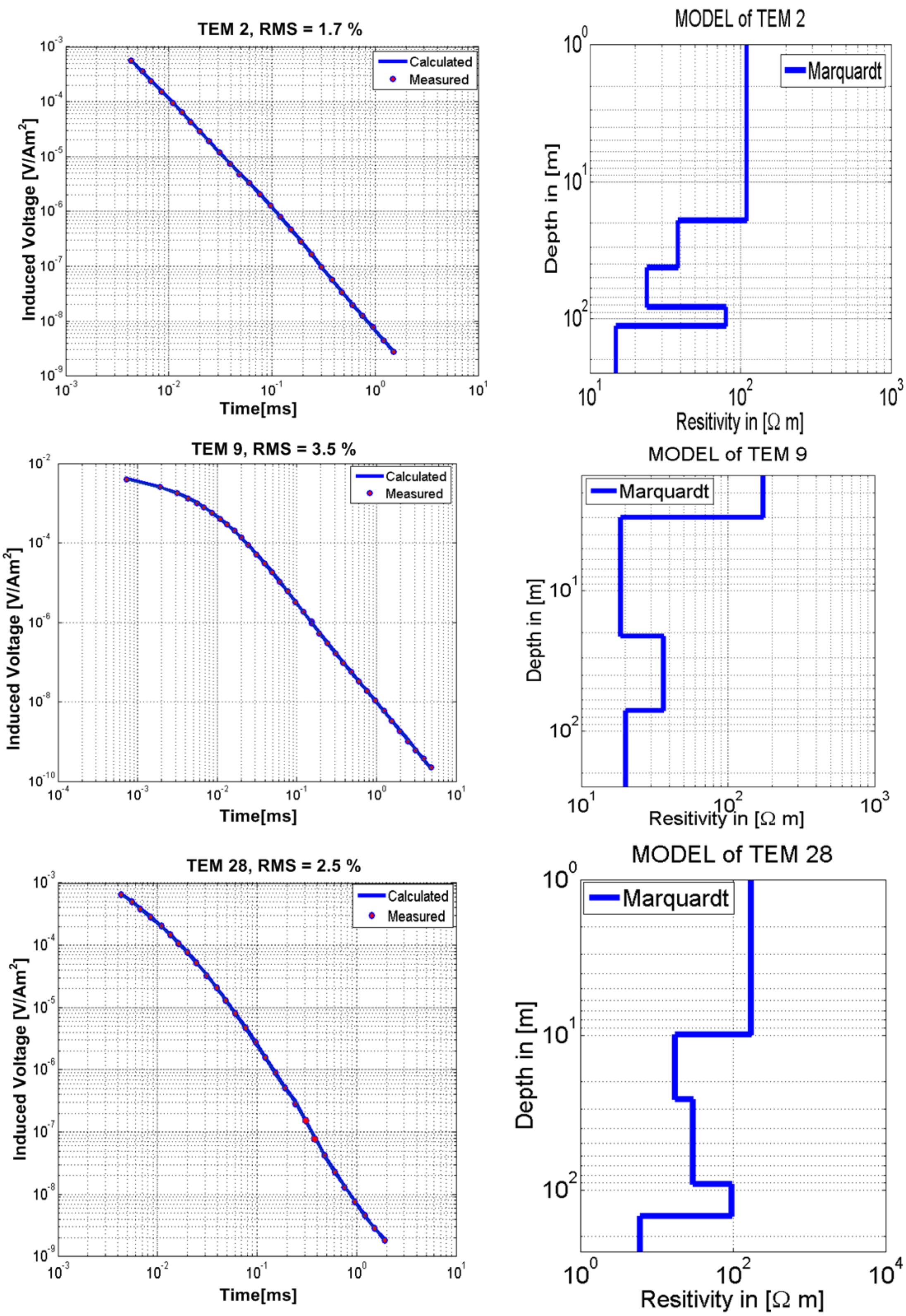

Figure 5.13: *1-D Marquardt inversion models for TEM station 2 located on reference site (lower terrace deposit), TEM station 28 on fans and TEM station 9 on holocene deposit.*

5.2.4 Comparison between 1-D Models and Borehole Data

In order to calibrate the geophysical models obtained after 1-D inversion, comparison between geophysical models and borehole data from reference sites (borehole S-1 and S-10) is performed. From borehole S-1, the data sets of RMT 1 and TEM 1 are available. RMT 2 and TEM 2 are from borehole S-10 as shown in chapter 4 (Figure 4.7).

These RMT and TEM data sets are interpreted by Marquardt inversion. Figure 5.14 shows the fitting between the measured and calculated data for RMT 1 and TEM 1 near the borehole S-1. The RMT model has three layers with a depth down to 35 m, whereas the TEM model shows five layers going down to 200 m.

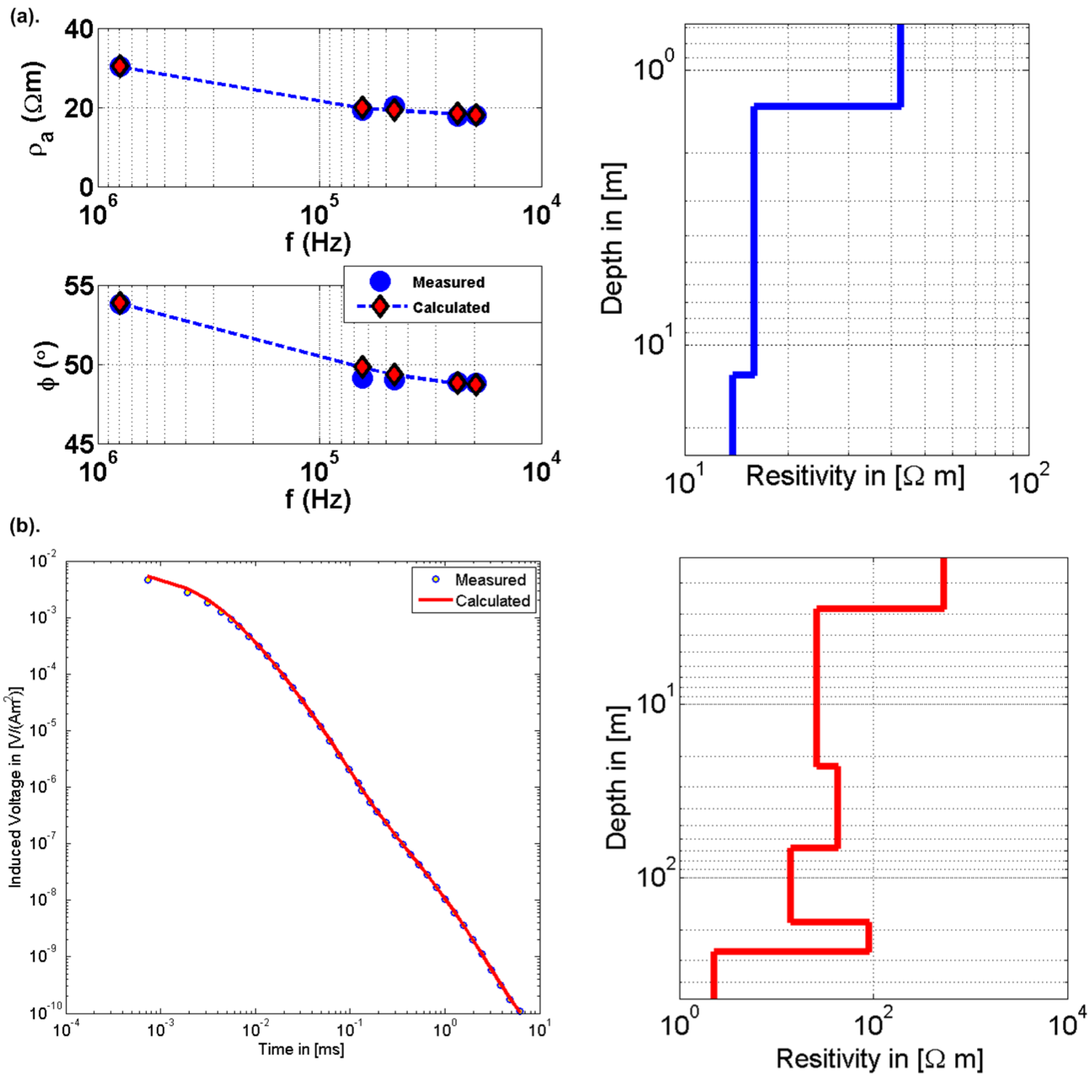

Figure 5.14: *(a) Fitting between measured and calculated RMT data, and 1-D Marquardt model of RMT 1. (b) Fitting between measured and calculated TEM data, and 1-D Marquardt model of TEM 1 at the reference site close to borehole S-1.*

The importance distribution of RMT and TEM model parameters from the boreholes S-1 and S-10 can be seen in Table 5.6. At borehole S-1, the resistivity (ρ) and thickness (h) of the RMT 1 data set is well-resolved with importance values of about 0.9. However, the TEM 1 data, ρ_1, ρ_5 and ρ_6 remain unresolved with importance values less than 0.5. The thickness of the first until the fifth layer ($h_1 - h_5$) is well-resolved with importance values of about 0.9.

The model parameters of RMT 2 are resolved well except the thickness of the second layer h_2 cannot be resolved with importance values smaller than 0.8 at the borehole S-10. In the TEM data, the resisitivity for the fourth layers (ρ_4) is not resolved with importance of 0.55. However, the other model parameters (ρ_1 - ρ_3, ρ_5 and h_1 - h_4) of TEM 2 are well-resolved (importance values more than 0.85). This indicates that the geophysical data (RMT and TEM) located in the borehole S-1 and S-10 have parameter models which are relatively resolved at all levels.

Table 5.6: *Importance values of RMT and TEM at boreholes S-1 and S-10*

	Inversion results							
	Borehole S-1				Borehole S-10			
	RMT 1		TEM 1		RMT 2		TEM 2	
		Imp		Imp		Imp		Imp
ρ_1	42.1	0.99	537.72	0.09	134.67	0.99	109	0.99
ρ_2	15.9	0.99	26.23	0.99	55.03	0.90	36.86	0.99
ρ_3	13.83	0.99	42.97	0.99	127.24	0.99	21.13	0.86
ρ_4			14.06	0.99			42.77	0.55
ρ_5			89.9	0.15			14.52	0.99
ρ_6			2.29	0.41				
h_1	1.35	0.99	2.8	0.99	7.1	0.92	19.77	0.99
h_2	11.48	0.91	19.9	0.99	6.5	0.56	46.58	0.96
h_3			45.31	0.99			69.99	0.91
h_4			114.18	0.97			120.40	0.99
h_5			87.6	0.93				
RMS[%]	2.7%		2%		5.6%		1.7%	

The correlation of borehole S-1 and the 1-D model of the Marquardt inversion for RMT 1 and TEM 1 can be seen in Figure 5.15. The TEM model has a good fitting with the borehole data for silty sand and it shows resistivity of 30 – 50 Ωm at depth of about 5 to 20 m. The RMT is more sensitive to the first layer, the silty clay sand. The TEM model at borehole S-1 cannot distinguish sandy clay and clay silt with marly clay. This layer is represented by sandy clay with a resistivity ranging from 50 – 80 Ωm located at a depth about 25 - 70 m. The TEM model identifies the low resistivities of silty clay and silty clay with gravel which are located at depths of about 80 m to 180 m. The model of TEM 1 cannot resolve silty clay sand. It

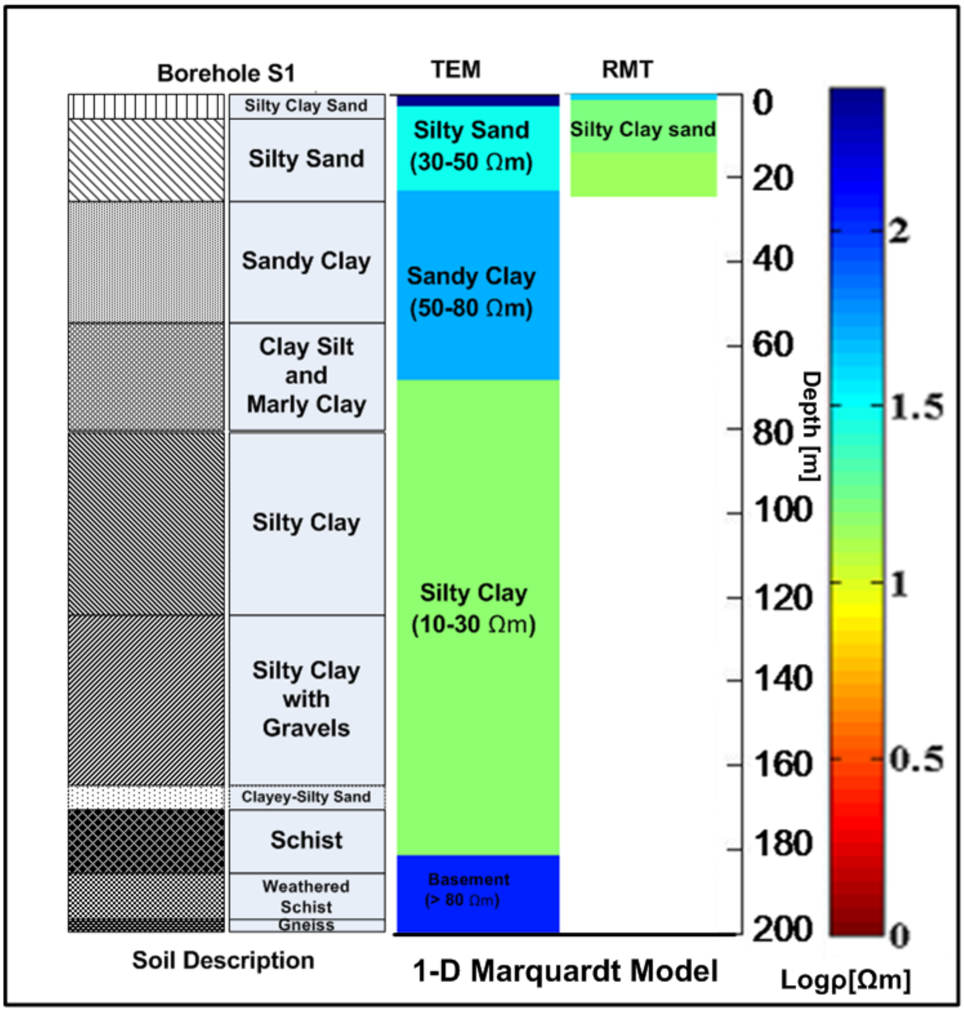

Figure 5.15: *Correlation of RMT and TEM data with borehole S-1.*

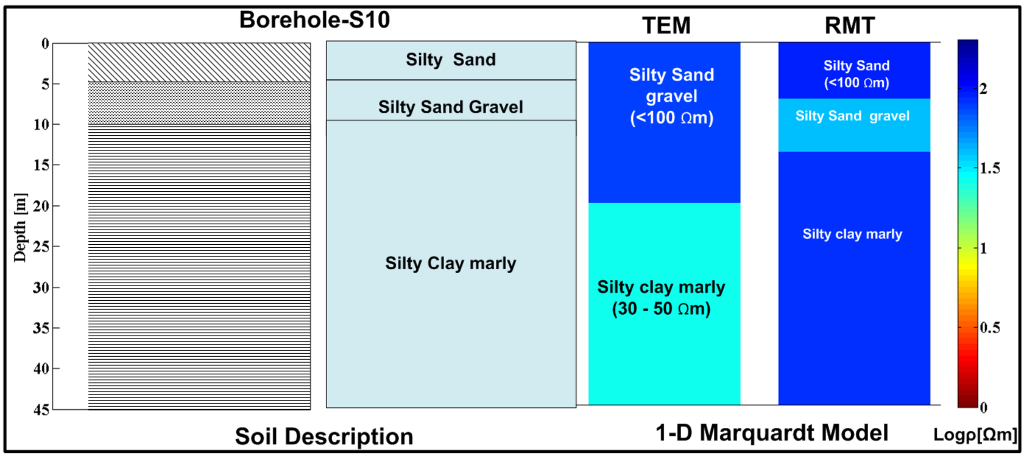

Figure 5.16: *Correlation of RMT and TEM data with borehole S-10.*

is possible to investigate the less resistive layer located above the conductive region due to TEM is being less sensitive [*Pellerin and Wannamaker*, 2005]. The basement layer consists of gneiss and schist at a depth about 180 m. This layer has a resistivity value higher than 80 Ωm.

The correlation of borehole S-10 with TEM 2 and RMT 2 is shown in Figure 5.16. The data set RMT 2 has a good fitting with silty sand and silty sand gravel at a depth of about 10 m in borehole data with a resistivity of more than 100 Ωm. A good fitting with model TEM 2 is also found, but only on depth below 20 m because TEM cannot resolve the surface layer. Generally, the correlation of borehole data and TEM model can be classified into five different layers with variying thicknesses (Table 5.7).

Table 5.7: *Resistivity value distribution from correlation between boreholes and geophysical data.*

Borehole S-1		Borehole S-10	
Type	Resistivity[Ω m]	Type	Resistivity[Ω m]
Silty clay	10 - 30	Silty sand gravel	> 100
Silty sand	30 - 50	Silty clay marly	30 - 50
Sandy clay	50 - 80		
Basement	> 80		

5.2.5 1-D Model of RMT Data on Profile 2

One dimensional conductivity model of RMT data has been obtained using Marquardt inversion. As an example, 1-D conductivity model from RMT data of profile 2 will be discussed in detail.

Figure 5.17 shows the RMT model of profile 2 up to depth of 40 m. Between 0 to 10 meters depth, it is dominated by marly silty sand with resistivity more than 100 Ωm located at station 49 - 71. Stations 72 - 75 are located on the holocene deposit. This layer is represented by silty clay with the resistivity 10 - 30 Ωm. Stations 49 - 57 and station 59 - 71 represent silty marly clay with resistivity between 30 - 50 Ωm at depth of 10 – 20 m. Station 58 indicates a fault structure along profile 2 because it has resisitivity (100 Ωm) contrasting to the adjacent stations.

Analysis of the Fault Structure

To analyze the existence of fault structure, two approaches are considered: one is associated to the resolution of model parameters i.e. importance value and the second is geology of the area.

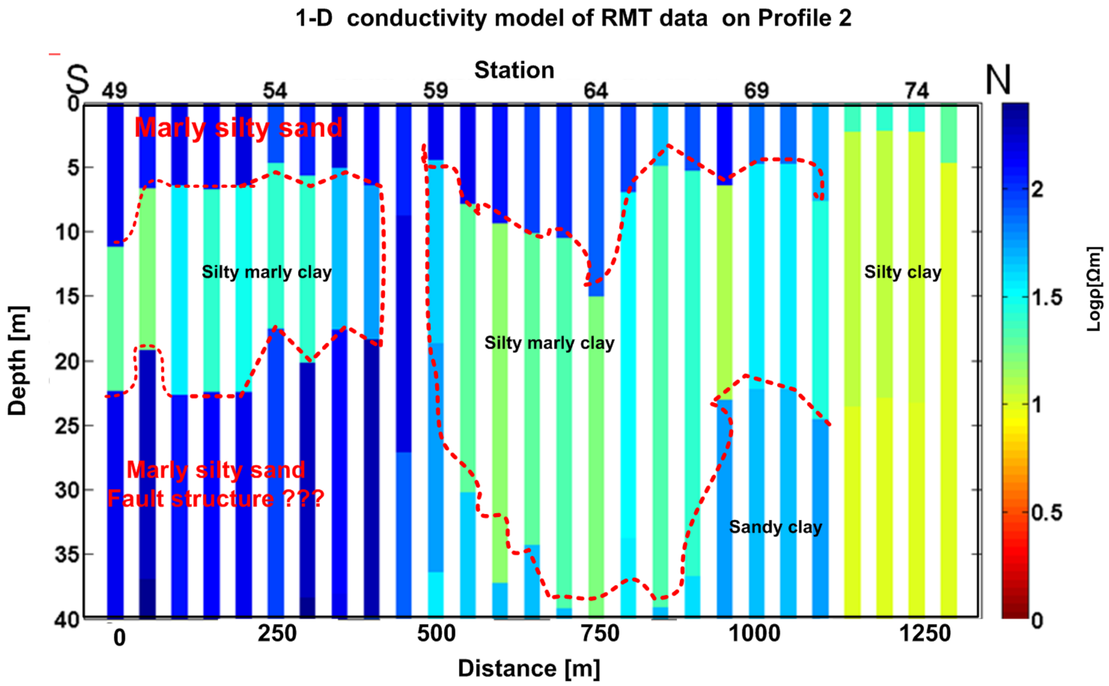

Figure 5.17: *1-D Marquardt model of RMT data on profile 2.*

1. **The importance parameter**

   Because RMT station 58 has a contrasting resistivity, the importance values for the three neighboring stations: station 57, 58 and 59 (Table 5.8) are examined. The resistivity of the first and second layers for all three stations are well-resolved (more than 0.85). Moreover, the thickness of first layer at station 58 is also well resolved. This confirms that the feature of fault structure at RMT station 58 is not an artifact.

Table 5.8: *Analysis of fault structure based on importance parameter*

	Station 57		Station 58		Station 59	
		Imp		Imp		Imp
ρ_1	77.29	0.85	99.05	0.99	142.08	0.85
ρ_2	35.21	0.85	155.1	0.86	44.04	0.9
ρ_3	133	0.47	69.08	0.99	53.73	0.85
h_1	5.7	0.65	11.43	0.85	4.49	0.81
h_2	9.28	0.65	13.2	0.71	14.18	0.50
RMS[%]	1.1		0.9		1.7	

2. **Geological view**

   Geologically, a fault structure is clearly visible in the RMT model of profile 2 (Figure 5.17) as follows: At 0 m - 400 m (Station 49 - 57), the second layer reaching down to around 25 m at most, is associated with silty marly clay. After a gap filled with marly silty sand which is also the material of the top layer and the third layer below, the silty marly clay continues as the second layer from 550 m - 1150 m (Stations 59 - 71). At station 58, located on this gap, no horizontal discontinuities are observed and the same material is found from top to bottom, namely marly silty sand. This may indicate a block having lowered down from the first layer, affected by the elasticity process du to an earthquake [*Psilovikos*, 1984].

From both analyses, it can be declared that the conductivity model of profile 2 indicates fault structure in the research area. However 1-D model of RMT is not suitable to resolve the specified type of fault structure. The 1-D marquardt model for profiles 1 and 3 can be found in appendix A.

5.2.6 1-D Model of TEM Data on Profiles 2 and 3

The 1-D model of TEM data has been realized using Marquardt and Occam inversions. 1-D conductivity models from TEM data of profile 2 and profile 3 will be discussed in detail. The Marquardt model of profile 1 and Occam models of profiles 1 - 3 can be found in appendix B.

Figure 5.18 shows the TEM model along profile 2 and it is consist of 27 stations (49 - 75). This model indicates five different structures such as silty clay, silty sand, sandy clay, marly silty sand and bedrock with varying thicknesses. The irregular distribution of layers in this model indicates that they have a complex structure and have been affected by seismic activity.

The model shows the bottom of boundary layers of fault structure at stations 56 - 59 and a depth down to 80 m. The resistive layers ranging over 150 Ωm is located at stations 49 – 54 and a depth of over 180 m. This layer is assumed to be associated with gneiss and schist or bedrock. This is appropriate with data from the borehole S-1 which indicates the top of basement layer is at a depth of over 180 m. However the top layers of TEM stations 49 - 69 cannot be resolved well because the top layer has a high resisitivity value (> 80 Ωm) addressed as metamorphic rock.

The one dimensional model at profile 3 consists of 32 stations (76 - 107) with 50 m of distance among them (Figure 5.19). This profile crosses two geological formations namely lower terrace deposit and holocene deposit. Vertically, the model of this profile can be classified into four layers. At profile meters 0 - 1200 m, the first layer is marly silty sand with resistivity values of more than 100 Ωm. It is located at a variety of depths ranging from 20 - 50 m. At profile meters 1400 -1600 m there is conductive layer (30 - 50 Ω m). This layer is associated with sandy clay and located in holocene deposit.

The second layer located beneath the first layer is indentified by silty sand. This layer has thicknesses variying between 40 - 170 m. The structure of this layer is

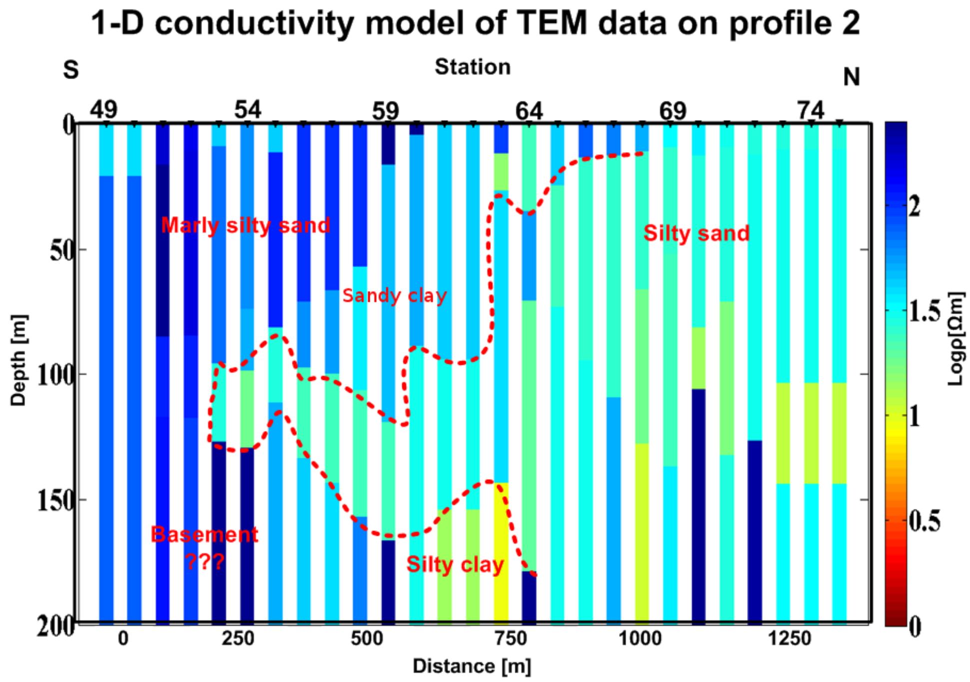

Figure 5.18: *1-D Marquardt model of TEM data on profile 2. The red dashed lines are indicating of layers boundaries.*

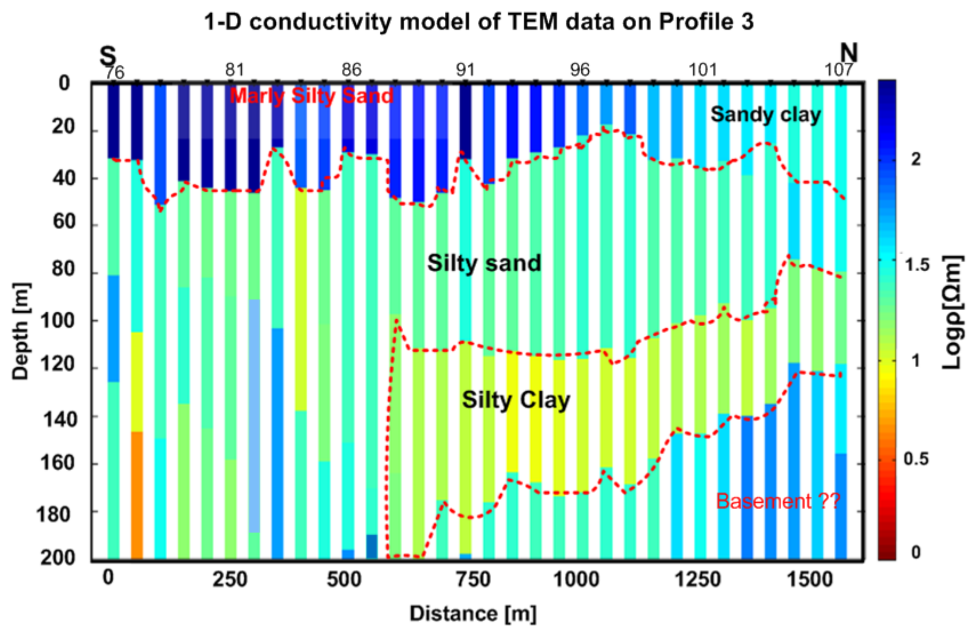

Figure 5.19: *1-D Marquardt model of TEM data on profile 3. The red dashed lines are indicating of layers boundaries.*

distributed horizontally from profile meters 0 - 1600 m. A third layer which has resistivity value < 10 Ωm, exists between profile meter of 600 - 1600 m. The layer is very conductive and it is interpreted as silty clay with various thicknesses (40 - 100 m) and located at a depth of around 100 to 160 m. The last layer located beneath is accumulated at profile meters 800 - 1600 m and has resistive value more than 80 Ωm, located at a depth more than 150 m. This layer can be interpreted as schist and gneiss. The bedrock is resolved in the models with importance values more than 0.8 (Figure 5.21).

5.2.7 Importances and Fitting of RMT and TEM Data

The distributions of importance values of RMT on profile 2 and TEM data on profile 3 is shown in Figure 5.20 and Figure 5.21. It is known that RMT model can well resolve the first and the second layer . However, TEM data is generally less sensitive to resolve the surface layer but well able to resolve the deeper layer. This shows RMT is more sensitive for shallow structures while TEM is effective for the deeper structure.

The RMS distribution of the 1-D models from RMT and TEM data at profile 2 can be seen in Figure 5.22. It shows that measured and calculated data of RMT and TEM fit well along profile 2 with RMS values are ranging from 0.5 – 5%.

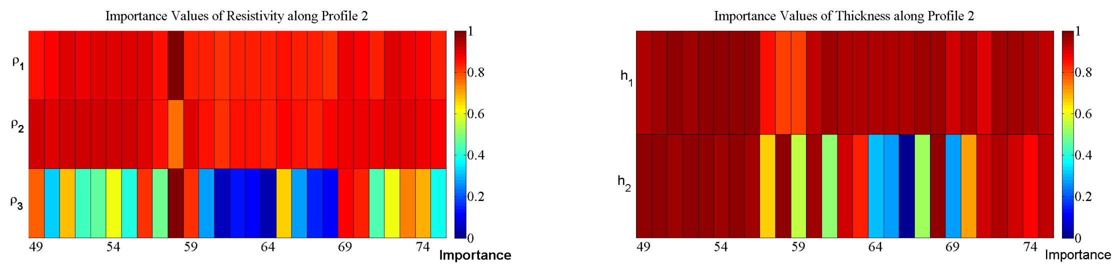

Figure 5.20: *Importance value distribution of RMT model along profile 2.*

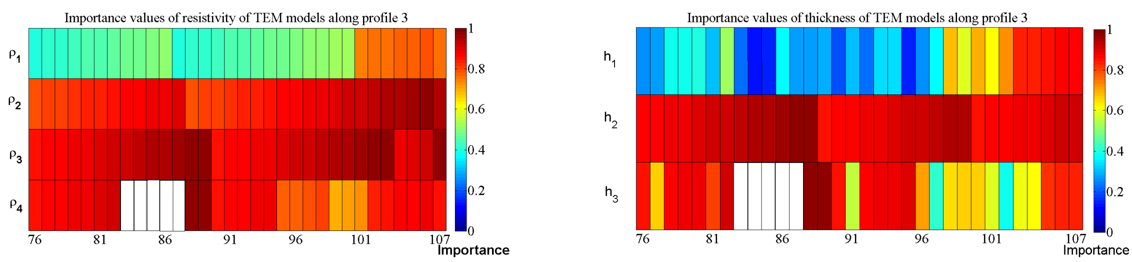

Figure 5.21: *Importance value distribution of TEM model along profile 3. The white cells show without model parameters.*

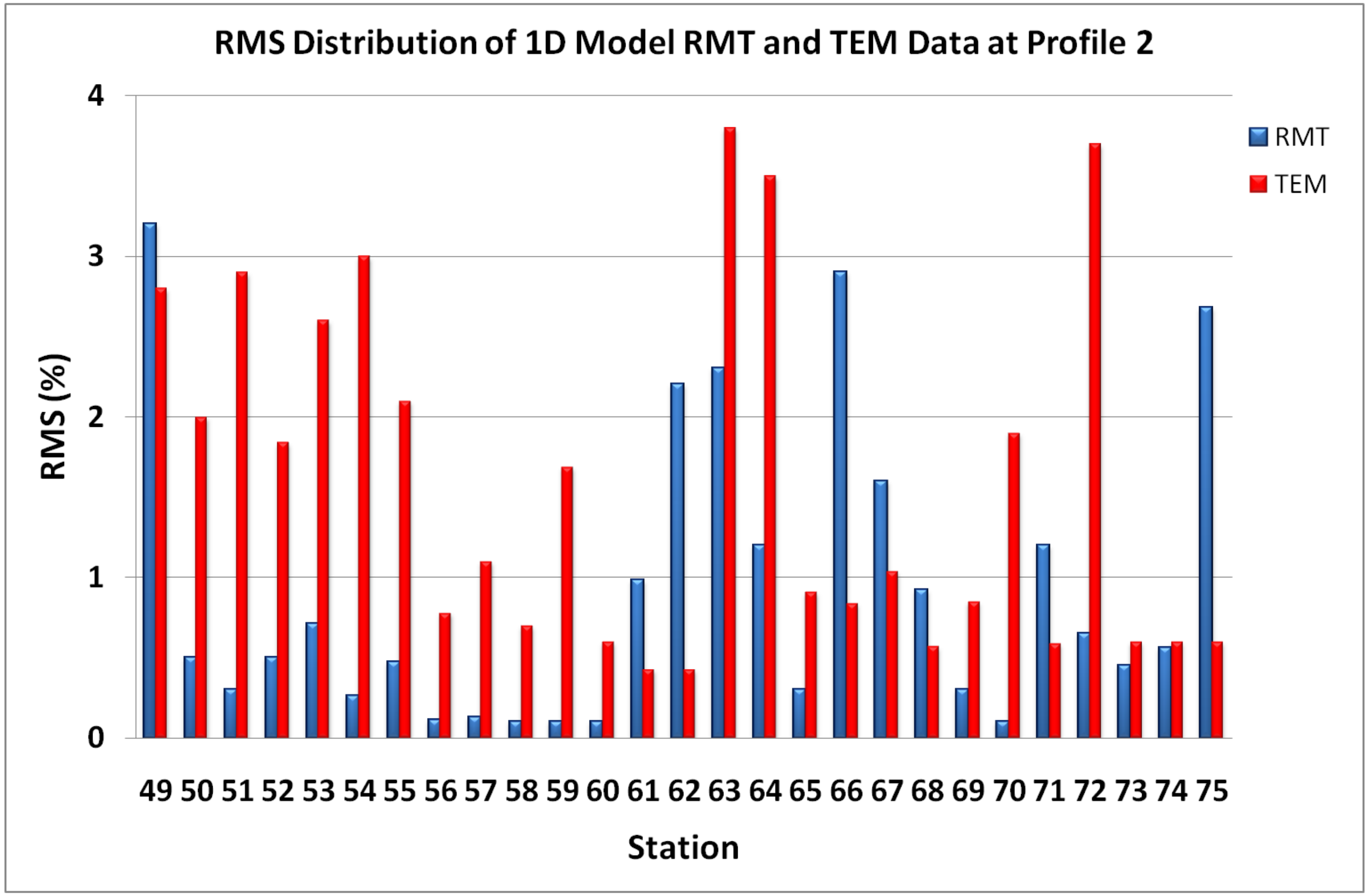

Figure 5.22: *RMS distribution of 1-D models of RMT and TEM data along profile 2.*

5.3 2-D Inversion of RMT Data

In this section, the 2-D models for profile 2 and profile 5 from RMT data will be explained. Profile 2 is located on a complex geological structure, which is crossing three different geological formations as described in chapter 4 (Figure 4.12). Parallel to profile 2, profile 5 is set up in NW and SE direction. Radio transmitters are solely available in the North and South to the research area, thus allowing only realizing TM mode RMT data with respect to the geological strike. In detail, the electric field was captured perpendicular to the strike of the Mygdonian Basin. All the interpreted sections correspond to TM-mode as in TE-mode, there were not enough signals available. For the 2-D inversion, the optimum choice of regularization parameter (λ) is necessary; therefore the models are calculated for different regularization parameters (see chapter 3 in section 3.2).

5.3.1 2-D Conductivity Models at Profiles 2 and 5

Figure 5.23 shows the 2-D inversion result for TM mode of profile 2 with a regularization parameter τ =15 and a starting model = 50 Ωm. It indicates metamorphic rock (marly silty sand) at a depth to 8 m underneath profile meters 0 - 1000 m. These layers has quite a high resistivity of more than 100 Ωm. Beneath these layers, profile meters 0 – 350 m and 600 – 1200 m are represented by conductive layers with resistivities of less than 50 Ωm interpreted as silty marly clay.

The fault structure is found underneath profile meters 400 - 600 m in the 2-D model of profile 2 in the Volvi Basin. It can be clearly seen at 10 to 25 m depth represented by silty marly clay of 30 - 50 Ωm. As explained in the chapter 5 about 1-D interpretation indicating a fault structure at profile 2, the 2-D model at the same profile of 2-D model shows that the lower layer (distance 0 - 500 m at a depth of about 20 – 40 m) has a resisitivity also associated with the surface structure, marly silty sand.

The existence of a fault structure in the research area has already been seen in 1-D RMT models (Figure 5.18) and now 2-D interpreted model is confirming it. However for further analyses, it is checked with data from profile 5 which is crossing the profile 2.

Figure 5.24 shows the 2-D model of profile 5 which also shows a normal fault structure. It can be clearly seen at profile meters 300 - 500 m containing marly silty sand. Meanwhile, at more than 10 m depth, the second layer begins with a resisitivity value of 10 - 30 Ωm, this layer is more conductive than the top layer and has been interpreted as silty marly clay. This layer continues along the whole profile line except from 300 - 500 m. This is the zone where also shows the profile 5 crosses profile 2, and the fault structure was observed. Both layers are the same resistivity as the layer identified as the fault structure at profile 2. Thus, it can be concluded that the 2-D models of profile 2 and profile 5 are mutually supportive and fit to each other (Figure 5.23 and Figure 5.24).

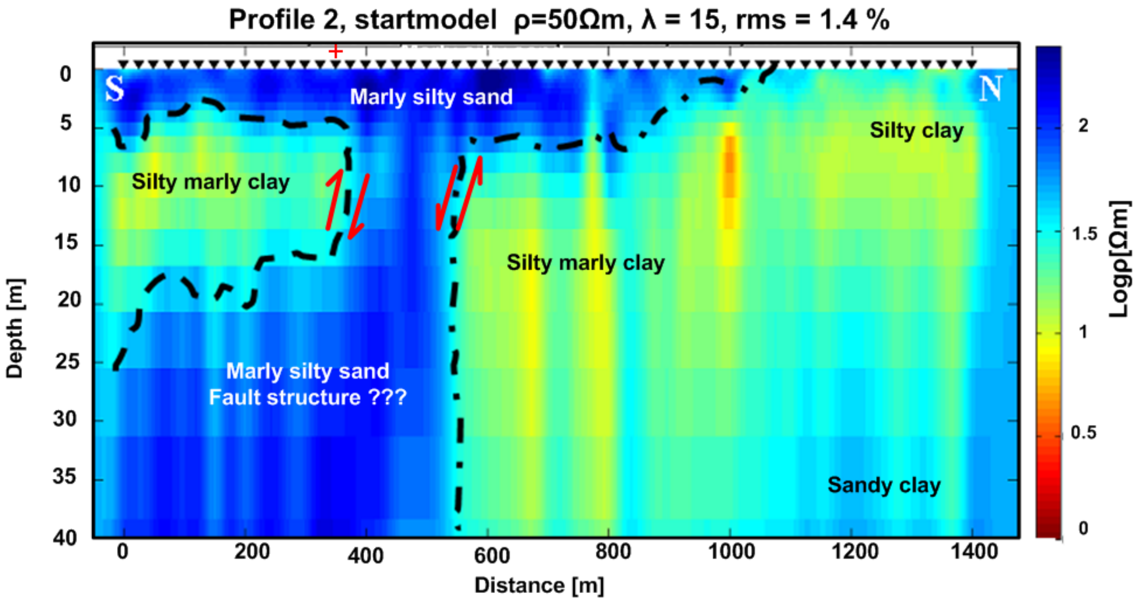

Figure 5.23: *2-D conductivity model of profile 2 in the direction from S to N. The boundaries of layers are outlined by black dashed dot lines, the red plus (+) is the location of station 15 and the red arrows indicate normal fault structure, the hanging wall drops relative to the footwall.*

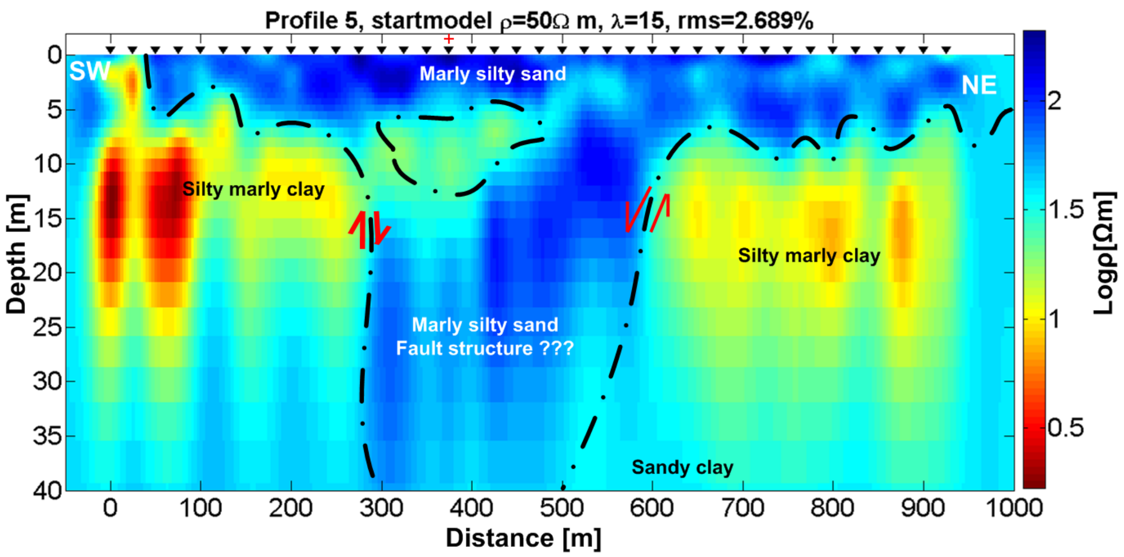

Figure 5.24: *2-D conductivity model of profile 5 in the direction from SW to NE. The boundaries of layers are outlined by black dashed dot lines, the red plus (+) is the location of station 16 and the red arrows indicate normal fault structure, the hanging wall drops relative to the footwall.*

From the interpretation results of profile 2 and profile 5, a fault structure is cleary visible. It is identified as the normal fault or *graben* structure or *graben* structure with the hanging wall having moved downward relative to the footwall, which was also found in Volvi Basin between Volvi and Langada lakes by *Papazachos et al.* [1979], *Arsovski* [1978], *Psilovikos* [1984], *Jongmans et al.* [1988], *Raptakis et al.* [2002].

5.3.2 Data Fitting of 2-D RMT at Profiles 2 and 5

Data quality and consistency of resistivity and phase of profile 2 and profile 5 are shown in Figure 5.25 and Figure 5.26. The data from the soundings curve of station 15 at profile 2 (Figure 5.25a) and station 16 at profile 5 show that the phase exceeds 45° thus indicating a good conductor in the deeper structure. Meanwhile, the resistive part of metamorphic rock is shown with a phase less than 45° (Figure 5.25b).

The fitting between measured and calculated data for both stations is good with RMS error values about 0.5 % for station 15 of profile 2 and 1.3% for station 16 of profile 5. The overall 2-D data of profile 2 and profile 5, respectively, have RMS error values of 1.4 % and 2.7 %.

Figure 5.26 shows a correlation of measured and calculated data for a frequency of 20 kHz on profile 2 and for a frequency of 78 kHz on profile 5. Profile meter 400 m indicates a phase less than 45° and it corresponds to the very resistive value associated with the fault structure (Figure 5.26a). In Figure 5.26b, phase less than 45° is shown at 550 m of profile 5. It corresponds to the fault structure with resistivity values of about 100 Ωm. Generally, measured and calculated data have a good fitting considering the complex and inhomogeneous geological structure, however, some misfit occurs due to 3-D effects in the research area.

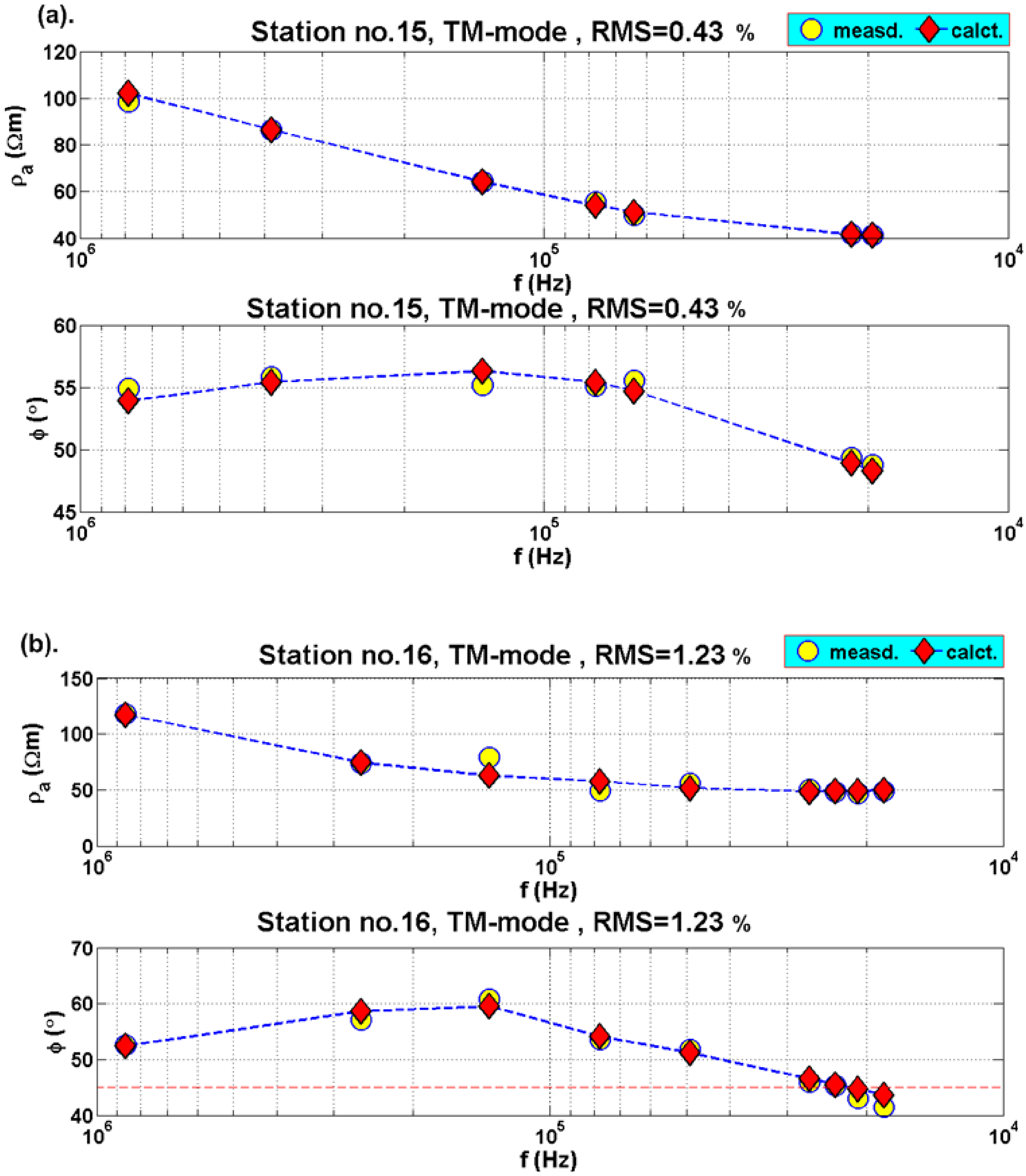

Figure 5.25: *Fitting of measured (yellow circles) and calculated (red diamonds) data from 2-D RMT inversion (a) at station 15 of profile 2 and (b) station 16 of profile 5 .*

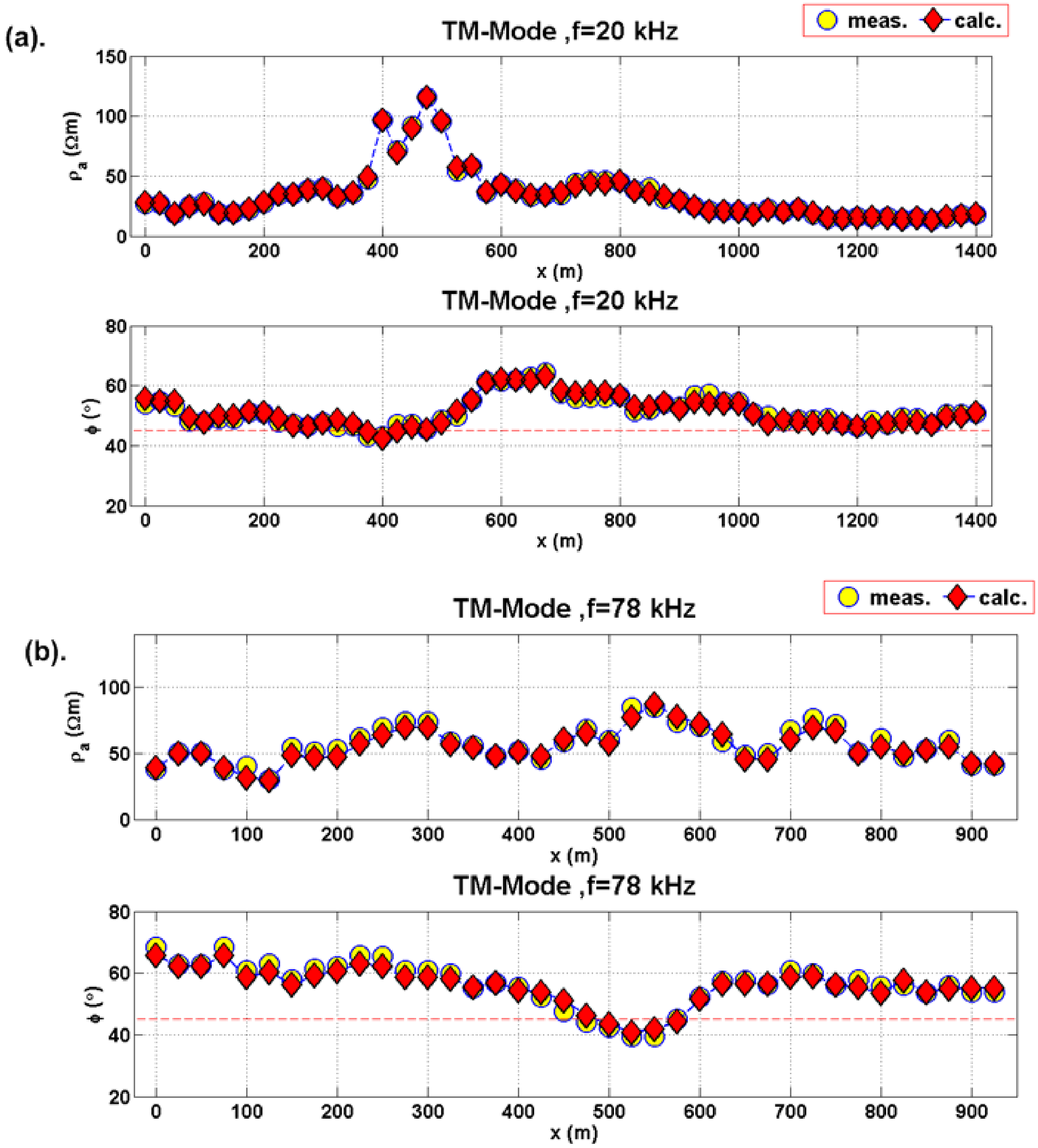

Figure 5.26: *Fitting of measured (yellow circles) and calculated (red diamonds) data from 2-D RMT inversion for selected frequencies (a) at frequency 20 kHz on profile 2 (b) at frequency 78 kHz on profile 5.*

5.4 Discussion of the Results

The indication of the fault structure can be seen clearly in the 1-D RMT model at a depth down to 35 m (Figure 5.17), however in the 1-D TEM model only the bottom boundary of it shown due to the resistive surface structure (Figure 5.18). But 1-D TEM model gives information of the subsurface structure down to 200 m depth and also resolves the top of basement in the research area (Figures 5.18 and 5.19).

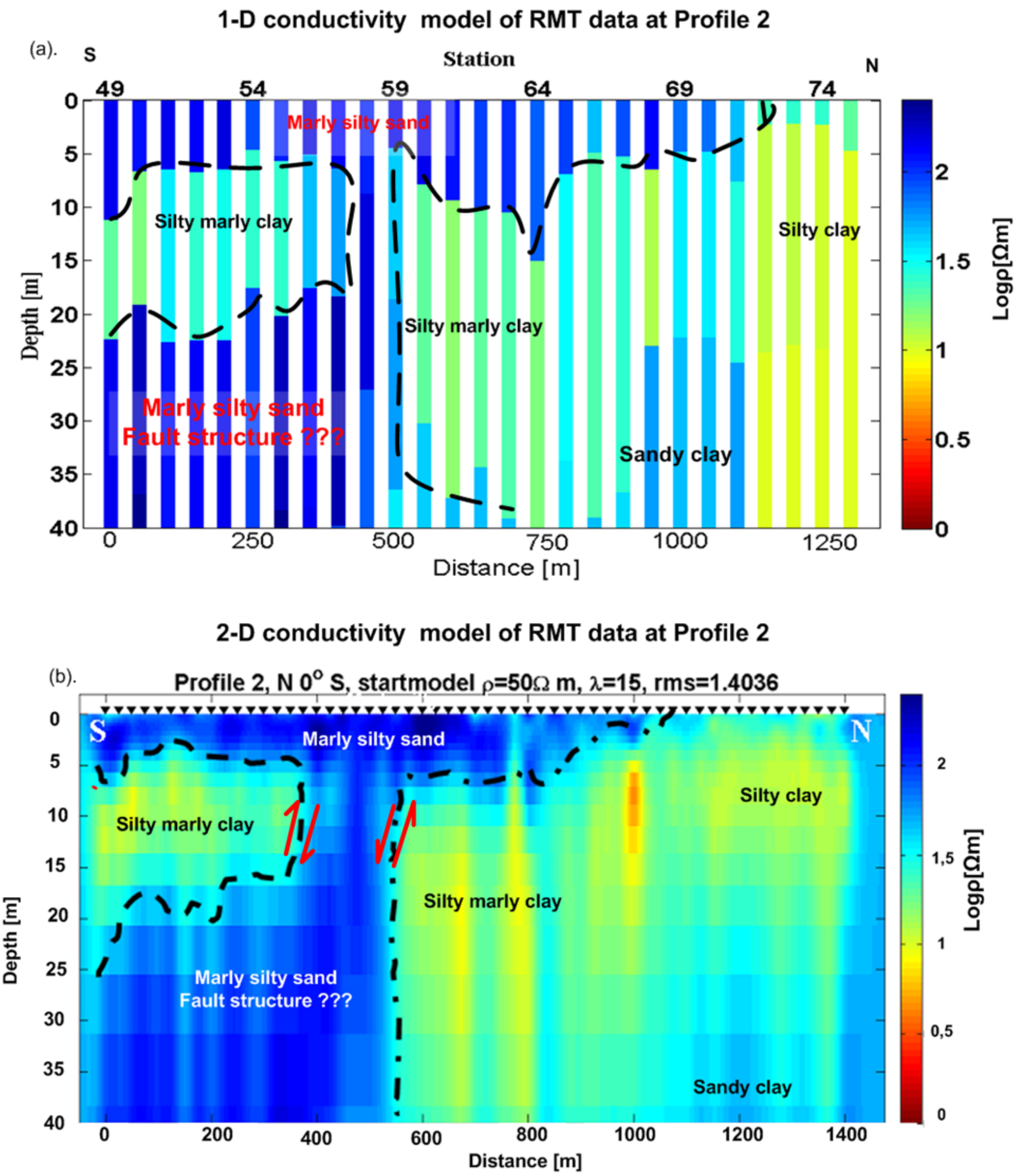

Figure 5.27: *Correlation of (a) 1-D and (b) 2-D conductivity models of RMT data at profile 2.*

A comparison of 1-D and 2-D models of RMT data from profile 2 is displayed in Figure 5.27. Both the conductive and the resistive structures in the model are resolved clearly by 1-D and 2-D inversions with almost similar resisitivity values. Moreover, the two models show an indication of a fault structure but in the 2-D model image, the fault structure is visible more clearly. Its type is recognized as a *graben* structure.

In order to provide detailed information about the distribution of the fault structure, the calculated 2-D models of all profile are displayed on the geological map (Figure 5.29). Profile 1 indicates two structures with contrasting conductivity; the conductive structure is associated with holocene deposit while the resistive structure is associated with lower terrace deposit. This shows the RMT data from profile 1 is matching with the geological map. This profile shows that the Northern part is dominated by resistive structures (lower terrace deposit) and the Southern part corresponds to conductive structures (holocene deposit).

The same result is also seen at profile 8 which can also match with the geological map (holocene deposit) accurately (see appendix F). The 2-D model of this profile is dominated with conductive resistivity (20 Ωm) and represented by silty sand. However, our model of the conductivity distribution contrasts with the geological map at the location where profiles 3 and 6 are crossing each other (see black arrows at Figure 5.29). The geological map indicates Lower terrace deposits whereas the conductivity model points towards Fans (Figure 5.28). This assumption is based on the resistivity contrast between the Fans (50-80 Ωm) and the Lower terrace deposits that exhibit a resistivity of more than 80 Ωm. Figure 5.29 allows to delineate the direction of the fault that is represented by the vertical resistive structure visible in profile 1, 2, 3, 4 and 5. From this analysis we conclude that that strike of the fault is N 70°E (red arrow at Figure 5.29). The overall analysis points towards a graben like setting of the fault system as displayed in Figure 5.29.

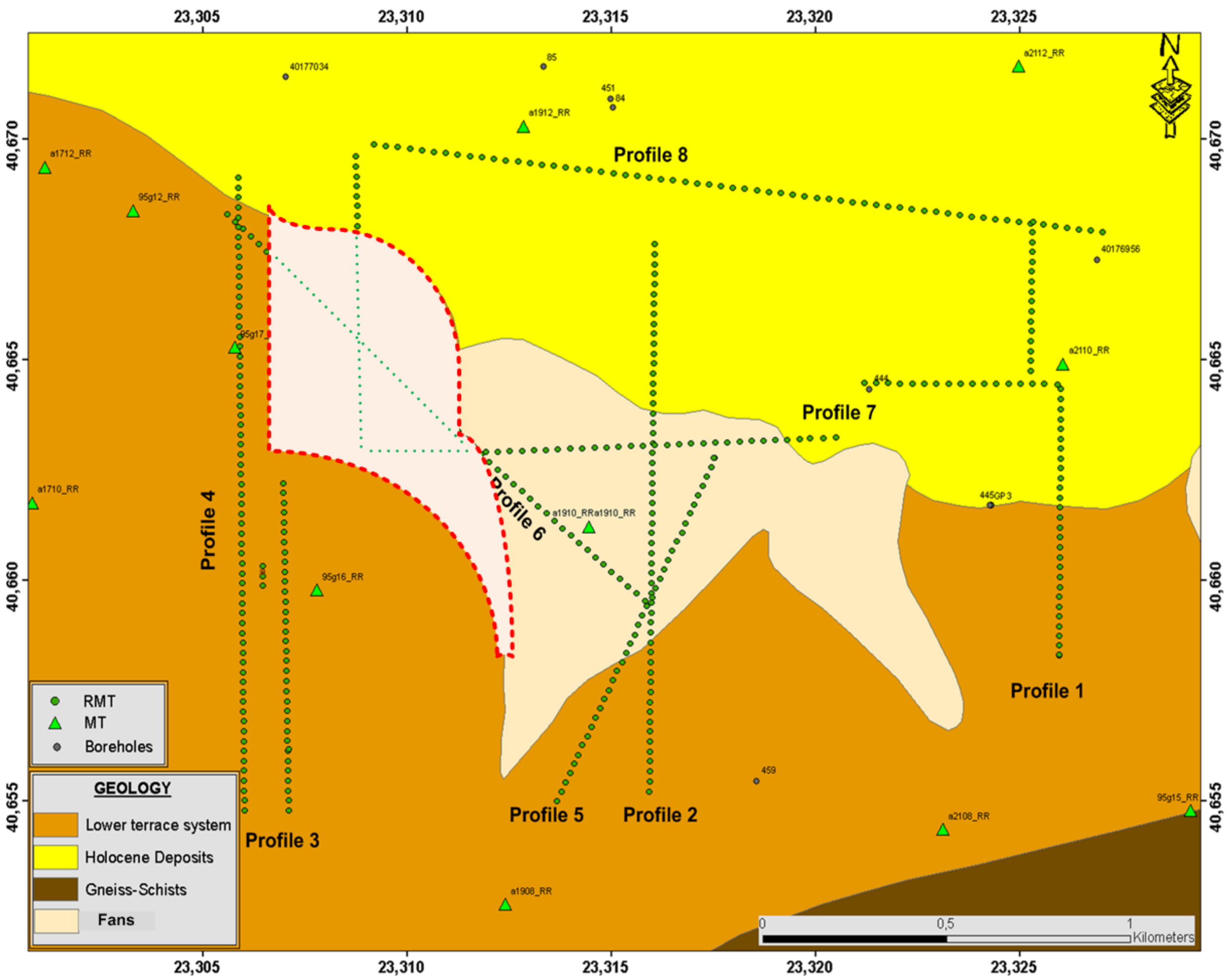

Figure 5.28: *The fixed part of the geological map is shown antique white lines and surrounded by dashed red lines previously considered to be lower terrace deposit and now found out to consist of fans.*

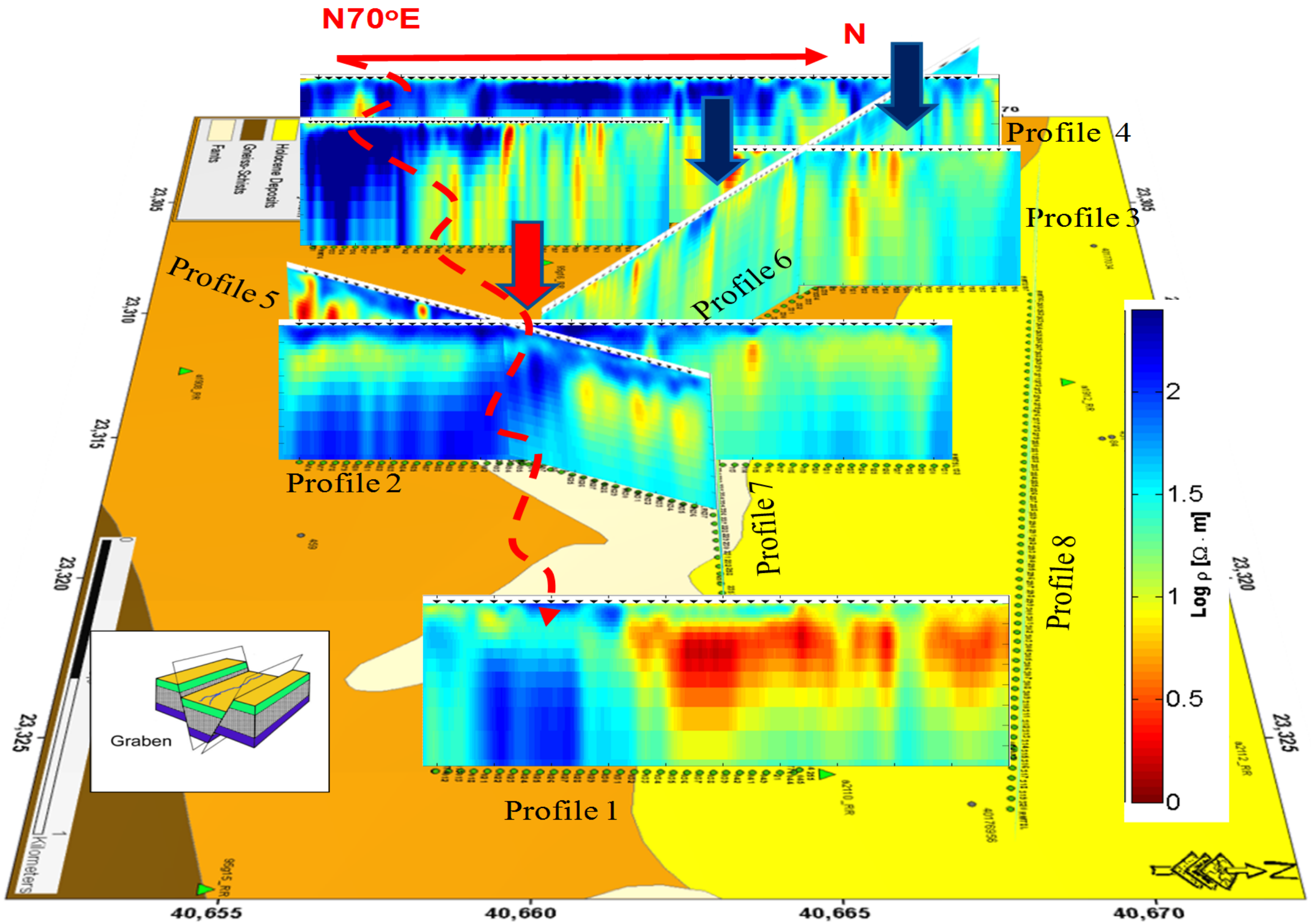

Figure 5.29: *Correlation of 2-D models of RMT data with the geological map. Dashed red lines show the approximate strike direction of fault structure namely N70° E. The red arrow describes the type of fault structure in the field (normal fault structure or garben structure (inset). The blue arrows show an area in which the geological map is different from RMT model result so that needs to fix the geological map.*

Chapter 6

Sequential and Joint Inversions

In chapter 5, single inversion of RMT and TEM data gave an impression of the sensitivity of each method. The RMT conductivity models can resolve the surface structure down to a depth of z $\approx$ 35 m. TEM is small enough to resolve the surface structure ($z < 10$ m), however it can resolve the deeper structure down to 200 m of depth, depending on the resistivity structure. Thus, the joint and sequential inversion of RMT and TEM data will yield resistivity information across the whole depth range available to the two individual methods.

TEM and RMT data measurements are performed at approximately the same sounding location as already explained in chapter 4 about the geophysical field campaign. This chapter will deal with the application of joint and sequential inversion. There are three main purposes for inverting RMT and TEM data together:

1. In order to overcome the problem of TEM soundings exploring the shallow near surface structure, joint inversion of RMT and TEM can provide detailed information from the shallow subsurface until the top of basement of the fault structure in the Volvi Basin.

2. The joint inversion aims to have a better resolution of the model parameters (i.e. resistivity ρ and thickness h). By using data from two different methods, it can decrease non-uniqueness and model ambiguity.

3. Due to technical problems during the TEM measurements in the field (see section 4.5), the information obtained from Nano TEM mode could not be used. This lack of information has left a void which can be filled with RMT data.

In this chapter, two techniques of joint inversion will be applied [*Jupp and Vozoff*, 1975]. The first is called sequential inversion in which the output of the 1-D RMT inversion is used as a priori information for the starting model which constrains the 1-D TEM inverted model. The second approach is inverting both, RMT and TEM data sets, simultaneously in the same 1-D inversion process.

Sequential and joint inversions for RMT and TEM data are realized using Marquardt in the EMUPLUS program which implements Singular Value Decomposition (SVD). In past research, Emuplus has been applied in joint inversions of DC and RMT by

Wiebe [2007]. In addition, this software was successfully validated by *Sudha* [2010] using synthetic data in joint inversion of DC and TEM based on a model formed by *Raiche et al.* [1985]. A comparison of borehole data with joint and sequential inversion results will also be described in this chapter.

6.1 Sequential Inversion

The sequential inversion has been performed using four different approaches in which model parameters are constrained (see section 3.1.8). The used model parameters are resistivity, thickness and calibration factor (CF). To facilitate the identification of each approach in the present chapter, they are labelled with these abbreviations:

1. All parameters (ρ_1, ρ_2 and h_1) are fixed with free CF → **All fix**
2. All parameters are fixed with fixed CF → **All fix CF**
3. All parameters are free with free CF → **All free**
4. All parameters are free with fixed CF → **All free CF**

The one dimensional model of sequential inversion with **All free** is shown in Figure 6.1. This model is obtained from the station TEM 50 which is inverted using a starting model from RMT information recorded at the same station (Figure 6.1). Obviously, the top structure of the sequential inversion model is formed by RMT model and the bottom is obtained from TEM data.

Table 6.1: *Models and importance parameters of single RMT, single TEM and sequential inversion on station 50*

	RMT	Imp	TEM	Imp	**All free**	Imp
$\rho_1[\Omega m]$	70	0.88	196.5	0.2	41	0.98
$\rho_2[\Omega m]$	10	0.99	35.1	0.77	83.5	0.91
$h_1[m]$	5.1	0.96	6.9	0.7	23.35	0.53
RMS[%]	0.5		2		3	

The analysis of importance values from single inversion of TEM and RMT data as well as sequential inversion is summarized in Table 6.1. The first and the second layer resistivities are well resolved with importance values of 0.98 and 0.91, respectively. The importances of the surface layers (ρ_1:0.98 and ρ_2:0.91) show they are better resolved than those of the TEM model for the same parameters (ρ_1:0.2 and ρ_2:0.77). This shows the resistivity of the surface layer for a sequential model of TEM is being improved by using a starting model derived from the 1-D RMT model for calculating a sequential model of TEM.

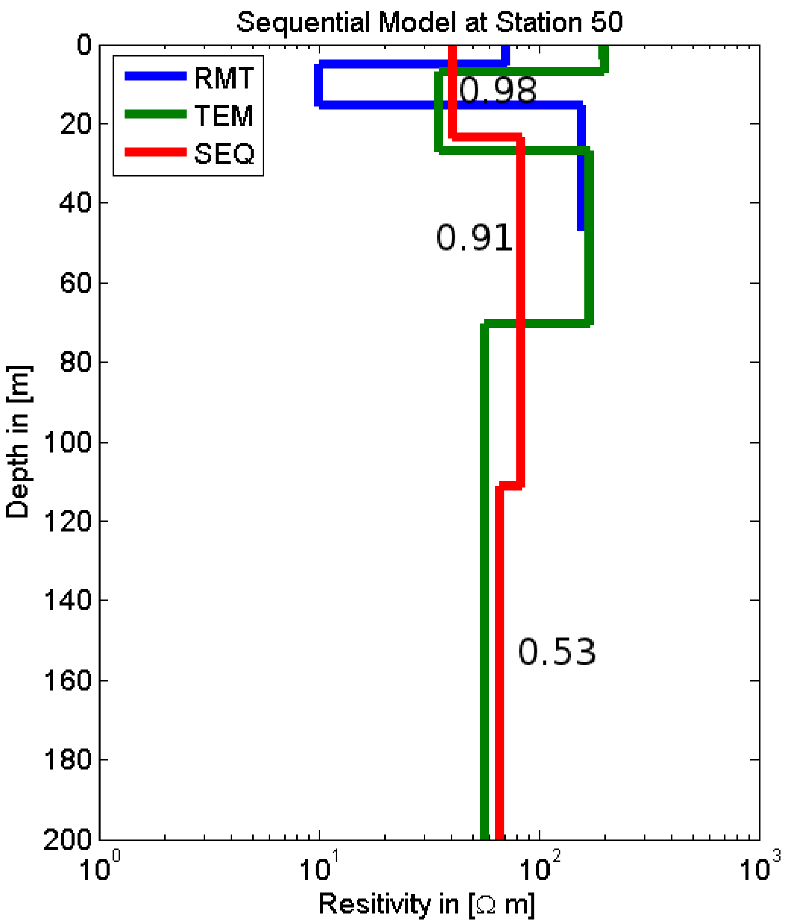

Figure 6.1: *1-D models of single RMT (blue), TEM (green) and sequential inversion* ***All free*** *(red) located at station 50. The numbers indicate the importance values of the resistivities from the sequential model.*

A comparison of the results of the different approaches of sequential inversion **(All fix, All fix CF, All free, All free CF)** is shown in Figure 6.2. Overall, the measured and calculated data have a good fitting. However, the model of **All fix CF** shows a greater RMS (5.5%) due to ρ_1, ρ_2, h_1 and the CF are being fixed.
The models of sequential inversion created with different approaches show a distribution of similar structures. However, for further analysis of model parameters, the importance values are calculated. As stated in chapter 5 section 5.2.3, the importance value is classified into three categories; important, unimportant and irrelevant. In this section, symbols will be used for each category, i.e. important (0.80 - 1) is represented by ⬤, unimportant (0.5 - 0.79) = ● and irrelevant $< 0.5 =$ •.

Examplary, the importances of three different stations (station 54, 58 and 70) are examined. As mentioned before, station 58 is located directly on the fault structure on profile 2, while stations 50 and 70 are respectively located on the left and right sides of the fault structure (Figure 6.3). Table 6.2 shows the importance distribution of station 54. The resistivities of the first and the second layers of **All free** models

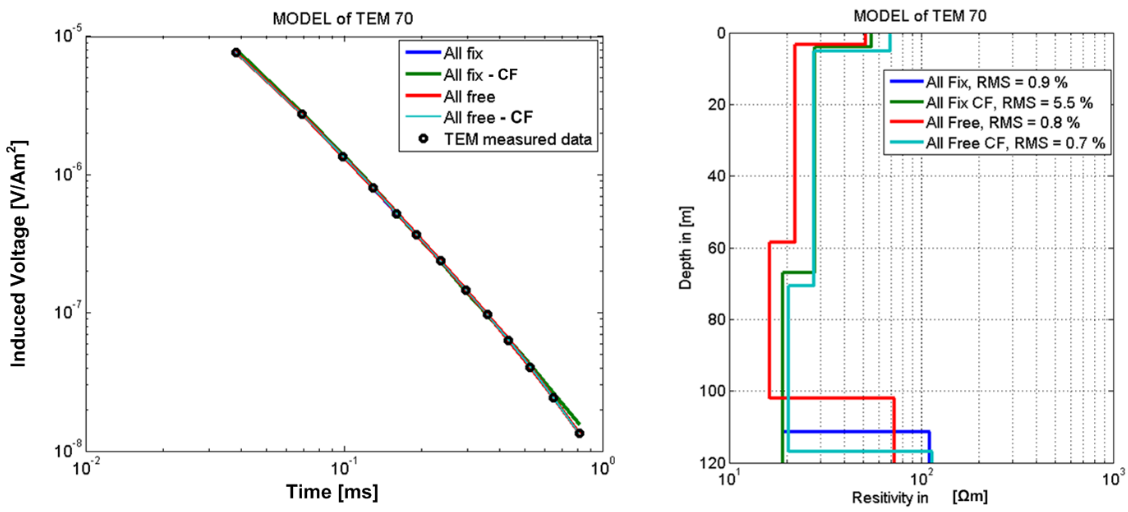

Figure 6.2: *Sequential inversion at station TEM 70. (Left) Fitting of measured data (black) and calculated data of the four approaches that is **All fix** (dark blue) **All fix CF** (green), **All free** (red), and **All free CF** (light blue). (Right) Four models of sequential inversion for **All fix** (0.9%), **All fix CF (5.5%)**, **All free (0.8%)** and **All free CF (0.7%)**.*

are well resolved. The resistivities of the third and fourth layers are unresolved (0.21 and 0.03). The importance values of the first and second layers for **All fix** and **All fix CF** are zero due to model parameters (resitivity and thickness) being fixed in the inversion process. The RMS errors of the four approaches have similar values about 3%.

The importance distribution of station 58 is shown in Table 6.3. The first layer ρ_1 of all models has a resistivity of 100 Ωm. This parameter is well resolved in the **All free** model with importance value of 0.88. Table 6.4 describes the importance values of station 70 located in holocene deposit. The resistivity value of the first layer is arround 30 Ωm and it is well-resolved, however ρ_2, ρ_3, ρ_4 and h_3 cannot be resolved (irrelevant).

The results of sequential models from four different approaches **(All fix, All fix CF, All free and All free CF)** at profile 2 can be seen in Figure 6.3. The four models show relatively similar structures, only a few of which have different patterns, i.e. at station 70, the resistivity value distribution is different from others. The comparison shows those four models are generally consistent with each other. The sequential models of four different approaches along profiles 1 and 3 can be found in appendix C. In addition, the interpolation of sequential 1-D models models along profiles 1 - 3 can also be found in appendix D.

The quality of the measured and calculated data for all sequential models at profile 2 can be seen in Figure 6.4. They generally show a good fit with RMS errors less than 5%. Only for few stations (7, 4, 15 and 24), the data fit has an RMS error higher than 5%. The average RMS error of all parameters are: **All fix** (2.2%), **All fix CF** (3.4%), **All free** (2.2%) and **All free CF** (2.2%).

Table 6.2: *Models and importance parameters of sequential inversion on station 54*

	All fix	Imp	**All fix CF**	Imp	**All free CF**	Imp	**All free**	Imp
$\rho_1[\Omega m]$	75	fix	75.2	fix	75.23	⬤	75.23	⬤
$\rho_2[\Omega m]$	97	fix	97.38	fix	97.38	•	97.38	⬤
$\rho_3[\Omega m]$	19	•	19.48	•	19.48	•	19.48	•
$\rho_4[\Omega m]$	370	•	370	•	370	•	370.4	•
$h_1[\Omega m]$	77.2	fix	77.2	fix	77.2	•	77.2	•
$h_2[\Omega m]$	30.21	●	30.21	●	30.21	⬤	30.21	⬤
$h_3[\Omega m]$	33.31	⬤	33.31	⬤	33.31	⬤	33.21	⬤
RMS[%]	3.79		3.79		3.09		3	

important (0.80 - 1) ⬤, unimportant (0.5 - 0.79) = ●, irrelevant $<$ 0.5 = •

Table 6.3: *Models and importance parameters of sequential inversion on station 58*

	All fix	Imp	**All fix CF**	Imp	**All free CF**	Imp	**All free**	Imp
$\rho_1[\Omega m]$	100.86	fix	100.86	fix	100.86	⬤	100.86	⬤
$\rho_2[\Omega m]$	36.49	fix	36.49	fix	36.49	⬤	36.49	⬤
$\rho_3[\Omega m]$	22.92	•	22.92	⬤	22.92	•	22.92	•
$\rho_4[\Omega m]$	70.2	•	70.2	•	70.2	•	70.2	•
$h_1[\Omega m]$	59.08	fix	59.08	fix	59.08	•	59.08	●
$h_2[\Omega m]$	50.38	●	50.38	●	50.38	●	50.38	●
$h_3[\Omega m]$	48.92	⬤	48.92	⬤	48.92	⬤	48.92	⬤
RMS[%]	0.65		0.65		0.65		0.65	

important (0.80 - 1) ⬤, unimportant (0.5 - 0.79) = ●, irrelevant $<$ 0.5 = •

Table 6.4: *Models and importance parameters of sequential inversion on station 70*

	All fix	Imp	**All fix CF**	Imp	**All free CF**	Imp	**All free**	Imp
$\rho_1[\Omega m]$	30.74	fix	30.74	fix	30.74	⬤	30.74	⬤
$\rho_2[\Omega m]$	15	fix	14.99	fix	15	•	15	•
$\rho_3[\Omega m]$	62.68	•	77.18	⬤	67.7	•	67.7	•
$\rho_4[\Omega m]$	282.5	•	289.2	•	235.94	•	235.94	•
$h_1[\Omega m]$	67.8	fix	67.84	fix	67.84	●	67.84	●
$h_2[\Omega m]$	28.2	●	28.2	⬤	28.23	⬤	28.23	●
$h_3[\Omega m]$	26.96	●	52.75	●	28.22	•	28.22	•
RMS[%]	0.9		5.5		0.8		0.7	
important (0.80 - 1) ⬤, unimportant (0.5 - 0.79) = ●, irrelevant < 0.5 = •								

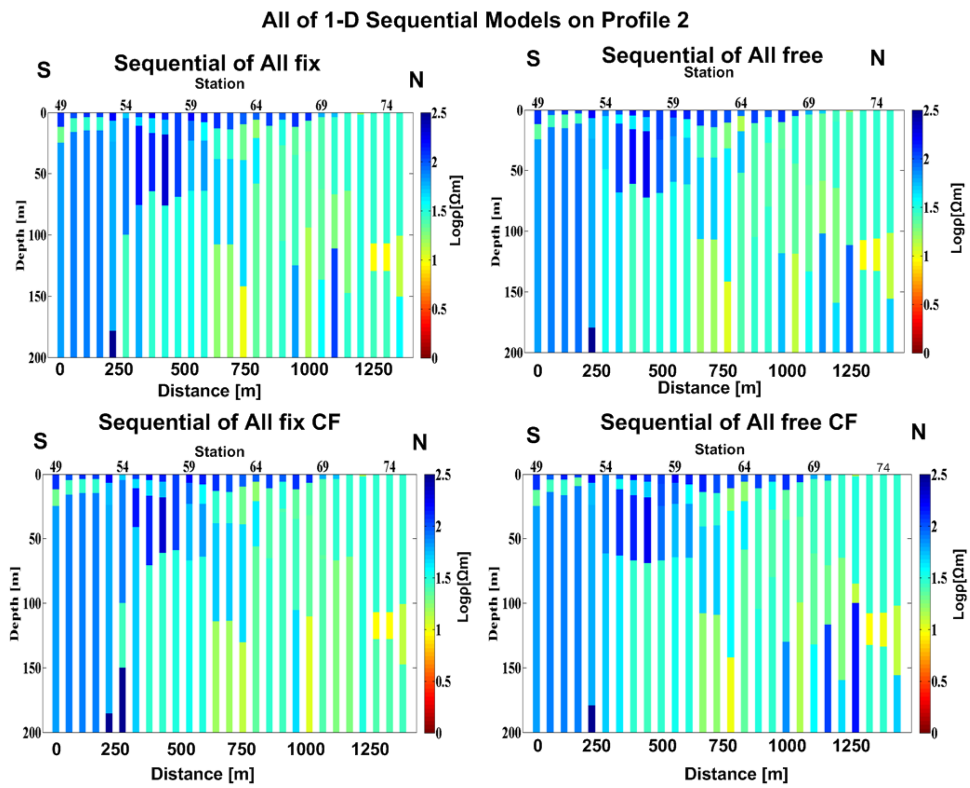

Figure 6.3: *All 1-D conductivity models of sequential inversion along profile 2. (a) All fix parameters (ρ_1, ρ_2 and h_1) with CF free (**All fix**). (b) All free parameters with CF free (**All free**). (c) All fix parameters with CF (**All fix CF**). (d) All free parameters with CF fix (**All free CF**).*

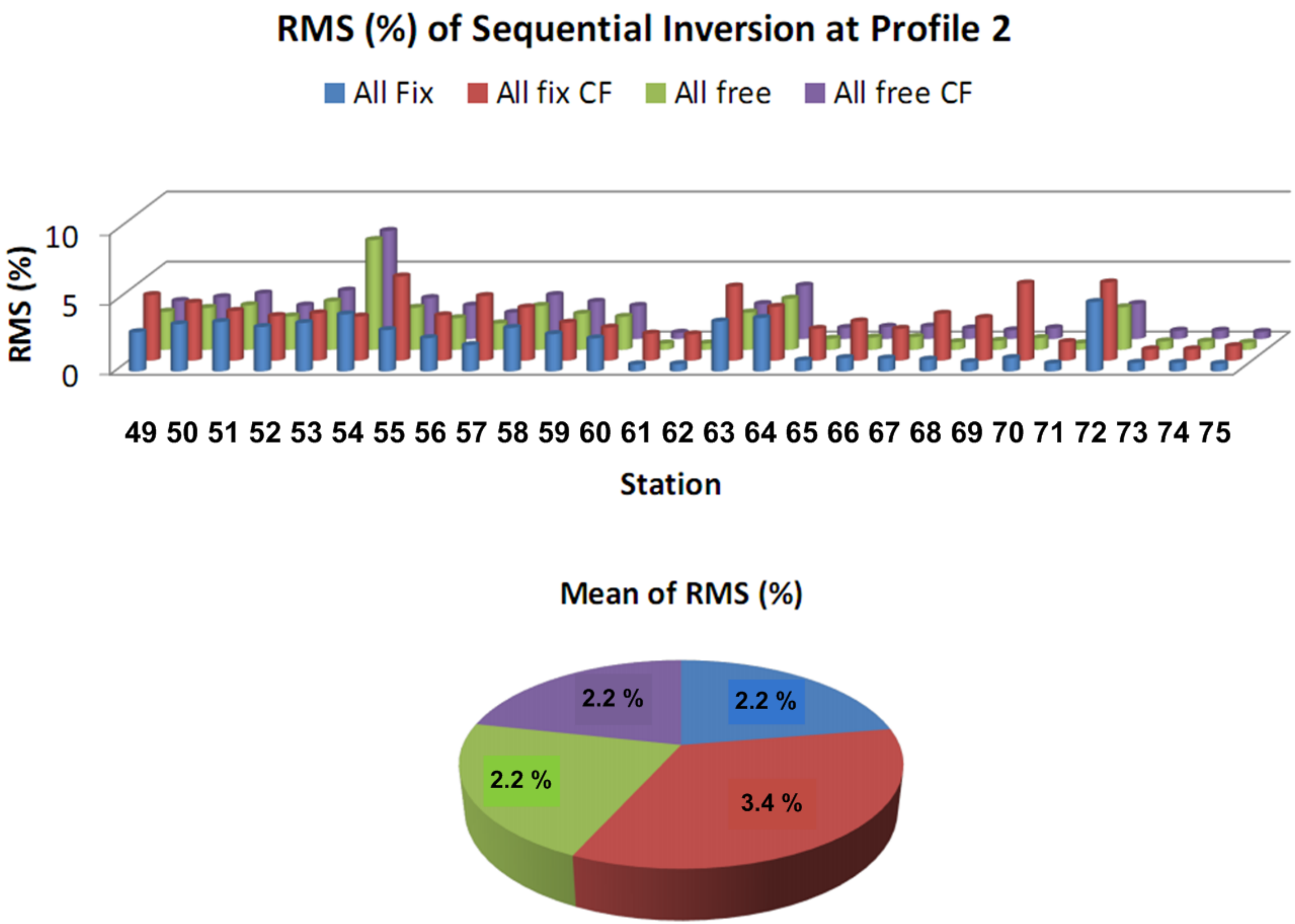

Figure 6.4: *All RMS errors of sequential inversion at profile 2.* ***All fix*** *(blue),* ***All fix CF*** *(red),* ***All free*** *(green) and* ***All free CF*** *(violet).*

6.2 Joint Inversion

Joint inversion of RMT and TEM data aims to overcome the limitation of the individual methods. The processing scheme of joint inversion implements the second order of the Marquardt algorithm using singular value decomposition (SVD). Due to increasing values of importance parameters, joint inversion can eliminate ambiguity of the individual RMT and TEM methods [*Vozoff and Jupp*, 1975].

Table 6.5 contains the results of the single RMT, TEM and joint inversions at boreholes S-1 and S-10. It shows the resistivity of (ρ_1, ρ_2 and h_1) as a result of the individual single RMT, TEM and joint inversions. At borehole S-1, the resistivity of single inversion of RMT data of the first and second layer (ρ_1 and ρ_2) are well resolved with importance of 0.99. However, the first layer resistivity of single TEM data cannot be resolved with importance of 0.09, but it is resolved well by joint inversion (importance of 0.99). For joint model at borehole S-10, the model parameters are resolved well with importance values more than of 0.95.

Table 6.5: *Models and importance parameters of single RMT, TEM and joint inversions at boreholes S-1 and S-10*

	Borehole S-1					
	RMT	**Imp**	**TEM**	**Imp**	**Joint**	**Imp**
ρ_1	42.1	0.99	537.72	0.09	82.98	0.99
ρ_2	15.98	0.99	25.71	0.99	28.81	0.99
h_1	1.35	0.99	2.6	0.99	2.8	0.99
	Borehole S-10					
	RMT	**Imp**	**TEM**	**Imp**	**Joint**	**Imp**
ρ_1	137	0.99	109	0.99	101.37	1
ρ_2	35.03	0.90	38.86	0.99	38.5	0.99
h_1	7.1	0.92	19.77	0.99	20.96	0.99

Figure 6.5a and b shows the data fitting between measured and calculated data of single and joint inversion of RMT and TEM data at the borehole S-1. In order to know the accuracy of the joint inversion model derived from data points of RMT 1 and TEM 1, its results are compared with borehole data of S-1. Generally, the comparison between joint inversion model and borehole data S-1 has a good fitting (Figure 6.5c).

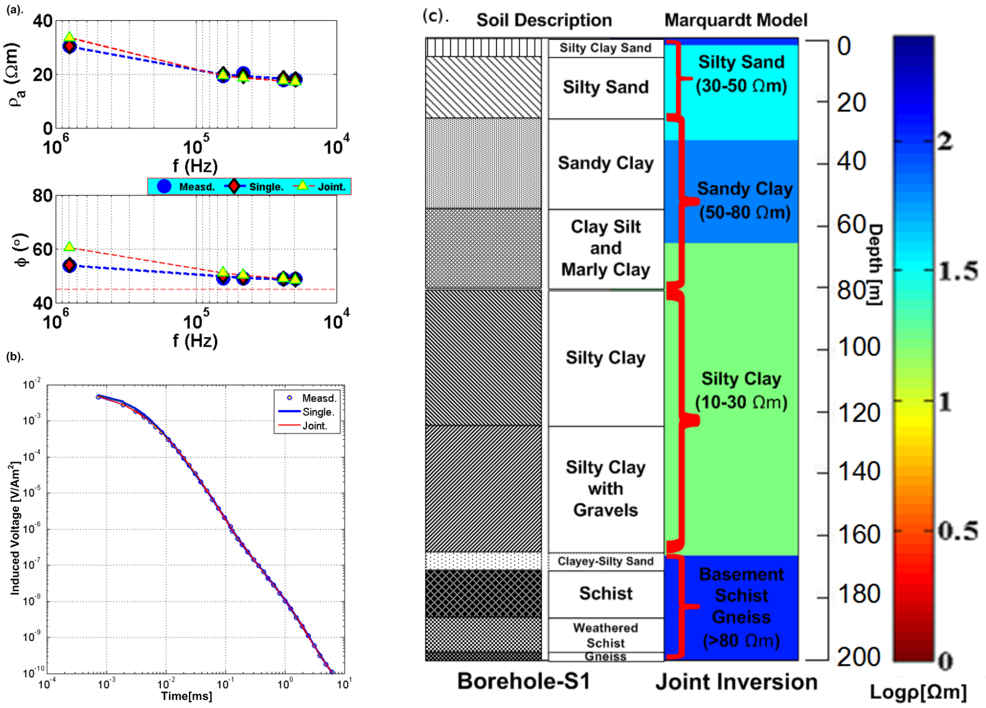

Figure 6.5: *(a) Fitting between measured data of RMT and calculated data of joint RMT and TEM inversion. (b) Fitting between measured data of TEM and calculated data of joint RMT and TEM inversion. (c) Correlation between joint RMT-2 and TEM-2 inversion model with borehole S-1.*

6.3 Discussion

In this section, the joint inversion along profile 2 will be described (Figure 6.6). The joint model has a resistive layer on the depths about 0 to 8 meters at station 49 to 67 of profile 2 . This layer is represented by metamorphic rock, marly silty sand, with resistivity value more than 100 Ωm. Stations 68 to 75 at the same depth and below are indicated by conductive layer namely sandy clay (10 to 30 Ωm). The resistivity distribution corresponds to the geological map in which the stations 68 to 75 are located in holocene deposit (Figure 4.15).

Stations 49 to 57 and 59 to 74 indicate more conductive layer than first one. This layer is silty clay with resistivity of 30 - 50 Ωm. As known from 1-D model of single inversion of TEM and RMT as well as the 2-D conductivity model of RMT data (chapter 5), a fault structure is located underneath profile 2. This is also visible in the joint inversion model. In the 1-D single models, the continuity of vertical fault structure cannot be clearly known while in joint inversion, it can be seen with thickness of 60 m from the surface. One dimensional models of joint RMT and TEM inversion along profiles 1 and 3 can be found in appendix E.

In order to get a better assessment of the resolution of model parameters, the importance parameters were calculated for resistivities and thicknesses [*Jupp and Vozoff*, 1977]. As examples, the parameters were obeserved (ρ_1, ρ_2 and h_1) as a result of the

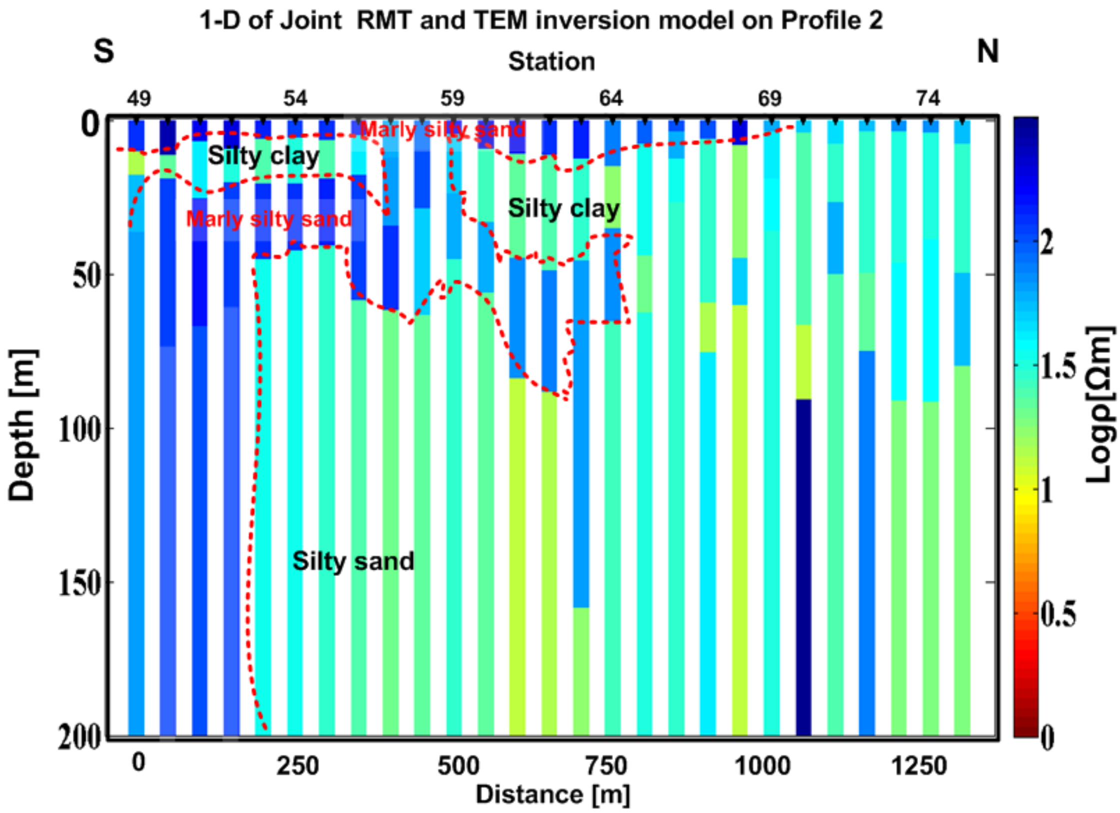

Figure 6.6: *1-D model of joint RMT and TEM inversion on profile 2. The red dashed lines are indicating the boundary of layers.*

individual single and joint inversions for stations 56, 58 and 64 (Tables 6.6 - 6.8). The thickness and resistivity of the first layer (ρ_1, h_1) of RMT inversion are well resolved for all models with importances of more than 0.80 for stations 56, 58 and 64. However, the correspondent parameters of TEM inversion cannot be resolved with importances of less than of 0.7, but they are resolved well by joint inversion. From these results, it can be concluded that the joint inversion gives better resolution in comparison with single inversions of RMT and TEM.

Table 6.6: *Model and importance parameters of RMT, TEM and joint inversion at station 56 on the Southern side of the fault structure*

	RMT	Imp	TEM	Imp	Joint	Imp
ρ_1	93.38	0.89	67.23	0.50	123.98	0.91
ρ_2	28.12	0.90	91.18	0.75	39.62	0.93
h_1	3.9	0.97	10.86	0.24	21.64	0.97

Table 6.7: *Model and importance parameters of RMT, TEM and joint inversion at station 58 on the fault structure*

	RMT	Imp	TEM	Imp	Joint	Imp
ρ_1	99.05	0.99	100.55	0.63	85.86	0.91
ρ_2	155.13	0.86	37.35	0.77	134.2	0.86
h_1	11.43	0.85	57.89	0.16	10.1	0.85

Table 6.8: *Model and importance parameters of RMT, TEM and joint inversion at station 64 on the Northern side of the fault structure*

	RMT	Imp	TEM	Imp	Joint	Imp
ρ_1	81.34	0.82	22.35	0.57	76.58	0.91
ρ_2	16.68	0.84	48.96	0.75	15.1	0.86
h_1	14	0.95	8.5	0.44	14.7	0.96

The distribution of importance values of joint RMT and TEM inversion along profile 2 can be seen in Figure 6.7. In general, the model parameters of joint inversion can be resolved at profile 2 with importance values of more than 0.85. However, the thicknesses of the last layer (h_3) cannot be resolved at some stations due to their location on a conductive structure.

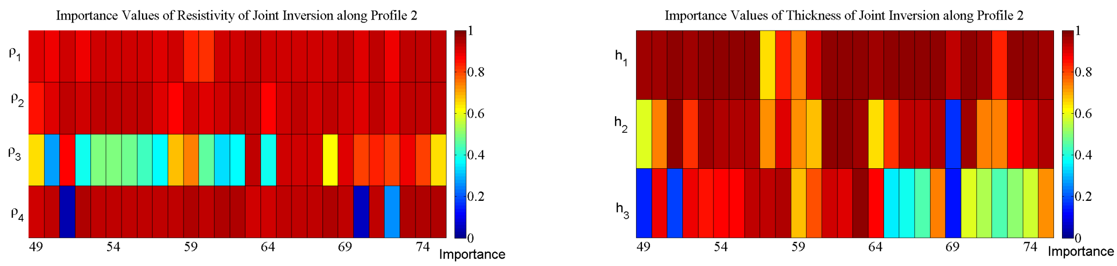

Figure 6.7: *Importance values distribution of joint inversion along profile 2.*

For further analysis of the accuracy of the joint and sequential model from RMT and TEM data, a comparison with single inversions models of RMT and TEM data is necessary which is shown in Figure 6.9: The shallow depth range from the surface down to 40 m shows basically the same features in both the sequential and joint conductivity models as it does in the RMT model.

In addition, a comparison of resistivity values at specific depths of the four models is also performed. Table 6.9 shows comparison of a resistivity values from single RMT, joint and sequential inversions for several selected stations (49, 56, 58, 60, 64, 62, 72 and 74) at the second layer with depth ranging from 14 to 20 m. There, the resistivities from all models are in a good agreement with each other.

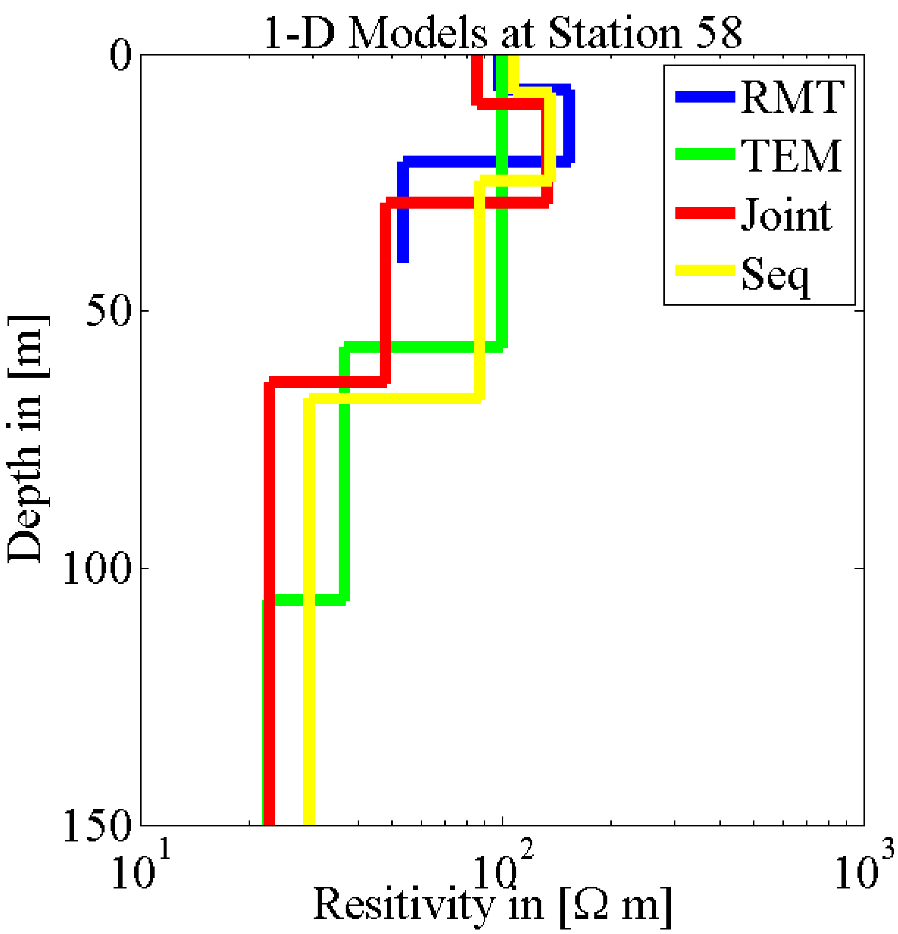

Figure 6.8: *1-D single RMT (blue), TEM (green), joint inversion (red) and sequential (yellow) models on fault structure (station 58).*

To get to know the depth distribution for the deeper layers, a comparison between the sequential, joint and the TEM models is conducted. Table 6.10 shows a comparison of the resistivity distributions from stations 49, 56, 58, 60, 64, 62, 72 and 74 at the third layer with depths of 75 to 90 m. There, the resistivity of the single inversion of TEM data shows a comparable result with the joint and sequential inversions. The 1-D models of single RMT, TEM and the joint inversion have a good agreement on fault structure at station 58 (Figure 6.8). In Figure 6.9 and Tables 6.9 and 6.10, the sequential and joint inversion are identified to have similar features, in the deeper parts as well.

From the above description, it can be stated that the joint and sequential models can both represent 1-D single inversion of RMT and TEM data. Joint and sequential inversions also have to be a solution for the technical problem in the field which damaged Nano TEM data sets: the missing information on the near surface structure is replaced with RMT data.

Table 6.9: *1-D models obtained from single RMT, sequential and joint inversions for selected stations on profile 2 at depth 14-20 m (the second layer).*

Station	**RMT**	**Sequential**	**Joint**
	$\rho[\Omega\text{m}]$	$\rho[\Omega\text{m}]$	$\rho[\Omega\text{m}]$
49	20.44	21.9	17.6
56	47.9	50.24	39.6
58	155.13	136.9	134.23
60	44.1	39.4	25.5
64	16.68	16.75	15.1
68	12.36	25.8	18.49
72	12.01	31.07	27.24
74	11.2	29.10	31.75

Table 6.10: *1-D models obtained from single TEM, sequential and joint inversions for selected stations on profile 2 at depth 75-90 m (the third layer).*

Station	**TEM**	**Sequential**	**Joint**
	$\rho[\Omega\text{m}]$	$\rho[\Omega\text{m}]$	$\rho[\Omega\text{m}]$
49	78.6	83.56	64.4
56	20.56	42.52	21.6
58	26.76	37.16	22.82
60	45.5	30.44	23.10
64	38.5	38.34	28.1
68	24.9	29.11	13.3
72	16.9	18.28	25.02
74	29.16	29.67	18.27

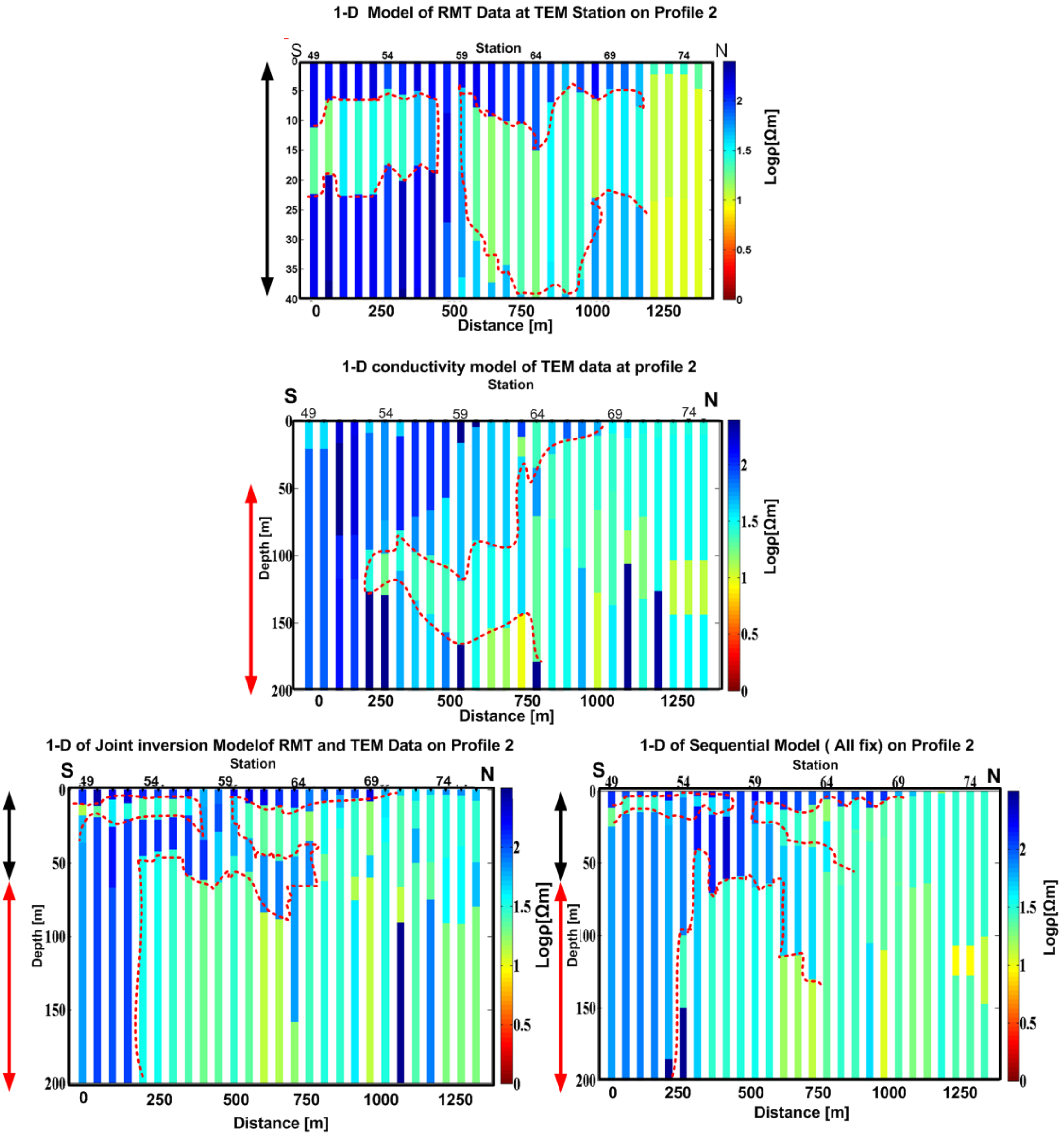

Figure 6.9: *1-D of single RMT (top), single TEM (middle), joint (bottom at left side) and sequential inversion models (bottom at right side) in profile 2, the red dashed lines are indicating layers boundaries to the left of different diagrams. The arrows highlight identical depth ranges down to 40 m (black arrows), the single RMT, joint and sequential models show basically the same structure, and for depths of more than 40 m (red arrows), joint and sequential models have similar features as the single TEM model.*

Chapter 7

Three-Dimensional Forward Modeling of RMT Data

According to the interpretation of 1-D and 2-D models in chapter 5, the research area has a complex geological structure. This is shown by the indication of a *graben* structure.

In addition, from the 2-D point of view, dealing with TE and TM modes, the RMT device separately records data from two pairs of transmitters. From the time series recorded with the RMT-F device, not the full impedance tensor elements were calculated. Only Z_{xy} and Z_{yx} (ρ_{xy}, ρ_{yx}, ϕ_{xy} and ϕ_{yx}) were obtained. As mentioned in section 5.3, it is difficult to fulfill the 2-D assumption regarding TE and TM mode for RMT data on a complex geological structure [*Newman et al.*, 2003]. In this case, it is essential to perform a 3-D interpretation which is done by means of 3-D forward modeling. In general, there are two main objectives of 3-D modeling:

1. Due to the complex geological structure in the research area, the 3-D modeling can provide adequate information on the fault structure.

2. The 3-D modeling gives a representative model for all conductivity structures in the research area. In this case, the 3-D model is constructed using the 2-D conductivity model and the geology as priori information.

In the past, several 3-D modeling studies were implemented to study the behavior of the response of 3-D magnetotelluric data [*Ting and Hohmann*, 1981, *Wannamaker et al.*, 1984, *Mackie and Madden*, 1993, *Weiss and Newman*, 2002].

7.1 Testing the Algorithm

Three dimensional simulations of this research area are performed using the finite-difference algorithm of *Mackie et al.* [1994]. 3-D forward modeling codes provide an estimation of the electromagnetic response given by a resistivity model. Besides resistivity, phase is an input parameter also used in 3-D modeling. The input model consists of rectangular model cells, each of which has specification with homogenous resistivity values. The present thesis uses two packages of programs are used to make simulation of 3-D modeling [*Mackie and Booker*, 1999]. They are:

1. **Mtd3fwd**
   This program calculates the magnetic and electric fields at the surface of a 3-D conductivity model.

2. **D3 to MT**
   This program calculates impedance, apparent resistivity and phase from the electric and magnetic fields as generated by **Mtd3fwd** package.

The development of a 3-D forward model is generally carried out over several steps. In order to get the proper model response, the first step is testing the codes with homogeneous and 2-D models. Originally, these codes are used in magnetotelluric data modeling in a frequency range from 10,000 Hz to 0.0001 Hz. For 3-D modeling of RMT data, the frequency range from 10 kHz to 1 MHz are implemented.

The second step is determining the primary structure of the model to be formed in 3-D modeling. Due to the large area modeled and the need for a sufficient amount of grid cells, this step is usually done first for the main structure only and then expanded to the whole area. The format of the 3-D grid cell for the input file for **Mtd3fwd** can be found in Appendix G.

In the last step, verification of the obtained model response is needed. This means checking the fit between measured field data and calculated synthetic data. In order to get the best data fit between 2-D measured and 3-D calculated response, a considerable amount models was calculated by trial and error procedure.

7.1.1 Homogeneous Half Space

In order to test the 3-D algorithm with a homogeneous model, the grid is constructed by a 3-D scheme. It consists of nodal columns nx, nodal rows ny and nz depends on the depth of the model. The size of the 3-D forward modeling is of 2.4×2.4 km^2 (Figure 7.1a). In connection with a wide survey area and frequency range of RMT, a grid with 2,178,000 cells is implemented (nx = 220, ny=220 and 45 layers (nz=45). A resistivity of 80 Ωm was used for the homogeneous model, as it was obtained from the average resistivity distribution in the area.

The 3-D algorithm calculates the full impedance tensor (Z_{xx}, Z_{yy}, Z_{xy} and Z_{yx}). As an example, station 30 has been chosen to show a calculation of apparent resistivity and phase (Figure 7.1b). Figure 7.1c shows that the Z_{xy}, Z_{yx} impedance values are zero and Z_{xy} has a value equal to Z_{yx} with an apparent resistivity of 80 Ωm and a phase of 45°. In Figure 7.1c and Figure 7.1d, the fitting between input and computed 3-D forward responses for selected frequency f = 833 kHz of Z_{xy} and Z_{yx} at X and Y direction are shown. The resulting apparent resistivity and phase confirm the homogeneous condition with impedances (Z_{xy} and Z_{yx}) of 80 Ωm and phases of 45°.

Those diagrams for selected station and frequency are in good agreement to 3-D response (Figure 7.1). Under this condition, the 3-D algorithm is compatible to perform RMT modeling and it is possible to employ the same size of grid cells for the input model in the next step of 3-D forward modeling.

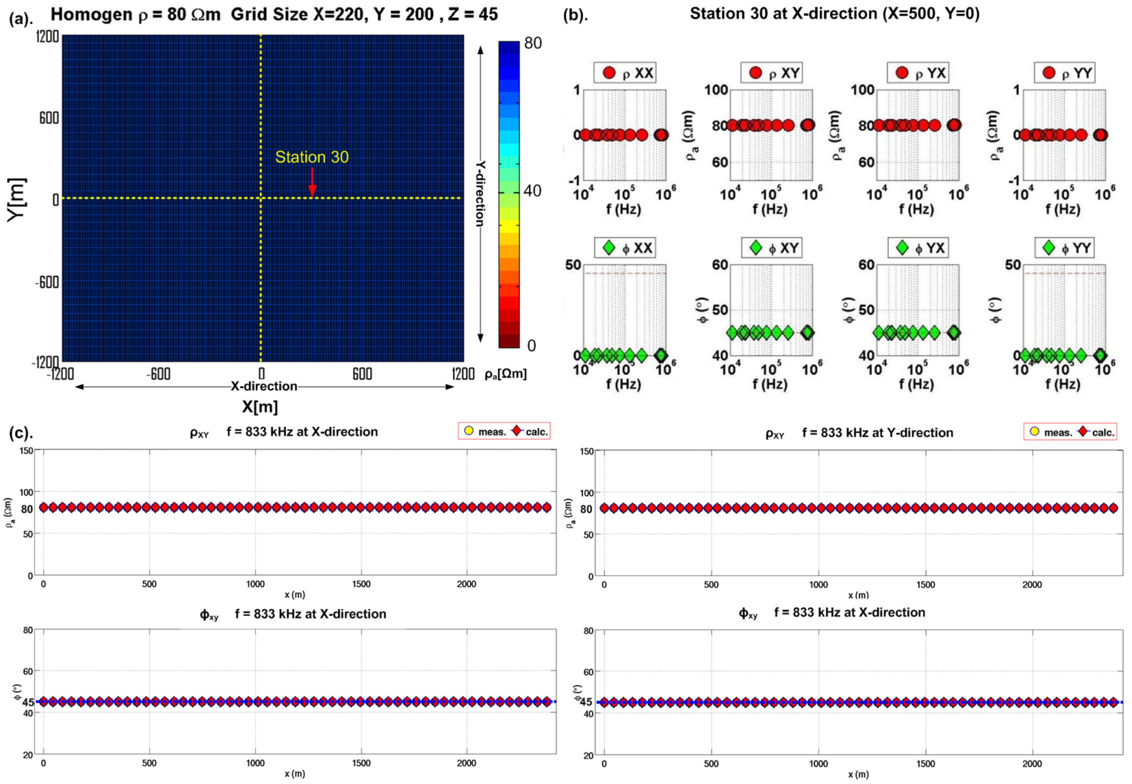

Figure 7.1: *(a) XY-section of homogeneous model with resistivity of 80 Ωm (b) Apparent resistivities (red circles) and phase (green diamonds) of 3-D forward responses for Z_{xx}, Z_{yy}, Z_{xy} and Z_{yx} at station 30 (X-direction) (c) Fitting impedance Z_{xy} between measured data (yellow circles) and calculated data (red diamonds) for a selected frequency (f = 833 kHz) in X-direction. (d) Fitting of Z_{yx} in Y-direction.*

7.1.2 Comparison between 2-D and 3-D Responses

In order to construct an appropriate 3-D RMT model, it is required to construct a model, which fulfills the boundary conditions, i.e. the grid has to be fine enough and extended far enough in the model space. For checking this, we can compare the calculated responses from Mackie's 3-D forward algorithm and Mackie's 2-D algorithm. The derivation of the 3-D model is based on the 2-D models. The grid used is the same as for the homogeneous halfspace model.

The 2-D model for testing the 3-D algorithm is shown in Figure 7.2. The model consists of there layers. The first and third layers are homogeneous with resistivities of 100 Ωm and depths of 0 m and 20 m, respectively. The second layer, between the first and third layer, has a thickness of 10 meters. This layer has three rectangular blocks. One block is conductive (10 Ωm) residing beneath two adjacent resistive blocks (100 Ωm).

From equation 2.19, the skin depth for the lowest frequency (10 kHz) and the highest frequency (1 MHz) can be obtained, using the resistivity of the first layer (100 Ω). The skin depth for the lowest and the highest frequencies are 5 m and 50.3 m, respectively. The slice view in Figure 7.2b cleary visualizes the model.

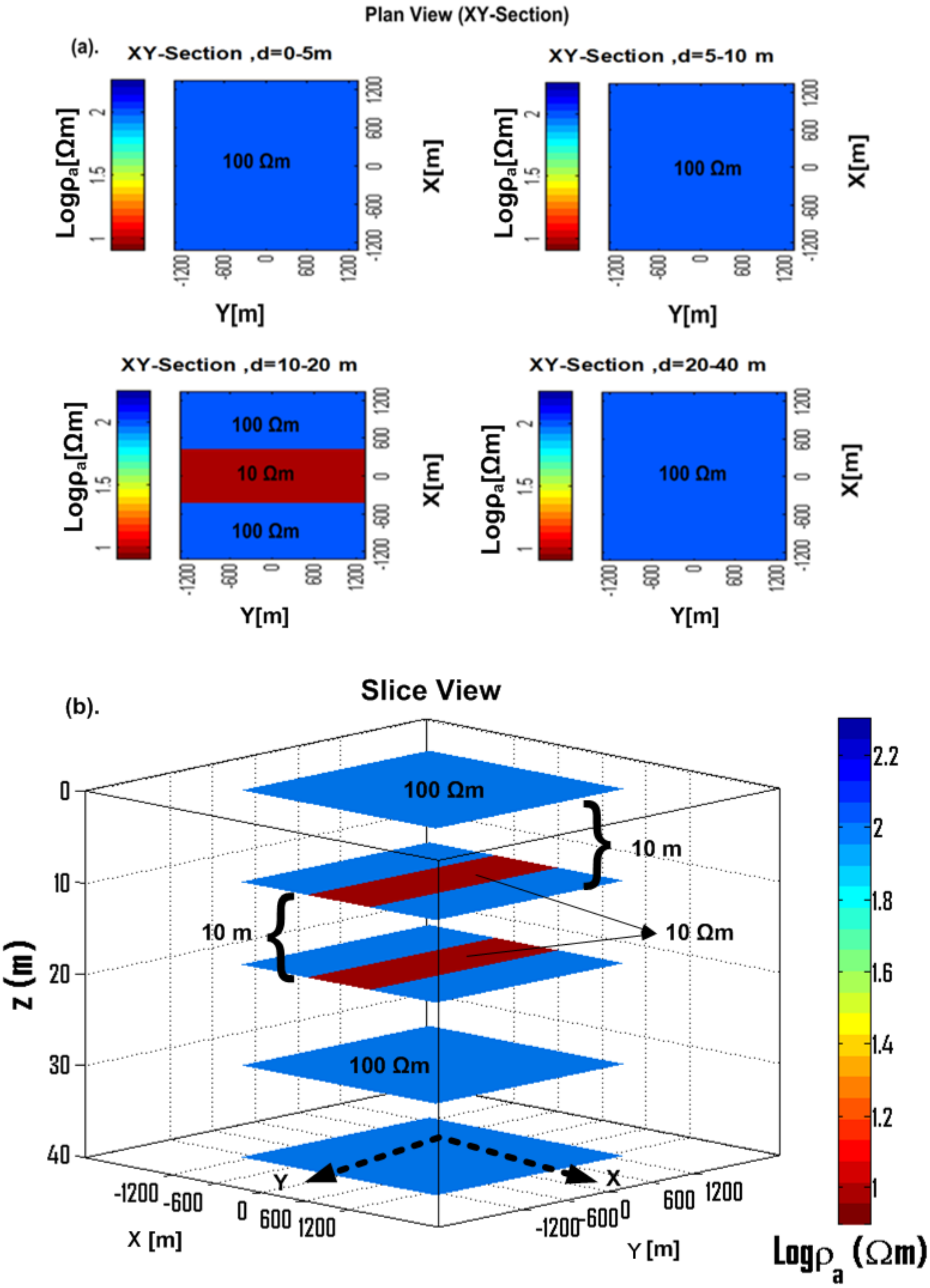

Figure 7.2: *2-D forward model used for 3-D forward modeling. (a) Plan view (XY-sections) for different depths. (b) Slice view of 3-D model, the black dashed lines show the X and Y direction.*

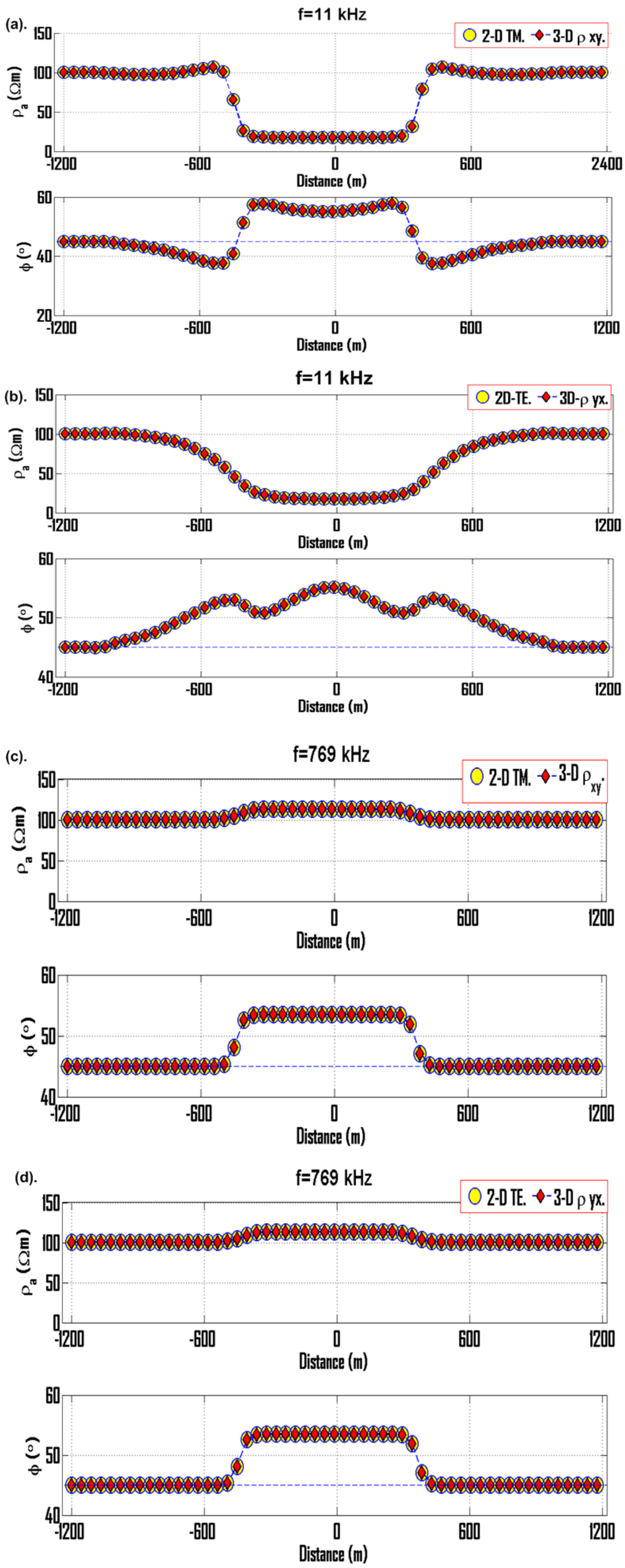

Figure 7.3: *2-D and 3-D calculated synthetic data derived from 2-D input model. (a) Fitting between 2-D TM mode and 3-D response of Z_{xy} component for $f = 11\ kHz$ and (b) $f = 11\ kHz$. Fitting between 2-D TE mode data and 3-D response of Z_{yx} component for (c) $f = 769\ kHz$ and (d) $f = 769\ kHz$.*

For a comparison between the 2-D and 3-D response, the Z_{xy} and Z_{yx} elements along the X-direction are calculated for the 2-D model (Figure 7.2): For frequencies $f = 11$ kHz and $f = 769$ kHz the 2-D and 3-D forward response for these components Z_{xy} and Z_{yx} are compared in Figure 7.3.

Figure 7.3a - Figure 7.3d show anomalous apparent resistivity character when crossing the 2-D body in X-direction in both, the TE and TM mode responses for 2-D and 3-D synthetic data. The apparent resistivity of ρ_{xy} is associated with B-polarization (TM), whereas E-polarization (TE) corresponds to ρ_{yx}. For both polarisations, the highest frequency of 769 kHz shows a local resistivity minimum right over the conductor. For frequency of 11 kHz which is related to a greater depth, the influence of the body on the resistivities and phases is visible for both 2-D and 3-D responses. Overall, there is a good comparison between the 2-D and the 3-D responses.

The E-polarisation apparent resistivities ρ_{yx} moves vary smoothly across the body, while the B-polarisation apparent resistivities ρ_{xy} are discontinues (see appendix H). Therefore, B-polarisation tend to resolve lateral conductivity variations better than E-polarisation resistivities [*Simpson and Bahr*, 1997].

7.2 3-D forward Modeling of the Study Area

After several tests of the 3-D algorithm with synthetic data have been performed, the next step is to construct a 3-D model of the study area from the models obtained from the 2-D inversion results.

7.2.1 Modeling of the Main Structure (Profile 2)

The 2-D RMT models indicate a normal fault structure in the Volvi basin. The normal fault can also be found when comparing all RMT profiles with the geological map in section 5.4. There is no subsurface resistivity information between the profiles, but this information can be provided by the 3-D forward modeling. 2-D inversion cannot resolve resistivity structures at the side of the profiles, whereas a 3-D model can reconstruct the structure over the whole area.

As explained in section 7.1 the 3-D modeling of the research area is conducted by determining the major structure from the 2-D RMT models. The major structure is associated with a normal fault structure, which can also be seen in the 2-D models from profile 2 and profile 5 (see chapter 5). Further, a 3-D model is constructed from the RMT model for profile 2 (see the red rectangle in Figure 7.4a).

Figure 7.4b shows the 3-D model for profile 2 at distance of 0 m until 1000 m from the South to the North. The background of this model is a 50 Ωm half space. Figure 7.4c shows the plane view model of the X-Y section for a depth $z = 10$ m. This model consists of three layers. The overburden is resistive (100 Ωm) with a thickness of 5 m. At the depth from 5 m to 25 m, the model consists of three blocks. The first and third blocks are conductive (30 Ωm and 10 Ωm) and the length for each blocks are 425 m and 300 m. The second block is residing beneath these layers with a length of 275 m. This block corresponds to the the fault structure and it has a resistivity of 100 Ωm, the same as the first layer (Figure 7.4b and Figure 7.4c). The third layer is located at a depth down to 25 m which consists of two blocks. The first block is resistive (100 Ωm) and the second block is very conductive (10 Ωm).

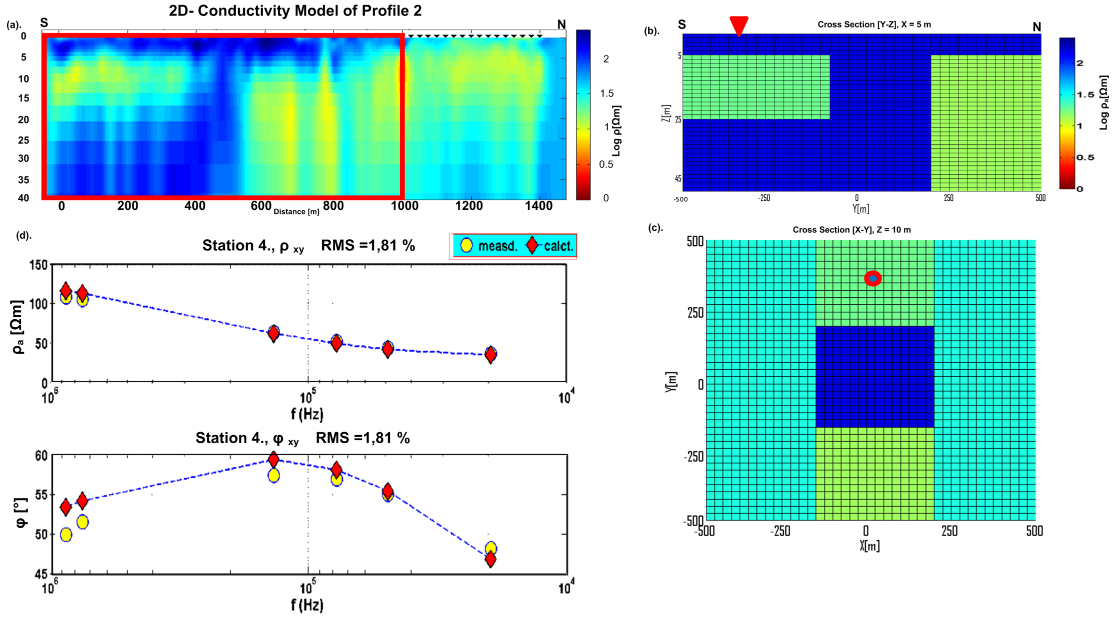

Figure 7.4: *3-D forward model for profile 2. (a) Two dimensional conductivity model for profile 2, (b) Cross section view of 3-D model for profile 2, (c) plane view (X-Y) of 3-D model of profile 2 at X = 10 m. (d) Fitting between 2-D measured data (yellow circles) with 3-D response of* ρ_{xy} *for station 4 (red diamonds).*

The comparison between measured and calculated 3-D synthetic data shows a good fitting. Examplary for this, the resistivities and phases of station 4 (Figure 7.4c). All interpreted data corresponds to Z_{xy}, as in Z_{yx} component not enough transmitter signals have been available, so the comparison between 2-D and 3-D response can only be done for the Z_{xy} component.

7.2.2 3-D Modeling of All Profiles

Once a good result for the major structure is achieved by 3-D forward modeling, the next step to be done is the 3-D modeling of all 2-D models together. To facilitate modeling, the very small structures from 2-D models are ignored.

In order to get an appropriate model, it is essential to adopt the information from the improved of the geological map (Figure 7.5a). For this model, the same grid is used as for the homogeneous and the 1-D model, as it has been well validated. The size of the model space is 2400 m × 2400 m × 50 m.

As mentioned before, in a process to obtain the final model with the best data fit, many models need to be calculated by a trial and error procedure. Due to the great number of cells needed for computational accuracy, the computation time is long. In this chapter, the final representative model for covering profiles 1 to 8 is shown.

An example of the development of a 3-D model for all profiles can be found in Appendix I.

The first step is constructing a representative model for the surface layer which is followed by a model for the next layer downward until the whole fault structure model are covered. The model parameters of the top layer are derived from a combination of the 2-D RMT conductivity model and the local geology. Figure 7.5b shows that the overburden layer is consisting of three blocks. The first block is conductive (20 Ωm) and it corresponds to holocene deposit. The second block is represented by fans and this block has a resistivity of 65 Ωm. The final block is filled out by lower terrace deposit and this layer is the most resistive (100 Ωm) of the blocks.

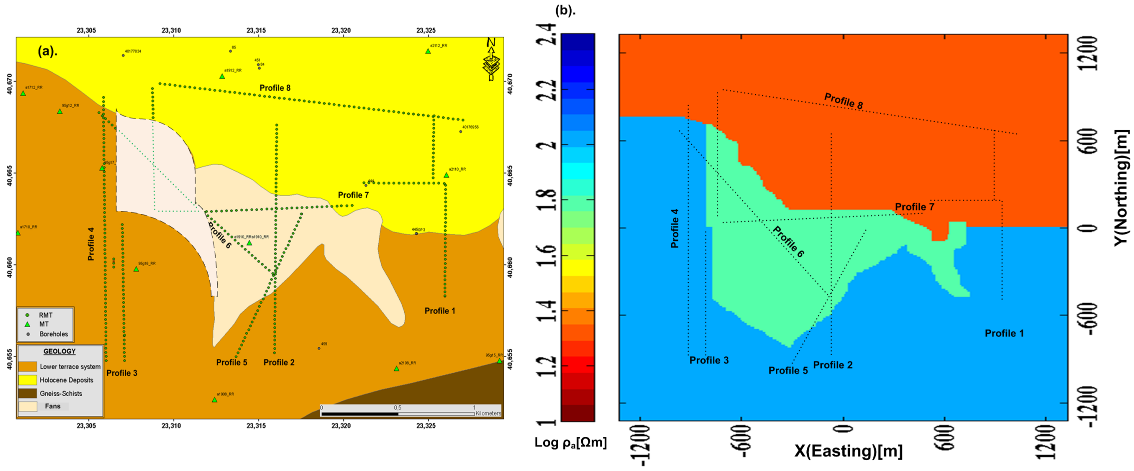

Figure 7.5: *(a) Improved local geological map of the research area. (b) 3-D forward model of the top layer in the research area consisting of three main blocks. The first block is holocene deposit (red), the second block is fans (green) and the lower terrace deposit is the third block (dark blue).*

Figure 7.5a shows the locations of all the RMT profiles and each profiles on the geological map are located at the same location on both the 3-D model and the geological map (Figure 7.5b). The profiles 1 until 4 have the same directions of N0°S. Profile 5 has a direction of N21°S. Profile 6 is in direction from NE to SW. Profile 7 is located on the fans and lower terrace deposit with a direction of N89°S. Profile 8 is situated on the lower terrace deposit with an angle of N98°S.

The fault structure located at 5 m depth can be seen in the X-Y section plane view in Figure 7.6b. This model is almost similar to the top layer model, but it is having a more complex geological structure along profile 2 and 5. It corresponds to the fault structure with a resistivity of 150 Ωm. The fault structure is represented by two rectangular blocks in dark blue color in Figure 7.6.

Profile 1 also indicates a fault structure (see the 2-D conductivity model of section 5.4). It is located at a depth of 20 m and it is related to the fault structure from profiles 2 and 5 highlighted by the black arrows in Figure 7.6e, the structure is visible on the Southern part of profiles 1, 2 and 5. From the 2-D model, we can derive the strike direction of the fault structure: N70°E. Some parts of profiles 3, 6 and 7 are filled with holocene deposits at depths of 5 - 20 m (see orange in Figure 7.6c), whereas above, they are previously composed by fans with a resistivity of 65 Ωm (see green colour in Figure 7.6a). It confirms the geological view where the main sedimentation of the Mygdonian basin is filled by lacustrine deposit [*Koufosa et al.*, 2005] (section 4.2).

From Figure 7.6d, we can observe the adjacent blocks along profiles 2 and 5 which are replaced with more conductive blocks (15 Ωm) at depths of more than 25 m. At the same depth, the fault structure in profile 1 is also filled by this conductive structure and it is associated by holocene deposit (see red circles in Figure 7.6). Figure 7.6b - 7.6e show that the fault structure is found from around 5 m to 25 m depth. As a result of the modeling, the fault structure is associated with a *graben* structure.

7.2.3 Fitting between Measured 2-D Data and Calculated 3-D Data

The 3D-model response is in good agreement with the 2-D models from measured data. As an example, profile 2 has been chosen to show a comparison between observed and predicted data. Figure 7.7b shows a fitting between observed and predicted data for selected stations in three geological formations: stations 5, 36 and 49 are located in the lower terrace deposit, fans and the holocene deposit, respectively (Figure 7.7a). They all have good fitting with an RMS between 1.3% to 3%.

The fitting for the exemplary frequency of 79 kHz along profile 2 (N 0° S) is presented in Figure 7.7c. Measured data and 3-D response of Z_{xy} impedance is fitting well together too, keeping in mind the geological complexity and inhomogeneous in this survey area. However, some misfits occur which are associated as 3-D effects. Due to the high resistivity at greater depth, the 2-D measured and 3-D predicted data have a consistent phase value of more than 45° at profile meter 450 m. This indicates the fault structure.

In conclusion, 3-D forward modeling of RMT data is able to represent all 2-D models and improve the model for the fault structure distribution. Moreover, according to the previous explanation, the 3-D model can identify the type of the fault structure in the Volvi Basin as a *graben* structure.

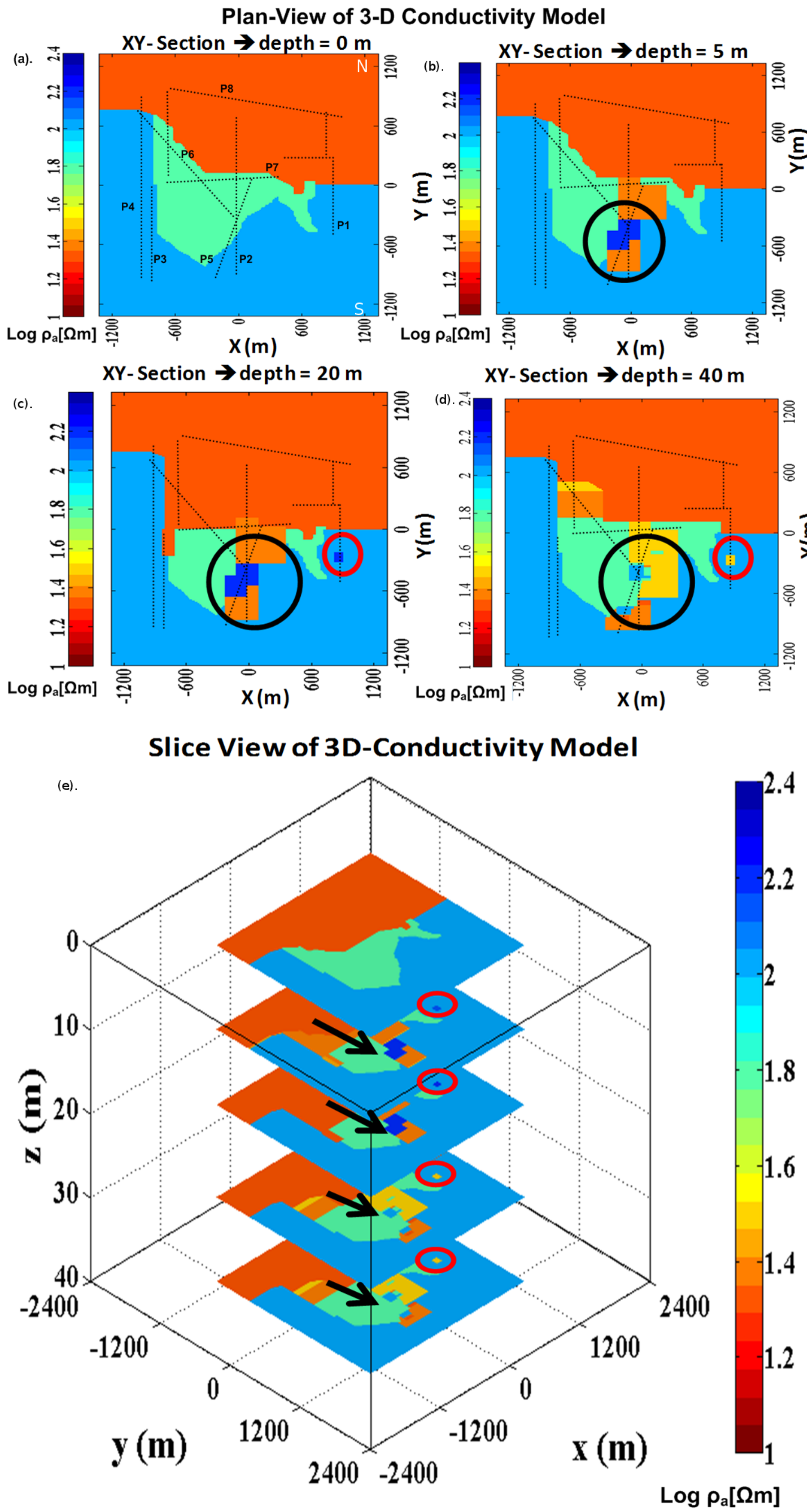

Figure 7.6: *3-D forward model constrcuted for all RMT profiles. (a- d) The X-Y plane views are for depths 0 m, 5 m, 20 m and 40 m. P1 - P8 are the profile numbers. (e) Slice view. The red circles and black arrows indicate the fault structure in profiles 2 and 5. The red circles constitute the fault structure in profile 1.*

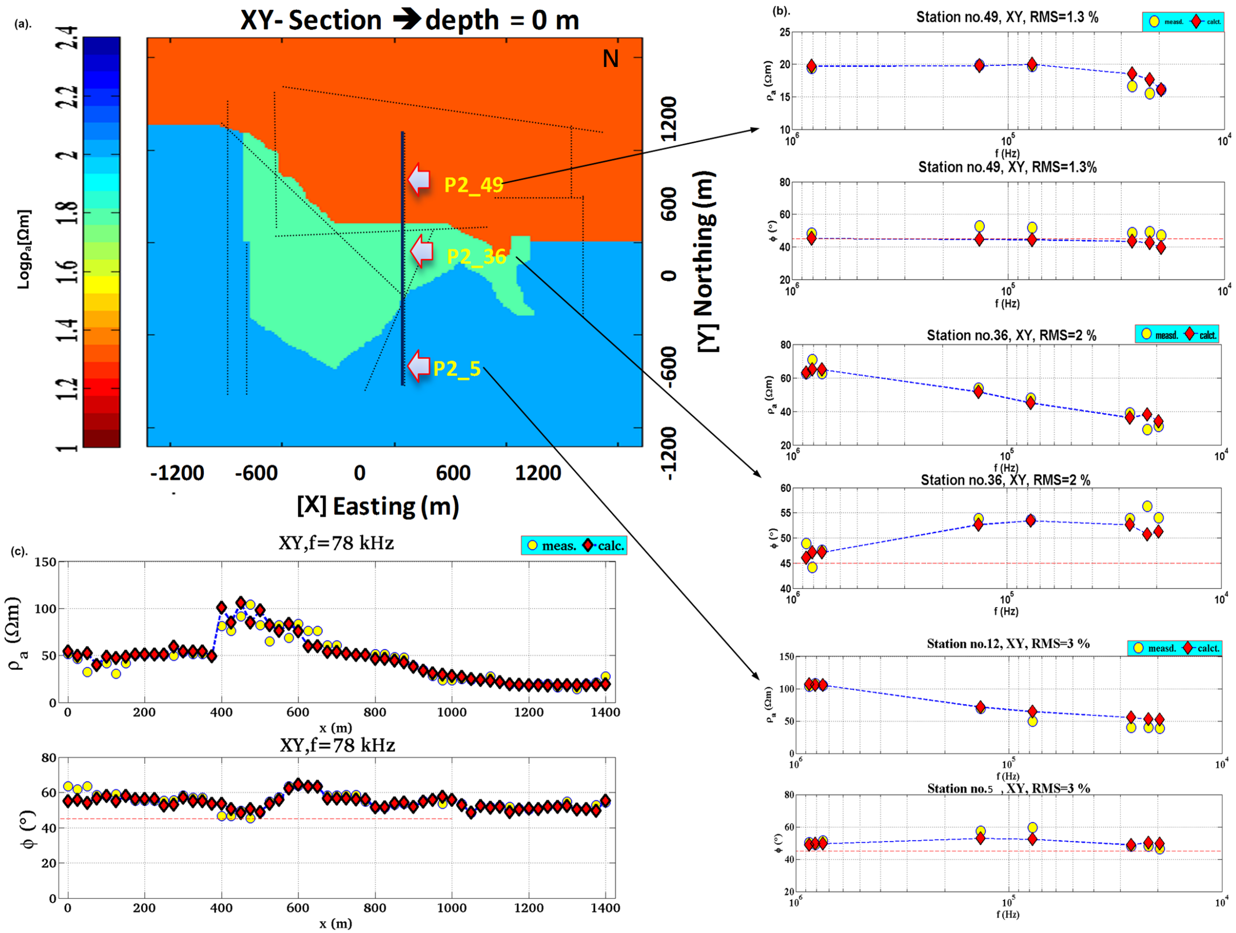

Figure 7.7: *(a) Location of RMT stations. (b) Fitting between measured (yellow circles) and 3-D synthetic data (red diamonds) for three selected stations (5, 36 and 49) in the three different geological formations. (c) Comparison of measured and calculated data for f=78 kHz plotted along the profile line 2.*

Chapter 8

Conclusions and Outlook

8.1 Conclusions

Radiomagnetotelluric (RMT) and Transientelectromagnetic (TEM) models have given a consistent description of the local geological structure on the Northeastern part of the EURO-SEISTEST in Volvi basin. The correlation between borehole data and geophysical data is generally good. Resistivity models of 1-D and 2-D show six layers that can be categorized according to their resistivity values. Each of those can be classified as metamorphic or sedimentary rocks. They are silty sand (10 - 30 Ωm), silty clay (10 - 30 Ωm), silty clay marly (30 – 50 Ωm), sandy clay (50 - 80 Ωm) and marly silty sand (> 80 Ωm) and basement (gneiss and schist) (> 80 Ωm) with varying thicknesses. From the information of borehole S-1, the top of basement is located at a depth of 180 m which can be resolved by TEM data.

Due to the high the resistivity of the top layer, the penetration depth of the RMT soundings is around 35 m. The TEM data gives detailed information on the lower structure down to a depth of 200 m. The correlation between 1-D and 2-D models shows a consistent result. According to the geological analysis and the inversion results, the fault structure is indicated by the 1-D RMT models of profile 2, however, its type cannot be identified in 1-D model.

The normal fault structure can be clearly seen in the 2-D conductivity models of profile 2 and 5 which is represented by marly silty sand. Measured and calculated data is well fit considering a complex and inhomogeneous geological structure. However, some misfits due to 3-D effects in the research area remain.

The interpretation of the 2-D RMT models from each profile provides results are supporting another. The surface structure of the 2-D RMT model also corresponds to the geological map except at a site within the intersection of RMT profiles 3 and 6 showing different results from the geological map. The 2-D models, however; may give a more accurate result, as the crossing among profiles 3 and 6 is consistent in all models. In this case, the 2-D model can provide an improvement on the existing geological map: the geological formation has previously been considered to be lower terrace deposit and is discovered to be fans. Based on the correlation between all 2-D conductivity models and the geological map, the normal fault structure with strike direction around N70°E in the Northeast of EURO-SEISTEST in the Volvi

Basin is identified.

The results of joint RMT and TEM and sequential TEM inversions give detailed information from the top until the deeper part of the normal fault structure in the northeast of the Volvi Basin. Joint and sequential inversions have proven to be able to replace the information on the shallow depths missing from the TEM data due to a technical problem with Nano TEM data.

The joint inversion of both data sets (RMT and TEM) has given improved resolution on the model parameters, if it is compared with single inversion. On the other side, the comparison of the resistivity distribution between 1-D single, joint and sequential inversions show a comparable result.

The 3-D modeling can provide a representative model of all conductivity structures in the research area. Three dimensional models provide a detail description of the normal fault structure at depths of about 5 to 25 m and thicknesses of 20 m. This is indicated by the phases higher than 45°. Measured data and 3-D response is fitting well.

The investigation of the fault structure carried out with RMT and TEM shows a clear graben structure in the Volvi basin. The combination of RMT and TEM methods has proven to be an effective tool to investigate this fault structure in the Volvi basin.

8.2 Outlook

Even though the study performed in the present thesis shows the existence of a fault structure and gives information on the top of basement, further detailed investigation shall be conducted due to the complex structure of the Volvi basin. Especially investigating the north and the south of the research area in order to know the horizontal continuity of the fault structure. For a detailed horizontal analysis of the fault structure, one may implement shorter spaced stations of RMT and TEM methods.

The vertical continuity of the fault structure could be analyzed by using a bigger transmitter loop with higher current or by using LOTEM methods. The geophysical results of the fault structure in the Volvi basin may be used for future assessment of earthquake in order to minimize the risk of earthquake damages.

Bibliography

Archie, G. E., The electrical resistivity log as an aid in determining some reservoir characteristics, *Petroleum Transactions of AIME*, *146*, 54–62, 1942.

Arsovski, M., Some elements of the arrangement of seismic foci in the Balkan region, *Bull. Inst. Geol. Rep.Soc. Macedonia*, *16*, 261–282, 1978.

Baker, C., D. Hatzfeld, H. Lyon-Caen, E. Papadimitriou and A. Rigo, Earthquake mechanisms of the Adriatic Sea and Western Greece: implications for the oceanic subduction-continental collision transition, *Geophysical Journal International*, *131*, 594–599, 1997.

Bastani, M., A. Savvaidis, L. Pedersen and T. Kalscheuer, CSRMT measurements in the frequency range of 1–250 kHz to map a normal fault in the Volvi basin, Greece, *Journal of Applied Geophysics*, *75*, 180–195, 2011.

Cagniard, L., Basic theory of magnetotelluric method of geophysical prospecting, *Geophysics*, *18*, 605–635, 1953.

Constable, S. C., R. L. Parker and C. G. Constable, Occam's inversion: A practical algorithm for generating smooth models from EM sounding data, *Geophysics*, *52*, 289–300, 1987.

Dennis, Z. R. and J. P. Cull, Transient electromagnetic surveys for the measurement of near-surface electrical anisotropy journal of applied geophysics, *Applied Geophysics*, *76*, 64–73, 2012.

Farag, S., I. K., *Multi-dimensional resistivity models of the shallow coal seams at the the opencast mine 'Garzweiler I' (Northwest of Cologne) inferred from Radiomagnetotelluric, Transient Electromagnetic and Laboratory data*, Dissertation, University of Cologne, 2005.

Farquharson, C. G. and D. W. Oldenburg, A comparison of automatic techniques for estimating the regularization parameter in non-linear inverse problems, *Geophysical Research Letters*, *156*, 411–425, 2004.

Fitterman, D. and W. L. Anderson, Effect of transmitter turn-off time on transient soundings, *Geoexploration*, *24*, 131–146, 1987.

Ghobarah, A., M. Saatcioglu, and I. Nistor, The impact of 26 December 2004 earthquake and tsunami on structures and infrastructure, *Engineering Structures*, *28*, 312–326, 2006.

Gurk, M., A. Savvaidis and M. Bastani, Tufa Deposits in the Mygdonian Basin (Northern Greece) studied with RMT, CSAMT, VLF and Self-Potential, in *Kolloquium Elektromagnetische Tiefenforschung*, 2007.

Hansen, P. C., Analysis of discrete ill-posed problems by means of L-curve, *SIAM Reviews*, *34*, 561–580, 1992.

Hanstein, T., Iterative und parametrisierte Dekonvolution für LOTEM Daten, in *Protokoll über das 14. Kolloquium Elektromagnetische Tiefenforschung*, 163–172, Deutschen Geophysikalischen Gesellschaft, 1992.

Harinarayana, T., Combination of EM and DC measurements for upper crustal studies, *Survey in Geophysics*, *20*, 257–278, 1999.

Helwig, S., Auswertung transient elektromagnetischer Meßdaten aus dem Makhtesh Ramon, Israel unter Benutzung rotationssymmetrischer Modelle, Diplomarbeit, Institut für Geophysik und Meteorologie, Universität zu Köln, 1994.

Helwig, S. L., J. Lange and T. Hanstein, Kombination dekonvolvierter Messkurven zu einem langen Transienten, in *Tagungaband der 63. Jahrestagung*, Deutschen Geophysikalischen Gesellschaft, 2003.

Huang, H., Depth of investigation for small broadband electromagnetic sensors, *Geophysics*, *70 (6)*, G135, 2005.

Hubert-Ferrari, A., A. Barka, E. Jacques, S. Nalbant, B. Meyer, R. Armijo, P. Tapponnier and G. C. P. King, Seismic hazard in the Marmara Sea region following the 17 August 1999 Izmit earthquake, *Nature*, *404*, 269–273, 2001.

Jongmans, D., K. Patilakis, D. Demanet, C. Raptakis, D. Horrent, T. G., K. Lontzetidis and J. Reipl, EURO-SEISTEST: Determination of the geological Stucture of the Volvi Basin and validation of the basin respone, *Bulletin of the Seismological Soceity of America*, *88*, 473 – 487, 1988.

Jupp, D. and K. Vozoff, Stable Iterative Methods for the Inversion of Geophysical Data, *Geophysical Journal of Royal and Astronomical Soceity*, *42*, 957–976, 1975.

Jupp, D. L. B. and K. Vozoff, Resolving anisotropy in layered media by joint inversion, *Geophysichal Prospecting*, *25*, 460–470, 1977.

Kaufman, A. A. and G. V. Keller, *Frequency and transient soundings*, Methods in Geochemistry and Geophysics, 16, Elsevier, 1983.

Koch, O., S. L. Helwig and N. Meqbel, Vertical near surface conductivity-anomaly detected at the Dead-Sea-Transform, in *Elektromagnetische Tiefenforschung, 20. Kolloquium*, Deutschen Geophysikalischen Gesellschaft, 2003.

Koufosa, G., G. Syridesa, D. Kostopoulosa and K. Koliadimoua, Preliminary results about the stratigraphy and the palaeoenvironment of Mygdonia Basin, Macedonia, Greece, *GEOBIOS, First European Palaeontological Congress*, *28*, 243–249, 2005.

Lange, J., *Joint Inversion von Central-Loop-TEM und Long-Offset-TEM Transienten am Beispiel von Messdaten aus Israel 2002*, Dissertation, Institut für Geophysik und Meteorologie, Universität zu Köln, 2003.

Levenberg, K., A method for the solution of certain nonlinear porblems in least squares, *Quarterly of Applied Mathematics*, *2*, 164–168, 1944.

Linde, N. and L. B. Pedersen, Characterization for a fractured using Radiomagnetotelluric (RMT) data, *Geophysics*, *69*, 1155–1165, 2004.

Lines, L. R. and S. Treitel, Tutorial: A review of least-squares inversion and its application to geophysical problems, *Geophysical Prospecting*, *32*, 159, 1984.

Mackie, R. and J. Booker, *Documentation for mtd3fwd and d3 to mt*, Masschutes Institute of Thechnology, Cambridge, Massachusets, July 1999.

Mackie, R. and T. Madden, Three dimensional magnetotelluric inversion using conjugate gradients, *Geophysical Journal International*, *115*, 215–229, 1993.

Mackie, R., J. Smith and T. Madden, Three-dimensional electromagnetic models using finite difference equations: The magnetotelluric example, *RADIO SCIENCE*, *29*, (4), 923–935, 1994.

Mackie, R., S. Rieven and W. L. Rodi, *User manual and software documentation for two-dimensional inversion of magnetotelluric data*, Masschutes Institute of Thechnology, Cambridge, Massachusets, July 1997.

Makris, J., A. Savvaidis and F. Vallianatos, MT data analysis from a survey in the Mygdonia basin (Northern Greece), *Annals of Geophysics*, *45*, N.2, 2002.

Manakou, M., D. Raptakis, F. Chavez-Garcia, P. Apostolidis and K. Pitilakis, 3D soil structure of the Mygdonian basin for site respone analysis, *Soil Dynamics and Earthquake Engineering*, *30*, 1198–1211, 2010.

Marquardt, D., An algorithm for least squares estimation of non-linear parameters, *SIAM Journal of Applied Mathematics*, *11*, 431–441, 1963.

McNeill, J. D., *Use of electromagnetic methods for groundwater studies*, 191–218, Society of Exploration Geophysicists, 1990.

McNeill, J. D. and V. Labson, *Geological mapping using VLF radio fields*, 191–218, Society of Exploration Geophysicists, 1990.

Meju, M. A., Joint inversion of TEM and distorted MT sounding: Some effective practical considerations, *Geophysics*, *61*, 56–65, 1996.

Menke, W., *Geophysical data analysis: Discrete inverse theory*, Academic Press Inc., Orlando, Florida, 1984.

Mercier, J., E. Carey-Gailhardis, N. Mouyaris, K. Simeakis, T. Roundoyannis and C. Anghelidhis, Structural analysis of recent and active faults and regional state of stress in the epicentral area of the 1978 Thessaloniki earthquakes (Northern Greece), *Tectonics*, *2*, 577 – 600, 1983.

Microkor and St. Petersburg University, *RMT-F1 and SM25 user manual*, Microkor and St. Petersburg University, 2005.

Mollidor, L., Central-Loop-TEM auf dem Holzmaar, Eifel, Diplomarbeit, Institut für Geophysik und Meteorologie, Universität zu Köln, 2008.

Mosegaard, K. and A. Tarantola, Monte Carlo sampling of solutions to inverse problem, *Journal of Geophyscal Research*, *100 no. B7*, 12,431–12,447, 1995.

Nabighian, M. N., Quasi-static transient response of a conducting half-space an approximate representation, *Geophysics*, *44*, (10), 1700–1705, 1979.

Newman, G. A., G. W. Hohmann and W. L. Anderson, Transient electromagnetic response of a three-dimensional body in a layered earth, *Geophysical Journal International*, *51*, (8), 1608–1627, 1986.

Newman, G., S. Recher, B. Tezkan and M. Neubauer, 3-D inversion of a scalar Radiomagnetotelluric field data set, *Geophysics*, *68*, 791–802, 2003.

Palacky, G. J., Resistivity characteristics of geologic targets, in *Electromagnetic Methods in Applied Geophysics*, Bd. 1, 106–121, Society of Exploration Geophysicists, 1988.

Papazachos, B. and C. Papazachou, The earthquake of Greece, Ziti Publications, Thessalonikhi, 1997.

Papazachos, B., D. Mountrakis, A. Psilovikos and G. Leventakis, Surface fault traces and fault plane solutions on the May-June 1978 major shocks in the Thessalonikhi area, Greece, *Tectonicphysics*, *53*, 171–183, 1979.

Papen, M. V., Spatial Constrained Inversion von In-Loop TEM Daten zur Bestimmung der Grundwasserkontamination in Roorkee, Indien, Diplomarbeit, Universität zu Köln Institut für Geophysik und Meteorologie, 2011.

Pavlides, S., D. Mountrakis, A. Kilias and M. Tranos, The role of strike-slip movements in the extensional area of the Northern Aegean (Greece), *Annales Tectonicae*, *4*, 196–211, 1990.

Pedersen, L. B., M. Bastani and L. Dynesius, Groundwater exploration using combined Controlled-Source and Radiomagnetotelluric, *Geophysics*, *70*, G8–G15, 2005.

Pellerin, L. and P. E. Wannamaker, Multi-dimensional electromagnetic modeling and inversion with application to near-surface earth investigations, *Computers and electronics in agriculture*, *46*, 71–102, 2005.

Persson, L. and L. B. Pedersen, The importance of displacement currents in RMT measurements in high resistivity environments, *Journal of Applied Geophysics*, *51*, (1), 11 – 20, 2002.

Psilovikos, A., Geomorphologichal ans structural modification of the serbomecadonian massif during the neotectonic stage, *Tectonicphysics*, *110*, 27–45, 1984.

Raiche, A., D. Jupp and H. Rutter, The joint use of coincident loop transient electromagnetic and schlumberger sounding to resolve layered structures, *Geophysics*, *50*, 1618–1627, 1985.

Raptakis, D. D., F. Chavez-Garcia, M. K. and P. K., Site effect at Eurositetest – I. Determination of the valley structure and confrontation of observations with 1D analysis, *Soil dynamic and earthquake Engineering*, *19*, 1 –22, 2002.

Rodi, W. and R. L. Mackie, Nonlinear conjugate gradients algorithm for 2-D magnetotelluric inversion, *Geophysics*, *66*, (1), 174–187, 2001.

Sambridge, M. and K. Mosegaard, Monte Carlo in Geophysical Inverse Problem, *Review of Geophysichs*, *40,3*, 2002.

Savvaidis, A., L. B. Pedersen, G. Tsokas and D. G.J., Structure of the Mygdonian Basin (N.Greece) inferred from MT and gravity data, *Tectonicphysics*, *317*, 171–186, 2000.

Scholl, C., Die periodizität von sendesignalen bei Long-Offset Transient electromagnetics, Diplomarbeit, Institut für Geophysik und Meteorologie, Universität zu Köln, 2001.

Scholl, C., *The influence of multidimensional structures on the interpretation of LOTEM data with one-dimensional models and the application to data from Israel*, Dissertation, Institut für Geophysik und Meteorologie, Universität zu Köln, 2005.

Schwinn, W., 1D Joint Inversion Radiomagnetotellurik (RMT) und Transientelektromagnetik Daten (TEM):eine Anwendung zur Grundwasser exploration in Grundfor, Danemark, Diplomarbeit, 1999.

Semblat, J., M. Kham, E. Parara, P. Bard, K. Pitilakis, K. Makra and D. Raptakis, Seismic wave amplification: Basin geometry vs soil layering, *Soil Dynamics and Earthquake Engineering*, *25*, 529–538, 2005.

Shaw, B. and J. Jackson, Earthquake mechanisms and active tectonics of the Hellenic subduction zone, *Geophysical Journal International*, *181*, 966–984, 2010.

Simpson, F. and K. Bahr, *Practical Magnetotellurics*, Cambridge University Press, 1997.

Sims, W., F. Bostik and H. Smith, The estimation of magnetotelluric impedance tensor elements from measure data, *Geophysics*, *36*, 938, 1971.

Soufleris, C. and G. Stewart, A source study of the Thessaloniki (Northern Greece) 1978 earthquake sequence, *Geophysical Journal of the Royal Astronomical Society*, *67*, 343–358, 1981.

Spies, B. R., Depth of investigation in electromagnetic sounding methods, *Geophysics*, *54*, 872–888, 1989.

Spies, B. R. and F. C. Frischknecht, Electromagnetic Sounding, in *Electromagnetic methods in applied geophysics*, Society of Exploration Geophysicists, 1991.

Steuer, A., Kombinierte Auswertung von Messungen mit Transientelektromagnetik und Radiomagnetotellurik zur Grundwassererkundung im Becken von Ouarzazate (Marokko), Diplomarbeit, 2002.

Stiefelhagen, W. and I. Müller, Radio Frequency Electromagnetics (RF-EM)—extended VLF applied to hydrogeology., in *Extended Abstracts, 59th European Association of Exploration Geophysicists Conference and Technical Exhibition*, F–46., 1997.

Strack, K. M., *Exploration with deep transient electromagnetics*, Methods in Geochemistry and Geophysics, Elsevier, Amsterdam, 1992.

Sudha, K., *Near-surface studies using geoelectrical and EM techniques in Northern India*, Dissertation, Indian Institute of Techonology Roorkee, 2010.

Swift, C.M., J., *A magnetotelluric investigation of an electrical conductivity anomaly in the shoutwestern United States*, Dissertation, Mass. Inst. Tech., 1967.

Sørensen, K. I., E. Auken, N. B. Christensen and L. Pellerin, *An Integrated Approach for Hydrogeophysical Investigations: New Technologies and a Case History*, chapter 21, Vol II, Near-surface Geophysics, 2004.

Takahashi, T., M. Goto, H. Yoshida, H. Sumino and H. Matsui, Infectious Diseases after the 2011 Great East Japan Earthquake, *Journal of Experimental & Clinical Medicine*, *4*, 20–23, 2012.

Tezkan, B., A review of environmental applications of quasi-stationary electromagnetic techniques, *Surveys in Geophysics*, *20*, 279–308, 1999.

Tezkan, B., *Radiomagnetotellurics, in Groundwater Geophysics, A Tool for Hydrogeology*, 295–316, Springer-Verlag, 2009.

Tezkan, B. and A. Saraev, A new broadband radiomagentotellurics instruments: application to near surface investigations, *Near Suface Geophysics*, *6(4)*, 245, 2008.

Tezkan, B., M. Goldman, S. Greinwald, A. Hördt, I. Müller, F. Neubauer and G. Zacher, A joint application of Radiomagentotellurics and Transient electromagnetics to the investigation of waste deposit in Cologne (Germany), *Journal of Applied Geophysics*, *34*, 199–212, 1996.

Tezkan, B., A. Hördt and M. Gobashy, Two dimensional Radiomagnetotelluric investigation of industrial and domestic waste, *Journal of Applied Geophysics*, *44*, 237–256, 2000.

Thanassoulas, C., *Geophysical study of the Mygdonian basin and the surrounding area*, Dissertation, University of Thessaloniki, 1983.

Thanassoulas, C., G. Tselentis and G. Traganos, A preliminary resistivity investigation (VES) of the Lagada hot springs area in the Northern Greece, *Gheothermics*, *16*, 227–238, 1987.

Tikhonov, A. N., On determining electrical characteristics of the deep layers of the Earth's crust, *Dokl. Akad. Nauk SSSR*, *73*, 295, 1950.

Ting, S. and G. Hohmann, Integral equation modeling of three-dimensional magnetotelluric response, *Geophysics*, *46*, 182–197, 1981.

Tranos, D., E. Papadimitriou and A. Kilias, Thessaloniki-Gerakarou Fault Zone (TGFZ): the western extension of the 1978 Thessaloniki earthquake fault (Northern Greece) and seismic hazard assessment, *Tectonic*, *25*, 2109–2123, 2003.

Turberg, P., I. Müller and F. Flury, Hydrogeological investigation of porous environments by Radiomagnetotelluric resistivity, *Journal of Applied Geophysics*, *31*, 133–143, 1994.

Usgs.gov, Earthquake Glossary - graben, http://earthquake.usgs.gov/learn/glossary, December 2011.

Vozoff, K., *The Magnetotelluric Method*, Society of Exploratino Geophysicists, Centre for Geophysichal Exploration Research, Macquarie University Sydney, N.S.W. 2109 Australia, 1987.

Vozoff, K. and D. L. B. Jupp, Joint inversion of Geophysical data, *Journal of Royal and Astronomical Society*, *42*, 977–991, 1975.

Wannamaker, P., , G. Hohmann and S. Ward, Magnetotelluric responses of three-dimensional bodies in layered earths, *Geophysics*, *49*, 1571–1533, 1984.

Ward, S. H. and G. W. Hohmann, *Electromagnetic theory for geophysical applications*, Society of Exploration Geophysicists, 1988.

Weiss, C. and G. Newman, Electromagnetic induction in a fully 3-D anisotropic earth, *Geophysics*, *67*, 1104–1114, 2002.

Wiebe, H., 1D-Joint-Inversion von Geoelektrik und Radiomagnetotellurik, Diplomarbeit, 2007.

Zacher, G., B. Tezkan, F. M. Neubauer, A. Hordt and I. Muller, Radiomagnetotellurics, a powerful tool for waste site exploration, *Journal of Environmental and Engineering Gophysics*, *1*, 139–160, 1996.

Zhdanov, M., *Geophysical inverse Theory and regularization problem*, Elseiver, 2002.

Zonge Engineering and Research Organisation Inc., *Zonge NT-20 Multi-purpose TEM Transmitter Instruction Manual*, Zonge Engineering and Research Organisation Inc., 3322 East Fort Lowell Road, Tucson, AZ 85716 USA, 2001.

Appendix A

1-D Conductivity Models of RMT Data

The 1-D conductivity models of RMT data on profile 1, profile 2 and profile 3

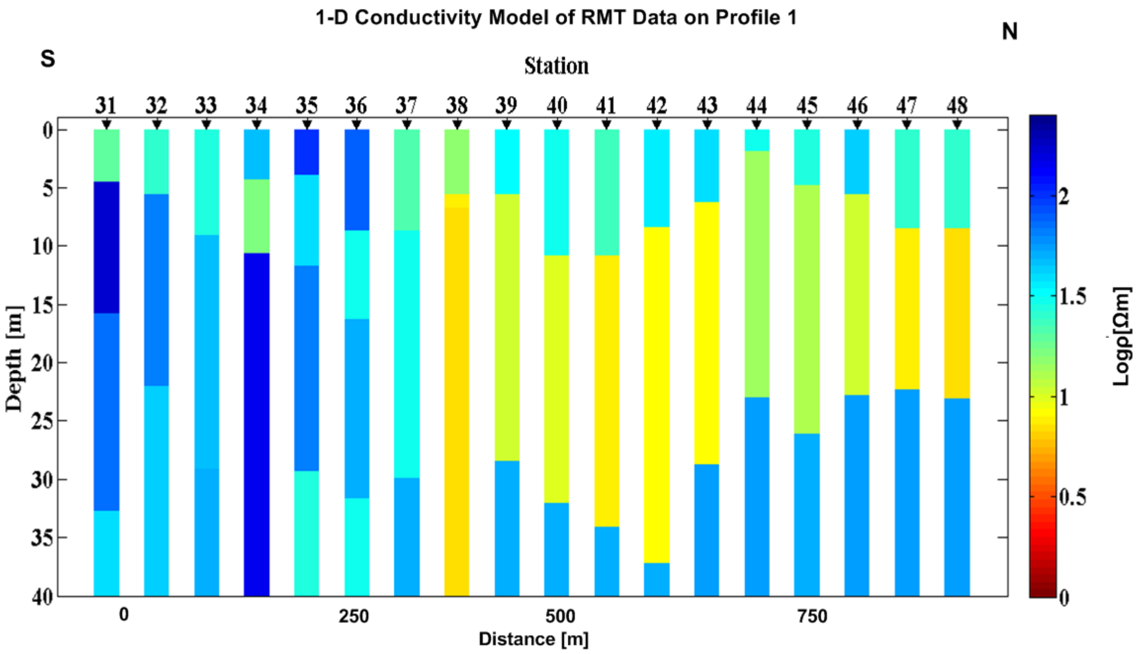

Figure A.1: *1-D conductivity model of RMT data on profile 1.*

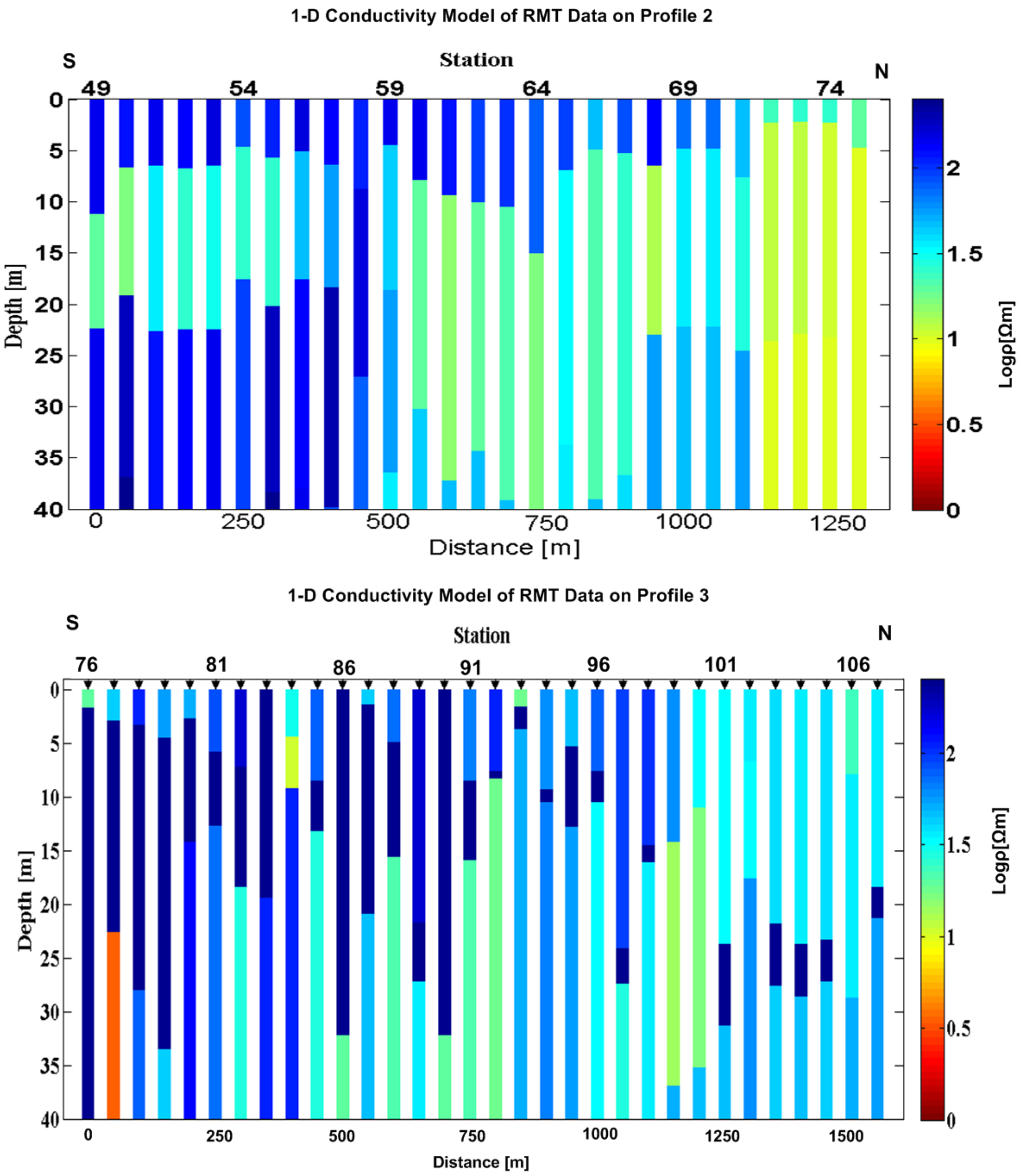

Figure A.2: *1-D conductivity model of RMT data on profile 2 (top) and profile 3 (bottom).*

Appendix B

1-D Conductivity Models of TEM Data

The 1-D conductivity models of TEM data on profiles 1, profile 2 and profile 3

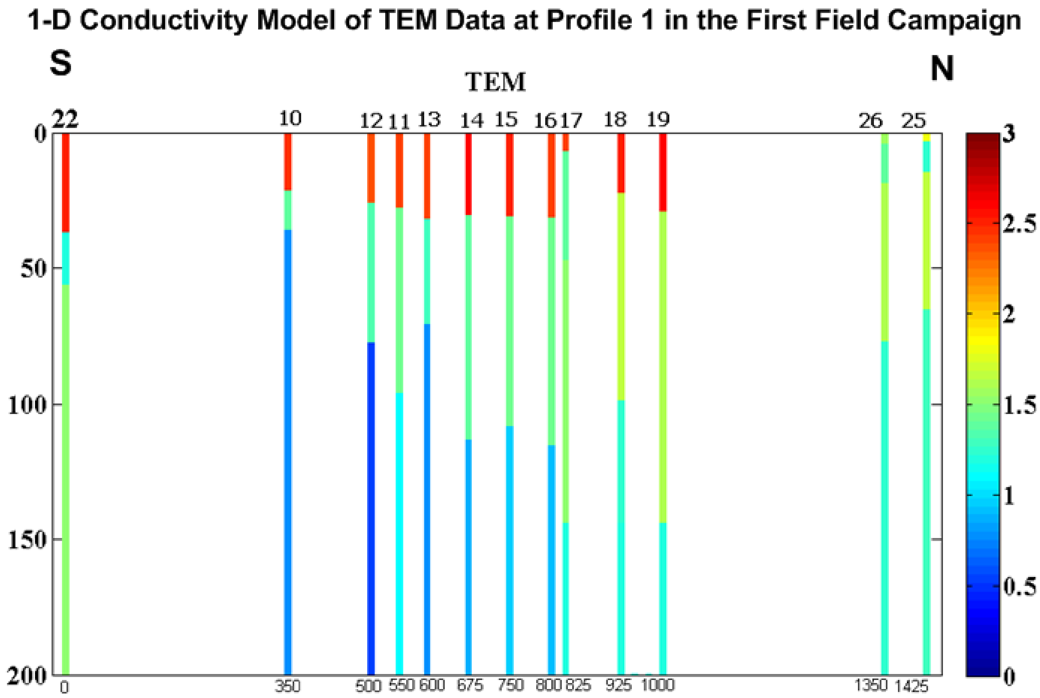

Figure B.1: *1-D conductivity model of TEM data on profile 1 in the first field campaign.*

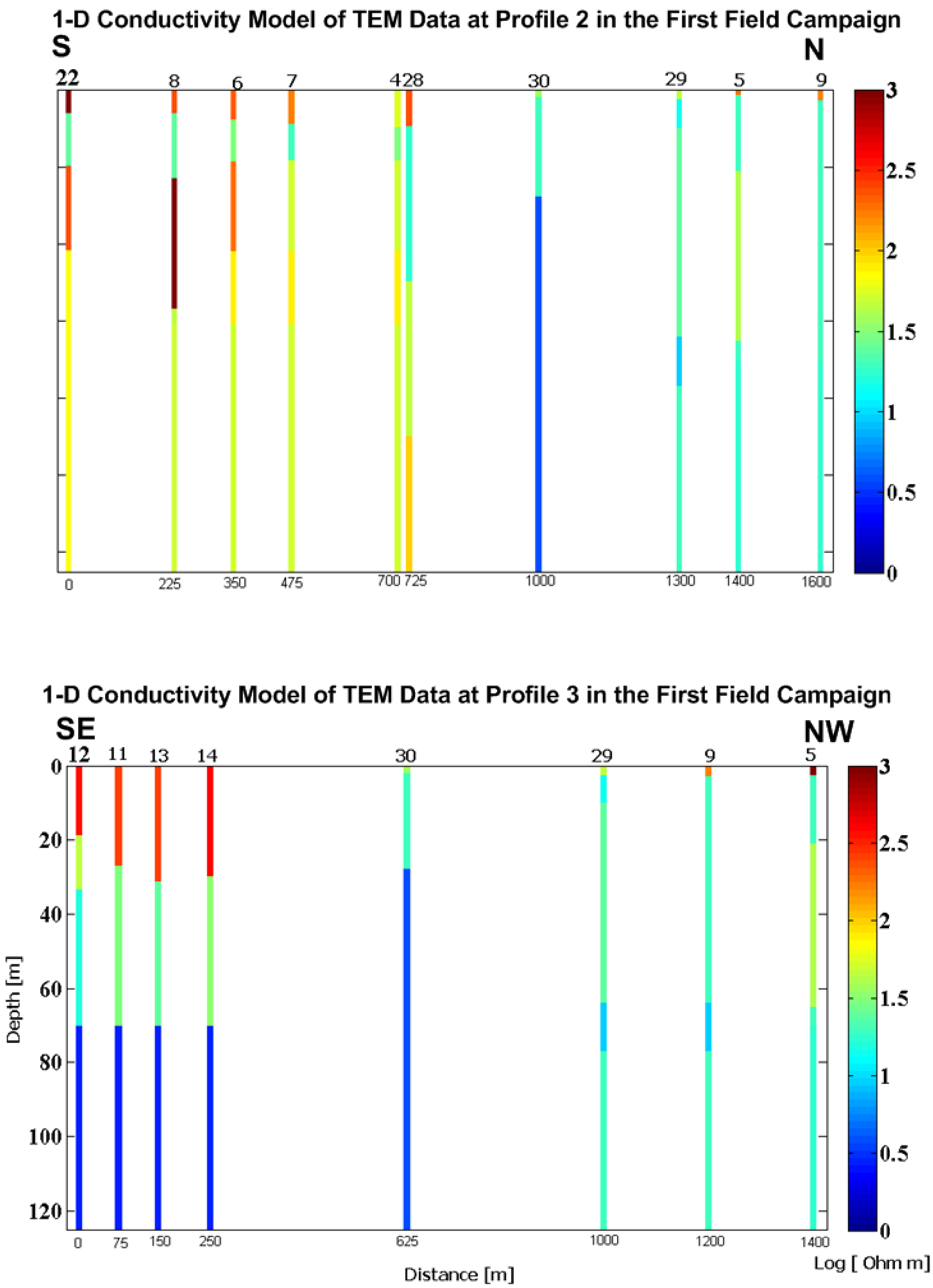

Figure B.2: *1-D conductivity model of TEM data in the first field campaign.*

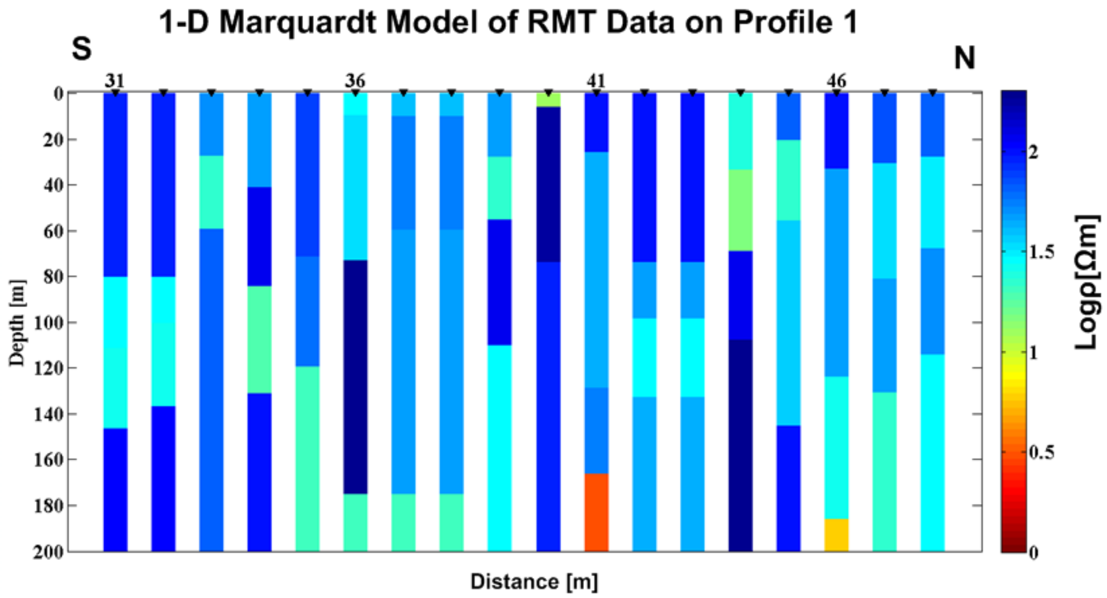

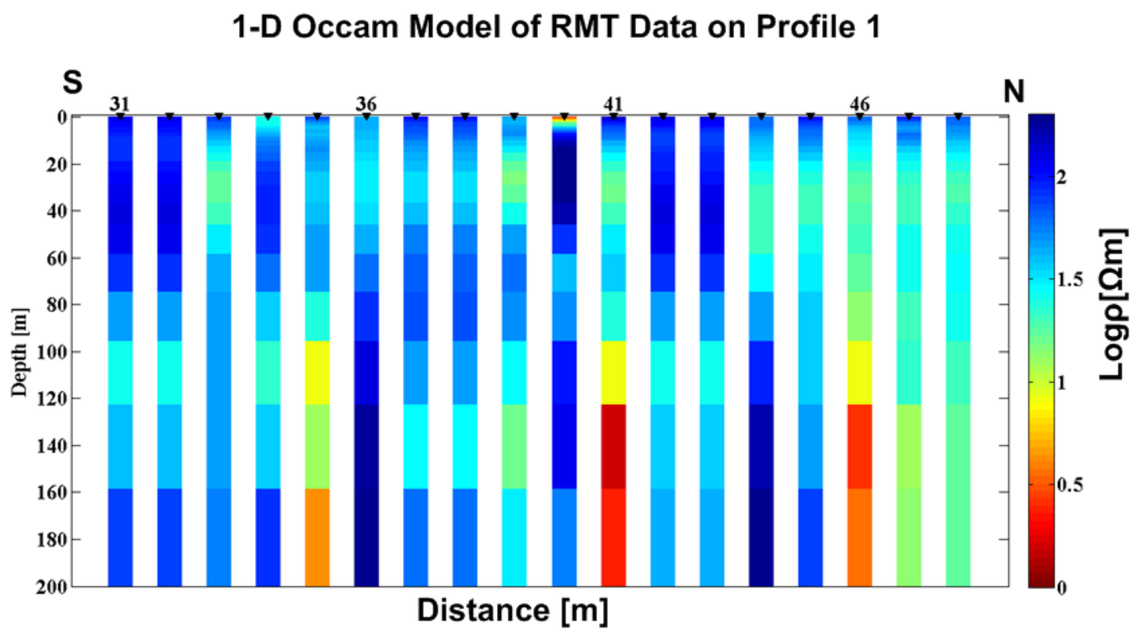

Figure B.3: *(a) 1-D Marquardt model of TEM data on profile 1. (b) 1-D Occam's model of TEM data on profile 1.*

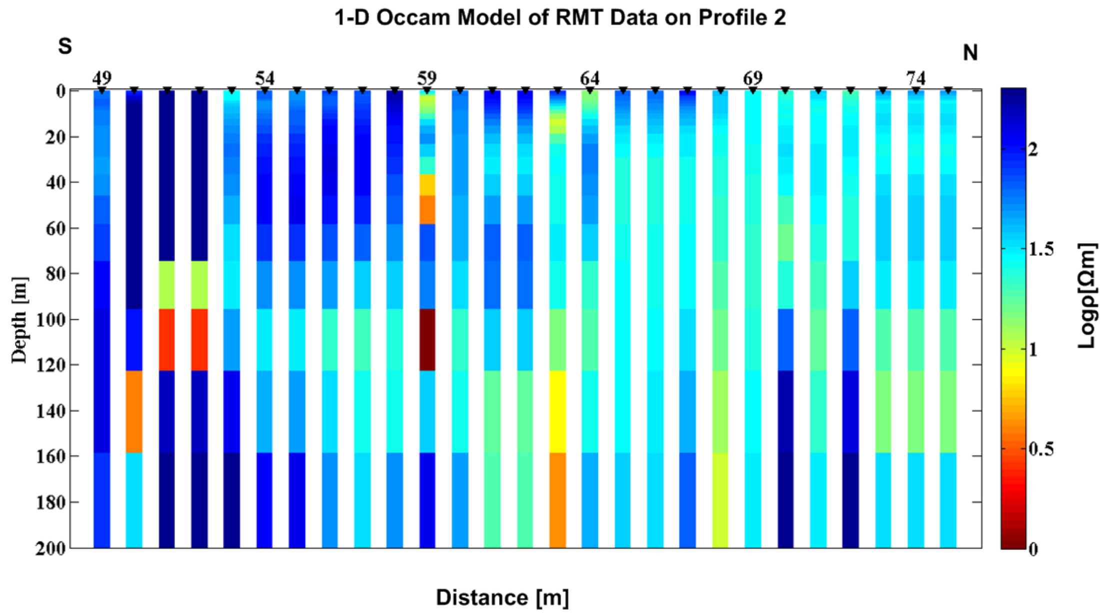

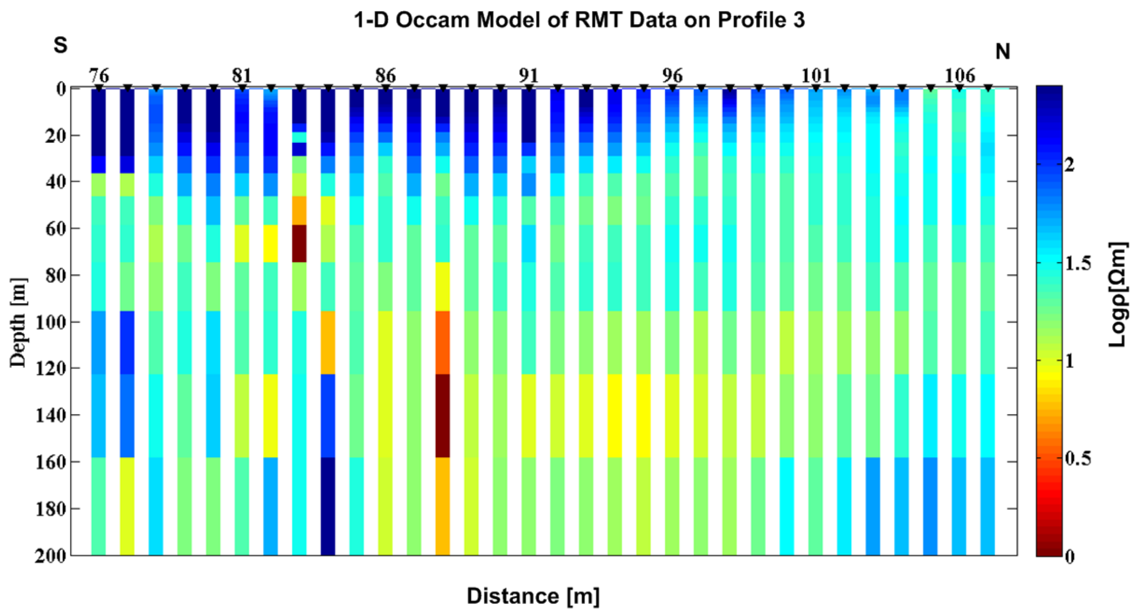

Figure B.4: *(a) 1-D Occam's model of TEM data on profile 2. (b) 1-D Occam's model of TEM data on profile 3.*

Appendix C

1-D Conductivity Models of Sequential Inversion

The 1-D conductivity models of sequential inversion for four different approaches on profile 1 and profile 3

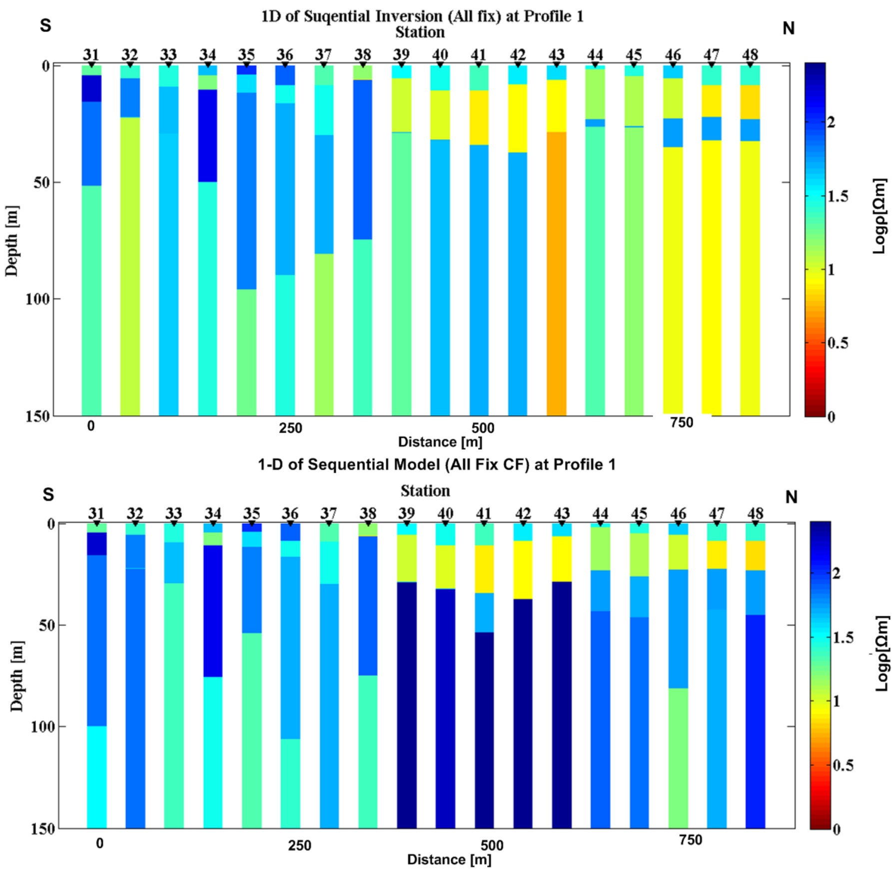

Figure C.1: *1-D conductivity models of sequential inversion of All fix (top) and All fix CF (bottom) at profile 1.*

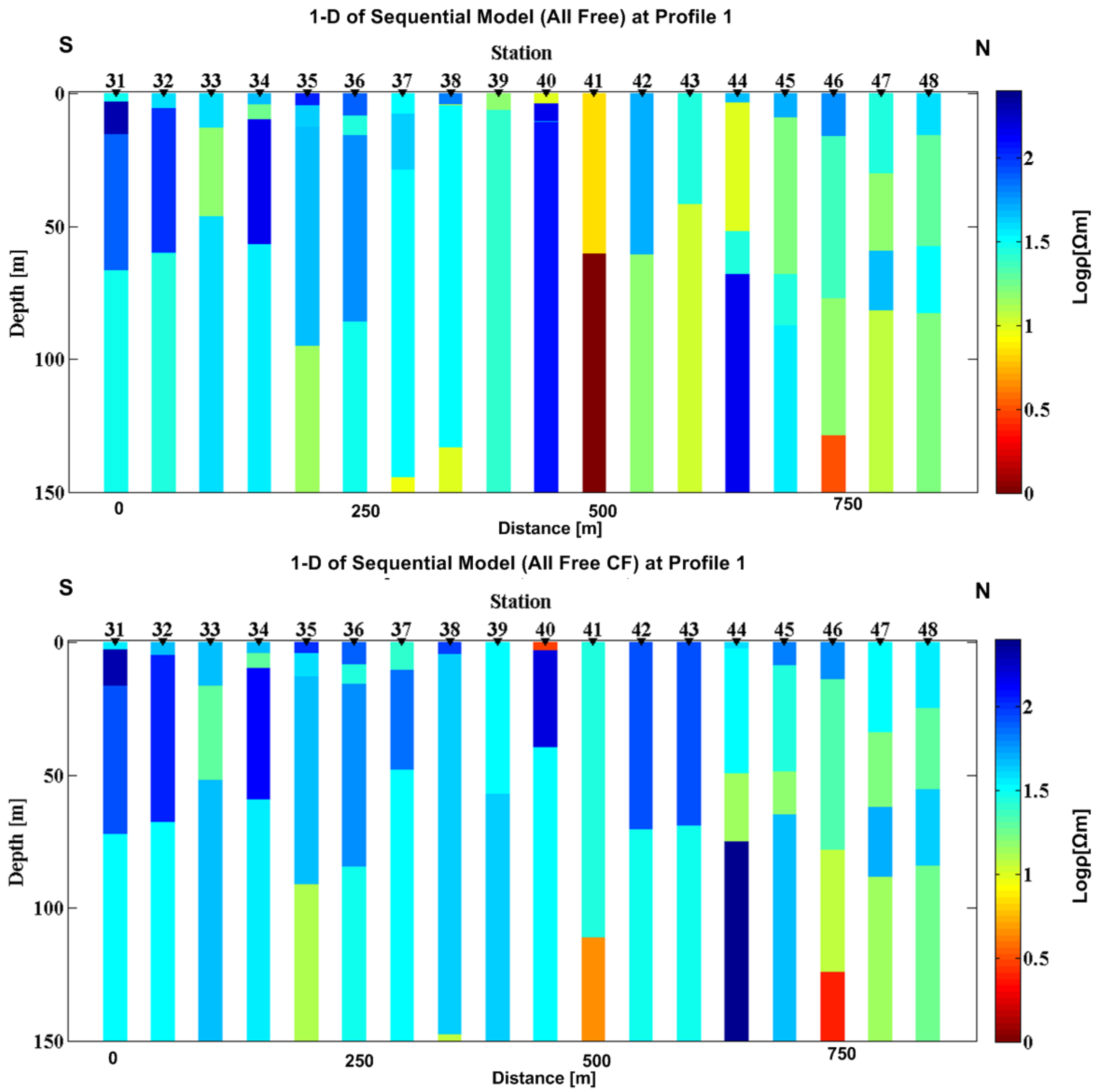

Figure C.2: *1-D conductivity models of sequential inversion of All free (top) and All free CF (bottom) at profile 1.*

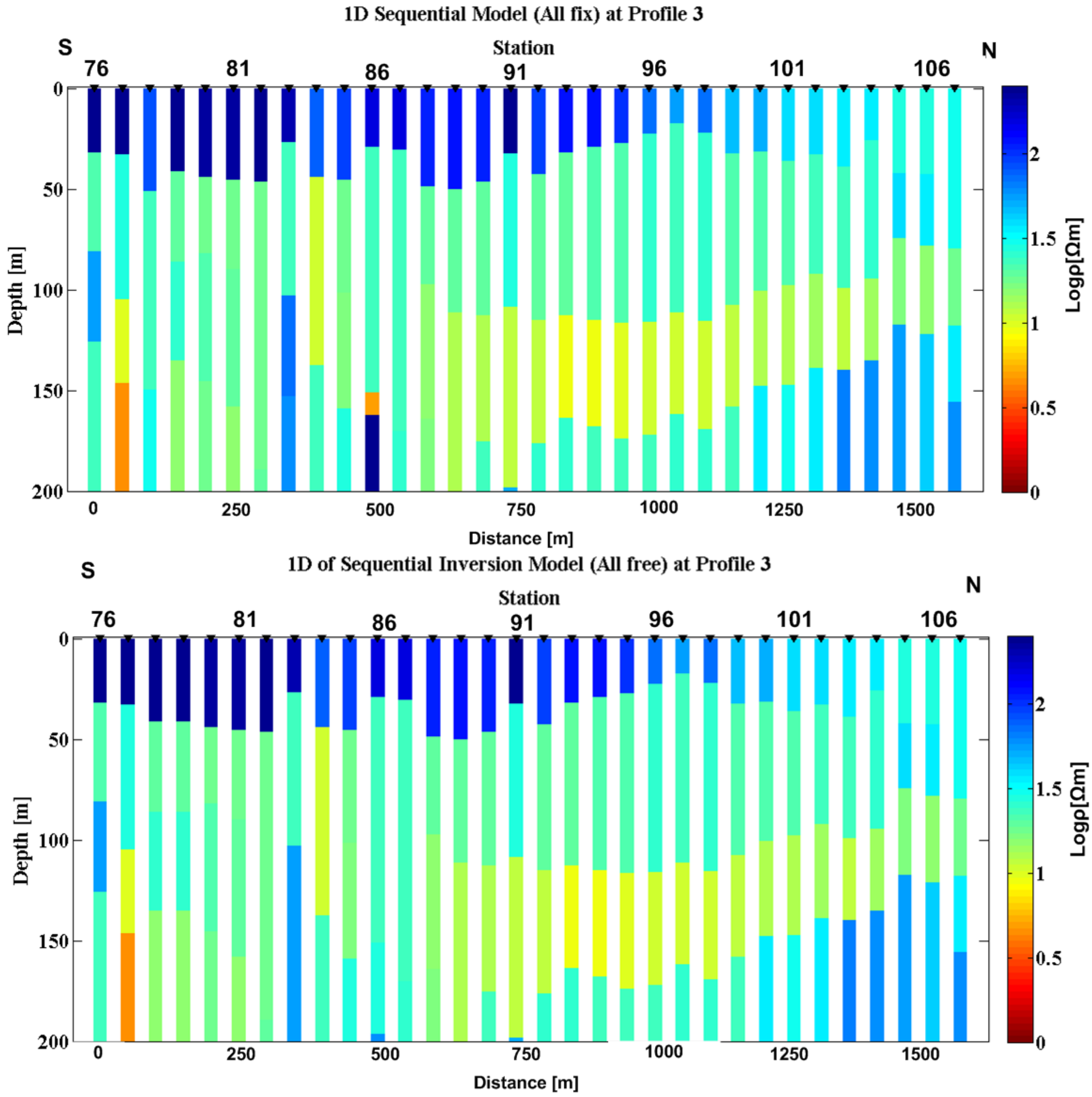

Figure C.3: *1-D conductivity models of sequential inversion of All fix (top) and All fix CF (bottom) at profile 3.*

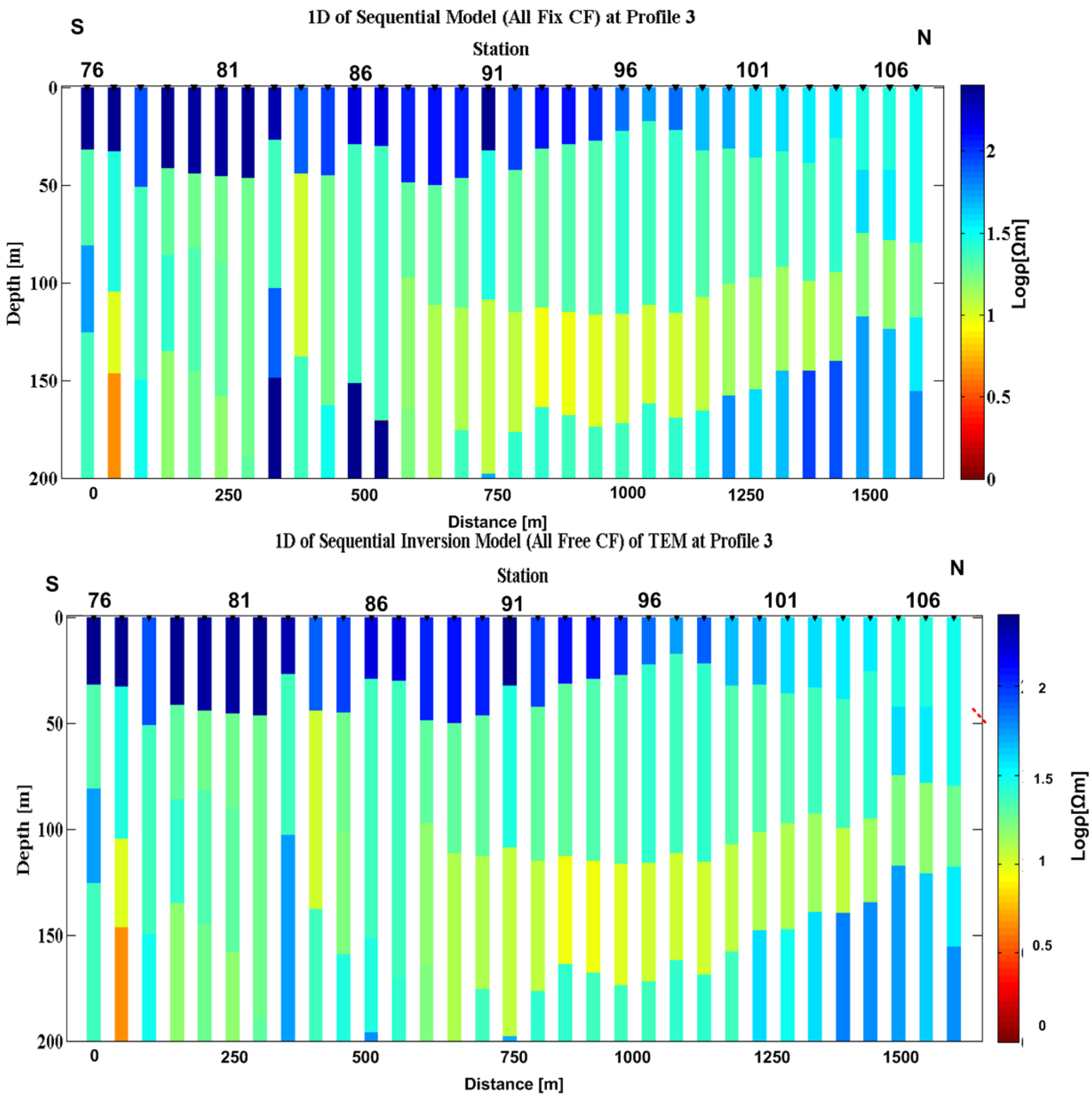

Figure C.4: *1-D conductivity models of sequential inversion of All free (top) and All free CF (bottom) at profile 3*

Appendix D

1-D Interpolation of Sequential Models

The 1-D interpolation of sequential models at profiles 1, 2 and profile 3.

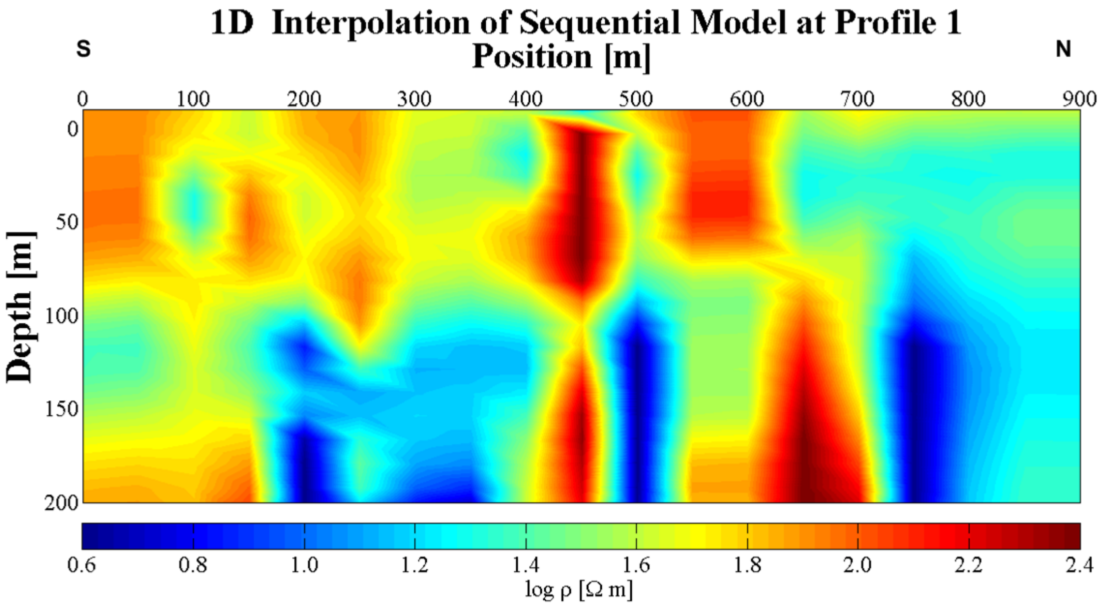

Figure D.1: *1-D interpolation of sequential model at profile 1.*

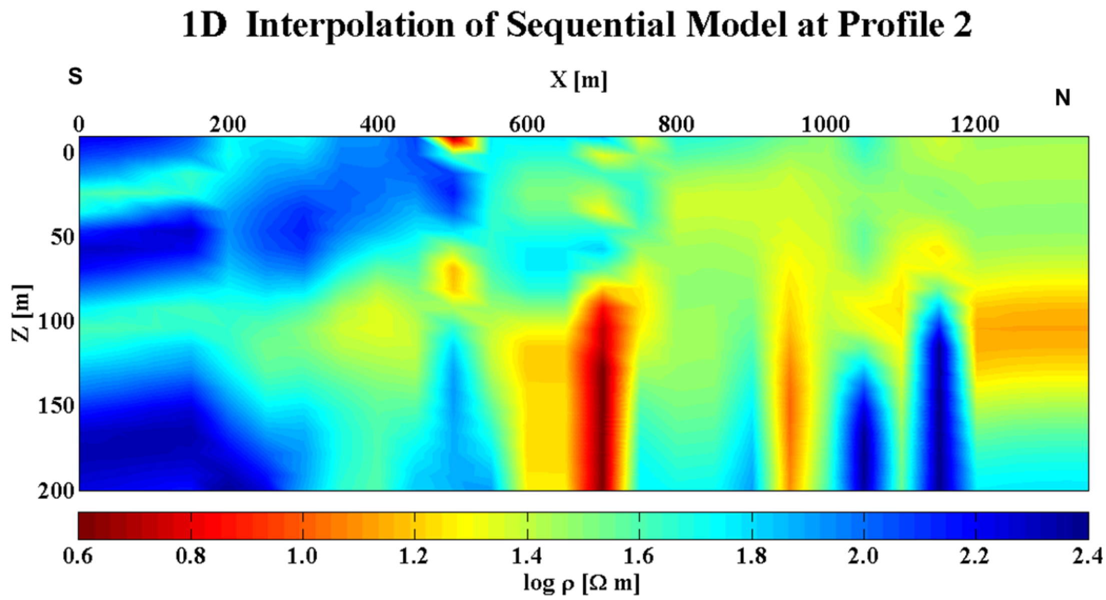

Figure D.2: *1-D interpolation of sequential model at profile 2.*

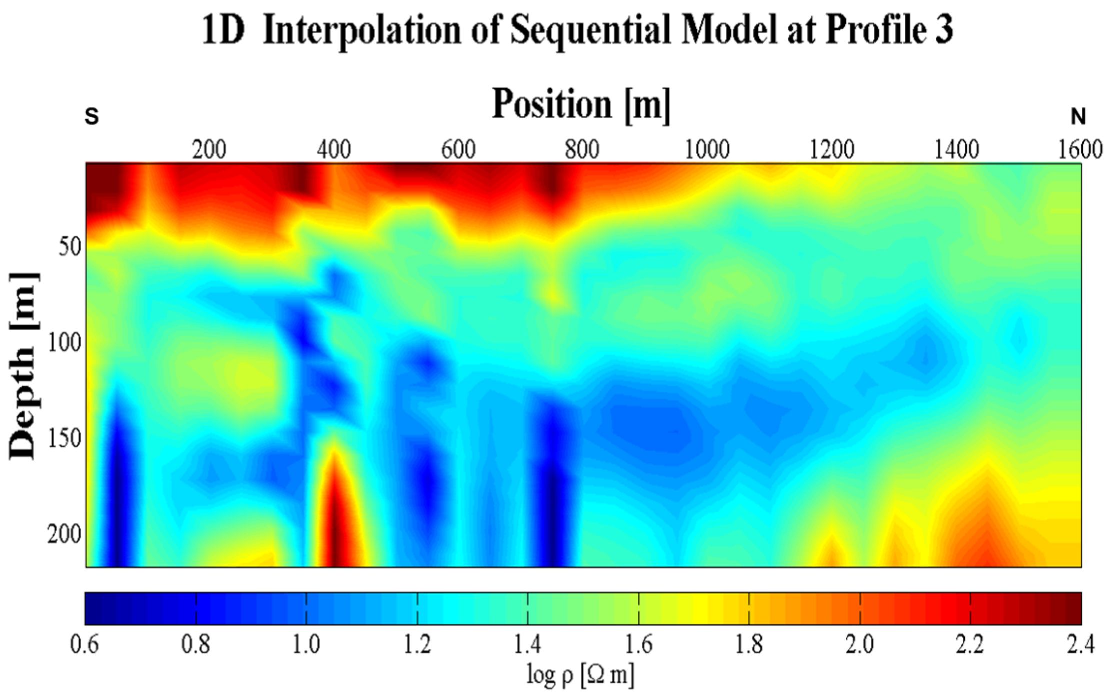

Figure D.3: *1-D interpolation of sequential model at profile 3.*

Appendix E

1-D Conductivity Models of Joint RMT and TEM Inversion

The 1-D conductivity models of joint RMT and TEM inversion at profile 1 and profile 3.

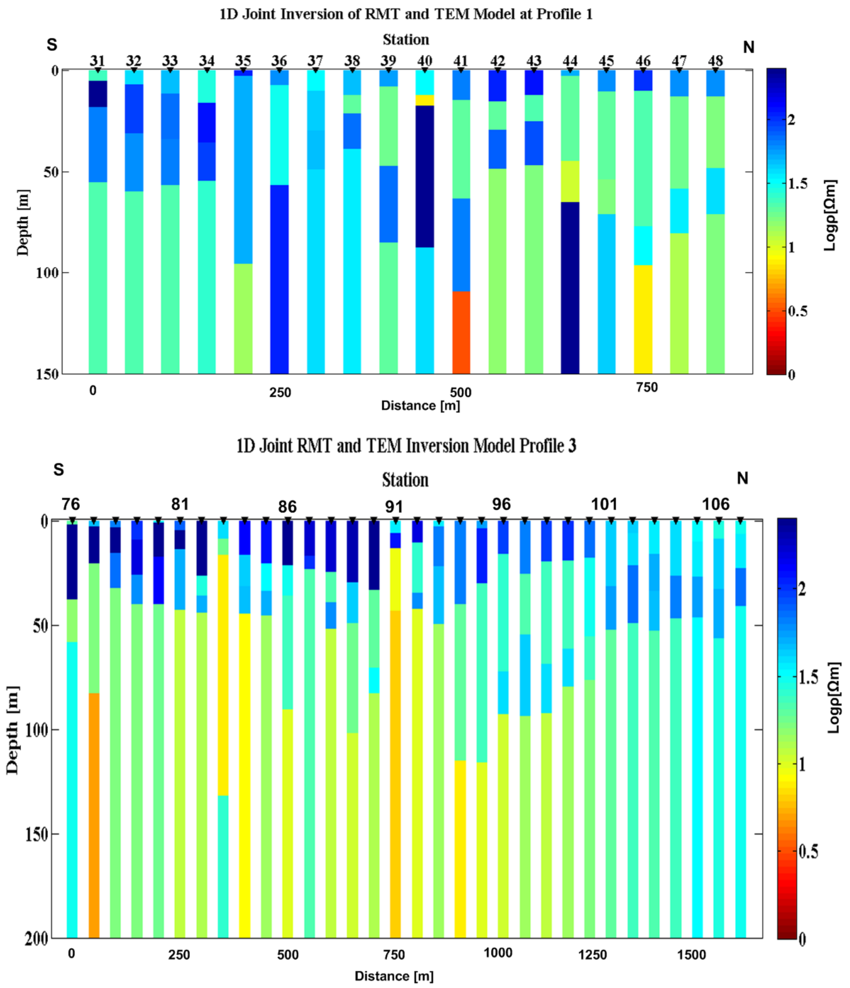

Figure E.1: *1-D conductivity model of joint RMT and TEM inversion at profiles 1 and 3.*

Appendix F

2-D Conductivity Models of RMT

The 2-D conductivity models of RMT on profile 7 and profile 8.

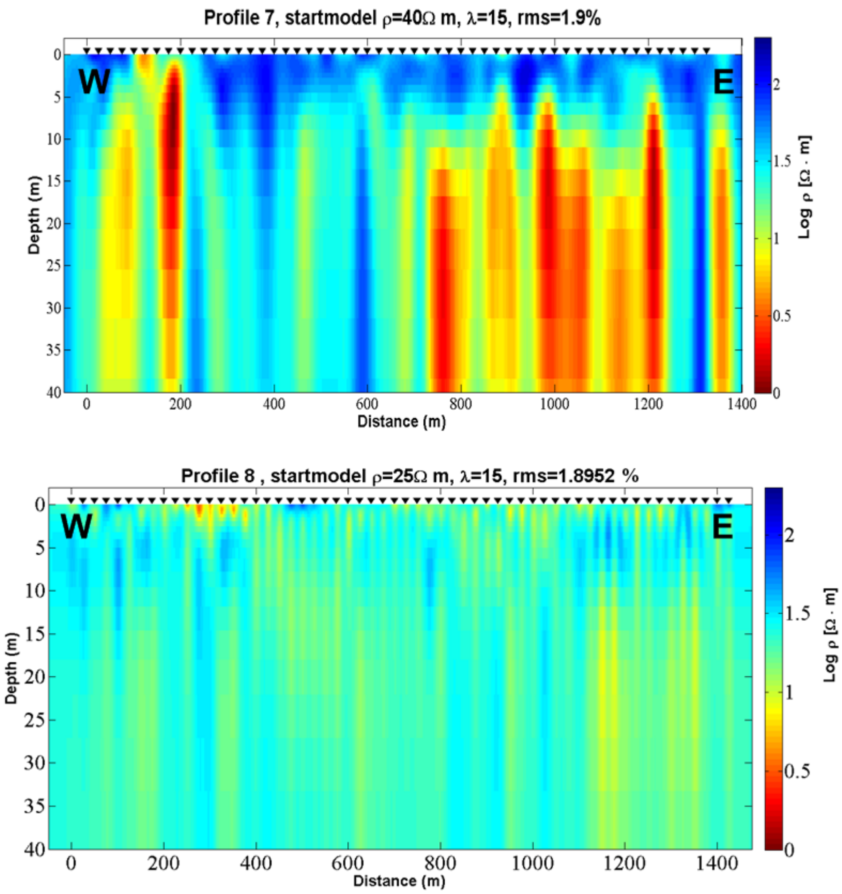

Figure F.1: *2-D conductivity models of RMT on profile 7 (top) and profile 8 (bottom).*

Appendix G

3-D Mesh Grid

The 3-D is performed with Mtd3fwd and D3 to MT. A manual for these can be found in [*Mackie and Booker*, 1999]. In this software, there are several possibilities can be changed by the user.

1. The boundary condition at the bottom is optionally using the impedance of a 1-D halfspace with the local resistivity at the base of the 3-D model. Using the 1-D impedance of a separate 1-D model is also allowed.

2. The 3-D input model can use a resistivity map (with "codes" from 1 to 99, plus 0 for air and -1 for sea water values).

3. The dimensions of the grids are set in a file dimens.h and they can be changed according to the model size before compilation.

Input file
There are four input files for running the program, with the following content: 3-D grid cells, periods, origin and 1-D background model file.
1. Period file:
NPER (number of period)
period, period
2. Background 1-D model file:
Nlayers (number of layers)
thickness (meters) resistivity (1st layer)
......
Dummy value (ignored) resistivity (last layer)
3. Origin file:
This file is used to compute the origin (x=0., y=0.) for the response position coordinatess. This file has alternate forms:
x0 = real number
y0 = real number
where x0 and y0 are the offsets in meters of the origin with the respect to the UPPER LEFT CORNER of the model.
x0 = interger (or interger .5)
y0 = interger (or interger .5)
where ix0 and iy0 are the indices of the block whose CENTER is used as the origin.

4. 3-D grid cells file:
In the following, optional info in () brackets indicates the commentary.
220 220 30 **(NX, NY, NZ)**
(X block sizes)
564.8 462.41 378.59 309.96 253.78 207.77 170.11 139.27 114.03 93.36 76.43 62.58 51.23 41.94 34.34 28.11 23.02 18.84 15.43 12.63 10.34 8.46 6.93 5.67 4.64 3.8 3.11 2.55 2.08 1.7 1.4 1.7 2.08 2.55 3.11 3.8 4.64 5.67 6.93 8.46 10.34 12.63 15.43 18.84 23.02 28.11 34.34 41.94 51.23 62.58 76.43 93.36 114.03 139.27 170.11 207.77 253.78 309.96 378.59 462.41 564.8

(Y block sizes)
564.8 462.41 378.59 309.96 253.78 207.77 170.11 139.27 114.03 93.36 76.43 62.58 51.23 41.94 34.34 28.11 23.02 18.84 15.43 12.63 10.34 8.46 6.93 5.67 4.64 3.8 3.11 2.55 2.08 1.7 1.4 1.7 2.08 2.55 3.11 3.8 4.64 5.67 6.93 8.46 10.34 12.63 15.43 18.84 23.02 28.11 34.34 41.94 51.23 62.58 76.43 93.36 114.03 139.27 170.11 207.77 253.78 309.96 378.59 462.41 564.8

(Z block sizes)
0.07 0.09 0.11 0.14 0.17 0.21 0.26 0.32 0.39 0.48 0.58 0.71 0.87 1.07 1.3 1.59 1.95 2.38 2.91 3.55 4.34 5.3 6.47 7.91 9.66 11.8 14.41 17.6 21.5 26.26
1 **(NZ (number of layer = first layer))**
1 1 1 1 1 1 1 1 1 1 1 1 1 1 1 1 1 1 1 1 1 1 1 1 1 1 1 1 1 . . . . 1**(nX=220)**
. . . .
2**(nY=220)** 2 2 2 2 2 2 2 2 2 2 2 2 2 2 2 2 2 2 2 2 2 2 2 2 2 . . . . 2**(nX=220)**
.
.
30 **(NZ (number of layer = 30))**
3 3 3 3 3 3 3 3 3 3 3 3 3 3 4 4 4 4 4 4 4 4 4 4 4 4 4 4 4 . . . . 4**(nX=220)**
. . . .
3**(nY=220)** 3 3 3 3 3 3 3 3 3 3 3 3 3 3 3 3 3 3 3 3 3 3 3 3 3 . . . . 3**(nX=220)**
0. 50. 100. 1000. 10. **(0. resistivity for air, 50. resistivity for code 1, 100. resistivity for code 2, 1000. resistivity for code 3, 10. resistivity for code 4)**.

Running the Program

Here, an example script to run 3-D Mtd3fwd, D3 to MT and rephind is shown:
To run the 3D forward code

```
!/bin/bash
\prisma3d220.rslt
./d3fwd ≪ EOF
prism3d220
periods
homogen3d220floor
1e^-4
100
EOF
```

The input file for D3 to MT:

```
\rm prisma3d220.mt
\rm prisma3d220.imp
./d3tomt ≪ EOF
prisma3d220
2
0
EOF
mkdir result
mv *.mt result
mv *.imp result
```

In order to justify the impedance due to certain coordinates in the grid cells, we can use the program rephind. The following is an input file for rephind:

```
./rephind ≪ EOF
all3d220
110
110 1
1
110 2
2
110 3
.
.
110
110 110
EOF
mkdir profile rephind
mv *.moddat profile rephind
```

Appendix H

3-D Modeling and Responses

The model consists of two adjacent rectangular blocks located in a three-layer host (Figure. H.1). Resistivity of one block is 100 Ωm and the adjacent block is more conductive by 1 Ωm (Figure. H.1b). The conductivity of rectangular blocks are 10 Ωm and those blocks have a dimension of 400 m width, 2400 m length and 5 m depth (Figure. H.1c). The cross section view shows the second layer of 100 Ωm with thickness lower than 20 m between the first layer and the third layer by a half space of resistivity 0.1 Ωm.

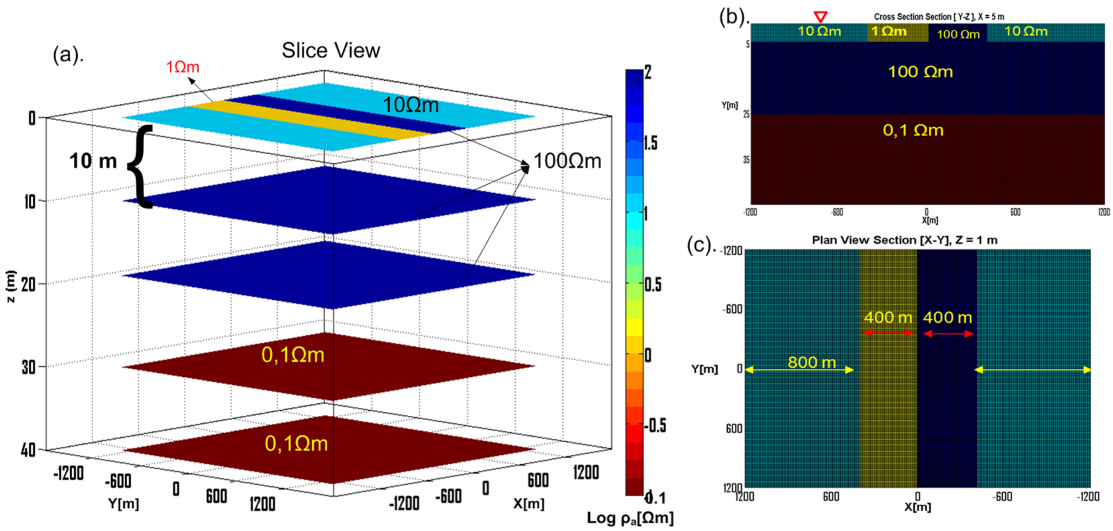

Figure H.1: *Three dimensional modeling (a). Slice view of 2-D model (b). Plan view of 2-D model.*

Figures H.2a and H.2b shows the Z_{xy} and Z_{yx} responses along the profile layer media across the center of body (X-direction in Figure H.1) at frequency of $f = 11$ kHz.

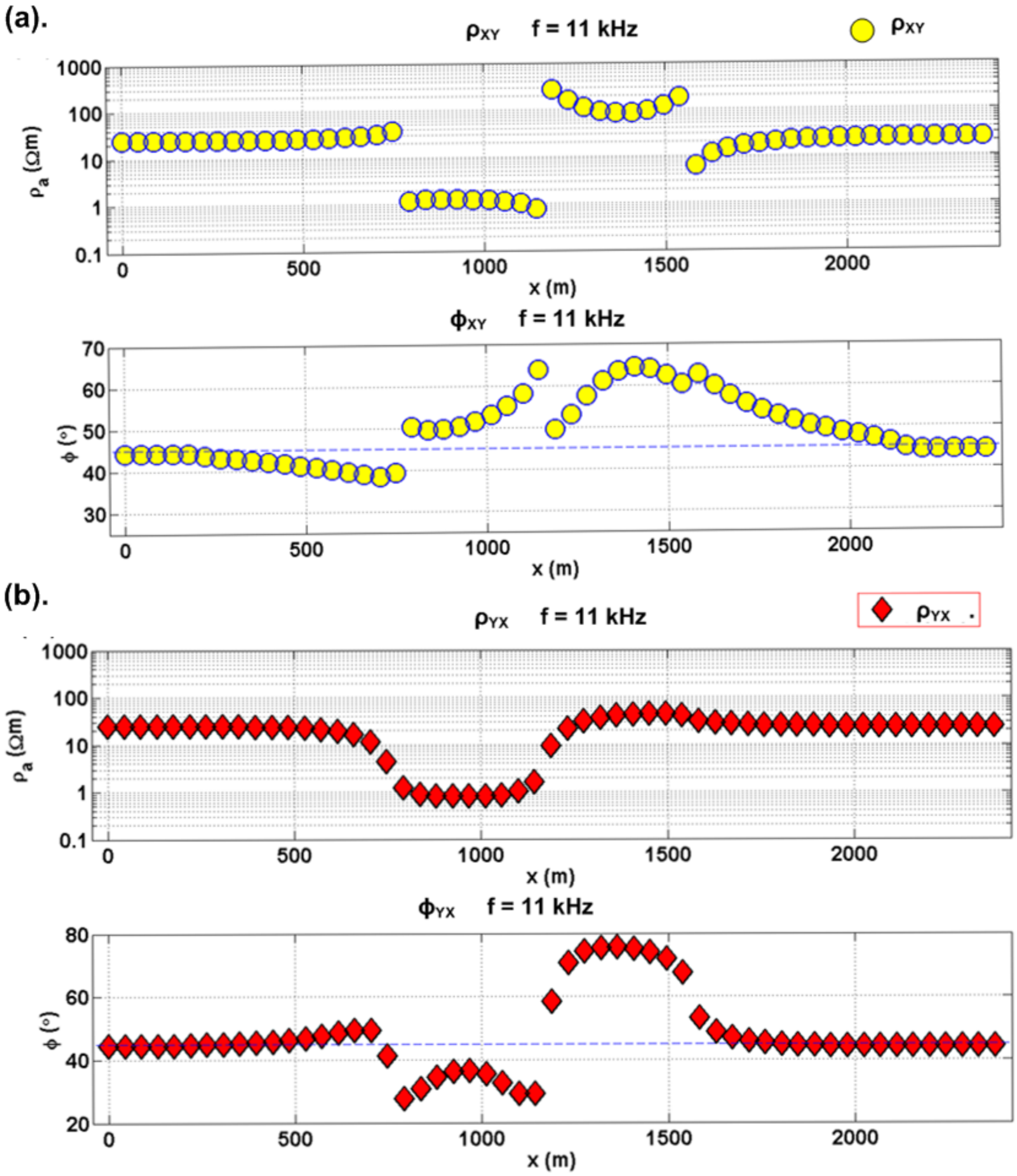

Figure H.2: *Three dimensional responses (a) Z_{xy} responses along the profile across the center of body at frequency of $f = 11$ kHz. (b) Z_{yx} responses along the profile across the center of body at frequency of $f = 11$ kHz.*

Appendix I

3-D Modeling of RMT Data

An example of the development of 3-D modeling of RMT data

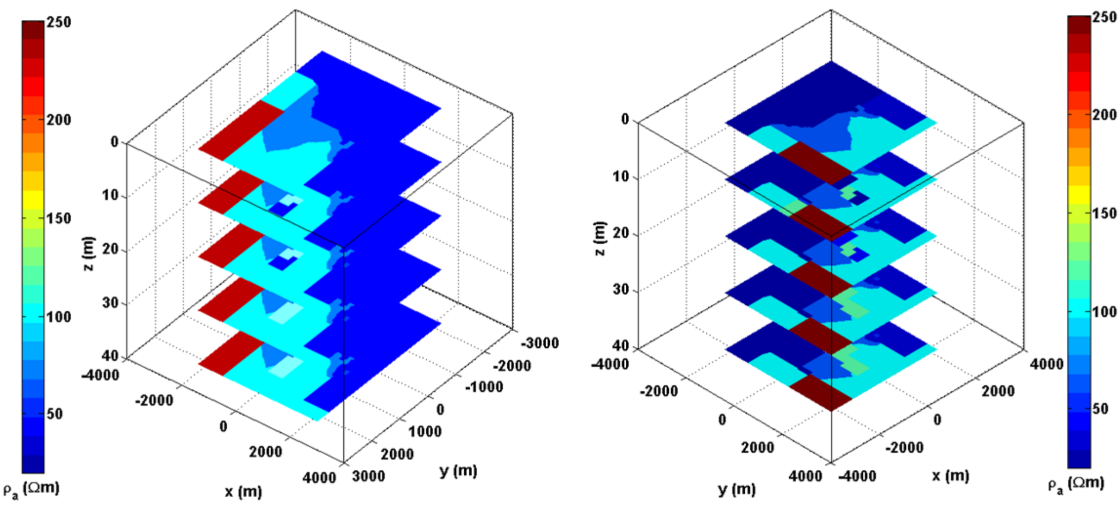

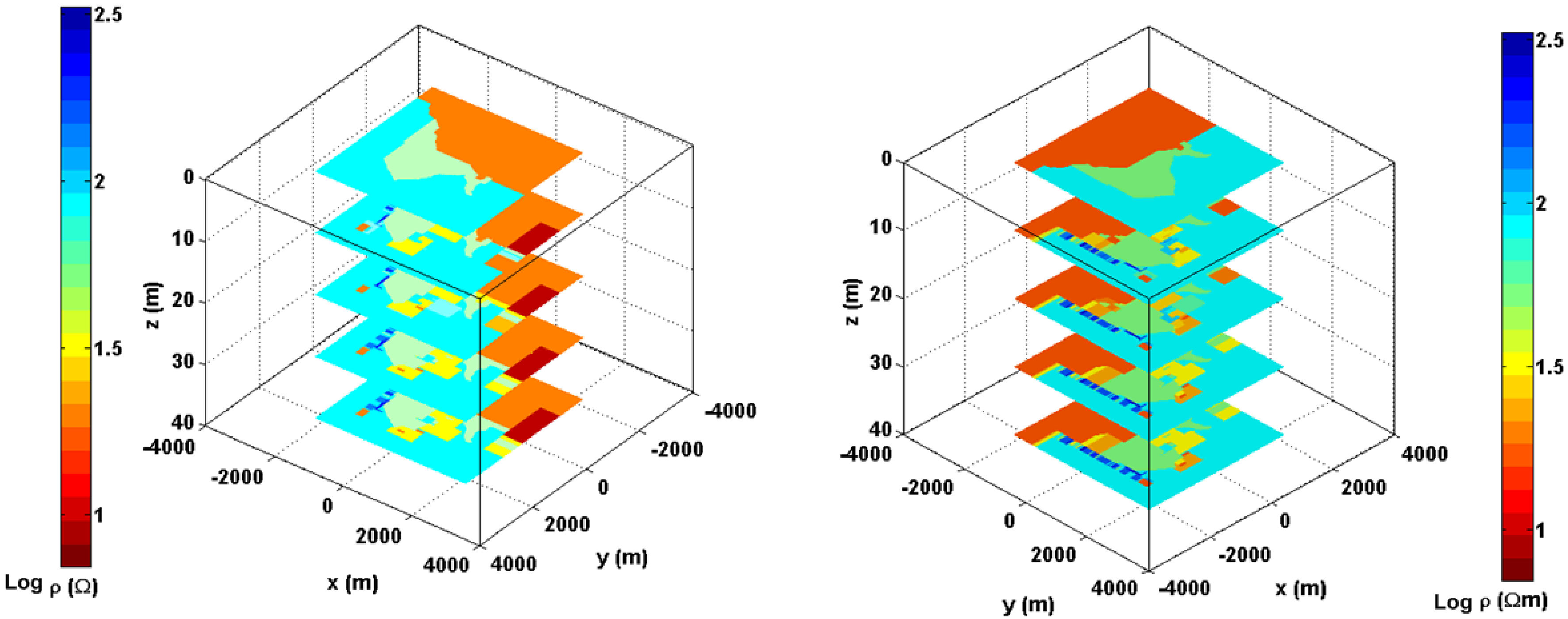

2.5
2
1.5
1
Log ρ (Ω)
0
10
20
30
40
z (m)
-4000
-2000
0
2000
4000
x (m)
-4000
-2000
0
2000
4000
y (m)
0
10
20
30
40
z (m)
-4000
-2000
0
2000
4000
y (m)
4000
2000
0
-2000
-4000
x (m)
2.5
2
1.5
1
Log ρ (Ωm)

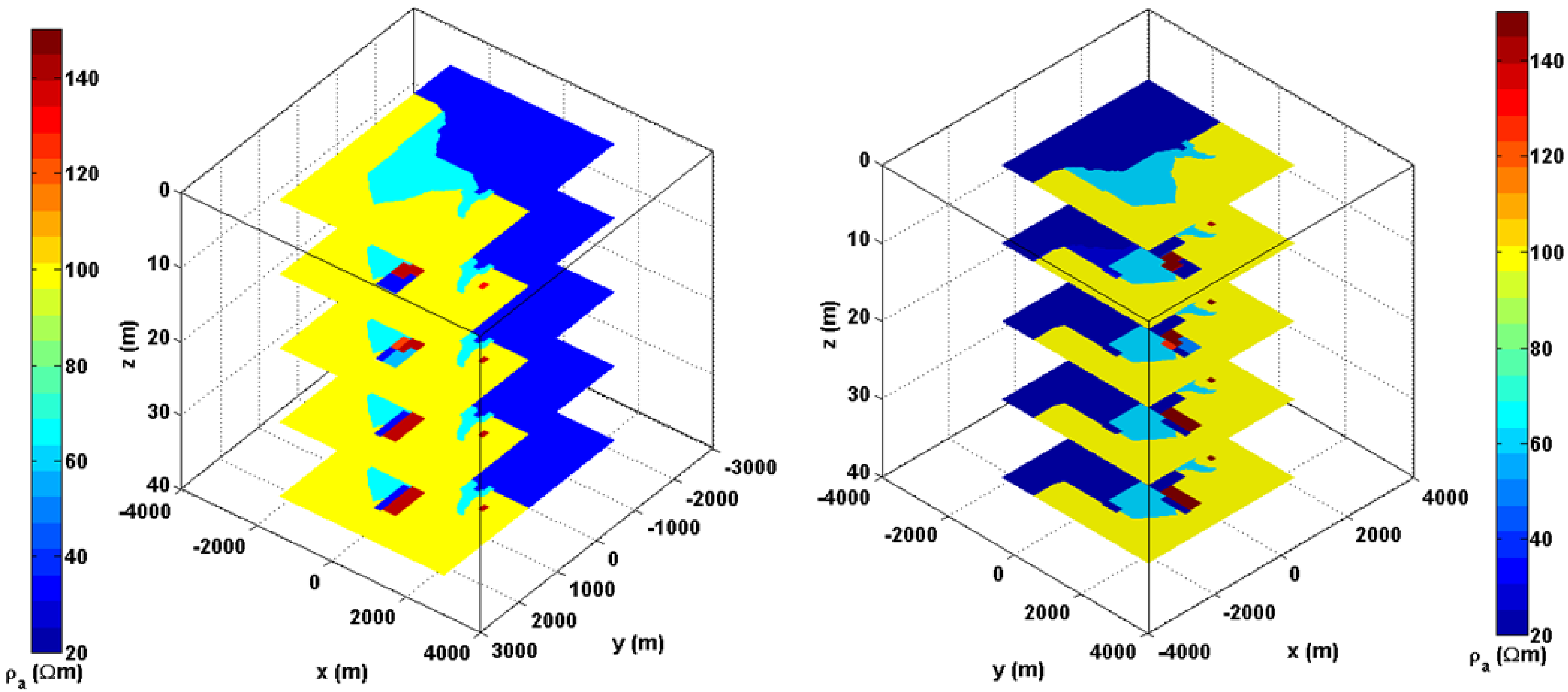

ρa (Ωm)
140
120
100
80
60
40
20
z (m)
0
10
20
30
40
x (m)
-4000
-2000
0
2000
4000
y (m)
-3000
-2000
-1000
0
1000
2000
3000

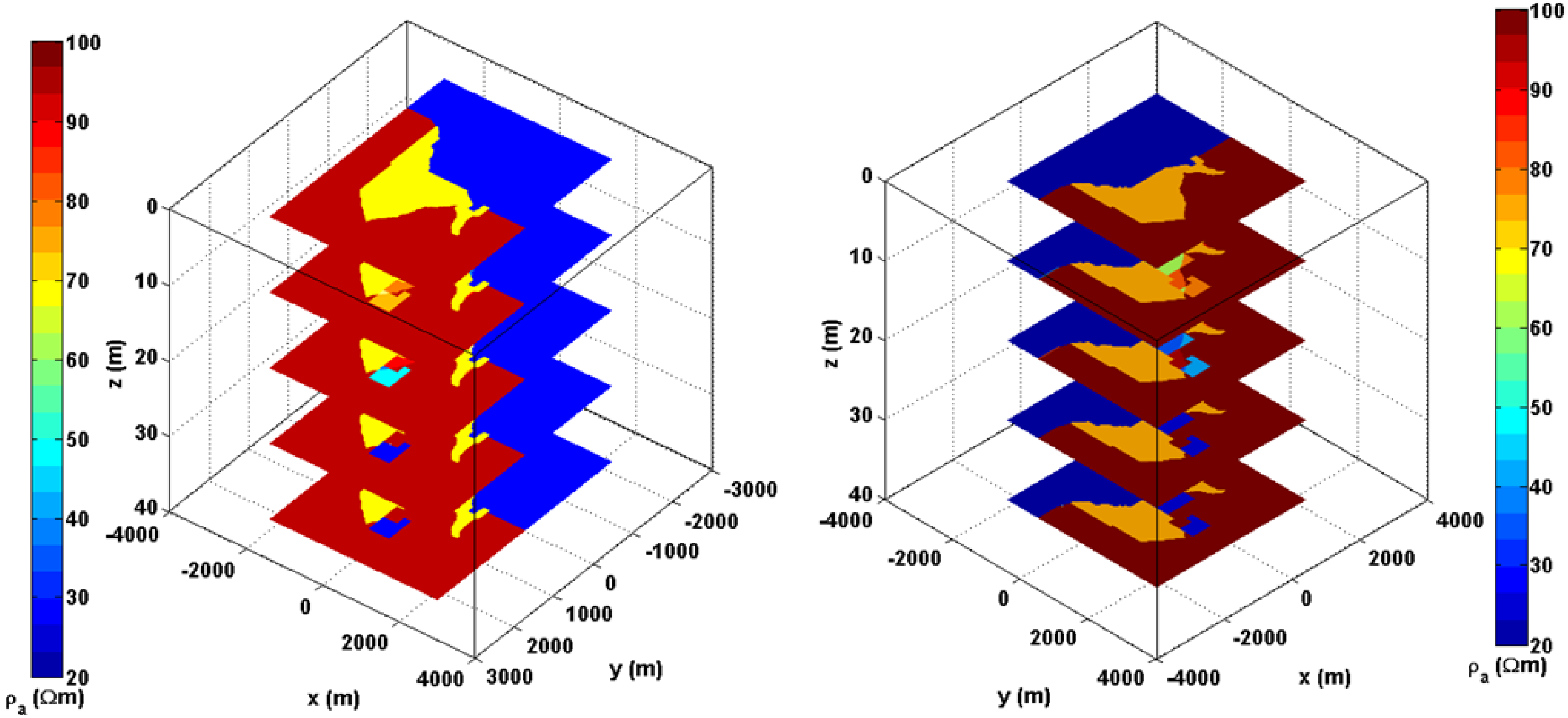

ρ_a (Ωm)
z (m)
x (m)
y (m)
y (m)
x (m)
z (m)
ρ_a (Ωm)

Appendix J

GPS Coordinates of RMT Data

GPS coordinatess of RMT data corresponding to the 2-D model of profile 1 - profile 8 based on WGS 84 system.

Table J.1: *GPS coordinates of RMT data of RMT 1 - RMT 30*

Station	Northing	Easting	Station	Northing	Easting
RMT1	N°40 39.330	E°23 18.893	RMT16	N°40 39.772	E°23 18.351
RMT2	N°40 39.708	E°23 18.887	RMT17	N°40 39.786	E°23 18.285
RMT3	N°40 39.330	E°23 18.893	RMT18	N°40 39.835	E°23 18.292
RMT4	N°40 39.708	E°23 18.887	RMT19	N°40 39.877	E°23 18.270
RMT5	N°40 40.104	E°23 18.901	RMT20	N°40 39.945	E°23 18.228
RMT6	N°40 39.513	E°23 18.900	RMT21	N°40 40.109	E°23 18.340
RMT7	N°40 39.584	E°23 18.861	RMT22	N°40 39.356	E°23 18.427
RMT8	N°40 39.449	E°23 18.926	RMT23	N°40 39.734	E°23 18.970
RMT9	N°40 40.194	E°23 18.978	RMT24	N°40 39.784	E°23 18.288
RMT10	N°40 39.545	E°23 18.454	RMT25	N°40 40.108	E°23 18.310
RMT11	N°40 39.651	E°23 18.387	RMT26	N°40 40.072	E°23 18.297
RMT12	N°40 39.624	E°23 18.389	RMT27	N°40 39.719	E°23 18.969
RMT13	N°40 39.679	E°23 18.394	RMT28	N°40 39.719	E°23 18.969
RMT14	N°40 39.717	E°23 18.405	RMT29	N°40 40.052	E°23 18.838
RMT15	N°40 39.750	E°23 18.367	RMT30	N°40 39.871	E°23 18.682

Table J.2: *GPS coordinatess of RMT data on profile 1*

Station	Northing	Easting	Station	Northing	Easting
RMT31	N°40 39.511	E°23 19.558	RMT53	N°40 39.805	E°23 19.560
RMT32	N°40 39.524	E°23 19.558	RMT54	N°40 39.819	E°23 19.560
RMT33	N°40 39.538	E°23 19.558	RMT55	N°40 39.832	E°23 19.560
RMT34	N°40 39.551	E°23 19.558	RMT56	N°40 39.860	E°23 19.561
RMT35	N°40 39.564	E°23 19.559	RMT57	N°40 39.860	E°23 19.561
RMT36	N°40 39.578	E°23 19.559	RMT58	N°40 39.873	E°23 19.561
RMT37	N°40 39.591	E°23 19.559	RMT59	N°40 39.898	E°23 19.516
RMT38	N°40 39.604	E°23 19.559	RMT60	N°40 39.911	E°23 19.517
RMT39	N°40 39.618	E°23 19.559	RMT61	N°40 39.925	E°23 19.517
RMT40	N°40 39.631	E°23 19.559	RMT62	N°40 39.952	E°23 19.517
RMT41	N°40 39.645	E°23 19.559	RMT63	N°40 39.965	E°23 19.517
RMT42	N°40 39.658	E°23 19.559	RMT64	N°40 39.979	E°23 19.517
RMT43	N°40 39.672	E°23 19.559	RMT65	N°40 39.992	E°23 19.518
RMT44	N°40 39.685	E°23 19.559	RMT66	N°40 40.006	E°23 19.518
RMT45	N°40 39.699	E°23 19.560	RMT67	N°40 40.019	E°23 19.518
RMT46	N°40 39.712	E°23 19.560	RMT68	N°40 40.033	E°23 19.518
RMT47	N°40 39.725	E°23 19.560	RMT69	N°40 40.046	E°23 19.519
RMT48	N°40 39.739	E°23 19.560	RMT70	N°40 40.060	E°23 19.519
RMT49	N°40 39.752	E°23 19.560	RMT71	N°40 40.073	E°23 19.519
RMT50	N°40 39.765	E°23 19.560	RMT72	N°40 40.087	E°23 19.519
RMT51	N°40 39.779	E°23 19.560	RMT73	N°40 40.100	E°23 19.519
RMT52	N°40 39.792	E°23 19.560			

Table J.3: *GPS coordinatess of RMT data on profile 2*

Station	Northing	Easting	Station	Northing	Easting
RMT74	N°40 39.326	E°23 18.956	RMT105	N°40 39.705	E°23 18.960
RMT77	N°40 39.340	E°23 18.957	RMT106	N°40 39.718	E°23 18.960
RMT78	N°40 39.353	E°23 18.957	RMT107	N°40 39.732	E°23 18.960
RMT79	N°40 39.367	E°23 18.957	RMT108	N°40 39.745	E°23 18.961
RMT80	N°40 39.381	E°23 18.957	RMT109	N°40 39.759	E°23 18.961
RMT81	N°40 39.394	E°23 18.957	RMT110	N°40 39.773	E°23 18.961
RMT82	N°40 39.407	E°23 18.957	RMT111	N°40 39.786	E°23 18.961
RMT83	N°40 39.421	E°23 18.957	RMT112	N°40 39.800	E°23 18.961
RMT84	N°40 39.434	E°23 18.957	RMT113	N°40 39.813	E°23 18.961
RMT85	N°40 39.448	E°23 18.958	RMT114	N°40 39.827	E°23 18.962
RMT87	N°40 39.461	E°23 18.958	RMT115	N°40 39.840	E°23 18.962
RMT88	N°40 39.475	E°23 18.958	RMT116	N°40 39.854	E°23 18.962
RMT89	N°40 39.488	E°23 18.958	RMT117	N°40 39.867	E°23 18.962
RMT90	N°40 39.502	E°23 18.958	RMT118	N°40 39.881	E°23 18.962
RMT91	N°40 39.515	E°23 18.958	RMT119	N°40 39.895	E°23 18.962
RMT92	N°40 39.529	E°23 18.958	RMT120	N°40 39.908	E°23 18.962
RMT93	N°40 39.542	E°23 18.958	RMT121	N°40 39.921	E°23 18.962
RMT94	N°40 39.556	E°23 18.959	RMT122	N°40 39.935	E°23 18.963
RMT95	N°40 39.569	E°23 18.959	RMT123	N°40 39.948	E°23 18.963
RMT96	N°40 39.583	E°23 18.959	RMT124	N°40 39.962	E°23 18.963
RMT97	N°40 39.596	E°23 18.959	RMT125	N°40 39.976	E°23 18.963
RMT98	N°40 39.610	E°23 18.959	RMT126	N°40 39.989	E°23 18.963
RMT99	N°40 39.623	E°23 18.959	RMT127	N°40 40.002	E°23 18.963
RMT100	N°40 39.637	E°23 18.960	RMT128	N°40 40.016	E°23 18.963
RMT101	N°40 39.650	E°23 18.960	RMT129	N°40 40.030	E°23 18.964
RMT102	N°40 39.664	E°23 18.960	RMT130	N°40 40.043	E°23 18.964
RMT103	N°40 39.677	E°23 18.960	RMT131	N°40 40.057	E°23 18.964
RMT104	N°40 39.691	E°23 18.960	RMT132	N°40 40.070	E°23 18.964

Table J.4: *GPS coordinatess of RMT data on profile 3*

Station	Northing	Easting	Station	Northing	Easting
RMT133	N°40 39.314	E°23 18.426	RMT167	N°40 39.732	E°23 18.419
RMT134	N°40 39.327	E°23 18.426	RMT168	N°40 39.745	E°23 18.419
RMT136	N°40 39.341	E°23 18.426	RMT169	N°40 39.812	E°23 18.536
RMT137	N°40 39.354	E°23 18.425	RMT170	N°40 39.825	E°23 18.535
RMT138	N°40 39.368	E°23 18.425	RMT171	N°40 39.839	E°23 18.535
RMT140	N°40 39.381	E°23 18.425	RMT172	N°40 39.852	E°23 18.534
RMT141	N°40 39.395	E°23 18.425	RMT173	N°40 39.866	E°23 18.534
RMT142	N°40 39.408	E°23 18.424	RMT174	N°40 39.879	E°23 18.534
RMT143	N°40 39.422	E°23 18.424	RMT175	N°40 39.893	E°23 18.533
RMT145	N°40 39.435	E°23 18.424	RMT176	N°40 39.906	E°23 18.533
RMT146	N°40 39.449	E°23 18.424	RMT177	N°40 39.920	E°23 18.533
RMT147	N°40 39.463	E°23 18.424	RMT178	N°40 39.933	E°23 18.532
RMT148	N°40 39.476	E°23 18.423	RMT179	N°40 39.946	E°23 18.532
RMT149	N°40 39.490	E°23 18.423	RMT180	N°40 39.960	E°23 18.531
RMT150	N°40 39.504	E°23 18.423	RMT181	N°40 39.974	E°23 18.531
RMT151	N°40 39.517	E°23 18.423	RMT182	N°40 39.987	E°23 18.531
RMT152	N°40 39.531	E°23 18.422	RMT183	N°40 40.000	E°23 18.530
RMT153	N°40 39.544	E°23 18.422	RMT184	N°40 40.014	E°23 18.530
RMT154	N°40 39.557	E°23 18.422	RMT185	N°40 40.027	E°23 18.530
RMT155	N°40 39.570	E°23 18.422	RMT186	N°40 40.041	E°23 18.529
RMT156	N°40 39.584	E°23 18.421	RMT187	N°40 40.054	E°23 18.529
RMT157	N°40 39.598	E°23 18.421	RMT188	N°40 40.068	E°23 18.529
RMT158	N°40 39.611	E°23 18.421	RMT189	N°40 40.081	E°23 18.528
RMT159	N°40 39.625	E°23 18.421	RMT190	N°40 40.095	E°23 18.528
RMT160	N°40 39.638	E°23 18.420	RMT191	N°40 40.109	E°23 18.527
RMT161	N°40 39.652	E°23 18.420	RMT192	N°40 40.122	E°23 18.527
RMT162	N°40 39.665	E°23 18.420	RMT193	N°40 40.136	E°23 18.527
RMT163	N°40 39.679	E°23 18.420	RMT194	N°40 40.149	E°23 18.526
RMT164	N°40 39.692	E°23 18.420	RMT195	N°40 40.163	E°23 18.526
RMT165	N°40 39.705	E°23 18.419	RMT196	N°40 40.176	E°23 18.526
RMT166	N°40 39.719	E°23 18.419	RMT197	N°40 40.189	E°23 18.525

Table J.5: *GPS coordinatess of RMT data on profile 4*

Station	Northing	Easting	Station	Northing	Easting
RMT198	N°40 39.314	E°23 18.361	RMT229	N°40 39.730	E°23 18.357
RMT199	N°40 39.327	E°23 18.361	RMT230	N°40 39.744	E°23 18.357
RMT200	N°40 39.341	E°23 18.361	RMT231	N°40 39.757	E°23 18.356
RMT201	N°40 39.354	E°23 18.361	RMT232	N°40 39.771	E°23 18.356
RMT202	N°40 39.368	E°23 18.361	RMT233	N°40 39.784	E°23 18.356
RMT203	N°40 39.381	E°23 18.360	RMT234	N°40 39.798	E°23 18.356
RMT204	N°40 39.395	E°23 18.360	RMT235	N°40 39.811	E°23 18.356
RMT205	N°40 39.408	E°23 18.360	RMT236	N°40 39.824	E°23 18.356
RMT206	N°40 39.422	E°23 18.360	RMT237	N°40 39.838	E°23 18.355
RMT207	N°40 39.435	E°23 18.360	RMT238	N°40 39.851	E°23 18.355
RMT208	N°40 39.448	E°23 18.360	RMT239	N°40 39.864	E°23 18.355
RMT209	N°40 39.461	E°23 18.360	RMT240	N°40 39.877	E°23 18.355
RMT210	N°40 39.475	E°23 18.359	RMT241	N°40 39.891	E°23 18.355
RMT211	N°40 39.488	E°23 18.359	RMT242	N°40 39.904	E°23 18.355
RMT212	N°40 39.502	E°23 18.359	RMT243	N°40 39.918	E°23 18.355
RMT213	N°40 39.515	E°23 18.359	RMT244	N°40 39.931	E°23 18.354
RMT214	N°40 39.528	E°23 18.359	RMT245	N°40 39.945	E°23 18.354
RMT215	N°40 39.542	E°23 18.359	RMT246	N°40 39.958	E°23 18.354
RMT216	N°40 39.555	E°23 18.359	RMT247	N°40 39.972	E°23 18.354
RMT217	N°40 39.569	E°23 18.358	RMT248	N°40 39.985	E°23 18.354
RMT218	N°40 39.582	E°23 18.358	RMT249	N°40 39.999	E°23 18.354
RMT219	N°40 39.595	E°23 18.358	RMT250	N°40 40.013	E°23 18.354
RMT220	N°40 39.609	E°23 18.358	RMT251	N°40 40.026	E°23 18.353
RMT221	N°40 39.623	E°23 18.358	RMT252	N°40 40.039	E°23 18.353
RMT222	N°40 39.636	E°23 18.358	RMT253	N°40 40.053	E°23 18.353
RMT223	N°40 39.650	E°23 18.357	RMT254	N°40 40.066	E°23 18.353
RMT224	N°40 39.663	E°23 18.357	RMT255	N°40 40.080	E°23 18.353
RMT225	N°40 39.676	E°23 18.357	RMT256	N°40 40.093	E°23 18.353
RMT226	N°40 39.690	E°23 18.357	RMT257	N°40 40.120	E°23 18.352
RMT227	N°40 39.704	E°23 18.357	RMT258	N°40 40.134	E°23 18.352
RMT228	N°40 39.717	E°23 18.357	RMT259	N°40 40.147	E°23 18.352

Table J.6: *GPS coordinatess of RMT data on profile 5*

Station	Northing	Easting
RMT260	N°40 39.326	E°23 18.827
RMT261	N°40 39.338	E°23 18.833
RMT262	N°40 39.351	E°23 18.840
RMT263	N°40 39.364	E°23 18.846
RMT264	N°40 39.376	E°23 18.852
RMT265	N°40 39.389	E°23 18.858
RMT266	N°40 39.401	E°23 18.865
RMT267	N°40 39.414	E°23 18.871
RMT268	N°40 39.427	E°23 18.877
RMT269	N°40 39.439	E°23 18.884
RMT270	N°40 39.452	E°23 18.890
RMT271	N°40 39.464	E°23 18.897
RMT272	N°40 39.477	E°23 18.903
RMT273	N°40 39.490	E°23 18.909
RMT274	N°40 39.502	E°23 18.916
RMT275	N°40 39.515	E°23 18.922
RMT276	N°40 39.527	E°23 18.928
RMT277	N°40 39.539	E°23 18.935
RMT278	N°40 39.553	E°23 18.940
RMT279	N°40 39.565	E°23 18.946
RMT280	N°40 39.578	E°23 18.953
RMT281	N°40 39.590	E°23 18.960
RMT282	N°40 39.603	E°23 18.965
RMT283	N°40 39.615	E°23 18.972
RMT284	N°40 39.628	E°23 18.978
RMT285	N°40 39.641	E°23 18.984
RMT286	N°40 39.654	E°23 18.990
RMT287	N°40 39.666	E°23 18.997
RMT288	N°40 39.678	E°23 19.004
RMT289	N°40 39.691	E°23 19.009
RMT290	N°40 39.704	E°23 19.016
RMT291	N°40 39.716	E°23 19.022
RMT292	N°40 39.729	E°23 19.028
RMT293	N°40 39.742	E°23 19.035
RMT294	N°40 39.754	E°23 19.041
RMT295	N°40 39.767	E°23 19.048
RMT296	N°40 39.780	E°23 19.052

Table J.7: *GPS coordinatess of RMT data on profile 6*

Station	Northing	Easting	Station	Northing	Easting
RMT296	N°40 39.605	E°23 18.925	RMT322	N°40 39.856	E°23 18.629
RMT297	N°40 39.595	E°23 18.937	RMT323	N°40 39.866	E°23 18.617
RMT298	N°40 39.624	E°23 18.900	RMT324	N°40 39.876	E°23 18.606
RMT299	N°40 39.674	E°23 18.841	RMT325	N°40 39.886	E°23 18.594
RMT300	N°40 39.664	E°23 18.853	RMT326	N°40 39.897	E°23 18.582
RMT301	N°40 39.655	E°23 18.865	RMT327	N°40 39.907	E°23 18.571
RMT302	N°40 39.644	E°23 18.877	RMT328	N°40 39.917	E°23 18.559
RMT303	N°40 39.635	E°23 18.889	RMT329	N°40 39.927	E°23 18.547
RMT304	N°40 39.615	E°23 18.913	RMT330	N°40 39.938	E°23 18.535
RMT305	N°40 39.724	E°23 18.781	RMT331	N°40 39.958	E°23 18.512
RMT306	N°40 39.714	E°23 18.793	RMT332	N°40 39.948	E°23 18.523
RMT307	N°40 39.704	E°23 18.805	RMT333	N°40 39.968	E°23 18.500
RMT308	N°40 39.694	E°23 18.817	RMT334	N°40 39.979	E°23 18.488
RMT309	N°40 39.684	E°23 18.829	RMT335	N°40 39.989	E°23 18.477
RMT310	N°40 39.774	E°23 18.721	RMT336	N°40 39.999	E°23 18.465
RMT311	N°40 39.764	E°23 18.733	RMT337	N°40 40.009	E°23 18.453
RMT312	N°40 39.754	E°23 18.745	RMT338	N°40 40.019	E°23 18.442
RMT313	N°40 39.744	E°23 18.757	RMT339	N°40 40.029	E°23 18.430
RMT314	N°40 39.734	E°23 18.769	RMT340	N°40 40.040	E°23 18.418
RMT315	N°40 39.795	E°23 18.699	RMT341	N°40 40.050	E°23 18.406
RMT316	N°40 39.784	E°23 18.709	RMT342	N°40 40.060	E°23 18.394
RMT317	N°40 39.805	E°23 18.687	RMT343	N°40 40.070	E°23 18.383
RMT318	N°40 39.815	E°23 18.676	RMT344	N°40 40.081	E°23 18.371
RMT319	N°40 39.826	E°23 18.664	RMT345	N°40 40.091	E°23 18.359
RMT320	N°40 39.836	E°23 18.652	RMT346	N°40 40.101	E°23 18.348
RMT321	N°40 39.846	E°23 18.641			

Table J.8: *GPS coordinatess of RMT data on profile 7*

Station	Northing	Easting
RMT347	N°40 39.781	E°23 18.557
RMT348	N°40 39.782	E°23 18.574
RMT349	N°40 39.782	E°23 18.592
RMT350	N°40 39.783	E°23 18.610
RMT351	N°40 39.784	E°23 18.628
RMT352	N°40 39.784	E°23 18.645
RMT353	N°40 39.785	E°23 18.663
RMT354	N°40 39.786	E°23 18.681
RMT355	N°40 39.787	E°23 18.698
RMT356	N°40 39.787	E°23 18.716
RMT357	N°40 39.788	E°23 18.733
RMT358	N°40 39.789	E°23 18.751
RMT359	N°40 39.789	E°23 18.769
RMT360	N°40 39.790	E°23 18.787
RMT361	N°40 39.791	E°23 18.804
RMT362	N°40 39.791	E°23 18.822
RMT363	N°40 39.792	E°23 18.840
RMT364	N°40 39.793	E°23 18.858
RMT365	N°40 39.793	E°23 18.876
RMT366	N°40 39.794	E°23 18.893
RMT367	N°40 39.795	E°23 18.911
RMT368	N°40 39.796	E°23 18.929
RMT369	N°40 39.796	E°23 18.947
RMT370	N°40 39.797	E°23 18.965
RMT371	N°40 39.798	E°23 18.982
RMT372	N°40 39.798	E°23 19.000
RMT373	N°40 39.799	E°23 19.018
RMT374	N°40 39.800	E°23 19.036
RMT375	N°40 39.800	E°23 19.053
RMT376	N°40 39.801	E°23 19.071
RMT377	N°40 39.802	E°23 19.089
RMT378	N°40 39.802	E°23 19.106
RMT379	N°40 39.803	E°23 19.124
RMT380	N°40 39.804	E°23 19.142
RMT381	N°40 39.804	E°23 19.159
RMT382	N°40 39.807	E°23 19.212
RMT383	N°40 39.807	E°23 19.230

Table J.9: *GPS coordinatess of RMT data on profile 8*

Station	Northing	Easting	Station	Northing	Easting
RMT384	N°40 40.204	E°23 18.569	RMT415	N°40 40.143	E°23 19.114
RMT385	N°40 40.202	E°23 18.587	RMT416	N°40 40.141	E°23 19.132
RMT386	N°40 40.200	E°23 18.604	RMT417	N°40 40.139	E°23 19.149
RMT387	N°40 40.198	E°23 18.622	RMT418	N°40 40.137	E°23 19.167
RMT388	N°40 40.196	E°23 18.640	RMT419	N°40 40.135	E°23 19.185
RMT389	N°40 40.194	E°23 18.657	RMT420	N°40 40.133	E°23 19.202
RMT390	N°40 40.192	E°23 18.675	RMT421	N°40 40.131	E°23 19.220
RMT391	N°40 40.190	E°23 18.692	RMT422	N°40 40.130	E°23 19.238
RMT392	N°40 40.188	E°23 18.710	RMT423	N°40 40.128	E°23 19.255
RMT393	N°40 40.186	E°23 18.728	RMT424	N°40 40.126	E°23 19.273
RMT394	N°40 40.184	E°23 18.745	RMT425	N°40 40.124	E°23 19.290
RMT395	N°40 40.182	E°23 18.763	RMT426	N°40 40.122	E°23 19.307
RMT396	N°40 40.180	E°23 18.781	RMT427	N°40 40.120	E°23 19.324
RMT397	N°40 40.178	E°23 18.798	RMT428	N°40 40.118	E°23 19.342
RMT398	N°40 40.176	E°23 18.816	RMT429	N°40 40.116	E°23 19.360
RMT399	N°40 40.175	E°23 18.833	RMT430	N°40 40.114	E°23 19.377
RMT400	N°40 40.173	E°23 18.851	RMT431	N°40 40.112	E°23 19.395
RMT401	N°40 40.171	E°23 18.868	RMT432	N°40 40.110	E°23 19.413
RMT402	N°40 40.169	E°23 18.886	RMT433	N°40 40.108	E°23 19.430
RMT403	N°40 40.167	E°23 18.903	RMT434	N°40 40.106	E°23 19.447
RMT404	N°40 40.165	E°23 18.921	RMT435	N°40 40.104	E°23 19.465
RMT405	N°40 40.163	E°23 18.938	RMT436	N°40 40.102	E°23 19.482
RMT406	N°40 40.161	E°23 18.956	RMT437	N°40 40.100	E°23 19.500
RMT407	N°40 40.159	E°23 18.974	RMT438	N°40 40.098	E°23 19.517
RMT408	N°40 40.157	E°23 18.991	RMT439	N°40 40.097	E°23 19.535
RMT409	N°40 40.155	E°23 19.009	RMT440	N°40 40.095	E°23 19.552
RMT410	N°40 40.153	E°23 19.026	RMT441	N°40 40.093	E°23 19.570
RMT411	N°40 40.151	E°23 19.044	RMT442	N°40 40.091	E°23 19.588
RMT412	N°40 40.149	E°23 19.061	RMT443	N°40 40.089	E°23 19.605
RMT413	N°40 40.147	E°23 19.079			
RMT414	N°40 40.145	E°23 19.097			

Appendix K

GPS Coordinates of TEM Data

Table K.1: *GPS coordinates of TEM data on TEM 1 - TEM 30 and profile 1*

TEM 1 - 18			Profile 1		
TEM1	N°40 39.330	E°23 18.893	TEM31	N°40 39.562	E°23 19.533
TEM2	N°40 39.708	E°23 18.887	TEM32	N°40 39.592	E°23 19.534
TEM3	N°40 39.330	E°23 18.893	TEM33	N°40 39.618	E°23 19.531
TEM4	N°40 39.708	E°23 18.887	TEM34	N°40 39.644	E°23 19.531
TEM5	N°40 40.104	E°23 18.901	TEM35	N°40 39.671	E°23 19.531
TEM6	N°40 39.513	E°23 18.900	TEM36	N°40 39.691	E°23 19.569
TEM7	N°40 39.584	E°23 18.861	TEM37	N°40 39.717	E°23 19.569
TEM8	N°40 39.449	E°23 18.926	TEM38	N°40 39.745	E°23 19.568
TEM9	N°40 40.194	E°23 18.978	TEM39	N°40 39.771	E°23 19.567
TEM10	N°40 39.545	E°23 18.454	TEM40	N°40 39.798	E°23 19.567
TEM11	N°40 39.651	E°23 18.387	TEM41	N°40 39.825	E°23 19.566
TEM12	N°40 39.624	E°23 18.389	TEM42	N°40 39.852	E°23 19.566
TEM13	N°40 39.679	E°23 18.394	TEM43	N°40 39.879	E°23 19.566
TEM14	N°40 39.717	E°23 18.405	TEM44	N°40 39.907	E°23 19.511
TEM15	N°40 39.750	E°23 18.367	TEM45	N°40 39.934	E°23 19.511
TEM16	N°40 39.772	E°23 18.351	TEM46	N°40 39.961	E°23 19.512
TEM17	N°40 39.786	E°23 18.285	TEM47	N°40 39.988	E°23 19.512
TEM18	N°40 39.835	E°23 18.292	TEM48	N°40 40.015	E°23 19.513
TEM 19 - 30					
TEM19	N°40 39.877	E°23 18.270	TEM25	N°40 40.108	E°23 18.310
TEM20	N°40 39.945	E°23 18.228	TEM26	N°40 40.072	E°23 18.297
TEM21	N°40 40.109	E°23 18.340	TEM27	N°40 39.719	E°23 18.969
TEM22	N°40 39.356	E°23 18.427	TEM28	N°40 39.719	E°23 18.969
TEM23	N°40 39.734	E°23 18.970	TEM29	N°40 40.052	E°23 18.838
TEM24	N°40 39.784	E°23 18.288	TEM30	N°40 39.871	E°23 18.682

Table K.2: *GPS coordinates of TEM data on profile 2 and profile 3*

Profile 2			Profile 3		
TEM49	N°40 39.329	E°23 18.9557	TEM76	N°40 39.356	E°23 18.427
TEM50	N°40 39.353	E°23 18.9577	TEM77	N°40 39.384	E°23 18.427
TEM51	N°40 39.381	E°23 18.957	TEM78	N°40 39.411	E°23 18.427
TEM52	N°40 39.407	E°23 18.957	TEM79	N°40 39.438	E°23 18.427
TEM53	N°40 39.434	E°23 18.957	TEM80	N°40 39.465	E°23 18.427
TEM54	N°40 39.461	E°23 18.958	TEM81	N°40 39.492	E°23 18.428
TEM55	N°40 39.488	E°23 18.958	TEM82	N°40 39.519	E°23 18.428
TEM56	N°40 39.515	E°23 18.958	TEM83	N°40 39.546	E°23 18.428
TEM57	N°40 39.542	E°23 18.958	TEM84	N°40 39.572	E°23 18.428
TEM58	N°40 39.569	E°23 18.959	TEM85	N°40 39.600	E°23 18.428
TEM59	N°40 39.596	E°23 18.959	TEM86	N°40 39.627	E°23 18.429
TEM60	N°40 39.623	E°23 18.959	TEM87	N°40 39.624	E°23 18.389
TEM61	N°40 39.650	E°23 18.960	TEM88	N°40 39.681	E°23 18.429
TEM62	N°40 39.677	E°23 18.960	TEM89	N°40 39.707	E°23 18.429
TEM63	N°40 39.705	E°23 18.960	TEM90	N°40 39.734	E°23 18.429
TEM64	N°40 39.732	E°23 18.960	TEM91	N°40 39.762	E°23 18.429
TEM65	N°40 39.759	E°23 18.961	TEM92	N°40 39.778	E°23 18.515
TEM66	N°40 39.786	E°23 18.961	TEM93	N°40 39.806	E°23 18.512
TEM67	N°40 39.813	E°23 18.961	TEM94	N°40 39.833	E°23 18.512
TEM68	N°40 39.840	E°23 18.962	TEM95	N°40 39.860	E°23 18.512
TEM69	N°40 39.867	E°23 18.962	TEM96	N°40 39.890	E°23 18.510
TEM70	N°40 39.895	E°23 18.961	TEM97	N°40 39.913	E°23 18.512
TEM71	N°40 39.921	E°23 18.962	TEM98	N°40 39.940	E°23 18.511
TEM72	N°40 39.948	E°23 18.962	TEM99	N°40 39.967	E°23 18.511
TEM73	N°40 39.975	E°23 18.963	TEM100	N°40 39.994	E°23 18.511
TEM74	N°40 40.002	E°23 18.962	TEM101	N°40 40.021	E°23 18.511
TEM75	N°40 40.030	E°23 18.964	TEM102	N°40 40.048	E°23 18.511
			TEM103	N°40 40.075	E°23 18.511
			TEM104	N°40 40.102	E°23 18.511
			TEM105	N°40 40.129	E°23 18.511
			TEM106	N°40 40.156	E°23 18.511
			TEM107	N°40 40.183	E°23 18.511

Acknowledgment

There are absolutely a lot of parties who have helped and supported me during conducting the research for this thesis. Thus, I can't complete this thesis without giving high appreciation and gratitude to them and some authorities.

I would like to profusely thank to the Prof. Dr. Bülent Tezkan who has been my supervisor and patiently given me guidance in learning Electromagnetics. I highly appreciate all inputs and discussions throughout my study and research at University of Cologne. I would like to thank to Prof. Dr. Andreas Junge for appraising this thesis.

I also would like to thank to Dr. Marcus Gurk who has shared the Marie Curie Project during performing measurements in Greece. Great thanks to Martin Biolik, Klaus Lippert, Pritam Yogeshwar and Cristian Plog for helping me during the field campaign. Without good team work, I don't assure to obtain much field data. I would like to thank to Rainer Bergers who has helped me in preparing all matters prior to going to the field, handling the requirements and giving inputs for all problems during the study. To Dr. Alexandros Savvaidis and Elena Zargli from ITSAK, I highly deliver my gratitude for all accesses provided during conducting the research in the area, for all help with providing geological maps.

Here, I would like to say much thank to Timo Zettl, Dr. Kumari Sudha, Michael von Papen, Pritam Yogeshwar and Jan Witke for giving me constructive criticism and reviewing my manuscript.

I've felt a very tremendous atmosphere during studying here and a sense of belonging and solidarity does gives me so meaningful relationships especially to Michael von Papen, Klaus Lippert, Pritam Yogeshwar, Amir Haroon, Dr. Kumari Sudha, Annika Rödder, Laura Pascharat, Yvonne Tuchscherer, Jan Wittke, Rudolf Eröss, Jan Köhler, Juliane Adrian, Hannah Großbach, Daniel Steinbach, Ayca Ardali, Sven Jacobsen, Mario Seufert and Lorentz Roth. My room mates, Martin Biolik and Timo Zettl, thanks. Also, I would like thank to Andreas Busse for helping me much in setting up my computer. And great thanks to those of my friends whom I can't mention all for your supports. I would be so proud if you don't forget to wear the **blue tricots** when the next football match comes.

I would like to deliver my best gratitude to Dr. Komang Anggayana, Prof. Dr. Umar Fauzi and Dr. Wahyudi Parnadi for giving me advice to study successfully.

I would like to express deepest gratitude to my perents. Finally, I would like to profusely thank my wife and my daughter for being patient and always giving me support so I could finish this thesis. Thanks you very much, Yayuk Hidayati Widodo.

Your work to take of care Rania Ayu Widya Ramadhani Widodo is equally precious as this study.

Erklärung

Ich versichere, dass ich die von mir vorgelegte Dissertation selbständig angefertigt, die benutzten Quellen und Hilfsmittel vollständig angegeben und die Stellen der Arbeit - einschliesslich Abbildungen und Tabellen und Karten, die anderen Werken im Wortlaut oder dem Sinn nach entnommen sind, in jedem Einzelfall als Entlehnung kenntlich gemacht habe; dass diese Dissertation noch keiner anderen Fakultät oder Universität zur Prüfung vorgelegen hat; dass sie abgesehen von unten angegebenen Teilpublikationen - noch nicht veröffentlicht worden ist sowie, dass ich eine solche Veröffentlichung vor Abschluss des Promotionsverfahrens nicht vornehmen werde. Die Bestimmungen dieser Promotionordnung sind mir bekannt. Die von mir vorgelegte Dissertation ist von Prof. Dr. B. Tezkan betreut worden.

Köln, April 2012

Widodo

Teilpublikationen

List of publications and extended abstract while at the institute of Geophysics and Meteorology (IGM), University of Cologne:

1. Widodo, Gurk M., Tezkan B., Site Effect assessment in the Magdonion Basin using RMT and TEM data, Schumucker-Weidelt Kolloqium proceedings ISSN 2190-7021, 2009.

2. Widodo, Tezkan B., Gurk M., Site Effect assessment using RMT and TEM soundings on active Fault, Northern Greece, EMIW Proceeding, 2009.

3. Widodo, Tezkan B., Gurk M., Investigation on an Active Fault using RMT and TEM in Mygdonian Basin, Asian Physic Symposium (APS) Proceedings, Volume 1325, pp. 147-150 (2010), DOI: 10.1063/1.3537884, 2010.

4. Widodo, Tezkan B., Gurk M., Investigation on an Active Fault using RMT and TEM soundings, École Doctorale Des Sciences De La Terre, Congrès des Doctorands Proceedings, 2011.

5. Widodo, Tezkan B., Gurk M., Studies of A Fault Structure Using Electromagnetic Techniques in Mygdonian Basin, Nortern Greece, Schumucker-Weidelt Kolloqium proceedings, 2011.

Widodo

Adresse:	Theresienstr. 64 50931 Köln
Telefon:	0221/4706131
E-Mail:	widodo@geo.uni-koeln.de
Geburtsdatum:	13.04.1978
Geburtsort:	Tuban, Ost Java (Indonesia)
Staatsangehorigkeit:	Indonesisch

Schulbildung:	
1984-1990	SDN Sidomulyo 33-Grundschule, Tuban - Ost Java
1990-1996	SMPN 3-SMAN 1-Gymnasium, Tuban - Ost Java

Universität	
1997-2002	Sriwijaya University, Süd Sumatra Abschluß: Bachelor of Technique (S.T) Bergbauingenieur (Explorationsgeophysiker)
2005-2007	Institute Technology of Bandung, West Java Abschluss: Master of Technique (M.T.) Bergbauingenieur (Explorationsgeophysiker)
Seit WS 2008	Universität zu Köln Institute für Geophysik und Meteorologie Wissenschaftlicher Mitarbeiter Studienfach: Geophysik - Promotion